

## ABSTRACT

SALMON, MICHAEL EDWARD. The Growth and Characterization of Alkylphosphonic Acid Self-Assembled Nanofibers. (Under the direction of Dr. Phillip E. Russell.)

The focus of this research was to investigate the formation and properties of novel Self-Assembled Nanofibers (SANs) created by the treatment of aluminum with solutions of short chain-length alkylphosphonic acids (APAs) in ethanol. A special emphasis was placed on the creation of APA SANs isolated from the immersed aluminum source and development of analysis techniques for artifact reduced characterization of as-grown individual SANs.

Novel immersion growth techniques were devised for the reproducible creation of supported and unsupported isolated methylphosphonic acid (C1), propylphosphonic acid (C3), and pentylphosphonic acid (C5) SANs on  $\text{Si}_3\text{N}_4$  and aluminum coated ProtoChips<sup>TM</sup> DuraSiN<sup>TM</sup>  $\text{Si}_3\text{N}_4$  meshes respectively. Additionally, a novel biased immersion growth technique was developed, increasing growth rates as well as allowing for APA SAN deposition onto a variety of substrates including Au microelectrodes.

A combination of complimentary analysis techniques including: Atomic force microscopy (AFM), Scanning Transmission Electron Microscopy (STEM), Energy Dispersive Spectrometry (EDS), X-Ray Photoelectron Spectroscopy (XPS), and Electron Energy Loss Spectroscopy (EELS) were utilized to characterize the morphology, composition and chemistry of isolated individual APA SANs. STEM and AFM revealed individual APA SANs are actually composed of layered fibril bundles. Qualitative compositional analysis showed APA SANs were primarily composed of oxygen, carbon, phosphorus, and aluminum with phosphorus:aluminum ratios determined to be between 1.5 and 4.2. Quantitative XPS and EELS analysis provided further evidence that the detected aluminum was non-metallic and likely oxidized. STEM with EELS was utilized to

definitively correlate the presence of aluminum, phosphorus, oxygen, and carbon to a 5 nm region of several overlapping unsupported C1 SANs.

Thermal analysis of APA SANs on Al as well as isolated on  $\text{Si}_3\text{N}_4$  revealed a nearly 5X increase in thermal stability as compared to the ~ 100C-120C melting points of pure APAs. AFM nanoindentation and nanoscratching were utilized to investigate the mechanical response of individual APA SANs. Evidence of cracking and layering were observed in good agreement with the STEM fibril observations. The reduced elastic modulus,  $E^*$ , or stiffness, was estimated utilizing a Hertzian mechanics analysis of AFM nanoindentation data and determined to range from ~ 10GPa to 1 GPa varying inversely with chain-length. Electric Force Microscopy (EFM) of C1 SANs revealed no evidence of conductivity as compared to a control sample consisting of Focused Ion Beam (FIB) deposited platinum nanowires on  $\text{Si}_3\text{N}_4$ . Additionally, Current-Voltage (IV) measurements were made on individual APA SANs deposited on gold microelectrodes again with no evidence of conductivity.

THE GROWTH AND CHARACTERIZATION OF ALKYLPHOSPHONIC ACID SELF-  
ASSEMBLED NANOFIBERS

by

MICHAEL EDWARD SALMON

A dissertation submitted to the Graduate Faculty of  
North Carolina State University  
in partial fulfillment of the  
Requirements for the Degree of  
Doctor of Philosophy

MATERIALS SCIENCE AND ENGINEERING

Raleigh

2006

APPROVED BY:

---

Dr. Dieter P. Griffis

---

Dr. Richard J. Spontak

---

Dr. John M. Mackenzie

---

Dr. Phillip E. Russell  
Chair of Advisory Committee

## **DEDICATION**

This work is dedicated to two people that have always inspired, supported and believed in me,

My parents:

Ted and Nancy Salmon

This work is also dedicated to a dear friend and guru:

Mike Watt

## **IN MEMORY**

This work is in fond memory to a friend and long time companion who was with me every step of the way.

Mr. Lunch (1994-2006)

## **BIOGRAPHY**

Michael Edward Salmon was born April 16<sup>th</sup> 1974 in Falmouth, MA. He was raised in Chapel Hill, NC since the age of two and graduated from Chapel Hill High School in 1992. He attended Pitzer College from 1992 through 1994. In the summer of 1994, he moved to Raleigh, NC with aspirations of becoming an engineer. In the spring of 1998 he received his B.S. in Materials Science and Engineering from North Carolina State University. In December of 2002 he received his Masters of Materials Science Degree from North Carolina State University along his way towards completion of a Ph.D in Materials Science and Engineering.

## ACKNOWLEDGEMENTS

The completion of this process has spanned many years and I believe that without the continued help and support from so many, I would likely have not made it through. It is with such gratitude that I would like to recognize and acknowledge the people and organizations that have made immeasurable contributions in support of me and my work.

- Dr. Phillip Russell
- Dr. Dieter Griffis, Dr. John Mackenzie, Dr. Richard Spontak, and Dr. Barry Troughton
- The AIF staff, past and present: Dr. Fred Stevie, Chuck Mooney, Roberto Garcia, Dr. Dale Batchelor, Dr. Frank Zhu, and Rich Fiore.
- Kristin Bunker and all the students of AIF, past and present: John Richards, Konrad Jarausch, Curt Progl, Anthony Garetto, Chad Parish, Jitty Gu.
- LORD Corporation
- Materials Analytical Services, Inc.
- David Nackashi and Protochips
- Edna Deas
- My parents, Nancy and Ted
- My sister, Wendy
- My good friends: Dr. John Walker, Greg Eyman, Pete Yancey, Donovan Leonard, Neal Pearson, Susan Humphries, and Aimee Argote
- Erin Bell

# TABLE OF CONTENTS

LIST OF FIGURES .....	viii
LIST OF TABLES .....	xxiii
LIST OF ACRONYMS .....	xxiv

## 1. Introduction and Overview

1.1. Introduction to Engineering of Structure at the Nanoscale .....	1
1.1.1. Introduction to Self-Assembly – Engineering From the “Bottom Up” .....	2
1.1.2. Self-Assembled Monolayers (SAMs) .....	5
1.2. Research Motivation .....	7
1.3. Dissertation Structure .....	10
1.4. References .....	11

## 2. Analytical Techniques

2.1. Introduction .....	14
2.2. Atomic Force Microscopy (AFM) .....	14
2.2.1. Contact Mode .....	15
2.2.2. Intermittent Contact or Tapping Mode .....	16
2.3. Scanning Electron Microscopy (SEM) .....	17
2.4. Scanning Transmission Electron Microscopy (STEM) .....	19
2.5. X-Ray Photoelectron Spectroscopy (XPS) .....	21
2.6. Focused Ion Beam (FIB) .....	22
2.7. Figures .....	24
2.8. References .....	27

## 3. Growth

3.1. Introduction .....	29
3.2. Supported SAN Growth .....	30
3.2.1. SAN Growth on Evaporated Aluminum Coated Glass Slides .....	30
3.2.1.1. Increased Immersion Solution Temperature .....	33
3.2.1.2. Increased Immersion Solution Concentration .....	33
3.2.1.3. Immersion in Phosphonic Acid (C0) Based Solution .....	35
3.2.1.4. Immersion in Aqueous Solution .....	36
3.2.1.5. SAN Growth on the Backside Glass .....	37
3.2.2. SAN Growth on Si <sub>3</sub> N <sub>4</sub> and Solution Transport of Aluminum .....	38
3.2.3. Growth of Gallium Based APA SANs .....	39
3.2.4. Patterning Aluminum on Si <sub>3</sub> N <sub>4</sub> Growth Surfaces .....	40
3.2.4.1. STEM Analysis of SAN Growth on Patterned Si <sub>3</sub> N <sub>4</sub> TEM Grids .....	41
3.2.5. Isolating Nanofiber Growth .....	42
3.2.5.1. Time Resolved Growth of APA SANs .....	43
3.3. Unsupported APA SANs .....	44
3.3.1. ProtoChips™ Si <sub>3</sub> N <sub>4</sub> TEM Meshes .....	44
3.3.2. Creation of Novel SAN Membranes .....	44
3.3.3. Time Resolved Growth of APA SAN Membranes .....	46
3.4. Development of a Novel Biased Growth Technique .....	47

3.4.1. Proof of Concept.....	48
3.4.2. Utilizing a Highly Doped Silicon Cathode.....	49
3.4.3. Deposition on Si <sub>3</sub> N <sub>4</sub> for STEM EDS Analysis.....	50
3.5. Discussion.....	52
3.6. Figures.....	55
3.6. References.....	76
<b>4. Structure and Composition</b>	
4.1. Introduction.....	77
4.2. Supported APA SANs.....	79
4.2.1. Aluminum Coated Glass Substrates.....	79
4.2.1.1. AFM and FE-SEM of C1 SANs.....	79
4.2.1.2. XRD of C1 SANs.....	81
4.2.1.3. SEM and EDS of C1 Micro Fibers.....	83
4.2.2. Si <sub>3</sub> N <sub>4</sub> Substrates.....	84
4.2.2.1. XPS.....	85
4.2.2.2. AFM and FE-SEM.....	88
4.2.2.3. FIB Cross-Sections of C1 SANs.....	90
4.2.2.3.1. STEM and EDS of FIB Cross-Sections.....	90
4.3. Unsupported APA SANs.....	93
4.3.1. C1 SAN Membranes – 6 Week Immersion.....	93
4.3.1.1. STEM and EDS.....	93
4.3.2. C1, C3, and C5 SAN Membranes.....	96
4.3.2.1. STEM of C1, C3, and C5 SAN Membranes.....	97
4.3.2.2. Measurement of C1 SAN Fibrils.....	98
4.3.2.3. EDS of Individual C1, C3, and C5 SANs.....	99
4.3.2.4. STEM EELS of C1 SANs.....	100
4.4. Discussion.....	105
4.5. Figures.....	111
4.6. Tables.....	137
4.7. References.....	139
<b>5. Thermal Stability</b>	
5.1. Introduction.....	142
5.2. Ex-situ Annealing of C1 SANs on Aluminum.....	145
5.2.1. Experimental details.....	145
5.2.2. Results.....	146
5.3. In-situ annealing of C1 SANs on Si <sub>3</sub> N <sub>4</sub> .....	148
5.3.1. Experimental details.....	148
5.4.2. Results.....	149
5.4. Ex-situ annealing of C1, C3, and C5 SANs on Si <sub>3</sub> N <sub>4</sub> .....	152
5.4.1. Experimental details.....	152
5.4.2. Results.....	153
5.5. Discussion.....	156
5.6. Figures.....	158
5.7. References.....	165

<b>6. Mechanical Stability</b>	
6.1. Introduction	167
6.2. Qualitative STEM Analysis of Fractured C1 SAN Membranes	169
6.2.1. E-Beam Manipulation of a Broken C1 SAN Membrane with STEM	170
6.3. Nanoindentation	172
6.3.1. General AFM Nanoindentation Procedure	174
6.3.2. Qualitative Analysis of Sample Stiffness	175
6.3.3.1. Determination of Suitable Cantilevers	177
6.3.3.2. Observation of Cracking in C5 SANs	178
6.3.3. Quantification of AFM Nanoindentation Measurements	178
6.3.3.1. Double Spring Model	178
6.3.3.2. Converting to Force vs. Displacement	179
6.3.3.3. Elastic Modulus Determination Using Hertzian Contact Model	180
6.3.3.3.1. Determination of Tip End Radius	182
6.3.4. Quantitative AFM Nanoindentation of APA SANs on Si <sub>3</sub> N <sub>4</sub>	184
6.3.4.1. C5 SANs	185
6.3.4.2. C3 SANs	187
6.3.4.3. C1 SANs	188
6.3.4.4. Comparison of C1, C3, and C5 SANs Stiffness	188
6.4. AFM Nanoscratching of C3 SANs	190
6.4.1. Nanoscratching Experimental Details	191
6.4.2. Results and Discussion	191
6.5. Discussion	194
6.6. Figures	196
6.7. Tables	221
6.8. References	222
<b>7. Electrical Properties</b>	
7.1. Introduction	225
7.2. Electric Force Microscopy	227
7.2.1. Experimental Setup	228
7.2.2. Results	230
7.3. Single C1 SAN Devices	232
7.3.1. Results	233
7.4. Discussion	236
7.5. Figures	238
7.6. References	246
<b>8. Conclusions</b>	
8.1. The Contribution	249
8.2. Future Work	252
8.3. References	254

## LIST OF FIGURES

Figure 2.1.	Schematic of a scanned sample AFM in contact mode .....	24
Figure 2.2.	Schematic of a scanned sample AFM in tapping mode .....	24
Figure 2.3.	Schematic of the primary components of a typical SEM .....	25
Figure 2.4.	Useful signals generated from electron beam-sample interactions.....	25
Figure 2.5.	Schematic of the primary components of a dedicated STEM.....	26
Figure 3.1.	1 $\mu$ m x 1 $\mu$ m AFM height image of typical evaporation deposited aluminum film on glass prior to immersion. 50 nm Z-range.....	55
Figure 3.2.	General immersion growth technique .....	56
Figure 3.3.	AFM tapping mode height images of nanofiber growth on Al surface. Evaporated Al film was exposed to 0.1wt% (8.3mM) C-1/EtOH solution over a 177 day period. Arrows denote linear fibrous structures observed after only 1 day of growth.....	56
Figure 3.4.	A 2 $\mu$ m TM-AFM image (height left 150nm z-range, phase right) showing the branching and network structure of the fibers in the 28 day growth sample Phase Image shows increased details of sub-fiber structures present along with compositional contrast between the fiber and the background Al film.....	57
Figure 3.5.	500 nm TM-AFM image 150nm z range. Non-uniform segmented structure observed, tip shape induced artifacts? Overlap, branching common, diameters range 5 - 100 nm. (height = diameter).....	57
Figure 3.6.	FE-SEM image of nanofiber mat that is formed on the Al surface after 84 days (left image). The upper left corner of the image shows what appears to be mechanical deformation of the nanofiber mat by tweezers. It is also easy to see the porous nature of the large precipitates previously observed with AFM. The right image with inset is a comparison of AFM and SEM images taken of different regions on the same 84 day immersion sample. FE-SEM was performed uncoated at low voltage. AFM and SEM images are the same scale. ....	58

Figure 3.7.	Comparison of SAN growth on two Al coated glass substrates immersed in 0.1 wt% C-1/EtOH solutions. The left image shows SAN growth after 9 day immersion @ 40C while the right image is of typical SAN growth after 28 day immersion @ room temperature. Both are 5 $\mu$ m AFM height images.....	58
Figure 3.8.	FE-SEM images of a C1 microfabric. The microfabric was grown by immersion of an Al coated glass slide in an 83 mM C1/EtOH solution for 19 days. The large image is a zoom of the curled region seen in the image in the upper left. ....	59
Figure 3.9.	The top images are an SEM SE image and corresponding EDS maps of Si, P, and Al on an acicular microfiber crystal grown by immersion of an Al coated glass slide in 83 mM C1/EtOH solution for 19 days. The bottom images are higher magnification SEM images from different areas from the same sample showing the variety of structuring present.....	60
Figure 3.10.	5 $\mu$ m AFM height images of Al film immersed in 8.3 mM C1/EtOH and C0/EtOH. No fibers were observed without using an alkyl-phosphonic acid. ....	60
Figure 3.11.	1 $\mu$ m tapping mode AFM height images of 18 M $\Omega$ H <sub>2</sub> O, 200nm Al on glass, AFM height images sample translucent after 11 days immersion time. ....	61
Figure 3.12.	Nanofibers found on the glass surface where no Al was initially deposited, the backside of the Al coated glass 177 day immersion sample. ....	61
Figure 3.13.	EDS analysis, 5 KV accelerating voltage, of an as received Si <sub>3</sub> N <sub>4</sub> TEM membrane before and after immersion and in a 8.3 mM C1/EtOH solution for 60 days along with a piece of Al coated glass. Image B is a 2 $\mu$ m tapping mode AFM height image, w/50 nm z range, showing that SAN growth can occur on adjacent substrates with no Al present on the growth surface after immersion in 8.3 mM C1 solution for 60 days. ....	62
Figure 3.14.	SEM image of SiN thin film window TEM substrate – SPI supplies. The entire substrate is 3 mm x 3mm x 200 $\mu$ m in size with ~ 1 mm <sup>2</sup> Si <sub>3</sub> N <sub>4</sub> window.....	63

Figure 3.15.	Tapping mode AFM height image of Ga nanofibers on SiN, image (a). Lower magnification Z-Contrast, image (b) of nanofiber network as grown directly on an electron transparent Si <sub>3</sub> N <sub>4</sub> film. Higher magnification Z-Contrast STEM image (c) showing a close up of the branched nanofiber structures.....	64
Figure 3.16.	Z-Contrast STEM image of Ga nanofiber on amorphous Si <sub>3</sub> N <sub>4</sub> , shows the presence of fibril structures within the SAN. EDS spectra of the center of the same SAN showing the presence of Ga. ....	65
Figure 3.17.	Patterned evaporation of Al on Si <sub>3</sub> N <sub>4</sub> thin film windows. ....	65
Figure 3.18.	A comparison of Bright Field (BF) and Dark Field HAADF (Z-Contrast) Images SANs grown on 150 nm Si <sub>3</sub> N <sub>4</sub> after 30 day immersion time. ....	66
Figure 3.19.	A Comparison of SANs as grown on 50 nm Si <sub>3</sub> N <sub>4</sub> membranes for different immersion times. Longer growth resulted in a thicker mat giving poorer contrast between individual SANs and obscuring their internal structuing. The SANs were relatively stable under the 200KV beam at moderate magnifications <750KX, but significant damage was observed to occur at higher magnifications of 1MX+.....	66
Figure 3.20.	5 μm x 5 μm AFM TappingMode™ Height Images showing the growth of APA SANs on Si <sub>3</sub> N <sub>4</sub> for C1, C3, and C5 over three weeks. The scan areas are located some distance ~ 1-2 mm away from the initially deposited Al. All images taken using a Digital Instruments Dimension 3000 AFM with budget sensors, Si tapping tips, k ≈ 3N/m, 1 Hz scan rate.....	67
Figure 3.21.	FE-SEM SE image of Al coated Protochips DuraSiN mesh with 4 um holes 10 um pitch in 200 nm thick SiN thin film window.....	68
Figure 3.22.	STEM ZC images of clump of unsupported fibers grown on patterned Al ProtoHips DuraSin mesh. These were the only unsupported nanofibers observed on the entire sample. ....	68
Figure 3.23.	Tapping mode AFM height and phase image of a single nanofiber membrane as grown on a ProtoChips™ DuraSIN™ TEM mesh. ....	69
Figure 3.24.	STEM SE images of increasing magnification (a-c) showing the structure of a 4 μm unsupported SAN membrane on an Al coated ProtoChips™ DuraSiN™ mesh. The Al coated substrate was immersed in 8.3 mM C1/EtOH solution for 6 weeks. ....	70

Figure 3.25.	STEM SE images of C1 SAN membranes after 1 week of immersion in 8.3 mM C1/EtOH solution.....	71
Figure 3.26.	STEM Secondary Electron (STEM-SE) images of the time resolved growth of unsupported C1 and C5 SAN membranes over 3 weeks immersion time. C3 nanofiber membranes were not observed for the 1 and 2 week samples. Only the 3 week sample exhibited intact membranes. The C1 membranes were the most robust. The corrosion of Al around the edge of the hole is clearly seen in the 3 week C1 image.....	72
Figure 3.27.	The left image is the experimental setup for biasing experiments. The right image shows the electrodes after an experiment showing the removal of Al on the immersed area of the anode (arrow). .....	73
Figure 3.28.	The left image is an optical micrograph of Aluminum coated glass anode and cathode after 24 hrs of immersion in 8.3 mM C-1 solution under 3.5 V DC bias. Right image is a 5 $\mu\text{m}$ AFM tapping mode phase image of resulting SAN on remaining Al of the cathode.....	73
Figure 3.29.	Tapping mode AFM height and phase image showing the result of nanofiber growth on a highly doped Si cathode after 5 hrs of immersion in 8.3 mM C-1/EtOH solution at 3.5 V DC bias.....	74
Figure 3.30.	Tapping mode AFM height and phase images of the Si cathode after 24 hrs of immersion at 3.5 V bias. ....	74
Figure 3.31.	STEM with EDS analysis of C1 SANs grown directly on a Protochips <sup>TM</sup> DuraSIN <sup>TM</sup> Si <sub>3</sub> N <sub>4</sub> membrane using a biased growth method.....	75
Figure 4.1.	C1 nanofibers grown on Al. AFM tapping mode images with 150 nm z range. 2000 nm (a) and 500 nm (b) height and phase image pairs. Olympus tapping cantilever. ....	111
Figure 4.2.	Two FE-SEM Images taken of the same area of the same 28 day immersion sample at two different accelerating voltages: 1.0 kV, image (a), and 3 kV, image (b). The increased dark contrast using 3 kV reveals the presence of sub-surface corrosion pits.....	112
Figure 4.3.	A comparison between LV-FESEM and AFM tapping mode phase (inset) images of the same C1 nanofibers sample showing similar nodular features present along the length of the fibers. The images are the same scale.....	112

Figure 4.4.	Low voltage FE-SEM image of a single large C1 nanofiber from the same 84 day sample as imaged in Figure 2. The use of a very low accelerating voltage, in this case 500V improves the surface detail at high magnification while minimizing damage to the nanofibers. This image confirms that the fibers do indeed branch and Inset 1 denotes triangular surface defect structures associated with the branching. Inset 2 denotes another possible defect structure along the length of the fiber. Unfiltered image with histogram stretch to increase contrast of fibers. ....	113
Figure 4.5.	FE-SEM images of the surface of an evaporated Al surface after immersion in 8.3 mM C1/EtOH solution for 84 days. Image (a), is essentially the same field of view as the 2 um AFM image in Figure 1 (a) and shows the multi-layered character of the nanofabric. The nanofiber morphology is very similar to the AFM images although there appears to be a bit better edge details with the SEM. Image (b) show the details of one of the precipitates as it appears to be a highly defected clump of nanofibers. Images were histogram stretched and a slight, 1 px, Gaussian blur applied to increase the contrast and reduce noise. ....	114
Figure 4.6.	SEM image and EDS mapping of C1 microfibers formed after immersion of an Al coated glass slide in a 83 mM C1/EtOH solution for 19 days. EDS mapping shows that the Al and P are highly localized to the fiber structures. ....	114
Figure 4.7.	XRD results from Al films after 365 day exposures to: immersion in EtOH, air, and immersion in an 8.3 mM solution of C1 in EtOH .....	115
Figure 4.8.	XPS P 2p and Al 2p data from C1, C3, and C5 nanofibers grown on Si <sub>3</sub> N <sub>4</sub> .....	116
Figure 4.9.	A comparison of C1 SAN fibril morphology observed with FE-SEM and AFM. The FE-SEM image shows the formation of SANs as well as the corrosion of the Al film at the interface with the underlying Si <sub>3</sub> N <sub>4</sub> film after immersion for 3 weeks. The inset is a tapping mode phase image of C1 SANs (inset) at the same scale as the FE-SEM image. Both images are of the same sample, taken from different regions of the sample. ....	117
Figure 4.10.	3D image of the same C1 SAN shown previously in Figure 8. Here we can see the fibril morphology of the fibrils are not parallel to the substrate surface but instead are layered at ~ 30 deg angle. 50 nm Z scale.....	117

Figure 4.11.	FIB Cross-section through individual C1 SANs on Si <sub>3</sub> N <sub>4</sub> . Image (a) shows an overview SE image of the entire cross-section. Inset (b) shows higher magnification TE and ZC images of the same group of C1 SANs. ....	118
Figure 4.12.	Higher magnification SE, TE, and ZC STEM images of two Cu coated C1 SANs on Si <sub>3</sub> N <sub>4</sub> . ....	119
Figure 4.13.	A 1000 KX TE (a) and ZC (b) images of a single Cu coated C1 SAN on Si <sub>3</sub> N <sub>4</sub> . The arrow in (b) denotes interesting geometric feature observed within the SAN. EDS analysis was performed on the C1 SAN at the spot denoted in (a) and the results shown (c). The results of a semi-quantitative EDS analysis are shown in (d). ....	120
Figure 4.14.	AFM tapping mode height and phase images of a C3 3 week SAN, image (a). The images were acquired utilizing very high damping of a force modulation cantilever ( $k \sim 4$ N/m) at 2.5 Hz scan rate. Observation of fibrils and cross-sectional analysis of the observed layered fibrils, image (b). ....	121
Figure 4.15.	Higher magnification AFM tapping mode height and phase images of C3 SAN from Figure 8 image (a). This image was taken using the same scan parameters as the image in Figure 8 and was the next image in sequence showing that the sub-fiber corrugations scale with scan size and there is good correlation between the features seen in Figure 9 with those observed in the previous scan in Figure 8 image (a) indicating repeatability between scans. ....	122
Figure 4.16.	High damping tapping mode AFM height and phase image of a C5 SAN on Si <sub>3</sub> N <sub>4</sub> showing evidence of an oriented corrugated molecular substructure. ....	123
Figure 4.17.	STEM SE images of unsupported 4 $\mu$ m C1 nanofiber membranes after immersion of an Al coated ProtoChips <sup>TM</sup> DuraSiN <sup>TM</sup> membrane in 8.3 mM C1/EtOH solution for 42 days. Image (a) shows the overall morphology of an individual membrane. Image (b) shows a higher magnification of an edge region of a different membrane showing the complex layering, sub-fiber detail, and residual webbing between certain fibers. Images histogram stretched and slightly Gaussian blurred to improve contrast and reduce noise. ....	124

Figure 4.18.	A Secondary Electron (SE) (a), Z - Contrast (ZC) (b), and Bright Field (TE) (c), images of the same region of nanofibers in a C1 membrane. The SE image provides surface details while the ZC and TE images provide information about the internal structures. These are also sequential slow scans and the effect of the beam on the smallest fiber (1) in the center of (a) can be seen in (b) and (c) as it breaks due to beam interactions. It is also of interest to note the increased nanofiber widths (2) in the SE image vs. ZC and TE hinting at possible surface structural differences. Raw images with slight 1 px Gaussian blurs.....	125
Figure 4.19.	Sequential SE (a) and ZC (b) images taken of the same group of C1 nanofibers, 42 day growth. Some type of contamination coating or surface film is clearly evident in comparing the SE (a) the ZC images (b). Raw images with slight histogram stretching. ....	126
Figure 4.20.	STEM TE image of a C1 nanofiber cluster and the corresponding EDS mapping of P, O, Al, and C. The Mapping provides further evidence of a C surface layer is seen as increased fiber widths in the C map compared to the P, O, and Al maps.....	126
Figure 4.21.	STEM ZC image with insets showing indicating the presence of both bundled fibrils and layered structures within nanofiber cores. Inset 1 and 2 are digital zooms of two fibers showing markedly different structures. The images have been histogram stretched, slightly Gaussian blurred and unsharp-masked to increase the contrast of the central nanofiber core structures.....	127
Figure 4.22.	STEM ZC image of overlapping nanofibers showing evidence of fibrils and layering within individual nanofibers. Unfiltered image with only slight histogram stretch and gamma correction to increase contrast.....	127
Figure 4.23.	STEM ZC images of C1 1 week SAN membrane showing how individual SANs are composed of bunches of fibrils that vary in width from ~ 5 – 20 nm wide.....	128
Figure 4.24.	STEM ZC image of an individual C1 SAN showing the internal fibril sub-structure. The fibrils appear to have a ribbon like morphology and are observed to twist along their lengths.....	128
Figure 4.25.	STEM ZC images of C3 (a) and C5 (b) SANs after 1 week immersion. In both images there is evidence of fibril structures within the C3 and C5 SAN, but are less definitive than with C1. ....	129

Figure 4.26.	STEM ZC image of C1 nanofiber membrane after 1 week immersion time. Bundles of ~5nm wide fibril structures that comprise the individual C1 SANs. The lettered boxes, A-D, denote areas chosen for further FFT analysis of individual fibril widths as shown in Figure 4.23.....	129
Figure 4.27.	FFT analysis of fibril repeat distances within 128 x 128 px regions from Figure 4.26. Each individual region is first FFT filtered, then the FFT is blurred and histogram stretched. This is to increase the contrast of the FFT. Spots are then isolated and the spacings measured and reported looking for correlation in fibril spacings between each area. It is important to note that the accuracy of this analysis is severely limited due to the limited number of pixels comprising a single fibril, as well as effects on the image due to astigmatism of the scanning electron beam and orientation of the fibrils relative to the beam. ....	130
Figure 4.28.	Representative EDS spectra taken on individual unsupported C1, C3, and C5 SANs showing the presence of Al, O, P, C, Si, and Ca. The Si and Ca present are believed to be contaminants.....	131
Figure 4.29.	STEM ZC image (a) and corresponding qualitative EDS and semi-quantitative elemental analysis (b) of a single unsupported C1 SAN.....	132
Figure 4.30.	STEM Z-Contrast image of overlapping C1 SANs. X denotes the location of a 5 nm x 5 nm area utilized for EELS analysis.....	133
Figure 4.31.	Raw EELS spectrum (blue) acquired from the location denoted in Figure 4.30. with the Al, P, and C L <sub>2,3</sub> edges clearly visible. A power law background (red) was applied to the raw EELS data using a 10 eV window ahead of the Al edge. The resulting Al background corrected spectrum is shown in green. This definitively proves that Al, P, and C are present in the SAN structure. ....	134
Figure 4.32.	Al and P background corrected L edges. A power-law model was utilized for background correction.....	135
Figure 4.33.	Comparison of Al L edge from C1 SAN with Al L edges from EELS Atlas for Al metal and Alumina (Al <sub>2</sub> O <sub>3</sub> ). Edge onset for the C1 SAN is more similar to that for Alumina than for metallic Al, suggesting an Oxygen environment for the Al in the C1 SANs. All edges were power-law background corrected using a 10 eV energy window. The background correction for the C1 SANs may possibly be improved utilizing other models. ....	136

Figure 5.1.	A series of 5 $\mu\text{m}$ x 5 $\mu\text{m}$ AFM height images of a typical C1 SAN mat with precipitates acquired at room temperature $\sim 27\text{C}$ (a) and after 30 min anneals at 105C (b), 160C (c), 220C (d), 300C (e), 325C (f), 430C (g), 460C (h), and 490C (i).....	158
Figure 5.2.	Corresponding 1 $\mu\text{m}$ x 1 $\mu\text{m}$ AFM height images of the same sample as in Figure 5.1 acquired at the same temperatures: room temperature (a) and after 30 min anneals at 105C (b), 160C (c), 220C (d), 300C (e), 325C (f), 430C (g), 460C (h), and 490C (i). A melting event occurs between 430C and 460C with SAN structures still present after 490C (i).....	159
Figure 5.3.	5 $\mu\text{m}$ x 5 $\mu\text{m}$ AFM height images of C1 SANs on $\text{Si}_3\text{N}_4$ at room temperature (a), and after annealing under a vacuum of $\sim 1 \times 10^{-6}$ torr for 30 minutes at 450C (b), 500C (c).....	160
Figure 5.4.	AFM height images of the same area of C1 SANs on $\text{Si}_3\text{N}_4$ before (a), and after annealing in air for 30 minutes at 470C (b). The arrow in (a) and (b) point at the same nanofiber for reference within the images. Electronic zooms of the same nanofiber before (c), and after (d) reveal a significant decrease in fiber height due to annealing. The insets in (c) and (d) show the averaged cross-section of approximately the same region of the same nanofiber. ....	160
Figure 5.5.	Pairs of 5 $\mu\text{m}$ x 5 $\mu\text{m}$ AFM height image of APA SANs on $\text{Si}_3\text{N}_4$ taken at room temperature: C1 (a), C3 (b), and C5 (c) and after annealing for 30 min in air at 550C: C1 (d), C3 (e), and C5 (f). ....	161
Figure 5.6.	AFM height images of C5 SANs on $\text{Si}_3\text{N}_4$ taken after annealing in air for 12 hrs at 550°C, 5 $\mu\text{m}$ (a) & 1 $\mu\text{m}$ (b).....	161
Figure 5.7.	AFM 5 $\mu\text{m}$ and 1 $\mu\text{m}$ height image pairs of C1 SANs on $\text{Si}_3\text{N}_4$ taken after annealing in air for 30 min at 575°C (a) & (d), for 6 hrs at 600°C (b) & (e), and for 6 hrs at 650°C (c) & (f).....	162
Figure 5.8.	AFM 5 $\mu\text{m}$ and 1 $\mu\text{m}$ height image pairs of C3 SANs on $\text{Si}_3\text{N}_4$ taken after annealing in air for 30 min at 575°C (a) & (d), for 6 hrs at 600°C (b) & (e), and for 6 hrs at 650°C (c) & (f).....	163
Figure 5.9.	AFM 5 $\mu\text{m}$ and 1 $\mu\text{m}$ height image pairs of C5 SANs on $\text{Si}_3\text{N}_4$ taken after annealing in air for 30 in at 575°C (a) & (d), for 6 hrs at 600°C (b) & (e), and for 6 hrs at 650°C (c) & (f).....	164

Figure 6.1.	STEM SE image of the crack formed in an Al coated ProtoChips™ DuraSIN™ mesh (a) and an individual C1 SAN membrane (b) after puncturing with tweezers. In some cases the crack makes it all the way around a windows leaving membranes intact (a), but in many cases it propagates right through the SAN membranes in a brittle fashion often with small chips missing (b). .....	196
Figure 6.2.	STEM SE image of a broken C1 SAN membrane. The resulting jagged fracture edges as well as the remaining intact planar chips provide evidence of brittle fracture.....	197
Figure 6.3.	HAADF STEM SE image of two cracks propagating through a C1 SAN membrane with one large fiber impeding their progression (a). Investigation of the crack tip areas with Z-Contrast (b & c) clearly show the fracturing of the SAN layered structure. The arrows in (b) denote regions of layer cracking and sliding in a SAN that has not yet failed. ....	198
Figure 6.4.	Sequence of STEM SE images showing the progression of e-beam manipulation of a broken C1 SAN membrane (a-f). The broken membrane was folded over onto itself by first irradiating the entire membrane with the e-beam at low magnification (a & b). Next, the magnification was increased so that most of the e-beam scan was into vacuum, where the SAN membrane was noticed to flex upwards (c). The magnification was then lowered and the membrane was observed to relax (d). Then the magnification was increased to 5MX and the sample moved into the beam path which resulted in the membrane folding over onto itself (e). Finally the magnification was lowered to show the final state of the folded SAN membrane (f). .....	199
Figure 6.5.	An example of a typical AFM “force curve” of Cantilever Deflection vs. change in Piezo length obtained for a single indentation on a C5 SAN on Si <sub>3</sub> N <sub>4</sub> showing evidence of plastic deformation of the C5 SAN.....	200
Figure 6.6.	A Typical AFM force curve of Cantilever Deflection vs. change in Piezo length, taken on highly stiff Si <sub>3</sub> N <sub>4</sub> (E~ 180 GPA) sample using a Olympus tapping mode tip, k~ 66 N/m, and plotted from exported DI data using Excel. Since the sample is much stiffer than the cantilever, the only contributions to the deflection are from the cantilever where the slope of the linear portion of the extending and retracting data represents the sensitivity of the given cantilever. ....	201

Figure 6.7.	The difference in cantilever response as shown by a series of overlaid force curves obtained using the same NSC 15/50 $\mu$ masch cantilever on a 240 nm $\text{Si}_3\text{N}_4$ thin film on Si, a sputtered Au film, evaporated Al film, a PET film, and C-5 nanofiber on $\text{Si}_3\text{N}_4$ on Si. The force constant of the cantilever was estimated to be $k \sim 43$ N/m using the Sader method. Further more, with a little effort and a few simple assumptions we can model the retraction data to quantify the stiffness, or elastic modulus, of the samples as long as careful attention is paid to several experimental parameters. ....	202
Figure 6.8.	250 nm x 250 nm AFM tapping mode height images of a C5 nanofiber before (a) and after (b) a single 25 nN indentation. Image (c) is the height phase pair from the digitally zoomed area of interest depicted with the dotted lines in image (b). Cracks are clearly visible in the height image while the phase image clearly shows that entire regions have shifted relative to the fiber axis, shown by the white lines. ....	203
Figure 6.9.	AFM Nanoindentation Double Spring, Hertzian Contact Model before and during indentation with a spherical indenter into a nanofiber sample having a rectangular cross-sectional geometry. ....	204
Figure 6.10.	The conversion from Deflection vs. Piezo length to Force vs. Displacement utilizing the two spring model for a nanoindentation made in a C5 SAN on $\text{Si}_3\text{N}_4$ . A hertzian model (black line) has been applied to the retraction portion of the Force vs. Displacement plot. The fit of the model to the retraction data is very good. ....	204
Figure 6.11.	Shows the effect of 20 nm tip radius variations on the slope of a Hertzian fits where $E^* = 1, 5, 10,$ and $100$ GPa. ....	205
Figure 6.12.	Multiple indentations in the same location of a PET film with a known modulus of $\sim 4$ GPa. A hertzian fit (black line) estimates the tip radius to be 35 nm. ....	206
Figure 6.13.	SEM image of Micromasch TGT01 tip characterizer along with schematic and specifications, utilized for the determination of the tip end radius and geometry. ....	206
Figure 6.14.	3D AFM height images created by scanning a micromasch tip characterizer, TGT 01. The image of the tip is digitally zoomed in (b) and then to (c) for closer inspection of the tip end radius. The numbers 1 and 2 in image (c) correspond to the points in Figure 6.15. ....	207

Figure 6.15.	Corresponding AFM Height image to Figure 6.14 (c) zoomed in on the very end radius of the tip on the left. On the right are the corresponding horizontal and vertical cross sections through the end radius of the tip. The tip exhibits an end radius of $\sim 25$ nm in the horizontal and $\sim 15$ nm in the vertical directions.....	208
Figure 6.16	AFM height images of before (a & a2) and after (b & b2) a series of 10 indentations in the same spot of single C5 fiber on $\text{Si}_3\text{N}_4$ . .....	209
Figure 6.17.	Force curves from a series of 10 indentations made at the same spot into a single 40 nm tall C5 nanofiber on $\text{Si}_3\text{N}_4$ . The successive indentations were plotted in a way to better show the evolution of the fibers displacement over the entire series. ....	210
Figure 6.18.	The first six Force vs. Displacement curves from Figure 6.17 with corresponding Hertzian fits showing the trend of increasing modulus with increasing sample displacement.....	210
Figure 6.19.	AFM height images of overlapping C-5 nanofibers before (a), and after (b), a single $\sim 80$ nN indentation with AFM. ....	211
Figure 6.20.	Corresponding Force vs Displacement curve for the single indentation made into overlapping C-5 nanofibers on $\text{Si}_3\text{N}_4$ as shown in the previous image. ....	212
Figure 6.21.	AFM 3D Height images of a 50 nm wide by 10 nm tall C3 SAN on $\text{Si}_3\text{N}_4$ before (a) and after (b) a series of 10 indentations of progressively increasing loads. The shift of the fiber after indenting along with the linear shape of the indent suggest that each successive indentation was not made in the same place. ....	213
Figure 6.22.	Force curves from a series of 10 indents of 1 – 10 nm deflections (8.4 – 84 nN) in a C3 SAN. The 2 <sup>nd</sup> indent is left out because it was considered bad. ....	213
Figure 6.23.	The first six force curves from Figure 6.22, with Hertzian fits to the retraction curve of the 4 <sup>th</sup> and 6 <sup>th</sup> indents (black), showing nearly elastic response from the first 4 indents and then more plastic response after the 5th. An increase in modulus is seen with increased sample deformation.....	214

Figure 6.24.	135 nm x 135 nm AFM tapping mode height images of a single 50 nm wide by 11.5 nm tall C1 nanofiber on Si <sub>3</sub> N <sub>4</sub> before (a), after a ~84 nN indent (b), and after a ~168 nN indent in roughly the same place. The z-scale on each image is 20 nm. Subtle changes in the fiber morphology are observed as the fiber widens slightly as well as decreasing in height corresponding well with the observed sample displacements in Figure 6.25. ....	215
Figure 6.25.	Force vs. Displacement curves corresponding to the images in Figure 6.24. A Different type of deformation mechanism is noted as there is no discernable yield point like the C3 and C5 SANs. Hertzian fits estimate the modulus to be ~ 10.5 – 15 GPa for the two indentations.....	215
Figure 6.26.	A comparison of a representative Force vs. Displacement curves from each of the C1, C3, C5 SANs with one from the 4 GPa PET film series. The measured elastic moduli appears to increase with decreasing chainlength, from 1.5 GPa for the C5 to 10GPa for the C1 SANs. ....	216
Figure 6.27.	AFM height, phase and 3D images showing the sequential changes of a single C3 SAN before (a), after a 50 nm lateral deformation (b), and after an additional 100 nm lateral deformation (c). The arrows in the phase image of (c) denote what appears to be residual SAN left on the surface after it was moved to the right.....	217
Figure 6.28.	Is a series of thresholded AFM height images from Figure helping correlate the changes in SAN morphology with scratches applied. Image (a) is the before image with what is perceived to be two pinning sites where the SAN appears to be stuck to the Si <sub>3</sub> N <sub>4</sub> as well as the starting point for the scratches. Image (b) is an overlay of the result of the first 50 nm scratch (red) on top of the before image (white) with the scratch represented by the red arrow. Image (c) is an overlay of the results of a second scratch (blue) on top of image (b) with the second scratch represented by the blue arrow.....	218
Figure 6.29.	After the previous two scratches were made as seen in figure a third scratch was made directly adjacent to the previously observed lower pinning site. The image location was shifted in the y direction and a set of AFM height, phase, and 3D images obtained before the scratch (a) and then a 100 nm scratch was made in the x direction and another set of AFM height, phase, and 3D images obtained (b). The arrows in the phase image of (b) show the residual SAN left behind on the Si <sub>3</sub> N <sub>4</sub> surface after scratching and lateral translation of the SAN.....	219

Figure 6.30.	Analogous to Figure 6.28, Image (a) is a thresholded AFM height image of the SAN prior to lateral deformation. Image (b) is an overlay of the thresholded AFM height image of the SAN after a 100 nm lateral deformation (red) on top of image (a) (white) with the scratch represented by the blue arrow.....	220
Figure 7.1.	The patterned deposition of a 1 mm <sup>2</sup> x 100 nm thick Au electrode for making contact to C1 SANs grown on Si <sub>3</sub> N <sub>4</sub> utilizing a mask made from a broken out Si <sub>3</sub> N <sub>4</sub> TEM grid, image a. Then electrical contact is made to the isolated Au pad using thin Au wire and Ag paint, image b.....	238
Figure 7.2.	AFM height and EFM phase image of C1 SANs on Si <sub>3</sub> N <sub>4</sub> with a 30 nm thick Au electrode. The images were acquired while biasing the Au to 8 V relative to the tip which was scanned at a lift height of 20 nm. The conductive Au electrode appears darker while the SANs appear lighter in the EFM phase image indicating that they are insulating.....	239
Figure 7.3.	AFM height images with corresponding EFM frequency shift images of FIB deposited Pt lines contacting (a) and not in contact (b) with a Au electrode biased at -5 V relative to ground. The lift height was 20 nm and the tip was grounded. Each EFM image a small number of scan lines with the bias set to 0V, two groups in (a) and 1 group in (b) showing the effect due to sample bias. ....	240
Figure 7.4.	Optical Micrograph of Au microelectrode array utilized for creation of single SAN device. ....	241
Figure 7.5.	SEM image of Au electrode structures, upper left, and corresponding AFM height images, upper right, of the exposed Au micro electrodes (A-D). Areas A-C are essentially the same structure, just rotated. The lower images are cross-sectional analyses of area C showing the dimensions of the Au lines.....	242
Figure 7.6.	AFM height and phase image (a & b) of a single set of electrodes showing the results of 24 hr biased growth of C1 SANs. Height Image (c) shows a zoom in of the electrodes with individual SANs isolated between electrodes.....	243
Figure 7.7.	AFM height and phase images (a & b) of another electrode set showing more C1 SAN growth between electrodes. Image (c) is a height image zoom of the electrodes emphasizing the SAN growth showing in this case clusters of C1 SANs between the electrodes. ....	244

Figure 7.8. A FIB cross-section was created by cutting across the Au electrodes on one array similar to the one shown previously in Figure 7.7. The cross-section was then analyzed with a Hitachi HD-2000 STEM. Image (a) is an SE image showing an overview of the entire cross-section. Image (b) is a SE image showing a zoomed in region of the electrodes. The arrow denotes the individual Au electrode shown in image (c1) SE, (c2) Z-Contrast, and (c3) Bright field. It is clear to see that the Au lines actually sit at top SiO<sub>2</sub> pillars, ~ 20 – 25 nm above the regions between electrodes. ....245

## LIST OF TABLES

Table 4.1.	Measured XPS BE peak positions (eV) for the Al 2p 3/2 and P 2p 3/2 for C1, C3, and C5 samples. All spectra were calibrated to the C 1s peak at 285 eV. ....	137
Table 4.2.	Summary of the average elemental ratios of nine C1 SAN cross-sections as determined by Semi-Quantitative EDS analysis.....	137
Table 4.3.	Average atomic ratios and standard deviations for ten C1, two C3, and one C5 unsupported SANs as determined by Semi-Quantitative EDS analysis. ....	138
Table 6.1.	Summary of reduced modulus ( $E^*$ ) values for C1, C3, and C5 SANs. $E^*$ values were calculated by fitting of a Hertzian contact model to the retraction curves. All data was acquired utilizing the same cantilever having a spring constant of 8.4 N/m (Sader Method) and tip radius of 35 nm (characterizer and PET control).....	221
Table 6.2.	Summary of reduced modulus values for C5 SANs acquired with cantilevers of three different force constants: 0.73, 8.4, and 66 N/m. ....	221

## LIST OF ACRONYMS

APA	Alkylphosphonic Acid
C1	Methylphosphonic Acid
C3	Propylphosphonic Acid
C5	Pentylphosphonic Acid
C12	Dodecylphosphonic Acid
C18	Octadecylphosphonic Acid
SAM	Self Assembled Monolayer
SAN	Self Assembled Nanofiber
SPM	Scanned Probe Microscopy
AFM	Atomic Force Microscopy
TM-AFM	Tapping mode AFM
SEM	Scanning Electron Microscopy
XPS	X-Ray Photoelectron Spectroscopy
XRD	X-Ray Diffraction
EDS	Energy Dispersive X-Ray Spectrometry
STEM	Scanning Transmission Electron Microscopy
FIB	Focused Ion Beam
TEM	Transmission Electron Microscopy
(S)TEM	TEM with scanning capabilities
FESEM	Field Emission Scanning Electron Microscopy
ZC	Z-Contrast (HAADF) STEM image
SE	Secondary Electrons
TE	Bright Field STEM image
BSE	Backscattered Electrons
I-V	Current versus Voltage
Si	Silicon
Si <sub>3</sub> N <sub>4</sub>	Silicon Nitride
P	Phosphorous
C	Carbon
O	Oxygen
Al	Aluminum
Ca	Calcium

# 1 Introduction and Overview

## 1.1. Introduction to Engineering Structure at the Nanoscale

For thousands of years, the level at which physical manipulations could be made remained at a scale recognizable by the naked eye, but in the span of only 50 years, the engineering of materials has matured to the point that we now need highly specialized tools to help us both manipulate as well as *see* or understand what we have manipulated at the scale of individual atoms. As we have improved our tools to both create and visualize structure with finer and finer detail, much has been learned about how the physical properties of materials at our human scale are dependant on their composition and structure at the micro-scale and below. This ability to visualize and manipulate materials with such high resolution has lead to vast improvements in the performance of engineering materials allowing the building of structures of vast complexity, from sky scrapers to cruise ships, jet airplanes to space shuttles, automobiles to integrated circuits.

In addition to the advantages of engineering structure and properties of materials at smaller scales for increased performance and lower cost, materials often exhibit unique phenomena when their physical dimensions are reduced to a few nanometers. Some of these special properties of nanometer sized structures include size-dependant band gap of quantum dots [1.1], quantized, or ballistic conductance in multi-walled carbon nanotubes [1.2], single electron transistors [1.3] as well as metal-insulator transitions [1.4]. Quantum confinement of electrons within the potential wells of nanometer sized structures is also widely utilized for the production of light in Light Emitting Diodes (LEDs) [1.5]. Engineering of materials at the nanoscale may provide viable routes for an increase in the precision tailoring of a

material's electrical, optical, magnetic, and thermo-electric properties, creating a more efficient, whole base to expand the structural engineering possibilities at the macroscale.

The reliable engineering of materials at smaller and smaller scales, known as miniaturization, has been one of the most important challenges faced by a large number of high-technology industries, in particular the micro-electronics industry. With an ever-increasing number of consumer products containing integrated circuits, markets demand a reduction in the size of discrete device structures for improving both performance and profitability. This increase in performance, a doubling of integrated circuit complexity every 18 months commonly referred to as Moore's Law, was initially observed by the co-founder of Intel, Gordon Moore. Manufacturing techniques for the continued miniaturization of individual devices are quickly approaching some fundamental physical limitations associated with current top-down photolithography processes. This will eventually lead to a deviation from Moore's law if suitable alternatives are not implemented in time. A crossroads is coming where the limitations of macroscale machines for the creation of nanostructures and beyond will become antiquated, putting an end to their usefulness, and opening the door instead for mass device creation at the nanoscale utilizing different methods.

### **1.1.1. Introduction to Self-Assembly – Engineering From the “Bottom Up”**

On December 29<sup>th</sup>, 1959 at the annual meeting of the [American Physical Society](#) at the [California Institute of Technology \(Caltech\)](#), physicist Richard Feynman made his famous lecture entitled “There's Plenty of Room at the Bottom, ” widely credited as the beginning of what is now commonly referred to as *nanotechnology*. His insights about looking to nature and biological systems as examples for nanofabrication led to the current day classification

of self-assembled materials. Instead of molding materials into useful structures, Feynman argued for the utilization of the inherent properties of the smallest building blocks, letting them spontaneously form functional higher order structures themselves. These processes, following the laws of thermodynamics, would be self-correcting, self-directed, and self-limiting due to the inherent properties of the individual components [1.6], thereby allowing for the creation of smaller and more efficient devices with much higher precision than would be possible utilizing top down fabrication techniques.

This idea of utilizing materials from the bottom up, allowing for a material's natural ability to create higher order structure constitutes a paradigm shift in the way we as humans see and experience the physical world, as conventional Newtonian Mechanics does not readily apply at the nanoscale. The laws of Quantum Mechanics on the other hand are more readily applicable at the nanoscale. Although the ability to manipulate individual atoms or groups of atoms with scanned probe microscopies has become almost routine [1.7], it is at best a clumsy and inefficient way to deal with the precise positioning of the many atoms needed for a single integrated circuit. Creation of structure through self-assembly could be thought of as a complex dance, with many molecules or atoms and many possible outcomes. The dance continues ever onward with only those most energetically favorable interactions realizing their potential of creating higher order structure. In a sense the material creates its own unique structure based on the interpretation of all the possible outcomes by its constituent parts. Self-assembly, therefore, allows for the parallel creation of unique nanostructures through the inherent properties of the individual atoms or molecules involved.

While this is a great way to create large numbers of the same structures, there are still limitations to the specific placement of the created nanostructures as needed for macroscale

applications. It is this inability to direct exact spatial placement that is one of the major challenges facing the utilization of nanostructures for individual devices.

The usefulness of self-assembly techniques for engineering nanostructures is highly dependent on an engineer's ability to understand with a great deal of accuracy what is happening at the molecular and atomic scale as it relates to the changes they are making to the dance. Within self-assembled nanostructure fabrication is an engineering methodology with the potential to affect the physical properties of nanostructures by making subtle changes to the constituent building block molecules and environmental conditions, i.e. the dancers and the music. This has made high-resolution microscopy and spectroscopy techniques with nanometer and sub-nanometer spatial resolutions, such as Atomic Force Microscopy (AFM), Transmission Electron Microscopies (TEM), and Energy Dispersive X-Ray Spectrometry (EDS) such an important part of the investigations into nanostructural self-assembly. With the continuing advancements in high-resolution microscopy and analysis, self-assembly fabrication techniques are becoming an increasingly viable option for the successful engineering of nanostructural components.

The ability to perform high-resolution nanoanalysis provides the nano-engineer an ultra-sensitive feedback loop whereby they can visualize and measure the outcome of changes made to a variety of environmental conditions such as concentration levels or temperature, leaving the construction process up to the creativities of the individual atoms and molecules.

Ultimately, while the utilization of self-assembled processes for the controlled engineering of nanostructures has increased greatly over the past 10-20 years, it can still be considered in its infancy. Currently, self-assembly of structures are confined to one step growth methods. Nature again can serve as a model however, for self-assembly processes in

this arena include multiple steps in synchronicity. Self-assembly processes in nature seem to have built in feedback loops, or some type of inherent awareness that occurs for each level of complexity allowing for the assembly of even higher order structures. No matter how complex the final structure, as for instance with muscle tissue [1.8], the resulting multi-scale self-assembled structures are inherently dependant on the unique chemistry of the initial constituent molecular building blocks.

These molecules, known as amphiphiles, meaning *loving of both*, contain both polar (hydrophilic) and non-polar (hydrophobic) groups of atoms that are bound together by a strong chemical bond preventing dissociation. This situational duality contained within an individual molecule gives rise to their unique ability for creation of higher order structures within solutions[1.9]. If the concentration of amphiphiles in a solution is high enough, a situation will arise where the polar ends will associate with other polar groups and the non-polar groups will associate with other non-polar groups, leading to the spontaneous ordering of the molecules within solution[1.9]. Self-assembly formation mechanisms are the basis for the creation of a myriad of biological structures including membranes [1.10], microtubules [1.11], and actin filaments [1.12]. Depending on the complexity, concentration and geometry of the individual molecules, different higher order structures can arise, from monolayers to bilayers to vesicles and micelles [1.9].

### **1.1.2. Self-Assembled Monolayers**

Research into the directed self-assembly of molecules on solid surfaces has quite a long history. In the 1930's, a researcher named Blodgett successfully transferred a molecularly thick film to a solid surface utilizing Langmuir's previously published liquid-air interface

growth techniques [1.13]. The resulting monolayer film, which was transferred to the solid-air interface, became known as a Langmuir-Blodgett film. Through the application of Blodgett's techniques, custom multilayered monomolecular films on solid materials could endlessly be layered one after the other. Thus, by tailoring the chemistry of the individual molecules end groups one could tailor the entire chemistry of a given surface. Ten years later, Bigelow and Zisman revealed that monolayers could be spontaneously formed on a solid surface by immersion of the solid surface into a disordered solution containing active surfactant compounds within an organic solvent [1.14]. These films are referred to as self-assembled monolayers or SAM's.

The creation of SAM's on surfaces for use as corrosion inhibitors and adhesion promoters has been widely investigated with analysis techniques such as X-Ray Photoelectron Spectroscopy (XPS)[1.15]. A major advancement in understanding the structuring of SAM's has been due in no small part to the development of high resolution microscopies and more specifically scanned probe microscopies (SPM). Beginning in the early 1980's, the creation of the Scanning Tunneling Microscope (STM)[1.16] and then a short time later the Atomic Force Microscope (AFM)[1.17] allowed researchers to non-destructively examine a surface's atomic and molecular structure. While overall film thickness and orientation measurements were possible previously through the use of highly sensitive analytical techniques such as ellipsometry, XPS, and Fourier Transform Infrared Spectrometry (FTIR), SPM finally made it possible to examine the ordering, defect densities, packing factors, and molecular orientations with molecular and sub-molecular resolution. In addition to structural investigations, now the performance characteristics of individual molecular interactions with surfaces could be investigated with unprecedented sensitivity.

## 1.2. Research Motivation

This PhD dissertation documents the processes and techniques utilized for the characterization of a previously unreported, novel self-assembled material created with short chainlength APAs and aluminum or gallium. The intention has been to provide increased knowledge of APA Self-Assembled Nanofiber (SAN) formation, their structure, and properties in order to identify potential applications. Repeatable and in some cases novel growth methods, as well as the application of analysis techniques utilized for the characterization of APA SANs at the nanoscale are presented.

Since the discovery and commercialization of SPM, a variety of SAM physical properties have been investigated including but not limited to friction [1.18], adhesion and self-healing [1.19], electrical [1.20], and thermal response [1.21]. Much of this research has focused on idealized chemisorption type monolayer systems such as alkane-thiols on gold for investigation of 2D thin films using SPM [1.22]. While the studies of thiols on Au provided many important steps towards understanding the fundamental aspects of SAM formation, it was of interest to translate these *ideal* results into more industrial applications including metal oxide engineering materials.

Due to the large-scale industrial use of aluminum and Ferrous alloys, there are a wide variety of applications where the implementation of SAM films as adhesion promoters, corrosion inhibitors, and lubricants would prove to be of economic benefit. Utilization of SAMs for the creation of surface films also provides engineers unprecedented control over the surface properties of materials through the customization of individual SAM molecular chemistry.

The work presented here has its roots within John Richards' Master's thesis, NCSU 1997[1.23], which describes in detail his efforts towards understanding the formation of various alkyl-phosphonic acid (APA) SAM's on both evaporated aluminum thin films and mica surfaces. Alkyl-phosphonic acids (APAs) are linear molecules with a phosphonic acid  $\text{O}=\text{P}(\text{OH})_2$  head group and a methyl ( $\text{CH}_3$ ) end group joined together by a carbon (alkyl) chain of variable length. Richards examined the changes in the surface morphology of substrates immersed in various APA solutions over time utilizing Atomic Force Microscopy (AFM). Immersion solutions were typically created utilizing an appropriate amount of APA molecules dissolved in pure Ethanol (EtOH) forming 0.1 wt% or 8.3 mM solutions. This concentration was considered to be below the critical micelle concentration (CMC) for Octadecylphosphonic acid (C18) in EtOH, allowing the creation of isotropic solutions of even the longest and least soluble C18 molecules.

Richard's project was centered around the fact that APAs were reported to strongly react with the surface of aluminum forming stable SAMs [1.15]. In addition to the chemical affinity for the phosphonic acid with an aluminum surface, the easily tailored endgroup chemistry as well as its commercial availability made APA's a good choice for creation of SAMs on engineering surfaces such as Aluminum.

Although Richard's found that stable SAM films on aluminum were obtained when utilizing APA chain lengths greater than 12, he observed a drastic decrease in the corrosion performance of the treated aluminum films when examined with electrochemical techniques[1.23]. Believing that the decreased corrosion performance might be due to defects in the SAM film, shorter chainlength APAs were investigated in hopes of improving surface mobility through reduction of chain-chain interactions.

When using Alkyl chain lengths of 12 (C12), 8 (C8) and 1 (C1), strange “worm-like” structures were observed to grow on treated aluminum surfaces over time, with slower growth rates observed for the longer alkyl chains of 8 and 12. The “worm-like” structures were never observed to form on glass substrates treated with the same C1 solution for similar immersion times without the initially deposited aluminum present. Since the main effort of the project was to create stable monolayers, Richards noted the results but focused the remainder of his work on the longer chain-length, octadecylphosphonic acid (C18) SAM's never characterizing the growth or properties of these unknown structures.

The “worm-like” structures initially observed by Richards, were not predicted or generally a desired result at the time of their discovery. However, their formation now has increased relevance within nanotechnology research. Growth of APA SANs is now seen as a novel and possibly unique method for the formation of repeatable 1-Dimensional (1-D) nanostructures.

1-D nanostructures currently show great promise for a wide variety of economically important as well as ecologically impactful electro-optical applications [1.24, 25], which range from interconnects[1.26] to innovative solar cell technologies[1.27]. Additionally, work on aluminum-phosphates[1.28-35] and aluminum-phosphonate[1.36, 37] type materials have produced a wide variety of mesoporous (nm scale pores) and layered materials having important applications in advanced molecular sieves and catalysis. Layered metal-phosphonates utilizing metals such as Zr have also been identified to have important fuel cell applications[1.38]. It has been the promise of such applications as well as the desire to further the fundamental knowledge concerning the engineering of self-assembled nanostructures that has provided the motivation needed to complete this study.

### **1.3. Dissertation Structure**

This dissertation is organized in a way that will hopefully provide the reader quick and easy access to the information of interest to them. The document is broken into chapters, each of which focuses on a single aspect of the project. The chapters are organized into three main sections: background and instrumentation, growth and characterization, and conclusions and future work.

The first chapter introduces the reader to important background information concerning self-assembly as well as providing motivation for the research that has been conducted. The second chapter is a general reference of all the analytical techniques utilized for acquisition of the data presented in subsequent chapters. Chapter three documents the various methods utilized for the creation of SANs. Chapter four contains the results of specific analytical techniques utilized for understanding both the external and internal SAN structure as well as composition of individual SANs. Chapter five shows the effect of thermal anneals on various SAN samples as grown on both aluminum and  $\text{Si}_3\text{N}_4$  supports. Chapter six documents the analysis of the mechanical properties exhibited by the SANs both qualitatively and quantitatively. Chapter seven describes the efforts to understand the electronic properties of individual SANs. Chapter eight then summarizes the findings of this project, presenting the contributions made by this work to the scientific community at large, as well as raising new questions for future experimentation and possible pathways to further refine the current understanding of APA SANs.

## 1.5. References

- [1.1] Baskoutas, S. and A.F. Terzis, *The size-dependent band gap of semiconductor quantum dots*. Journal of Applied Physics, 2006. **99**(1): p. 013708.
- [1.2] Poncharal, P., et al., *Room temperature ballistic conduction in carbon nanotubes*. Journal of Physical Chemistry B, 2002. **106**(47): p. 12104-12118.
- [1.3] Fletcher, B.L., et al., *Microarrays of biomimetic cells formed by the controlled synthesis of carbon nanofiber membranes*. Nano Letters, 2004. **4**(10): p. 1809-1814.
- [1.4] Chakravorty, D., S. Banerjee, and T.K. Kundu, *Quantum confinement effect in nanocomposites*. Applied Surface Science, 2001. **182**(3-4): p. 251-257.
- [1.5] Coe, S., et al., *Electroluminescence from single monolayers of nanocrystals in molecular organic devices*. Nature, 2002. **420**(6917): p. 800-803.
- [1.6] Whitesides, G.M. and B. Grzybowski, *Self-assembly at all scales*. Science, 2002. **295**(5564): p. 2418-2421.
- [1.7] Huang, D.H., et al., *STM single atom manipulation technology and its physical mechanism*. Shanghai Jiaotong Daxue Xuebao/Journal of Shanghai Jiaotong University, 2001. **35**(2): p. 157-167.
- [1.8] Mackenzie, J.M., H.F. Epstein, and M.A. Goldstein, *Thin Filament Arrangement in Skeletal-Muscle*. Journal of Cell Biology, 1981. **91**(2): p. A348-A348.
- [1.9] Israelachvili, J.N., *Intermolecular and surface forces*. 2nd ed. 1991, London ; San Diego: Academic Press. xxi, 450 p.
- [1.10] Coster, H.G.L., *The physics of cell membranes*. Journal of Biological Physics, 2003. **29**(4): p. 363-99.
- [1.11] Engelborghs, Y., *Microtubules: dissipative structures formed by self-assembly*. Biosensors & Bioelectronics, 1994. **9**(9-10): p. 685-689.
- [1.12] Wong, E.W., P.E. Sheehan, and C.M. Lieber, *Nanobeam mechanics: Elasticity, strength, and toughness of nanorods and nanotubes*. Science, 1997. **277**(5334): p. 1971-1975.
- [1.13] Langmuir, I. and K.B. Blodgett, *Methods of investigation of monomolecular films*. Kolloid Zeitschrift, 1935. **73**: p. 257-263.
- [1.14] Bigelow, W.C., D.L. Pickett, and W.A. Zisman, *Oleophobic Monolayers .I. Films Adsorbed from Solution in Non-Polar Liquids*. Journal of Colloid Science, 1946. **1**(6): p. 513-538.

- [1.15] Folkers, J.P., et al., *Self-Assembled Monolayers of Long-Chain Hydroxamic Acids on the Native Oxides of Metals*. Langmuir, 1995. **11**(3): p. 813-824.
- [1.16] Binnig, G., et al., *7x7 Reconstruction on Si(111) Resolved in Real Space*. Physical Review Letters, 1983. **50**(2): p. 120-123.
- [1.17] Binnig, G., C.F. Quate, and C. Gerber, *Atomic Force Microscope*. Physical Review Letters, 1986. **56**(9): p. 930-933.
- [1.18] Yang, X.J. and S.S. Perry, *Friction and molecular order of alkanethiol self-assembled monolayers on Au(111) at elevated temperatures measured by atomic force microscopy*. Langmuir, 2003. **19**(15): p. 6135-6139.
- [1.19] Neves, B.R.A., et al., *Self-healing on OPA self-assembled monolayers*. Nanotechnology, 2001. **12**(3): p. 285-289.
- [1.20] Gomar-Nadal, E., et al., *Self-assembled monolayers of tetrathiafulvalene derivatives on Au(111): Organization and electrical properties*. Journal of Physical Chemistry B, 2004. **108**(22): p. 7213-7218.
- [1.21] Neves, B.R.A., et al., *Thermal stability study of self-assembled monolayers on mica*. Langmuir, 2000. **16**(6): p. 2409-2412.
- [1.22] Tamchang, S.W., et al., *Self-Assembled Monolayers on Gold Generated from Alkanethiols with the Structure Rnhcoch(2)Sh*. Langmuir, 1995. **11**(11): p. 4371-4382.
- [1.23] Richards, J.F., *Atomic force microscopy studies of microstructure and properties of self-assembled monolayers*. 1997, North Carolina State University. p. xii, 136 leaves.
- [1.24] Law, M., et al., *Nanoribbon waveguides for subwavelength photonics integration*. Science, 2004. **305**(5688): p. 1269-1273.
- [1.25] Goldberger, J., et al., *ZnO nanowire transistors*. Journal of Physical Chemistry B, 2005. **109**(1): p. 9-14.
- [1.26] Stan, M.R., et al., *Molecular electronics: From devices and interconnect to circuits and architecture*. Proceedings of the Ieee, 2003. **91**(11): p. 1940-1957.
- [1.27] Law, M., et al., *Nanowire dye-sensitized solar cells*. Nature Materials, 2005. **4**(6): p. 455-459.
- [1.28] Chen, J.S., W.Q. Pang, and R.R. Xu, *Mixed-bonded open-framework aluminophosphates and related layered materials*. Topics in Catalysis, 1999. **9**(1-2): p. 93-103.

- [1.29] Hu, Y.T., et al., *Thermochemical Study of the Relative Stability of Dense and Microporous Aluminophosphate Frameworks*. Chemistry of Materials, 1995. **7**(10): p. 1816-1823.
- [1.30] Girnus, I., et al., *Synthesis of Alpo4-5 Aluminumphosphate Molecular-Sieve Crystals for Membrane Applications by Microwave-Heating*. Advanced Materials, 1995. **7**(8): p. 711-&.
- [1.31] Prasad, S. and I. Balakrishnan, *Synthesis of a New Crystalline Aluminophosphate*. Journal of Materials Chemistry, 1992. **2**(10): p. 1087-1089.
- [1.32] Davis, M.E. and R.F. Lobo, *Zeolite and Molecular-Sieve Synthesis*. Chemistry of Materials, 1992. **4**(4): p. 756-768.
- [1.33] Goepper, M. and J.L. Guth, *Synthesis and Characterization of Alpo4-14a Molecular-Sieves*. Zeolites, 1991. **11**(5): p. 477-482.
- [1.34] Rudolf, P.R., C. Saldarriagamolina, and A. Clearfield, *Preparation and X-Ray-Powder Structure Solution of a Novel Aluminum Phosphate Molecular-Sieve, (Alpo4)3.(Ch3)4noh*. Journal of Physical Chemistry, 1986. **90**(23): p. 6122-6125.
- [1.35] Jacobs, H.O., et al., *Surface potential mapping: A qualitative material contrast in SPM*. Ultramicroscopy, 1997. **69**(1): p. 39-49.
- [1.36] Cabeza, A., et al., *Aluminum phenylphosphonates: A fertile family of compounds*. Inorganic Chemistry, 1998. **37**(17): p. 4168-4178.
- [1.37] Maeda, K., Y. Kiyozumi, and F. Mizukami, *Synthesis of the First Microporous Aluminum Phosphonate with Organic Groups Covalently Bonded to the Skeleton*. Angewandte Chemie-International Edition in English, 1994. **33**(22): p. 2335-2337.
- [1.38] Segawa, K., et al., *Molecular design of layered zirconium phosphonates for fuel cell applications*, in *Recent Advances in the Science and Technology of Zeolites and Related Materials, Pts a - C*. 2004. p. 1096-1102.

## **2 Analytical Techniques**

### **2.1 Introduction**

This section provides a general overview of the instrumentation utilized throughout this dissertation and also supports the specific analytical techniques presented in subsequent chapters. The purpose is to provide a basic theoretical understanding of the techniques here, so that the reader may better understand the presented results in later chapters. By consolidating this material here, I hope to create a reference document that is easier to navigate, allowing readers of various technical backgrounds access to the wealth of information gathered throughout the entire work.

### **2.2 Atomic Force Microscopy (AFM)**

Atomic Force Microscopy (AFM), developed by Binnig, Quate, and Gerber in 1986[2.1], belongs to the larger microscopy family known as Scanned Probe Microscopy (SPM). In SPM, an atomically, or nearly atomically, sharp probe scans the surface while held in close proximity to the sample by a piezo electric transducer. As the tip is translated, the interaction between the tip and the sample is monitored and a map of surface properties, or topography, is obtained. Since the interaction between the tip and the surface is highly localized and dependent on the tip-sample separation distance, a feedback mechanism is employed to precisely control the level of the interaction during the scan. Initially, the feedback loop utilized a tunneling current between the atomically sharp tip and the sample, in the form of Scanning Tunneling Microscopy[2.2]. This methodology however confined the SPM to analysis of conducting and semi-conducting samples, for it was difficult to control

the surface charge on insulating samples. Eventually, advancements in instrument design led to a force detection system allowing for observation of insulators as well as conductors. This was the birth of Atomic Force Microscopy.

### **2.2.1. Contact Mode**

A diagram of AFM Contact Mode is shown in Figure 2.1. An AFM utilizes a sharp tip mounted on the underside of a flexible cantilever of known stiffness. The tip is brought into contact with the sample until the desired force, i.e. desired cantilever deflection, is obtained. The cantilever deflection is measured by bouncing laser light off the back of the cantilever and onto a position sensitive photo diode (PSPD). Once in contact, the tip is scanned in an x-y raster pattern relative to the sample. Scanning is accomplished by the use of piezoelectric actuators allowing for the precise control of the probe sample interactions in x, y and z directions at all times. For observation of the sample topography in contact mode, the feedback loop monitors the tip deflection while scanning, attempting to keep it constant by applying a compensating voltage to the z piezo. The correction, or error signal, is created by the feedback loop and stored for each point collected in the entire scan. Comparing the error value to a calibrated known value for the sensitivity of the z-piezo gives the change in length of the piezo at any given point, which in turn is the topography of the sample. This is the typical detection scheme for most samples in contact mode excluding atomically flat samples where the topography is so slight it is best to simply monitor the cantilever deflection directly.

### **2.2.2. Intermittent Contact or Tapping Mode**

A diagram of AFM tapping or intermittent contact mode is shown in Figure 2.2. In tapping mode, an oscillating tip is employed to investigate the topography of a sample[2.3]. Similar to contact mode, whereby the tip is kept at a constant force, the feedback loop in tapping mode attempts to keep the tip at a constant damping level as it scans the sample. To do this, an additional piezo oscillates the cantilever near its resonance frequency causing the tip to deflect sinusoidally with some desired amplitude. As the tip is brought close to the surface and begins to interact with the surface, a decrease in the oscillation amplitude of the cantilever occurs. This decrease in amplitude, also known as damping, is monitored by the feedback loop. As the sample is scanned, the topography is mapped in much the same way as contact mode, but with the damping rather than the deflection held at a constant.

A major advantage to using intermittent contact is the near elimination of lateral forces while scanning, which allows softer samples to be imaged without the sample degradation typically found when using contact mode[2.4]. Another advantage to tapping mode is that one can monitor the phase signal as a surface is scanned. The phase image is derived from comparison of the driving signal phase with the detected signal phase. As the tip scans a sample, one can monitor changes in the reaction time by noting when the cantilever is pushed versus when the deflection is detected. Due to its high sensitivity, the phase signal is very useful for detecting edges and material property differences such as modulus or surface chemistry differences[2.5]. Unlike the topography image where the z scale information is quantitative in x, y and z directions, the phase image is typically only quantitative in the x and y directions.

## 2.3 Scanning Electron Microscopy (SEM)

Scanning Electron Microscopy (SEM) has its roots in Transmission Electron Microscopy (TEM). SEM, first realized by Von Ardenne in 1938, included the addition of scan coils onto a TEM. The beam was scanned across a thin sample capturing a Scanning Transmission Electron Microscopy (STEM) image from below the sample[2.6]. The first SEM utilized for imaging surfaces of materials was first described in 1942[2.7]. The instrument was constructed using an inverted column, with the electron gun at the bottom, electrostatic lenses, and electromagnetic scan coils. Over the next 13 years many improvements were made to the design of the SEM. Electromagnetic lenses replaced the electrostatic lenses previously utilized to focus the beam. A double-deflection scan system was added and stigmation coils incorporated, allowing for improved beam control[2.7]. Finally, the initial secondary electron detector was improved upon by the addition of a light pipe between the scintillator and the photomultiplier tube, markedly improving its efficiency[2.8]. All of these improvements were combined into the first commercial SEM, the Cambridge Scientific Instruments Mark I, first available in 1965. Over the next 40 years even more improvements to the design of the SEM occurred, from column design, to detectors and vacuum systems, as well as digital image acquisition. All of these modifications have improved both the resolution and overall usability of the SEM in today's world.

A typical SEM column, Figure 2.3, is composed of an electron gun, one or more condenser lenses, several apertures, an objective lens, and scan coils[2.9]. The electron gun generates a beam of electrons in a vacuum environment and accelerates them to energies in the range of 0.1 – 30KeV. As the electrons travel down the column towards the sample, the beam passes through a series of electromagnetic condenser lenses and fixed apertures to

collimate and reduce the initial spot size produced by the gun. The conditioned beam is focused on the sample surface by the objective lens where it interacts with the sample producing various signals, Figure 2.4, that, if an appropriate detector is used, can be used to form an image. The final spot size at the specimen is on the order of 10nm or less[2.9]. An SEM image is created by scanning the beam point by point in a raster pattern using the deflection system and correlating the collected signal to its position on the sample. The final magnification of the resulting image is simply the ratio of the size of the image on the viewing screen to the corresponding size of the raster scan on the sample surface.

The primary imaging method is through the collection of secondary electrons. Secondary electrons (SE), are defined as low energy,  $\sim 50$  eV or less, electrons that are the result of loosely bound outer shell specimen electrons gaining enough kinetic energy from the inelastic scattering events of the incident beam to escape the sample, thus allowing for collection by a SE detector. Due to their low energy, SE's are generally confined to carrying information about the sample topography. However, there are other imaging modes such as Specimen Current imaging (SC) and Back-Scattered Electron imaging (BSE) typically found on SEM's, which can provide information about other features such as composition or electronic properties. In addition to SE, SC, and BSE detectors, SEM's often have x-ray detectors and analyzers. Energy Dispersive X-Ray Spectroscopy (EDS) utilizes the characteristic x-rays generated by the beam-sample interactions to identify the elemental composition of the specimen for all elements with an atomic number greater than boron.

## 2.4 Scanning Transmission Electron Microscopy (STEM)

High-resolution Transmission Electron Microscopy (TEM) instrumentation is utilized to examine the internal structure of both organic and inorganic thin samples, which are electron transparent, overcoming the resolution limits of conventional optical microscopies. A “thin sample” is one that is on the order of at most a few hundred nanometers thick. In traditional TEM imaging mode, the thin specimen is illuminated with a nearly parallel beam of electrons, and the transmitted electrons are then focused by the objective lens and a number of post specimen lenses to form a real image. This is very analogous to the operation of a light microscope (Kohler illumination) except that the focal length of the magnetic lenses in a TEM can be changed by changing the lens current. STEM mode, on the other hand, is the operation of a TEM in spot mode, or convergent beam mode, with the addition of scan coils to raster the focused beam across the sample.

A diagram of a typical dedicated STEM is shown in Figure 2.5. The advantages of using STEM for highly localized nanoanalysis with Energy Dispersive X-Ray Spectroscopy (EDS) and Electron Energy Loss Spectroscopy (EELS) was realized in 1963 with the initial idea for production of a dedicated STEM[2.10]. Vacuum Generators (VG) Microscopes, Ltd. initially produced the first commercialized STEM systems. Currently there are several manufacturers of STEM's including Hitachi and JEOL. The Hitachi HD-2000 series of STEM's are truly dedicated STEM designs. The column design is more analogous to a Field Emission SEM than a conventional TEM. An electron beam is produced by a field emission type electron gun and accelerated to an energy of approximately 200-400keV with an initial crossover of ~ 5.0 nm. The column is capable of focusing the beam to a final spot at the sample of ~ 0.5 nm @ 1 nA of beam current[2.11].

Many useful detectable signals are created due to the interaction of the beam with the thin sample including SE, BSE, x-rays, photons, and Electron Hole Pairs (EHP), all of which can be used to create spatially important images. Additionally, a High-Angle Annular Dark Field (HAADF) detector, a Bright Field (BF) detector, or a spectrometer, as in the case of Electron Energy Loss Spectrometry (EELS), can be utilized to collect beam electrons that have passed through the sample. A HAADF detector collects incident beam electrons that have been forward scattered to relatively high angles typically between 50 mrad – 200 mrad. This angular range can be controlled with the post sample projector lens optimizing image contrast. Images produced through the use of HAADF are often referred to as ‘Z-Contrast’ images since the cross-section for Rutherford elastic scattering is proportional to  $Z^2$ [2.12, 13]. Throughout this work, HAADF images are also labeled ‘ZC’ images. In a sample, the higher Z regions will proportionally scatter more electrons than lower Z regions. This will then appear as a higher intensity in the produced image[2.12, 13]. If there are changes in topography, as is the case with APA SANs, there will also be contributions to the ZC image contrast due to thickness differences as it relates to average Z of the area irradiated by the beam.

In addition to the HAADF detector, there is a second detector below the sample, called the Bright Field (BF) detector. The BF detector collects the transmitted electrons scattered to lower angles. It is a circular detector placed beyond the HAADF detector along the optic axis, and the images created using it are referred to as ‘TE’ images throughout this work. The ZC and TE images obtained are correlated spatially, but carry different, but complementary, sample information.

## 2.5 X-ray Photoelectron Spectroscopy (XPS)

X-ray Photoelectron Spectroscopy (XPS) is utilized for the detection of changes in chemical composition and oxidation states on the surface of materials[2.14, 15]. Soft X-rays, 1200 eV in the case of the Riber instrument utilized for this work, are used to irradiate the sample causing photoelectrons to be emitted. The entire sample  $\sim 1 \text{ cm}^2$  is irradiated. An area of interest, about 3 mm on the Riber, is analyzed by collecting the emitted photoelectrons with a spectrometer. The elements and their chemical state, or valence, can be determined from the kinetic energies of the detected electrons. This technique is very surface sensitive as only electrons emitted from the first few layers of surface atoms can escape with characteristic energies intact. Subtle differences in peak shape and peak positioning yields important details about surface chemistry differences between samples.

The XPS Binding Energy scale is typically referenced to the advantageous carbon peak and assigning that value to 285 eV[2.14, 15]. Any peak shifts relative to this value can be quantified and assumed to be due to surface chemistry. XPS can also be used to determine the elemental surface composition of all non-volatile materials except hydrogen. It is also possible to perform XPS analyses at different depths in the sample by utilizing an Argon ion gun to sputter away surface layers between XPS scans. Angle resolved XPS was not available for use in this work.

## 2.6 Focused Ion Beam (FIB)

A Focused Ion Beam (FIB) can be thought of as an SEM that utilizes a focused probe of ions instead of electrons for both imaging the surface of a sample as well as for physically sputtering material with high levels of precision[2.16]. Instead of a field-emission electron gun, the FIB uses a field emission Liquid Metal Ion Source (LMIS) to generate a beam of ions. Typical commercial FIB's use a gallium LMIS. The ions are accelerated down a column, focused with lenses, and rastered with scan plates across the surface of the sample. The FIB can be utilized for imaging, deposition, or milling of materials. Deposition of materials, typically utilized to protect the area of interest from damage due to the incident beam, is accomplished by introduction of a precursor organo-metallic gas through a needle injection system placed close to the sample. Through control of the beam current with different condenser lens settings and aperture sizes, beam conditions can be optimally tailored for imaging, deposition, or milling as required.

A Hitachi FIB was utilized in this work to create 'lift-out' cross-sections of the C1 PA SANs grown on  $\text{Si}_3\text{N}_4$ . Typically, a protective layer of metal or carbon, ~200 nm–1000 nm is blanket coated onto the sample through sputtering or evaporation outside of the FIB machine. After the sample is introduced in the FIB, another protective layer is deposited on the area of interest. This protective layer is typically platinum (Pt) or tungsten (W) and is deposited by introducing a metal-organic precursor gas into the system through a needle near the area of ion beam impingement on the sample.

In the FIB system utilized for this work, a protective cap of W was deposited, then the areas around the deposition were milled away typically leaving a 20 mm x 4 mm x 5mm sized piece connected to the rest of the sample on only the left side. The pieces were then

welded to a nano-positionable needle through deposition of a small amount of W. The remainder of the sample was then milled away freeing the piece from the rest of the sample. The freed piece was then lifted away with the needle, welded onto a copper (Cu) half-grid, and milled with the ion beam from the top down leaving a free-standing cross-section on the order of 100 nm thick. The resulting thin sections were then imaged utilizing a HD-2000 dedicated STEM. This sample preparation protocol was provided by Hitachi High Technologies [2.11].

## 2.7 Figures

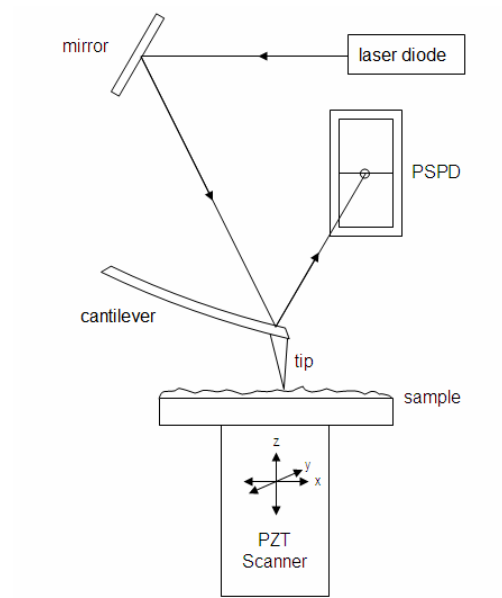


Figure 2.1. Schematic of a scanned sample AFM in contact mode [2.17]

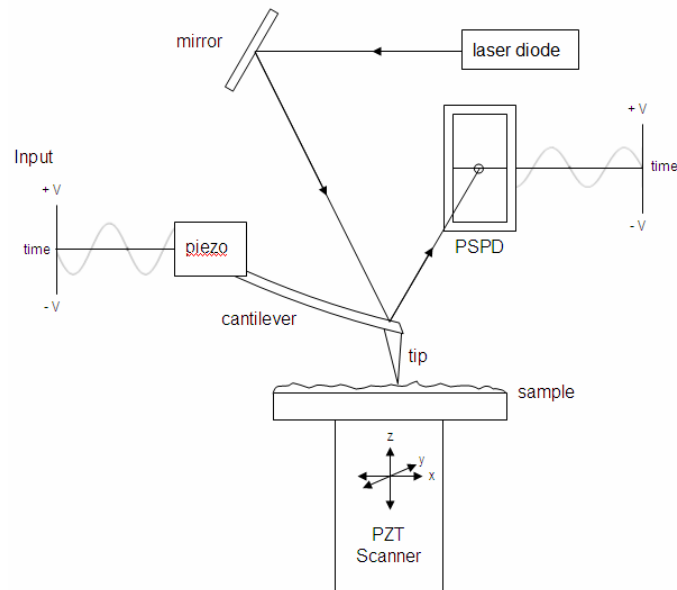


Figure 2.2. Schematic of a scanned sample AFM in tapping mode [2.17].

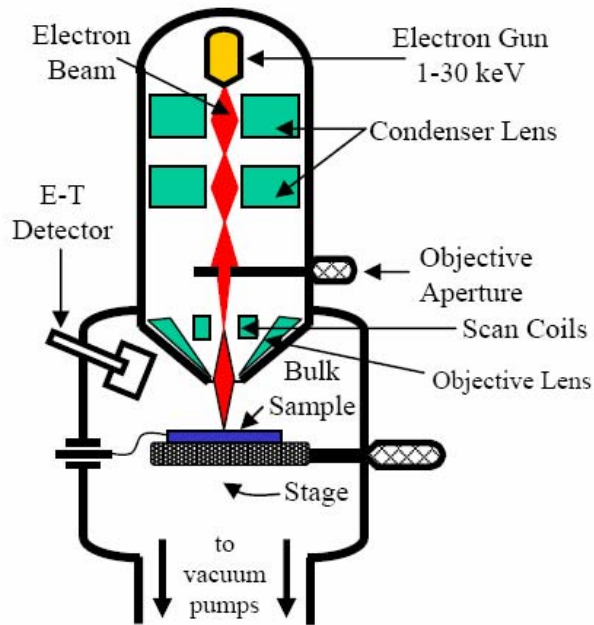


Figure 2.3. Schematic of the primary components of a typical SEM [2.9, 2.18].

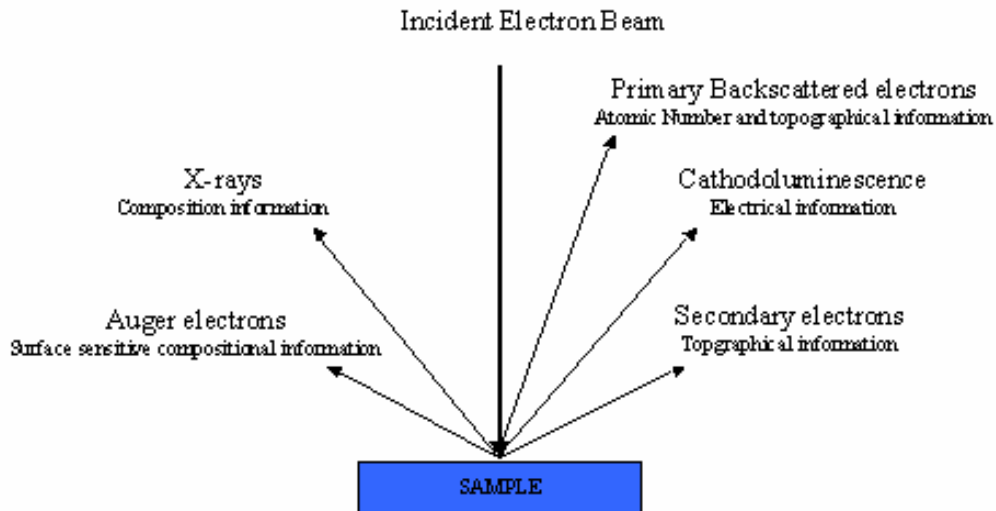


Figure 2.4. Useful signals generated from electron beam-sample interactions [2.9, 2.18].

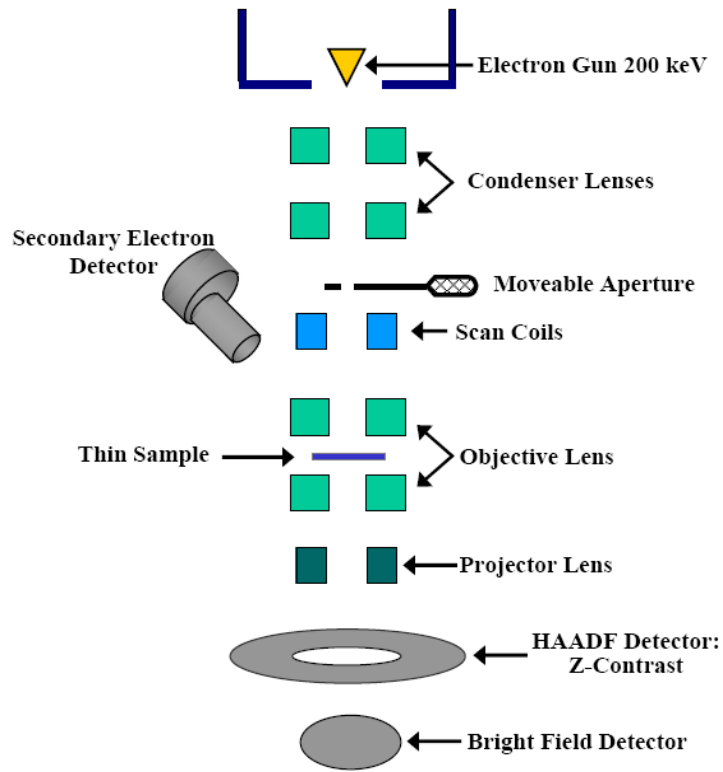


Figure 2.5. Schematic of the primary components of a dedicated STEM [2.13, 2.18]

## 2.7 References

- [2.1] Binnig, G., C.F. Quate, and C. Gerber, *Atomic Force Microscope*. Physical Review Letters, 1986. **56**(9): p. 930-933.
- [2.2] Binnig, G., et al., *Surface Studies by Scanning Tunneling Microscopy*. Physical Review Letters, 1982. **49**(1): p. 57-61.
- [2.3] Meyer, G. and N.M. Amer, *Novel Optical Approach to Atomic Force Microscopy*. Applied Physics Letters, 1988. **53**(12): p. 1045-1047.
- [2.4] Zhong, Q., et al., *Fractured Polymer Silica Fiber Surface Studied by Tapping Mode Atomic-Force Microscopy*. Surface Science, 1993. **290**(1-2): p. L688-L692.
- [2.5] Schmitz, I., et al., *Phase imaging as an extension to tapping mode AFM for the identification of material properties on humidity-sensitive surfaces*. Applied Surface Science, 1997. **115**(2): p. 190-198.
- [2.6] Ardene, M.v., *Zeitschrift fuer Technische Physik*, 1938. **19**: p. 553.
- [2.7] Smith, K.C.A. and C.W. Oatley, *The Scanning Electron Microscope and Its Fields of Application*. British Journal of Applied Physics, 1955. **6**(11): p. 391-399.
- [2.8] Everhart, T.E. and R.F.M. Thornley, *Wide-Band Detector for Micro-Microampere Low-Energy Electron Currents*. Journal of Scientific Instruments, 1960. **37**(7): p. 246-248.
- [2.9] Goldstein, J., *Scanning electron microscopy and x-ray microanalysis*. 3rd ed. 2003, New York: Kluwer Academic/Plenum Publishers. xix, 689 p.
- [2.10] Crewe, A.V., *Possible High-Resolution Scanning Microscope*. Journal of Applied Physics, 1964. **35**(10): p. 3075-&.
- [2.11] Hitachi High Technologies Americas, Inc., <http://www.hitachi-hta.com>, Schaumburg, IL.
- [2.12] Williams, D.B. and C.B. Carter, *Transmission electron microscopy : a textbook for materials science*. 1996, New York: Plenum Press. xxvii, 729 p.
- [2.13] Keyse, R.J., *Introduction to scanning transmission electron microscopy*, 1998, New York: Springer.
- [2.14] Barr, T.L., *Modern ESCA : the principles and practice of x-ray photoelectron spectroscopy*. 1994, Boca Raton: CRC Press. 358 p.
- [2.15] Nefedov, V.I., *X-ray photoelectron spectroscopy of solid surfaces*. 1st English ed. 1988, Utrecht, The Netherlands: VSP BV. vii, 191 p.

[2.16] Giannuzzi, L.A., F.A. Stevie, and Faculty Publication Collection (North Carolina State University), *Introduction to focused ion beams : instrumentation, theory, techniques, and practice*. 2005, New York: Springer. xiv, 357 p.

[2.17] Howland, R. and Benatar, L., *A Practical Guide to Scanning Probe Microscopy*, Park Scientific, 1993.

[2.18] Bunker, K.L., *Development and application of electron beam induced current and cathodoluminescence analytical techniques for characterization of gallium nitride-based devices*. PhD Dissertation, 2004, North Carolina State University, 243 p.

## **3 Growth**

### **3.1 Introduction**

A major focus of this project has been the reproducible creation of APA SAN samples suitable for various analytical characterization techniques with emphasis on creation of isolated individual SANs for highly localized nanoanalysis. This chapter catalogues all of the various growth techniques used for creation of the APA SAN samples, which were then utilized for this dissertation's analyses. The novel growth techniques are subdivided into three main categories: supported SANs (on a substrate), unsupported or free standing SANs (no substrate), and lastly, a biased growth technique applicable to deposition of APA SANs onto a variety of supported and/or unsupported substrates of various compositions and geometries. Finally, some possible growth mechanisms are discussed and related to reports in the literature concerning similar materials.

## **3.2. Supported SAN growth**

All SAN growth presented was performed by immersion of an appropriate substrate into an 8.3 mM solution of APA in Ethanol (EtOH) with either a source of metallic aluminum or gallium present, excepting the case of increased solution concentration, Section 3.2.1.2. Growth of SANs was initially believed to be confined to aluminum films deposited on glass. As the investigation continued it was found that APA SAN growth occurred on surfaces away from the initially deposited aluminum. This led to the eventual creation of patterned aluminum on chemically inert  $\text{Si}_3\text{N}_4$  substrates for the creation of SANs isolated away from the initial source of aluminum.

### **3.2.1. SAN Growth on Evaporated Aluminum Coated Glass Slides**

Initially, it was of interest to reproduce Richard's results by repeating his experimental procedure. Aluminum coated glass slides were immersed in a solution of methylphosphonic acid (C1) and EtOH. Fresh aluminum on glass substrates were created through the evaporation of 200 nm of 99.99% pure aluminum onto 1 x 3 inch glass optical microscope slides obtained from Fisher Scientific. The slides were pre-cleaned using a sulfuric acid/hydrogen peroxide mixture for ~10 minutes followed by a 5 minute DI  $\text{H}_2\text{O}$  rinse to remove all organics and improve adhesion of the aluminum to the glass. The aluminum was deposited by evaporation from a tungsten boat at  $\sim 2 \times 10^{-6}$  torr. The aluminum films were then imaged with AFM prior to immersion in solution. The aluminum films exhibited grain size distribution ranging from 20–200 nm and an average RMS roughness of 5-10 nm, Figure 3.1. The C1 utilized was obtained from Aldrich chemical company and used in as-received condition. The appropriate amount of C1 was dissolved in 95% EtOH to create 30 mL of

0.1wt% (8.3 mM) solution. The aluminum coated slides were broken into pieces measuring  $\sim 1 \text{ cm}^2$  and then immersed at room temperature into a 30 mL glass jar filled with the C1 solution in random orientations with the aluminum sides facing up. The jar was then tightly capped with its lid. After an appropriate length of time, each of the substrates was removed. A second set of 12 glass substrates, used as a control, were immersed in the same C1 solution. All samples were rinsed gently with pure EtOH, and dried with UHP Nitrogen immediately prior to analysis with AFM. This process is diagramed in Figure 3.2.

The samples were removed after 1, 2, 8, 28, 35, 84, 177, and 365 days and imaged with AFM. Figure 3.3 shows the progression of the aluminum surfaces after immersion in C1 solution for increasing lengths of time. SAN growth initiated within 24 hrs as denoted by the arrows in the 1-day image. A marked increase in SAN growth occurred between 8 and 28 days. It was difficult to determine the exact changes in their geometry due to possible tip convolution effects. The increase in growth is seen in the comparison of the 177 day image and the previous 28, 35, and 84 day images. The number of layers of SANs as well as precipitates continued to increase over time as the roughness of the surface continued to increase from the initial  $\sim 20 \text{ nm RMS}$  in as deposited aluminum to  $> 100 \text{ nm RMS}$  observed in the 177 day immersion sample.

To determine if SANs were present in the growth solution, droplets of the post-growth immersion solution were placed on a clean Si substrates and allowed to dry through evaporation. This formed a visible residue on the surface. The resulting residue was examined with AFM in various regions around. No fibers were observed, and it was thought that residual non-reacted C1 could be coating the surface obscuring the fibers. Therefore, the sample was rinsed in 95% EtOH and once again allowed to dry. This time the coating on the

surface was less noticeable. AFM was performed at a variety of areas similar to those previously examined and still no fibers were observed.

Typically, SANs on the aluminum surface exhibited fairly high densities,  $\sim 10\text{-}20$  fibers/ $\mu\text{m}^2$ , along with large,  $>250\text{nm}$ , porous precipitates after 4 weeks immersion time. Figure 3.4 shows the details of the SANs after 28 days of immersion. There are indications of possible branching and overlapping of the SANs. Sub-structural details along the lengths of the fibers are readily observed in the phase image of Figure 3.4. It is important to note that the material sensitivity of the AFM phase image reveals a distinct difference between the SANs (light colored) and the precipitates (darker colored).

Figure 3.5 is a zoomed-in region of the AFM image in Figure 3.4 showing some of the sub-structural and branching features that occurred in the SANs grown directly on the aluminum surface. It was difficult to tell whether the observed nodular structures were real or simply artifacts created by interactions with structures that have similar dimensions to that of a typical AFM tip end radius (10-50 nm reference). To verify the presence of these sub-structural features as observed with AFM, Field Emission Scanning Electron Microscopy (FE-SEM) was performed on the same 84-day sample using two different microscopes as seen in Figure 3.6. There was a strong correlation between the size and geometry of the SANs observed in the AFM and SEM. Similar nodular surface structures were observed with both techniques. Additionally, the FE-SEM provided an improved method for imaging larger areas on the sample's surface allowing for better coverage assessment over the entirety of the sample, which in this case showed quite uniform distribution of SANs and precipitates across the surface.

SAN growth directly on aluminum surfaces was found to be highly uniform and created what appeared to be a non-woven, fabric type structure. The individual SANs were typically 10-100 nm wide and in some cases as long as 15  $\mu\text{m}$ . Full coverage of the aluminum surface appeared to occur after  $\sim$  4 weeks of immersion. Porous precipitates grew in number and in size over time along with the SANs. It was difficult to distinguish the origin of these precipitates, although they appeared to be intertwined within or formed out of dense regions of SAN growth in both the AFM and SEM images.

#### **3.2.1.1. Increased Immersion Solution Temperature**

In an effort to increase the APA SAN growth rate, aluminum coated glass substrates in the same 8.3 mM C1/EtOH solution as in the previous experiment, but at elevated temperature. The temperature during growth was increased from 27C to 40C by placing the entire jar containing the solution and substrates into a controlled temperature oven. After only 9 days of growth at 40C, the amount of SAN growth on the surface was similar to that seen after 28 days at room temperature as seen in Figure 3.7. There was also a decrease in the amount of large precipitates when grown at an increased temperature. These observations suggested that the SAN morphology was more stable than the precipitates. This was in good agreement with the lower melting temperature of the precipitates as discussed in Chapter 5.

#### **3.2.1.2. Increased Immersion Solution Concentration**

To examine the effect of C1 concentration on SAN formation, the solution concentration of C1 in EtOH was increased 10X to 1.0 wt% (83 mM). Ten 1  $\text{cm}^2$  aluminum coated glass substrates were immersed in 30 mL of 83 mM C1/EtOH solution. The samples were

removed after 1, 2, 3, 12, and 19 days. By day 12, a white haze covered the entire surface and was denser around the edges of the substrate than in the center. By day 19, none of the original metallic aluminum was apparent. A translucent, whitish film was present on the glass' transparent surface where the aluminum had previously been. Crystalline structures were visible with the naked eye and thus the sample was deemed inappropriate for AFM. Instead, SEM was used to image the resulting film.

Figure 3.8 shows SEM images of the surface revealed that a microfabric had replaced the initially metallic aluminum on the glass surface. It appeared that the aluminum was converted from the edges inward. Control samples without C1 present showed no signs of luster change over the same time period. AFM of the control samples showed that the initial aluminum grain structure stayed intact. The microfabric cracked and peeled away from the glass surface after repeated evacuation in the SEM. Eventually the fabric rolled up on itself showing surprising flexibility. This type of flexibility was also observed in the unsupported SAN membranes described in Section 6.2.1.

The rate of fiber growth, average fiber size, and corrosion of aluminum all increased with increased C1 concentration. The fibers ranged in size from to tens of nm wide and hundreds of  $\mu\text{m}$  long to tens of  $\mu\text{m}$  wide and one mm long, some large enough to be visible with the naked eye. To gain a better understanding of the composition of the fibers, SEM with EDS was performed on an area of the sample with the large acicular crystal. Qualitative EDS identified the presence of both aluminum and phosphorus along with carbon, oxygen, and silicon. EDS mapping was performed of a smaller area having distinctive fibers above the substrate. Figure 3.9 includes the resulting EDS maps of aluminum, carbon, oxygen that aluminum and phosphorous were primarily present in the fiber structures relative to the

underlying glass. This was the first distinctive evidence that aluminum was being incorporated into the larger SAN fiber structures, as the aluminum signal came from the fibers and not the substrate where the aluminum was initially deposited. aluminum was also found in trace amounts in the underlying glass. It appeared that the original aluminum was converted from its metallic form and incorporated into self-organized fibrous forms, creating non-woven structured mats on glass substrates over time.

Unlike the SANs created with 8.3 mM C1 solutions, the fibers grown at 10X concentration are observed to be highly hydroscopic, similar to pure C1. Eventually, the entire microfabric formed into droplets on the glass surface after further exposure to ambient conditions over a few days. Initial reactions with water are thought to be seen as the smooth and bulbous regions overlaying the geometric fibrous structuring as seen in lower images of Figure 3.9.

### **3.2.1.3. Immersion in Phosphonic Acid (C0) Based Solution**

To examine the importance of the methyl group to SAN formation, solutions prepared with phosphonic acid (C0) were utilized instead of C1. C0 has identical chemistry as C1 with the exception of Hydrogen replacing the methyl group. It was hypothesized that without an alkyl group present, there should be no amphiphilic character to the C0 molecules. This should remove an ability to self-organize in the linear fashion observed for C1. Using the same procedure as described previously, aluminum coated substrates were immersed in 30 mL of 8.3 mM C0/EtOH solution and subsequently removed one at a time over a number of days.

Figure 3.10 shows a comparison of a C1 and a C0 treated aluminum samples after 35 and 46 days respectively. SANs were never observed on the aluminum substrates even after 7 weeks immersion in the C0 solution. Instead, small round structures were observed to form. These results suggest that utilizing phosphonic acids with an alkyl chain is important for the creation of the SAN's linear structure.

#### **3.2.1.4. Immersion in Aqueous Solution**

The majority of immersion experiments in this work utilized EtOH as the solvent for SAN growth in order to maintain continuity between this work and the work previously performed by Richards and Neves[3.1-9]. EtOH was initially utilized because of Octadecylphosphonic acid's (C18) low solubility in H<sub>2</sub>O[3.9]. The shorter chainlength APAs, as utilized for SAN growth, exhibited increased solubility in H<sub>2</sub>O. This made the formation of isotropic solutions possible. To examine the effect of using more polar solvent than EtOH, pure H<sub>2</sub>O was used instead. Ten substrates of 200 nm thick aluminum film evaporated on glass were immersed in 8.3 mM C-1/18 M-Ohm H<sub>2</sub>O. The samples were then removed after a set amount of time, rinsed in 18 M-Ohm H<sub>2</sub>O and imaged with AFM.

Figure 3.11 shows the evolution of the 200 nm thick aluminum surface after immersion in C1/H<sub>2</sub>O solution for 1 and 11 days respectively. After 1 day, many round nodules formed covering the entire surface, obscuring the original aluminum grain structure. It appeared that the surface was being etched or decorated, and the amount of etching was dependant on the grain orientation. By day 11 there was no longer any notion of grain structure, only nodular surface structures. After 20 days of immersion time, the substrates no longer visibly had any metallic aluminum left as they were completely translucent. These results were very similar

to the results of increased C1 concentration except that there was no visible fiber formation both visually or by AFM. Fibrous structures were never observed to grow even after 4 weeks of immersion at which point the last sample was removed and imaged.

### **3.2.1.5. SAN Growth on the Backside Glass**

In an attempt to determine whether SAN growth was isolated only to the immersed aluminum surfaces, AFM scans were performed on the backside glass surfaces of several samples from the experiments previously described. Figure 3.12 shows two AFM height images comparing the front aluminum coated side and the uncoated backside glass after immersion in an 8.3 mM C1/EtOH solution for 177 days. Interestingly, SAN growth was not confined to the aluminum coated surfaces but also occurred in much lower density on the non-coated surface as well. The observed SAN growth on the glass surfaces was generally much lower than the corresponding aluminum surfaces.

This was the first opportunity to perform elemental analysis on SANs without the remaining aluminum underneath. SEM with EDS was performed on the SANs as grown on the glass as shown in Figure 3.12. EDS detected the very small amounts of aluminum present which seemed to indicate the possibility of aluminum transport through the solution. To make sure that the aluminum signal was not coming from the glass, EDS was also performed on a clean glass slide. EDS revealed that there was also a small amount of aluminum present in the glass making it impossible to correlate the previously detected aluminum of the SANs on glass to the SAN structure.

In an effort to determine whether the SANs were forming directly on the immersed surfaces or being deposited on the surface when removed from solution, two samples were

made using the 177 day immersion solution. The first sample was created by placing a droplet of solution with a glass pipette onto the surface of a clean polished silicon substrate, allowing the droplet time to air dry. The droplet was composed of solution sampled from the bottom of the immersion jar near the remaining aluminum coated substrates. The second sample was created by dipping a second piece of silicon into the used solution for a few seconds and then removing it. It was then allowed to air dry. AFM was performed on several areas of each sample. No SANs were observed on either sample. Both samples were then rinsed with several drops of pure EtOH and dried with UHP N<sub>2</sub> and imaged again with AFM. Again no SANs were observed. The absence of SANs in solution depositions on silicon substrates seemed to indicate that SAN formation was occurring through a surface-initiated nucleation and growth mechanism. Future depositions of growth solutions were droplet coated onto Si<sub>3</sub>N<sub>4</sub> coated substrates as well. No SANs were ever observed through these kinds of immersion or droplet techniques further indicating that SAN growth is a surface initiated phenomenon.

### **3.2.2. SAN Growth on Si<sub>3</sub>N<sub>4</sub> and Solution Transport of Aluminum**

To definitively determine if aluminum was being transported through the solution and associated with the C1 SANs, C1 SANs were grown on Si<sub>3</sub>N<sub>4</sub> coated silicon TEM grids obtained from SPI supplies. The as-received grids were placed on top of an aluminum coated glass slide and immersed in 30 mL of 8.3 mM C-1/EtOH solution for 60 days, removed, rinsed with 95% EtOH and dried with UHP Nitrogen. EDS analysis using a Hitachi S3200-N variable pressure SEM fitted with an Oxford Instruments EDS was performed using 5 keV accelerating voltage on the Si<sub>3</sub>N<sub>4</sub> grids before and after immersion for 60 days as seen in

Figure 3.13. The EDS analysis was performed at 5 keV to increase surface sensitivity and for 100 sec live time to ensure significant signal to noise. No evidence of aluminum or phosphorus was observed on the as-received grids before immersion in the C1 solution. AFM of the as-received grids gave RMS roughness values of less than 1 nm and no sign of SAN structures before immersion.

EDS of the  $\text{Si}_3\text{N}_4$  grid's surface after a 60-day immersion clearly shows the presence of aluminum and phosphorus. AFM images of the same areas of the substrate correlated the SANs with the detected aluminum and phosphorus. This was the first evidence of aluminum correlated with the SANs structure.

### **3.2.3. Growth of Ga Based APA SANs**

All experiments suggested that in order to create C1 SANs a source of aluminum must be present in the growth solution. This was accomplished by immersing aluminum coated glass slides. To further understand the role of the aluminum in the formation of the SANs, it was of interest to try a different metal such as gallium. Gallium was chosen because it is in the same group as aluminum making it more similar in its valence electronic structure than other comparable metals. For this experiment, a 50 nm, electron transparent,  $\text{Si}_3\text{N}_4$  TEM thin film window obtained from SPI supplies, Figure 3.14, was utilized as the nanofiber growth surface. It was placed into an 8.3 mM C-1/EtOH solution along with 0.7 g of highly pure, granular gallium metal,  $\sim 500 \mu\text{m} - 1 \text{ mm}$  in diameter. A control was also created by immersion of another  $\text{Si}_3\text{N}_4$  substrate in the same amount of the same solution without gallium.

After 60 days, the  $\text{Si}_3\text{N}_4$  substrates were removed and rinsed with 95% EtOH and imaged with AFM and STEM w/EDS. AFM imaging of the substrate subjected to gallium in the solution, Figure 3.15 (a), revealed the presence of SANs. The SAN coverage was lower than experiments of similar immersion time using aluminum. Examination of several areas of the control sample with AFM showed no SAN formation.

The gallium C1 SAN sample was then examined using a Hitachi HD-2000 STEM with Noran Vantage EDS. Figures 3.15 (b-c) are STEM Z-Contrast images showing the gallium SAN network formed on the  $\text{Si}_3\text{N}_4$  substrate. Higher magnification images, Figure 3.16, provided important sub-fiber details as well as EDS compositional information, which did correlate the presence of gallium in SAN structures on a surface that previously had no gallium.

#### **3.2.4. Patterning Aluminum on $\text{Si}_3\text{N}_4$ Growth Surfaces**

C1 SANs were observed to grow well on previously clean  $\text{Si}_3\text{N}_4$  substrates when placed on top of aluminum coated glass immersed in C1 solution, section 3.2.2, but it took upwards of 6 days to form an entire mat. A patterned aluminum substrate was developed in an effort to increase the growth rate while also creating SANs isolated from the initial aluminum allowing for direct compositional analysis. The aluminum was patterned onto the substrates by masking the majority of the sample surface with a shadow mask, creating aluminum free areas for growth and analysis of the SANs.

In the first experiment, a SPI Supplies  $\text{Si}_3\text{N}_4$  TEM membrane (200 nm thick, SPI Part # 4120SN-BA), see Figure 3.14, was masked using a holder clip, and then ~200 nm aluminum was evaporated onto its surface. In addition to serving as an electron transparent window for

direct STEM analysis, supported areas on the sample also provided a surface that was mechanically very stiff as well as chemically inert in relation to the C1 solutions. The patterned substrate was then immersed into a 8.3 mM C1/EtOH solution for 11 days. After removal, the sample was rinsed with pure EtOH and dried with UHP N<sub>2</sub>. Figure 3.17 (a) shows an optical micrograph of the substrate after immersion. The changes in the aluminum film after immersion are clearly noticeable as a significant mottling of the metallic aluminum. There was a small area where the Si<sub>3</sub>N<sub>4</sub> film had delaminated from the underlying silicon support within the masked region before immersion, Figure 3.17 (b). AFM imaging of the Si<sub>3</sub>N<sub>4</sub>/Si interface revealed differences in the nanofiber growth on the two different surfaces. The SAN density was observed to decrease with increasing distance away from the Si<sub>3</sub>N<sub>4</sub> on the underlying Si, Figure 3.17 (c).

#### **3.2.4.1. STEM Analysis of SAN Growth on Patterned Si<sub>3</sub>N<sub>4</sub> TEM Grids**

Electron transparent Si<sub>3</sub>N<sub>4</sub> substrates obtained from SPI Supplies (200 nm thick, SPI Part #4120SN-BA) were partially coated with aluminum by simple shadow masking during evaporation of aluminum, Figure 3.18. Pieces of clean Si were utilized as masks. The patterned substrates were then immersed in 8.3 mM C1/EtOH solution for 8 and 30 days, after which they were removed, rinsed with 5 mL of pure EtOH, and blown dry with UHP N<sub>2</sub>. The substrates were immediately examined in a Hitachi HD-2000 STEM with a Noran Vantage EDS.

Figure 3.19 shows a comparison of the BF and ZC STEM images of the same area of SANs grown directly on the Si<sub>3</sub>N<sub>4</sub> window with no underlying Aluminum after 30 days of immersion. The immersion resulted in a SAN structure resembling a multilayered

nanofibrous mat. It was very difficult to delineate one SAN from another or to determine any internal SAN structuring, as the images contained information from many layers of fibers. Figure 3.20 is a comparison between samples after immersion for 8 and 30 days. These images show that shorter immersion times produce fewer more isolated individual SANs. It was difficult to examine the internal structures of the SANs due to obstruction from the underlying  $\text{Si}_3\text{N}_4$ .

### **3.2.5. Isolating Nanofiber Growth**

SANs were observed to form on aluminum surfaces after immersion in APA/EtOH solutions up to C12 by Richards[3.9]. The previous sections in this chapter have additionally shown that SAN growth was not isolated to metal surfaces, but could grow on a variety of surfaces immersed in the solution. C1 SANs were observed to prefer  $\text{Si}_3\text{N}_4$  surfaces to silicon or glass. Aluminum and gallium were directly correlated with the resulting SAN structures using a combination of AFM, SEM w/ EDS and STEM w/EDS. In an effort to create isolated SANs suitable for nanoanalysis, a combination of the previously described growth techniques was employed. Aluminum was patterned onto  $\text{Si}_3\text{N}_4$  coated silicon wafers which were broken into smaller pieces for use as immersion growth substrates. Once a reliable growth technique was created utilizing C1, other APAs with chain lengths of 3 (C3) and 5 (C5) were utilized to examine their effect on SAN growth and structure. The resulting isolated C1, C3, and C5 SANs on  $\text{Si}_3\text{N}_4$  coated Si substrates were then utilized for mechanical, electronic, thermal, and compositional analyses.

### 3.2.5.1. Time Resolved Growth of APA SANs

Semiconductor grade  $\text{Si}_3\text{N}_4$  on silicon was chosen as the growth surface for creating supported SANs for two main reasons: the previously observed high growth rates of C1 SANs on  $\text{Si}_3\text{N}_4$  and to provide consistency between the substrates utilized for supported and unsupported growth. The chemical, mechanical and electrical properties of  $\text{Si}_3\text{N}_4$  were also significant in the selection of this growth surface. ~200 nm of aluminum was patterned onto 240 nm of  $\text{Si}_3\text{N}_4$  coated silicon wafer. The patterned wafer was then cleaved into pieces, creating ~1  $\text{cm}^2$  substrates with ~.25  $\text{cm}^2$  of aluminum coverage. The evaporation of aluminum was performed utilizing a conventional tungsten filament evaporator with a liquid nitrogen cold trap, having a base pressure of  $5 \times 10^{-7}$  torr. The patterning was accomplished by simple shadow masking with a piece of silicon. 30 mL of 8.3 mM of C1, C3, and C5 in EtOH solutions were prepared in clean glass jars. Three of the 1  $\text{cm}^2$  aluminum patterned substrates were immersed in each of the 3 solutions. A substrate from each of the solutions was removed after 1 week, 2 weeks, and 3 weeks of immersion time, rinsed with pure EtOH and imaged with AFM. AFM images were obtained from several areas on each sample including the aluminum, the interface area between the aluminum and  $\text{Si}_3\text{N}_4$ , as well as some distance away from the aluminum. The results of the AFM imaging done on areas far from the initial aluminum can be seen in Figure 3.21.

Immersion of aluminum patterned substrates in solutions of C1, C3, and C5 all produced SANs over time on the  $\text{Si}_3\text{N}_4$  substrates. The supported C5 SANs exhibited the fastest growth rates as the entire  $\text{Si}_3\text{N}_4$  surface was covered after only 1 week of immersion time. The 3 week immersion samples from each chainlength were then subjected to further thermal, mechanical, and electrical analysis, presented elsewhere in Chapters 5, 6, and 7.

### 3.3. Unsupported APA SANs

Previous results of APA SAN growth on  $\text{Si}_3\text{N}_4$  thin film TEM windows allowed for direct inspection of fibers with STEM and EDS, but sub-fiber details appeared to be obstructed by interference with the underlying amorphous  $\text{Si}_3\text{N}_4$  support film. As determination of the molecular structure of individual SANs was of interest, it was proposed to grow unsupported SANs for analysis in STEM. Having SANs with no substrate would allow for direct inspection with STEM without the problems of substrate convolution or likely alterations due to sample preparation of a cross-section.

#### 3.3.1. ProtoChips<sup>TM</sup> $\text{Si}_3\text{N}_4$ TEM Meshes

Commercially available ProtoChips<sup>TM</sup> DuraSiN<sup>TM</sup> TEM meshes (<http://www.protochips.com>) were utilized as the substrates for nanofiber formation. Each DuraSiN<sup>TM</sup> mesh consisted of a 200 nm thick amorphous low stress  $\text{Si}_3\text{N}_4$  film supported by a 200  $\mu\text{m}$  thick Si frame etched from the backside all the way to the  $\text{Si}_3\text{N}_4$  side creating a thin film window as seen in Figure 3.22. The  $\text{Si}_3\text{N}_4$  thin film window was then further reactive-ion etched to create an array of 4  $\mu\text{m}$  holes with 10  $\mu\text{m}$  pitch. There are hundreds of holes on each substrate. Use of the DuraSiN<sup>TM</sup> meshes provided consistency with the previously developed supported growth substrates while additionally allowing for direct structural and compositional nanoanalysis without the influence of the substrate structure and composition.

#### 3.3.2. Creation of Novel SAN Membranes

99.99% aluminum was deposited onto one edge of a masked DuraSiN<sup>TM</sup> TEM mesh by evaporation. The aluminum roughly covered a 3 mm x 1mm area along the edge of the

substrate. A single substrate was then placed into 5 mL of 8.3 mM C1 solution for 20 days in a tightly capped glass jar. After removal from solution the sample was rinsed with ~ 1 mL of pure EtOH and examined with a HD-2000 STEM.

Only one hole in the entire membrane was found to have an unsupported SAN structure across it. Figure 3.23 shows two Z-contrast images of the observed unsupported SAN structure. They were considerably larger than those previously observed, but the presence of one SAN was proof of concept that unsupported SANs could be grown across 4  $\mu\text{m}$  openings. The lack of fiber growth on the entire sample was attributed to an insufficient supply of aluminum near the growth areas due to the initial patterning. It was then decided to blanket coat the entire surface of the DuraSiN<sup>TM</sup> TEM meshes with aluminum to increase the amount of aluminum present near the holes.

The two ProtoChips<sup>TM</sup> DuraSiN<sup>TM</sup> meshes were blanket coated with a ~200 nm thick evaporated aluminum film and placed in 5 mL of 8.3 mM C-1/EtOH solution in a glass jar and capped tightly. The first sample was removed after 6 weeks, rinsed with pure EtOH and blown dry with UHP N<sub>2</sub>. AFM of the aluminum coated thin film after immersion showed that a SAN fabric covered the entire surface including the holes. Figure 3.24 is an AFM image of a typical SAN membrane after 6 weeks of immersion. The membranes appeared to be recessed from the surface by nearly 500 nm. This SAN membrane survived multiple scans with the AFM in tapping mode. There appeared to be some residue on the membrane, which is more easily seen in the phase image. This residue could have possibly been some non-reacted C1, left behind due to insufficient rinsing after removal from solution.

Figure 3.25 (a) is a STEM SE image of a typical single C1 SAN membrane. As the membrane was examined with higher magnifications, Figure 3.25 (b) shows that the SANs

were composed of smaller fibrils, or layers of ribbons, with some sort of webbing present between the individual fibril bundles. Figure 3.25 (c) shows complex surface texturing was present as well. STEM ZC and TE images provided internal structural information, which is described more fully in Section 4.3.1.

### **3.3.3. Time Resolved Growth of APA SAN Membranes**

With the success of unsupported C1 SAN growth on aluminum coated DuraSiN™ TEM meshes, a series of nine samples were created using evaporated aluminum coated ProtoChips™ DuraSiN™. Three groups of three substrates were immersed in 8.3 mM solutions of C1, C3, and C5 in EtOH. Each substrate was immersed individually; aluminum coated side up, in 1 mL of solution in a small 10 mL glass vile with a tight fitting cap. A substrate from each chain length was removed after 1, 2, and 3 weeks, in a similar fashion to the samples created in section 3.2.5.1. Each of the samples was rinsed with pure EtOH and dried with UHP N<sub>2</sub> and imaged in the STEM.

Results of the immersion growth time study are seen in Figure 3.26 for C1, C3, and C5 SANs. Intact membranes of C1 and C5 SANs were formed even after immersion for 1 week. C1 SAN membranes were observed to be more resilient to STEM imaging than their C3 and C5 counterparts correlating with the nanoindentation results of individual supported C1, C3 and C5 SANs, presented in Chapter 6. In general, the growth of unsupported SANs allowed for direct structural and compositional nanoanalysis. The results are detailed later in Chapter 4.

### **3.4. Development of a Novel Biased Growth Technique**

There was strong evidence that nanofiber formation was due to self-organization of an aluminum corrosion product or complex. Since aluminum played an important role in SAN formation, it was thought that by increasing the amount of aluminum in the solution there should then be an increase in the observed SAN growth rates. One method for increasing the available aluminum in solution could have been through the utilization of aluminum salts. However, this would have made the system too complex. Therefore, it was determined that other methods of accelerating the corrosion of the previously utilized aluminum films in APA solutions would provide results more consistent with the rest of the work.

Since the corrosion of a metal typically involves electron transfer through a conductive medium, a simple electrochemical setup was envisioned, utilizing two aluminum coated slides as electrodes and C1 in EtOH solution as the conductive medium. A constant bias could then be applied between the two electrodes while immersed in the solution. Since the two electrodes were chemically identical, the application of a small bias, either or positive or negative, would drive the corrosion reaction forward on one of the electrodes, evolving more aluminum from the anode into the solution with an increase in SAN formation expected. While many different aspects and details of chemical reactions can be studied using electrochemistry, a full electrochemical study of the reactions occurring at the anode and the cathode was outside the scope of this work. The purpose of these simple electrochemical experiments was two fold: first, to attempt to increase APA SAN growth rates, and second, to show proof of concept for the novel biased deposition of SANs onto a variety of substrates.

For all biasing experiments, a Princeton Electronics Model 273A Potentiostat/Galvanostat was operated as a constant voltage source. Typically an electrochemical cell has three electrodes, referencing, working, and counter electrodes. However, for simple biasing at low voltages, it was found that the counter electrode can be connected to the reference electrode terminal to create a constant voltage source with varying current. The potential that is fed into the control input, or set by the internal voltage source, directly controls the voltage of the counter electrode.

A two electrode reaction cell was fabricated from a glass jar, the same type as utilized for all previous immersion experiments, using some screws and copper alligator clips, see Figure 3.27. Holes were drilled into the top of the jar and the clips were affixed with stainless steel screws and nuts and a seal made by the Teflon lid lining.

### **3.4.1. Proof of Concept**

For the initial experimental proof of concept, electrodes composed of the same 200 nm evaporated aluminum on glass were utilized. One glass slide was cut into pieces, ~4 cm x 1 cm, and clamped with the alligator clips into parallel positions with the aluminum sides facing each other at a distance of approximately 1 cm. Enough 8.3 mM C-1 in EtOH solution was put into the jar so that ~1 cm<sup>2</sup> of the aluminum coated electrodes were immersed in the solution when the top fitted with electrodes was put on tightly. The solution slightly wicked up the electrodes. A bias of 3.5 V was applied between the electrodes for 24 hrs. This initially produced a current of ~1.4  $\mu$ A. After 24 hrs the bias was turned off and the electrodes removed from the solution, rinsed in 95% EtOH, and imaged with AFM. The current at the time of removal was lower, ~0.5  $\mu$ A.

The results of the first biasing experiment showed highly accelerated SAN growth on the cathode due to biasing the aluminum electrodes at 3.5 V. The aluminum on the cathode remained more intact due to the addition of a complete nanofiber mat on the remaining aluminum surface, Figure 3.28. The aluminum along the edge of the immersed cathode was removed slightly, while the anode exhibited large areas of aluminum removal with SANs found on the remaining metal as well as the glass substrate between the remaining Aluminum. It was of interest that the removal of aluminum was confined not only to the anode but also along the edges of the cathode. The exact corrosion mechanisms are still unclear but warrant further investigation. Most importantly, this experiment showed that APA SAN growth rate could be greatly increased through application of a small 3.5V bias between aluminum electrodes in a 8.3 mM solution of C1 in EtOH.

### **3.4.2. Utilizing a Highly Doped Silicon Cathode**

Another variation of the biasing experiment was carried out using a 4 cm x 1cm piece of highly doped silicon (0.01 Ohm-cm) as a cathode instead of aluminum coated glass. Here the objective was the quick growth of isolated nanofibers, within 24 hrs or less, on a mechanically stiff and flat surface with defined chemistry for possible mechanical and electrical testing of individual nanofibers. Highly doped or degeneratively doped silicon was deemed a good candidate as the high levels of doping cause the silicon to act more like a metal than a semi-conductor. This would then provide a conductive electrode with a surface having sub-nm roughness, allowing for ease of AFM analyses and possible conductivity measurements.

The silicon cathode was removed after 5 hours of immersion and biased at 3.5 V relative to an aluminum coated glass electrode, rinsed with pure EtOH and imaged with AFM. Figure 3.29 shows a typical area of the immersed cathode along which very fine SANs formed along with small precipitates. The small round structures were present on the silicon before growth and presumed to be small oxide growths. After examination with AFM the immersed cathode was re-immersed in solution under 3.5V bias for 15 more hours to for 20 hours total growth time. Little to no changes in the SAN morphology was observed with AFM. This experiment showed that it was possible to form clearly isolated APA SANs on non-aluminum, specifically conductive silicon cathodes after 5 hours of immersion with a 3.5V bias.

### **3.4.3. Deposition on Si<sub>3</sub>N<sub>4</sub> for STEM EDS Analysis**

In an effort to try and combine the increased SAN growth rates of the biasing technique with the high growth affinity of clean Si<sub>3</sub>N<sub>4</sub> substrates a compound biasing technique was devised to examine the feasibility of growing C1 SANs on substrates other than the electrodes. This was seen as an adaptation of the previous results showing that isolated C1 SANs were created on clean Si<sub>3</sub>N<sub>4</sub> TEM membranes placed on top of aluminum coated glass slides while immersed in solution.

Two as-received Protochips<sup>TM</sup> DuraSIN<sup>TM</sup> 3mm TEM meshes (<http://www.protochips.com>) each consisting of a 100 nm Si<sub>3</sub>N<sub>4</sub> thin film, having 2 μm holes at a 10 μm pitch on a supportive Si frame were placed with the Si<sub>3</sub>N<sub>4</sub> side facing up at the bottom of a jar and immersed into 5 mL of 8.3 mM C1 in EtOH solution. Two aluminum coated glass electrodes were placed in a vertical manner faces roughly parallel ~1 cm apart

exposing  $\sim 0.5 \text{ cm}^2$  of each electrodes' aluminum to the immersion solution. Immersion with biasing at 3V was performed for 5 days at which point the bias was removed. The  $\text{Si}_3\text{N}_4$  substrates then remained immersed without biasing for another 5 days for a total of 10 days of immersion.

The immersed aluminum on the anode was completely gone after 1 day of biasing accompanying a drop in the observed current from  $\sim 1 \mu\text{A}$  to  $0.33 \mu\text{A}$ . One of the substrates was removed from solution, rinsed with pure EtOH and blown dry with UHP  $\text{N}_2$ . The sample was then analyzed with a Hitachi HD-2000 STEM equipped with a Noran Vantage X-Ray system. C1 SANs were observed to homogeneously cover the  $\text{Si}_3\text{N}_4$ , but none were found suspended over the holes. Figure 3.31 is a STEM ZC image of the resulting C1 SANs on  $\text{Si}_3\text{N}_4$  along with EDS results. The EDS results presented are an overlay three spectra taken with spot mode EDS from a cluster of fibers (red), a spot off of the fibers (green) and a spot analysis of an as received Protochips<sup>TM</sup> DuraSIN<sup>TM</sup> mesh (blue). The EDS spectra overlay clearly shows that the aluminum and Phosphorus are isolated to the SAN structure itself and not the surrounding  $\text{Si}_3\text{N}_4$ .

These SANs were quite different from any SANs previously created and analyzed during the course of this project. They had a more jagged appearance with what seemed to be small crystallites formed along the typical SAN structure. Additionally, a significantly increased Al:P ratio was observed with quantitative elemental analysis of the individual SANs. Instead of the typical Al:P ratio of .33-1, the SANs the biased deposition technique exhibited an aluminum:phosphorus ratio of  $\sim 10$ . This is a dramatically larger amount of aluminum than had been present in all other compositional analyses performed on C1 SANs in this work.

From these results it seems highly likely that the typical immersion growth technique utilized for the creation of APA SANs may have experienced an aluminum limited growth condition. Further investigation of biased deposition was warranted, but considered beyond the scope of this study.

### **3.5. Discussion**

After verifying the repeatability of C1 SAN growth on aluminum coated glass substrates as described in John Richard's NCSU Master's thesis, experimentation related to APA SAN growth was designed to accomplish two main goals. First, it was of interest to further understand the fundamental mechanisms of SAN growth and more specifically the role of aluminum in their formation. Secondly, growth methods were needed for the repeatable growth of isolated APA SAN samples suitable for application of high resolution, analytical techniques such as AFM and STEM, needed to understand changes in the SANs based upon subtle changes made in the system chemistry and environmental conditions.

By initially focusing experimentation on the first goal, understanding the growth mechanisms, the results of those experiments were then applied to the second goal of creating isolated SANs suitable for nanoanalysis, creating an iterative process. After several iterations, novel methods were developed for the successful isolation of APA SANs onto supported  $\text{Si}_3\text{N}_4$  coated silicon substrates as well as aluminum coated ProtoChips<sup>TM</sup> DuraSIN<sup>TM</sup> TEM meshes. These methods provided both supported and unsupported SAN samples on substrates with the same chemistry suitable for the various analytical techniques needed for characterization.

Phosphonic acid with an alkyl chain length of at least one carbon (C1) in a solution utilizing ethanol as a solvent, along with the presence of aluminum or gallium in the immersion solution, were all factors found to be necessary for the creation of APA SANs. No SANs were ever observed when depositing the same immersion solutions onto clean substrates, indicating that SAN growth was initiated on a substrate's surface while immersed instead of transferred from solution to surface upon substrate removal. In addition, APA SAN growth was not isolated to immersed metal surfaces. This allowed for creation of isolated SANs onto surfaces with previously characterized chemistries for direct compositional analysis with SEM EDS correlating the presence of aluminum with C1 SANs.

SAN growth rates were observed to be dependant on the corrosion rate of the immersed aluminum. A model of APA SAN growth is proposed where the APAs attack the surface of the aluminum, evolving either aluminum ions into solution or some sort of aluminum containing complex with the APAs. This complex then has a limited solubility in the solution, preferentially nucleating at sites on lower energy surfaces such as  $\text{Si}_3\text{N}_4$ . The growth of 1-D structures then occurs through the self-organization of APAs in the solution, resulting in either templated growth of aluminum hydroxide or formation of aluminum – APA polymers that bundle together forming an individual SAN. It is impossible to tell which is happening without further experimentation, but in either case SAN, growth appears to be regulated by the aluminum and APA concentrations in the solution.

While further experimentation will be required for further understanding of precise APA SAN growth mechanisms, synthesis of the results in this work led to a simple aluminum regulated APA SAN growth model. From this model, a novel electrochemical deposition method was developed enabling the growth of APA SANs onto a variety of substrates.

Further development of the presented biased deposition techniques as well as more thorough electrochemical experimentation should allow for development of methods having precise control of the concentration of a metal or multiple metals within a growth solution.

### 3.6. Figures

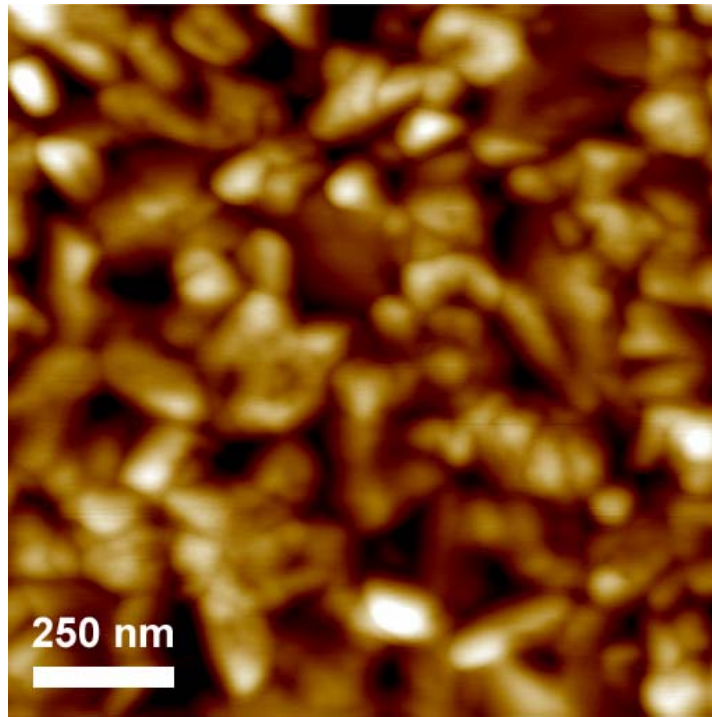


Figure 3.1.  $1\mu\text{m} \times 1\mu\text{m}$  AFM height image of typical evaporation deposited aluminum film on glass prior to immersion. 50 nm Z-range.

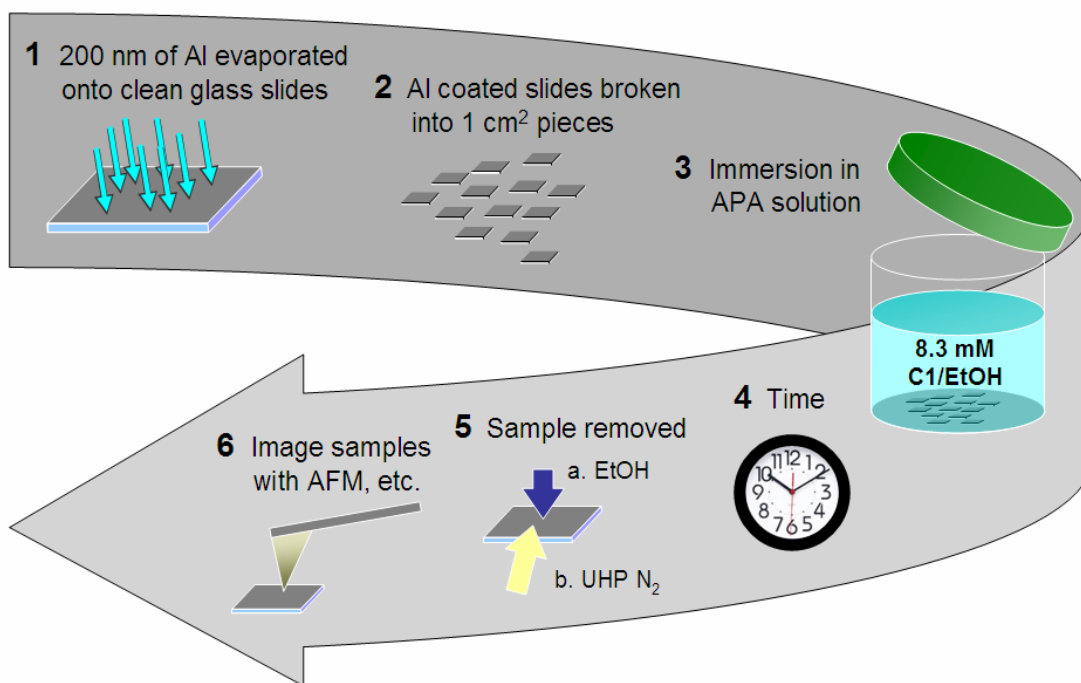


Figure 3.2. General immersion growth technique.

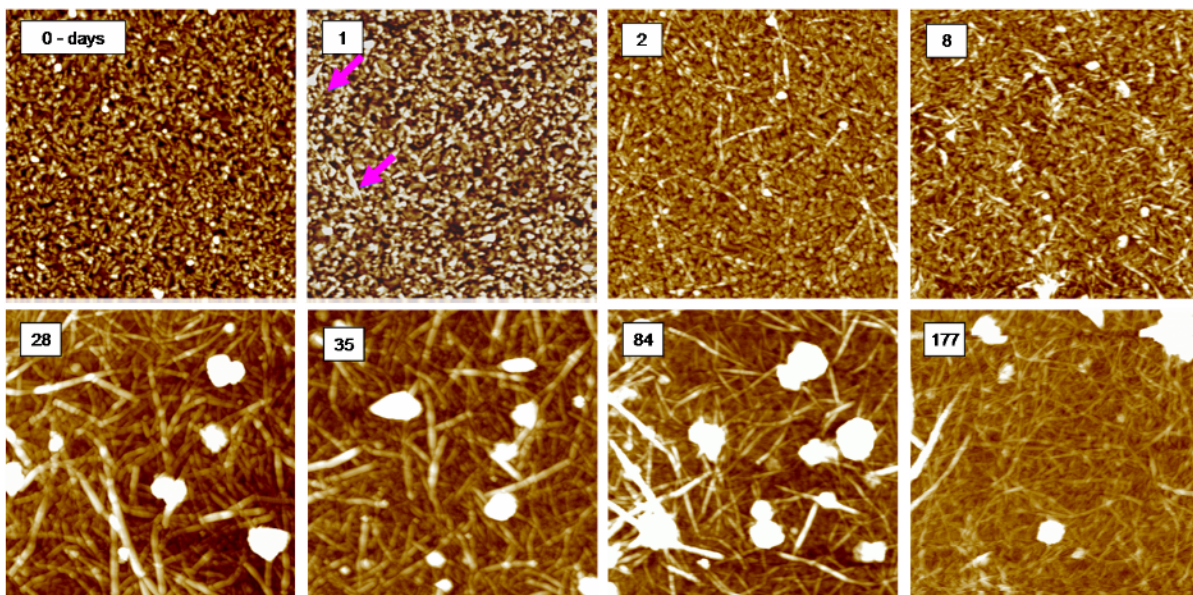


Figure 3.3. AFM tapping mode height images of nanofiber growth on aluminum surface. Evaporated aluminum film was exposed to 0.1wt% (8.3mM) C-1/EtOH solution over a 177 day period. Arrows denote linear fibrous structures observed after only 1 day of growth.

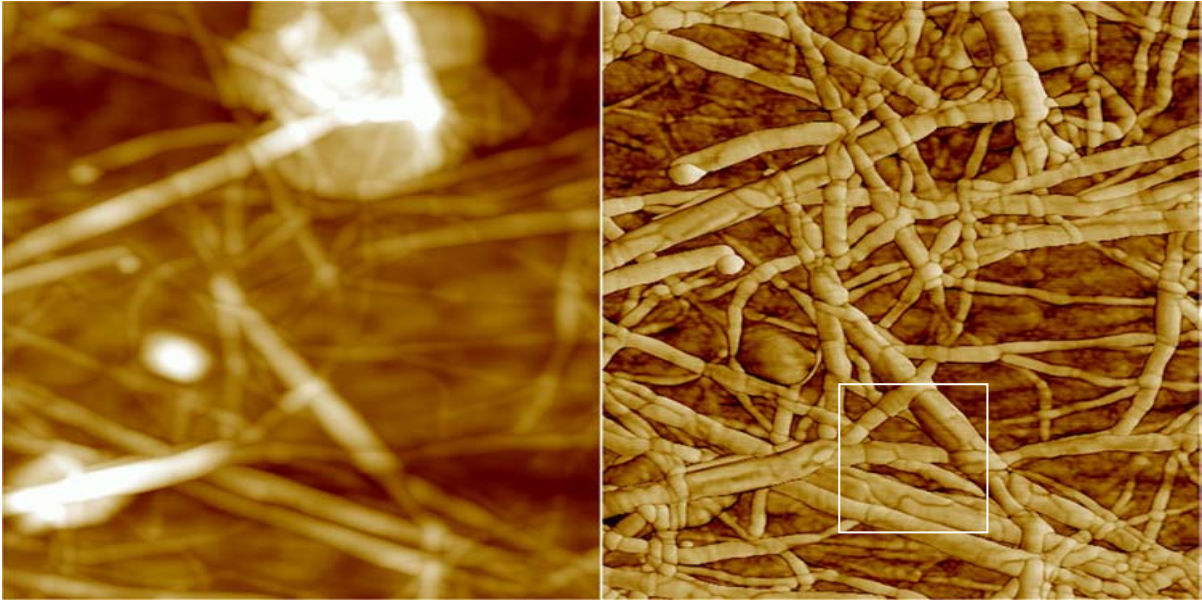


Figure 3.4. A 2  $\mu\text{m}$  TM-AFM image (height left 150nm z-range, phase right) showing the branching and network structure of the fibers in the 28 day growth sample Phase Image shows increased details of sub-fiber structures present along with compositional contrast between the fiber and the background aluminum film.

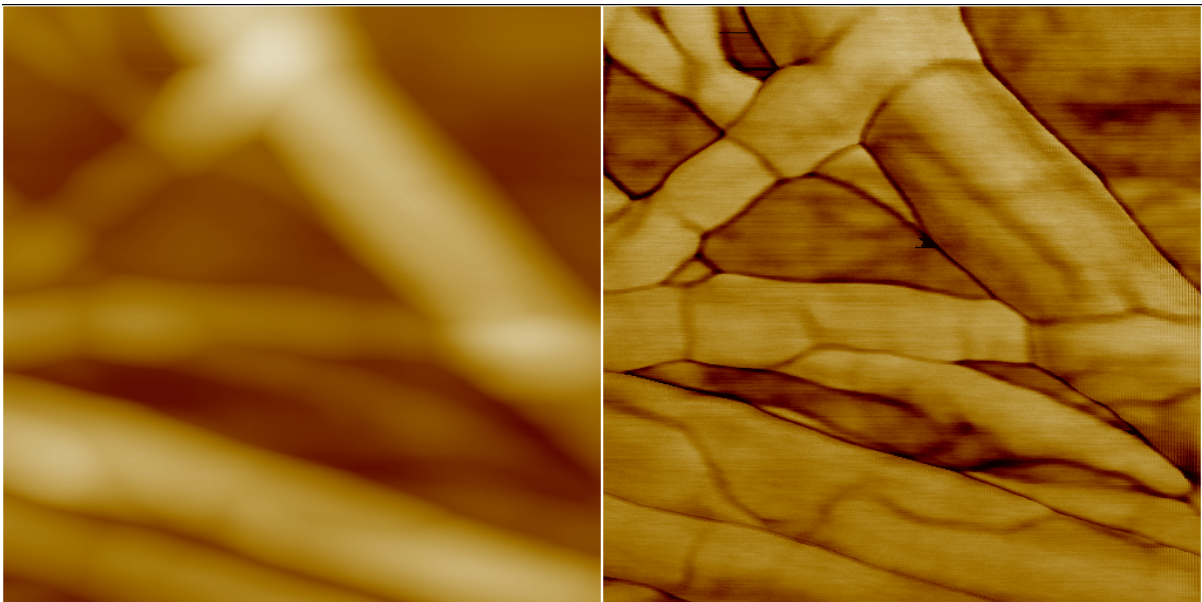


Figure 3.5. 500 nm TM-AFM image 150nm z range. Non-uniform segmented structure observed, tip shape induced artifacts? Overlap, branching common, diameters range 5 - 100 nm (height = diameter)

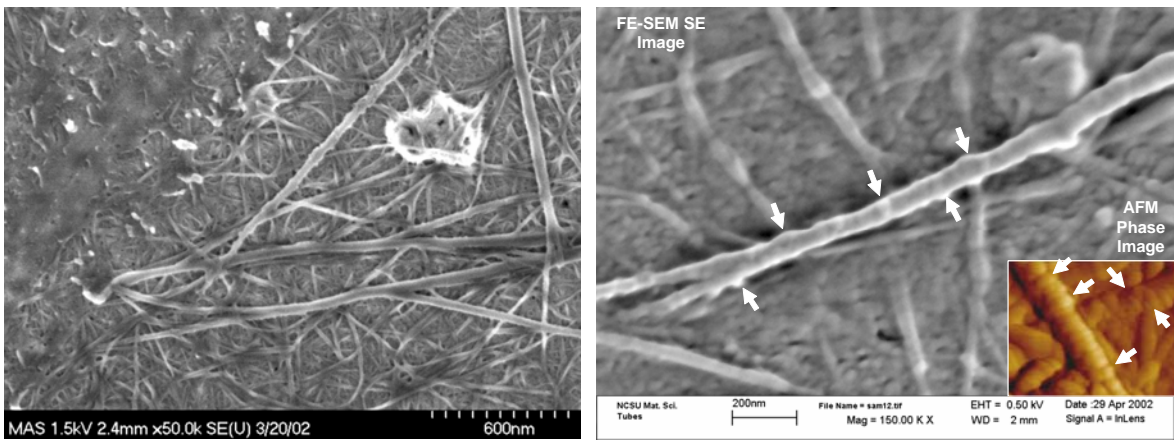
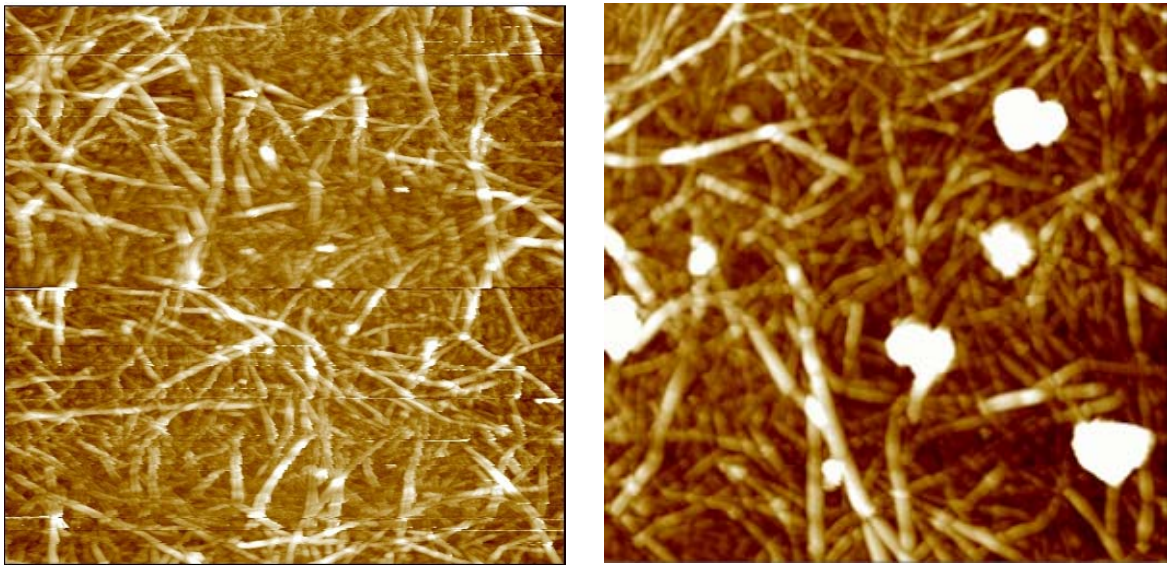


Figure 3.6. FE-SEM image of nanofiber mat that is formed on the aluminum surface after 84 days (left image). The upper left corner of the image shows what appears to be mechanical deformation of the nanofiber mat by tweezers. It is also easy to see the porous nature of the large precipitates previously observed with AFM. The right image with inset is a comparison of AFM and SEM images taken of different regions on the same 84 day immersion sample. FE-SEM was performed uncoated at low voltage. AFM and SEM images are the same scale.



9 days @ 40C

28 days @ RT

Figure 3.7. Comparison of SAN growth on two aluminum coated glass substrates immersed in 0.1 wt% C-1/EtOH solutions. The left image shows SAN growth after 9 day immersion @ 40C while the right image is of typical SAN growth after 28 day immersion @ room temperature. Both are 5 μm AFM height images.

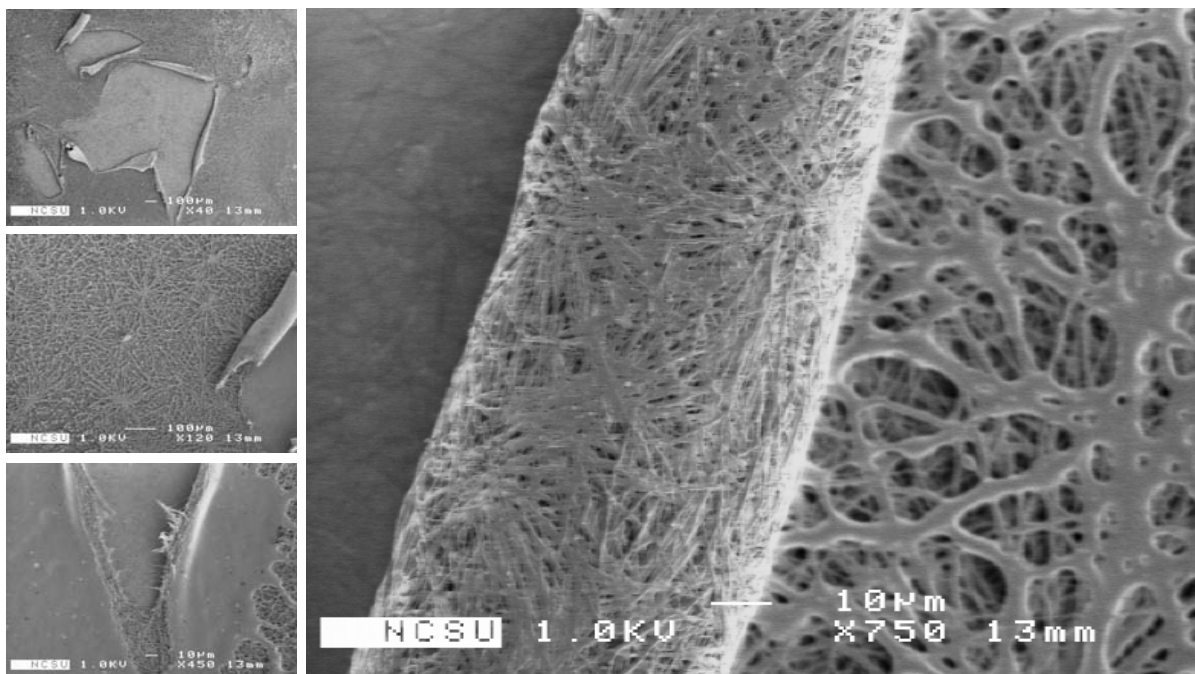


Figure 3.8. FE-SEM images of a C1 microfabric. The microfabric was grown by immersion of an aluminum coated glass slide in an 83 mM C1/EtOH solution for 19 days. The large image is a zoom of the curled region seen in the image in the upper left.

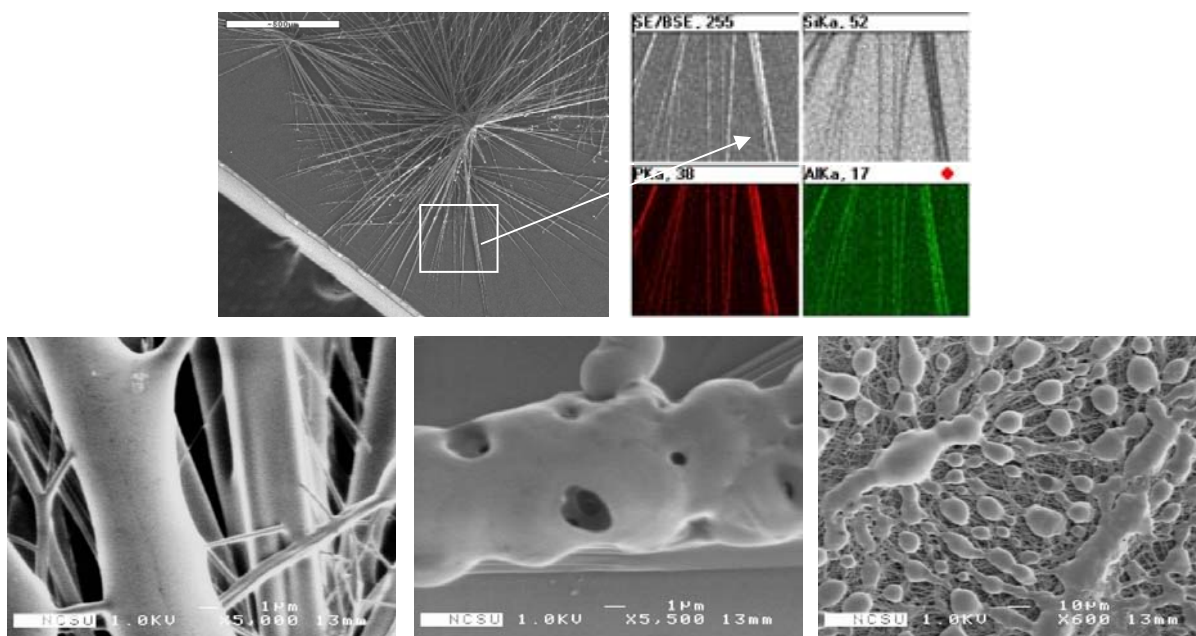
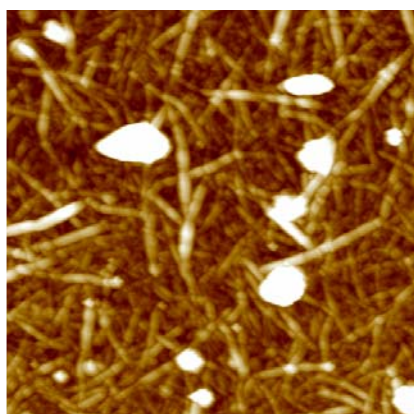


Figure 3.9. The top images are an SEM SE image and corresponding EDS maps of Si, P, and aluminum on an acicular microfiber crystal grown by immersion of an aluminum coated glass slide in 83 mM C1/EtOH solution for 19 days. The bottom images are higher magnification SEM images from different areas from the same sample showing the variety of structuring present.

MPA – 35 day immersion



PA – 46 day immersion

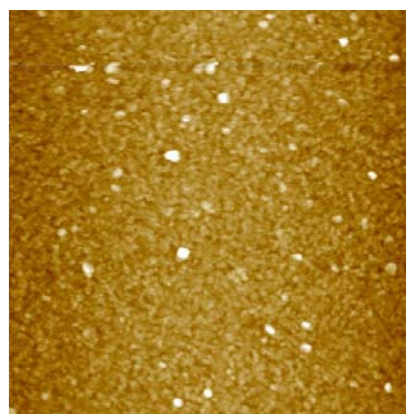


Figure 3.10. 5  $\mu\text{m}$  AFM height images of aluminum film immersed in 8.3 mM C1/EtOH and C0/EtOH. No fibers were observed without using an alkyl-phosphonic acid.

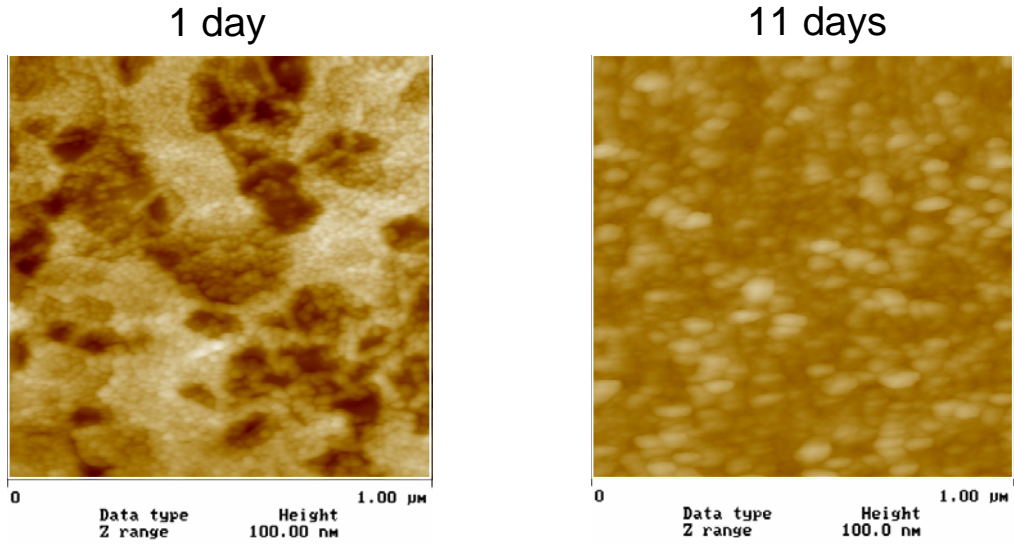


Figure 3.11. 1 μm tapping mode AFM height images of 18 MΩ H<sub>2</sub>O, 200nm aluminum on glass, AFM height images sample translucent after 11 days immersion time.

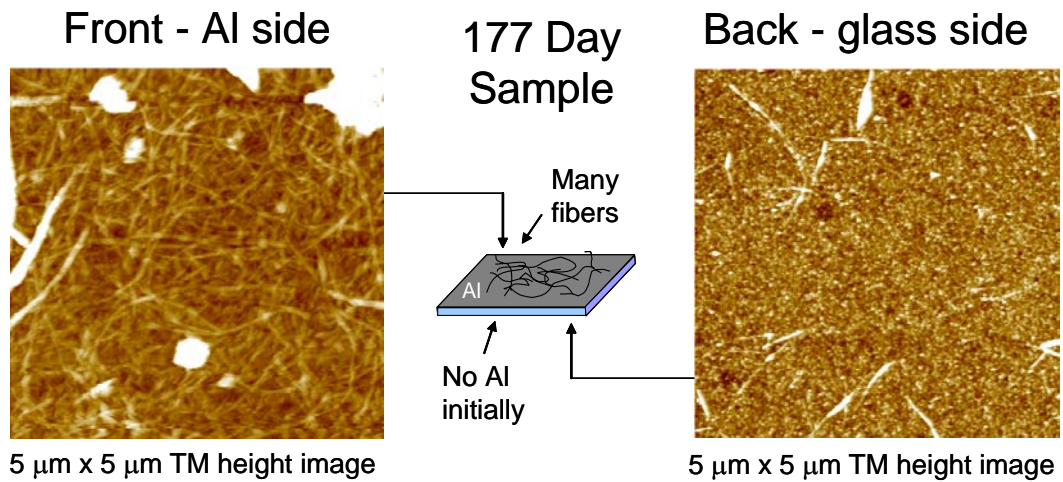


Figure 3.12. Nanofibers found on the glass surface where no aluminum was initially deposited, the backside of the aluminum coated glass 177 day immersion sample.

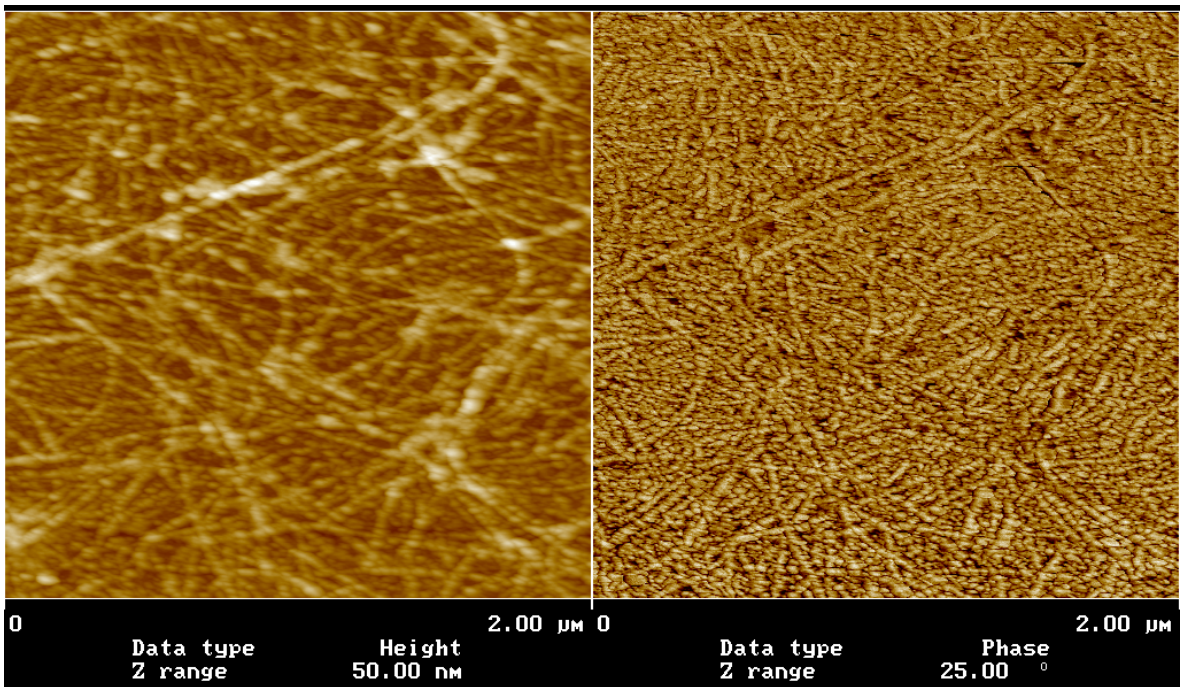
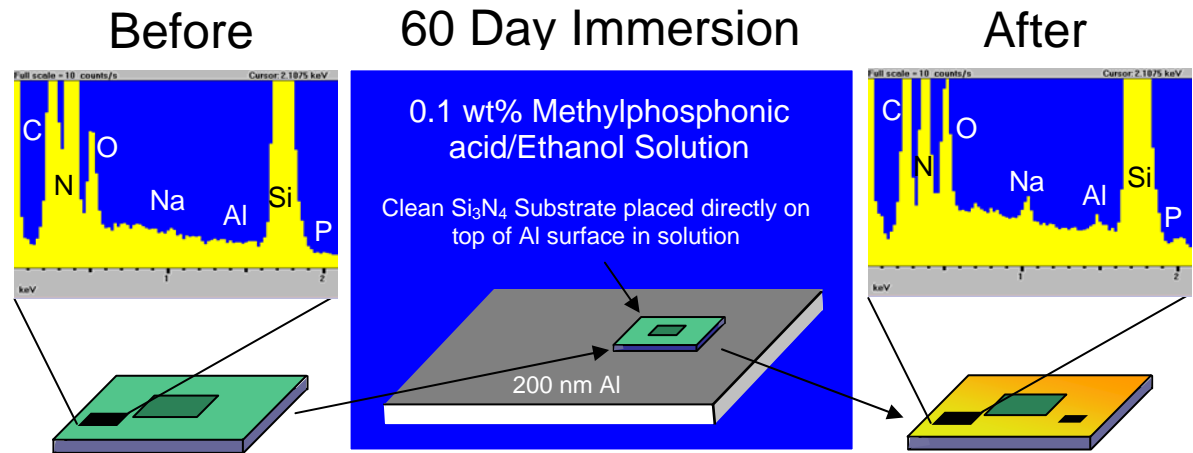


Figure 3.13. EDS analysis, 5 KV accelerating voltage, of an as received Si<sub>3</sub>N<sub>4</sub> TEM membrane before and after immersion and in a 8.3 mM C1/EtOH solution for 60 days along with a piece of aluminum coated glass. Image B is a 2  $\mu\text{m}$  tapping mode AFM height image, w/50 nm z range, showing that SAN growth can occur on adjacent substrates with no aluminum present on the growth surface after immersion in 8.3 mM C1 solution for 60 days.

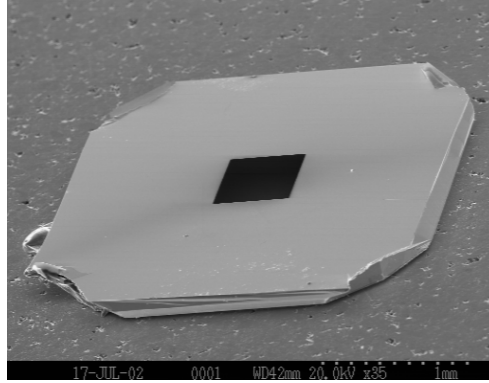


Figure 3.14. SEM image of SiN thin film window TEM substrate – SPI supplies. The entire substrate is 3 mm x 3mm x 200  $\mu\text{m}$  in size with  $\sim 1 \text{ mm}^2$   $\text{Si}_3\text{N}_4$  window.

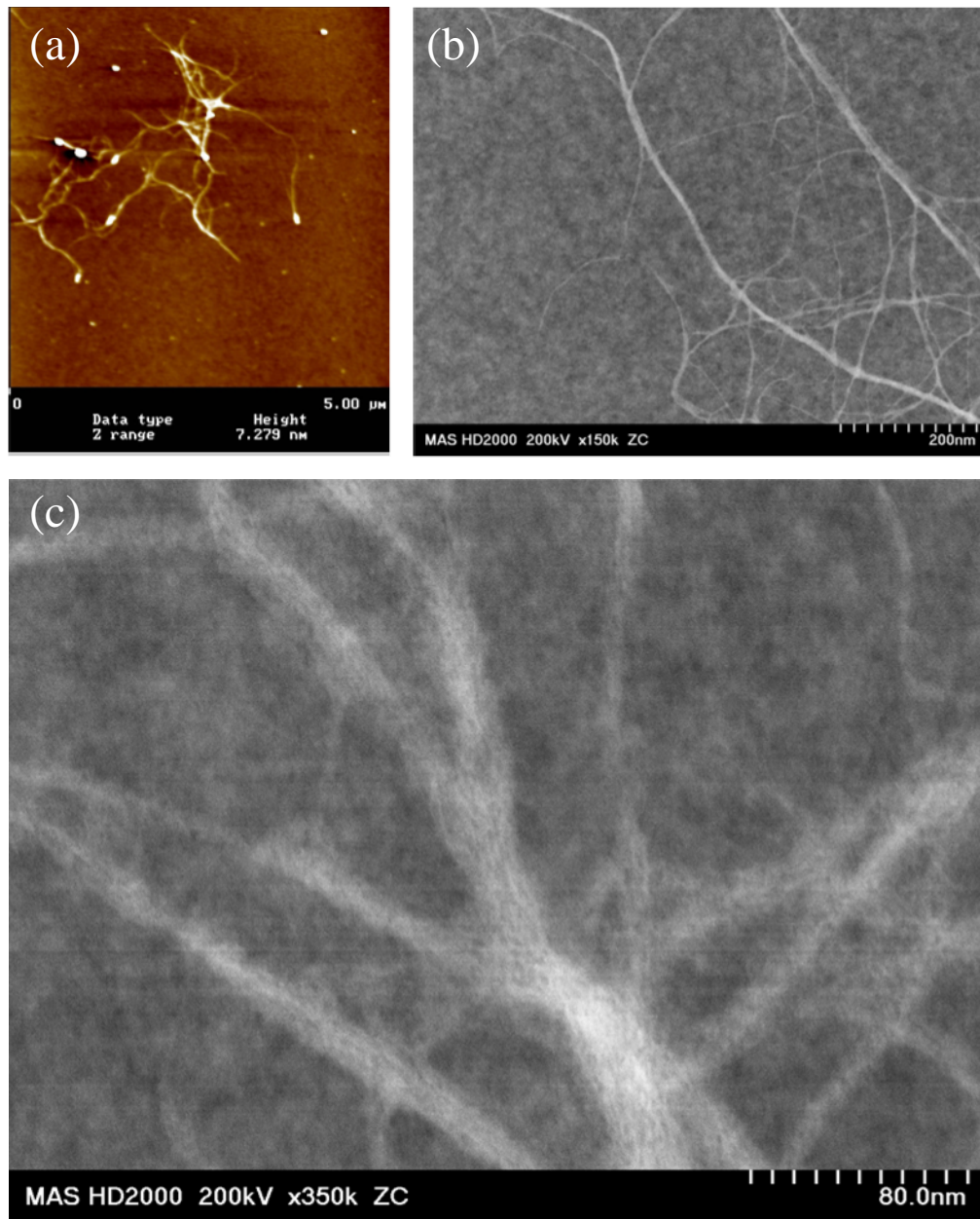


Figure 3.15. Tapping mode AFM height image of Ga nanofibers on SiN, image (a). Lower magnification Z-Contrast, image (b) of nanofiber network as grown directly on an electron transparent  $\text{Si}_3\text{N}_4$  film. Higher magnification Z-Contrast STEM image (c) showing a close up of the branched nanofiber structures.

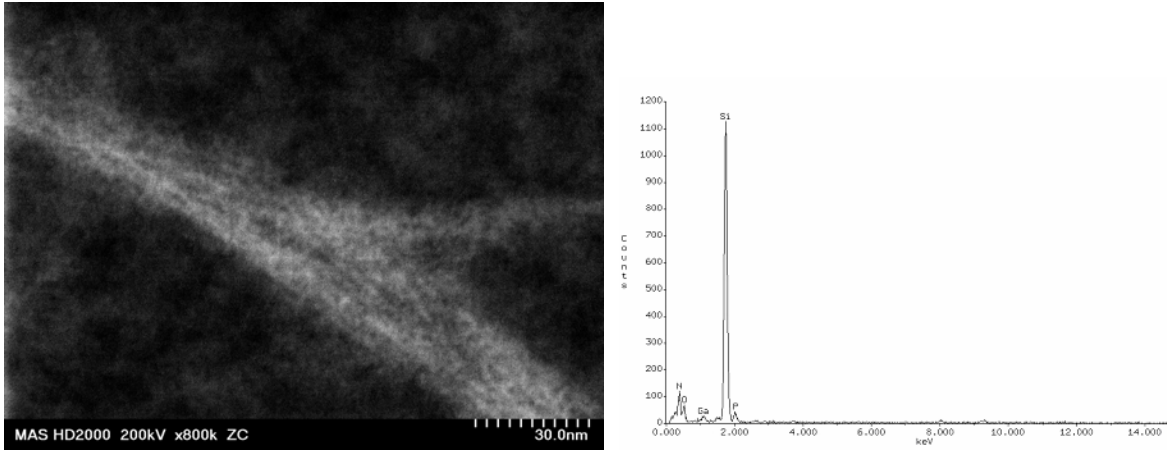


Figure 3.16. Z-Contrast STEM image of Ga nanofiber on amorphous  $\text{Si}_3\text{N}_4$ , shows the presence of fibril structures within the SAN. EDS spectra of the center of the same SAN showing the presence of Ga.

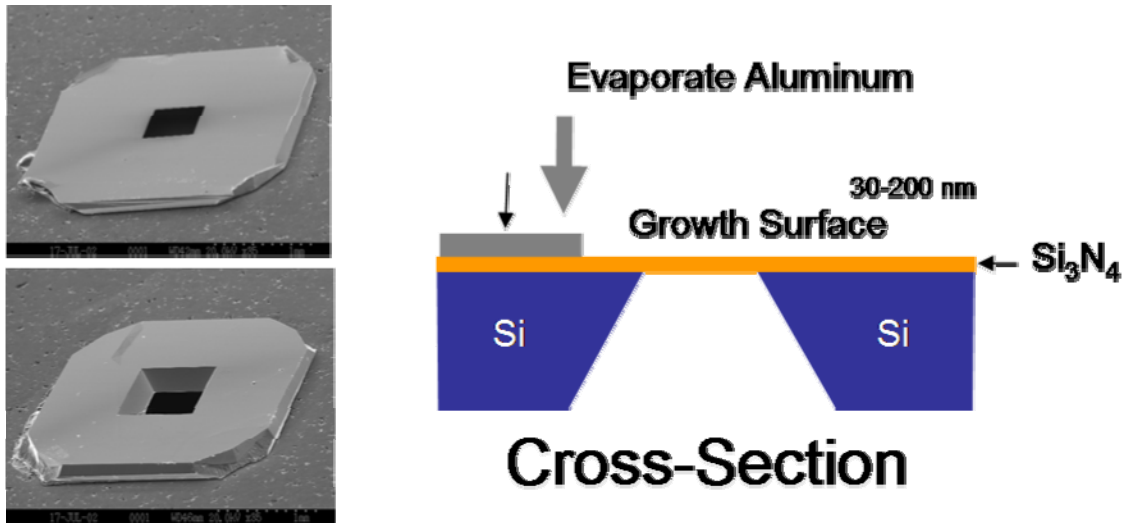
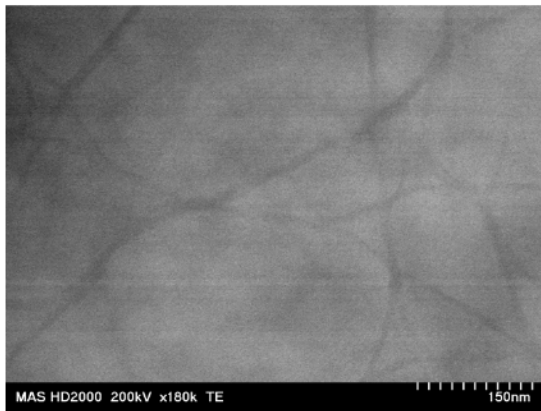


Figure 3.17. Patterned evaporation of aluminum on  $\text{Si}_3\text{N}_4$  thin film windows.

**Bright Field – Fibers Dark**



**HAADF – Fibers appear bright**

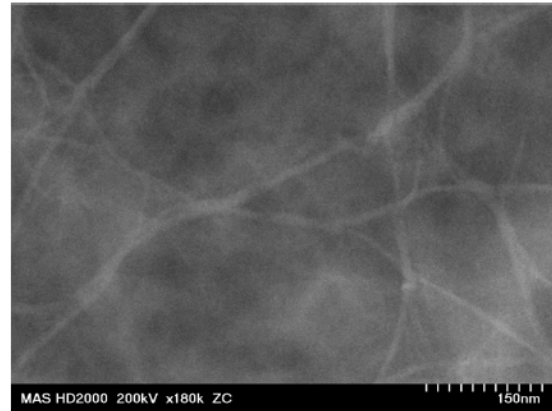
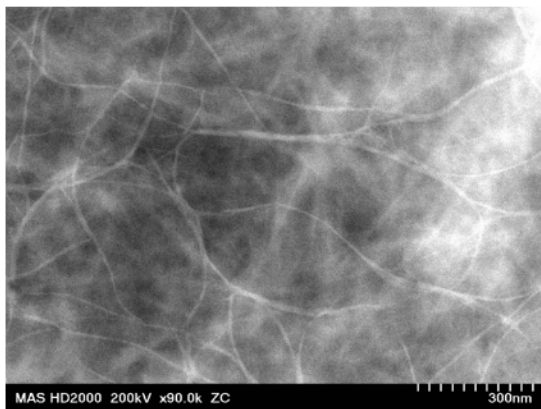


Figure 3.18. A comparison of Bright Field (BF) and Dark Field HAADF (Z-Contrast) Images SANs grown on 150 nm  $\text{Si}_3\text{N}_4$  after 30 day immersion time

**30 day immersion**



**8 day Immersion**

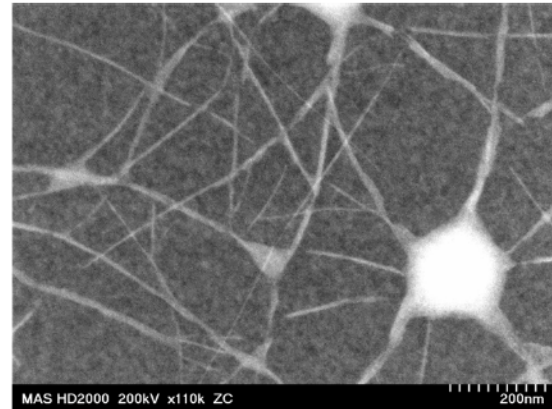


Figure 3.19. A Comparison of SANs as grown on 50 nm  $\text{Si}_3\text{N}_4$  membranes for different immersion times. Longer growth resulted in a thicker mat giving poorer contrast between individual SANs and obscuring their internal structuing. The SANs were relatively stable under the 200KV beam at moderate magnifications <750KX, but significant damage was observed to occur at higher magnifications of 1MX+.

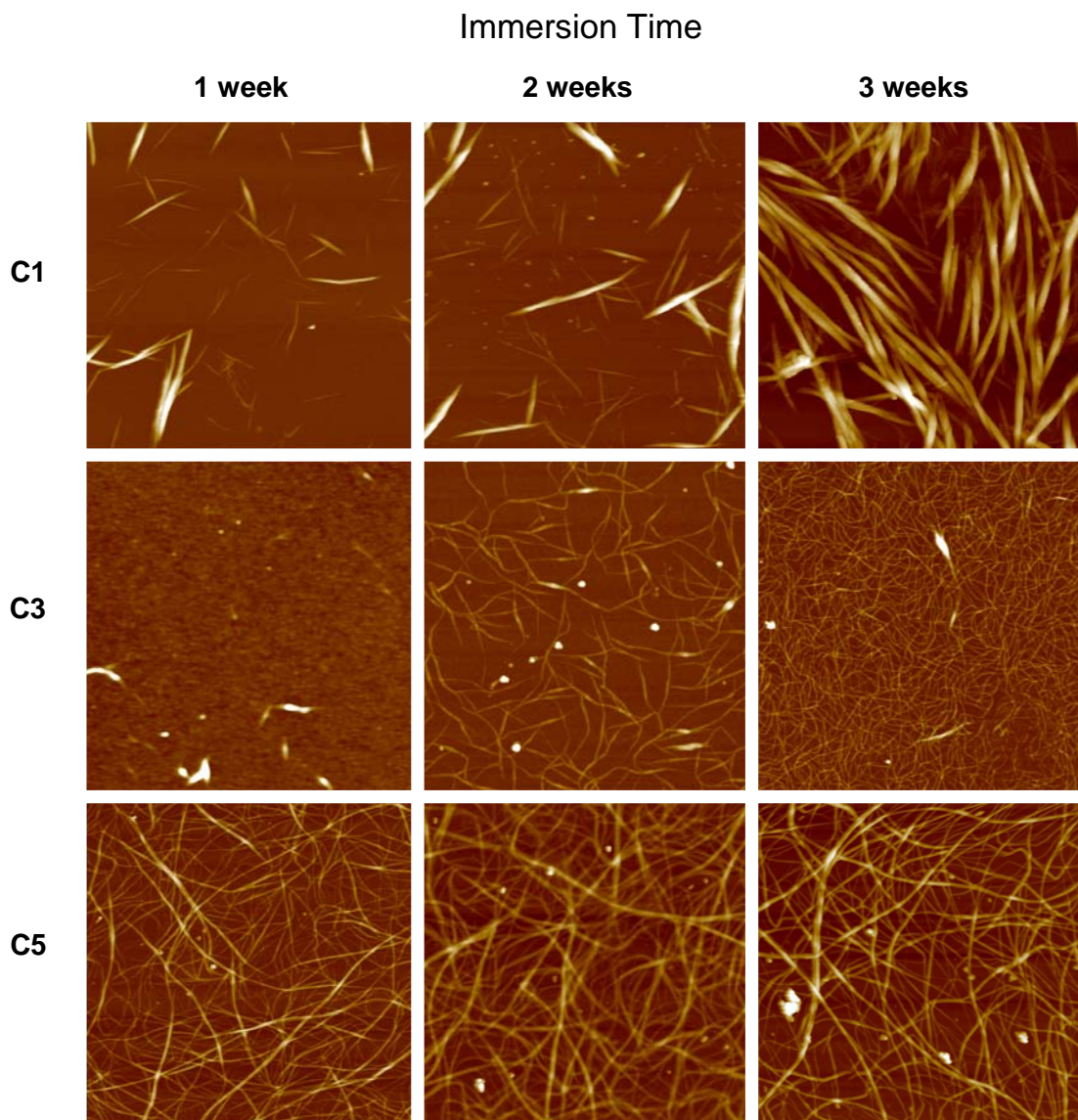


Figure 3.20. 5  $\mu\text{m}$  x 5  $\mu\text{m}$  AFM TappingMode™ Height Images showing the growth of APA SANs on  $\text{Si}_3\text{N}_4$  for C1, C3, and C5 over three weeks. The scan areas are located some distance  $\sim 1\text{-}2$  mm away from the initially deposited Al. All images taken using a Digital Instruments Dimension 3000 AFM with budget sensors, Si tapping tips,  $k \approx 3\text{N/m}$ , 1 Hz scan rate.

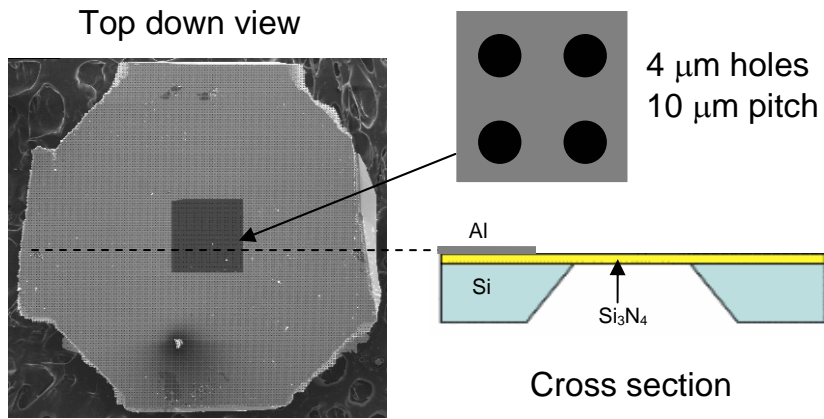


Figure 3.21. FE-SEM SE image of aluminum coated Protochips DuraSiN mesh with 4  $\mu\text{m}$  holes 10  $\mu\text{m}$  pitch in 200 nm thick SiN thin film window.

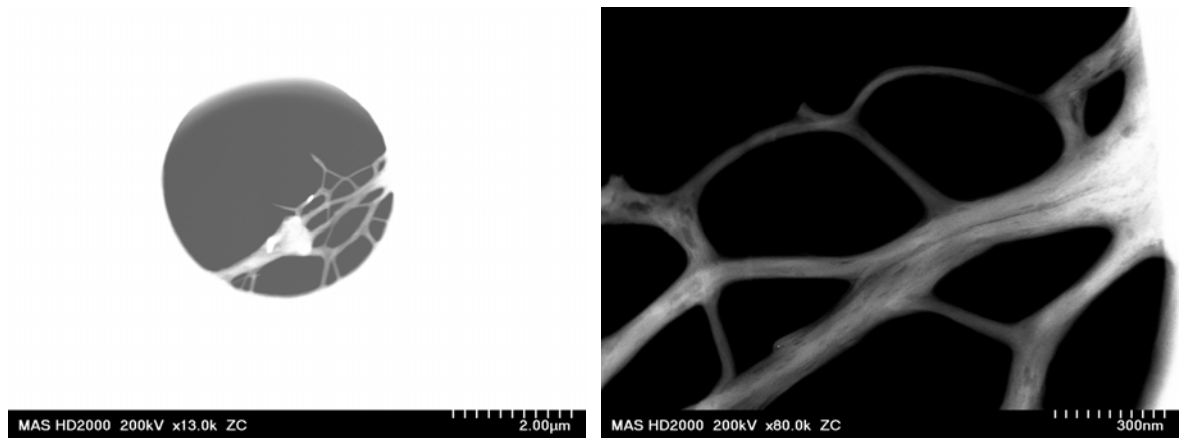


Figure 3.22. STEM ZC images of clump of unsupported fibers grown on patterned aluminum ProtoHips DuraSin mesh. These were the only unsupported nanofibers observed on the entire sample.

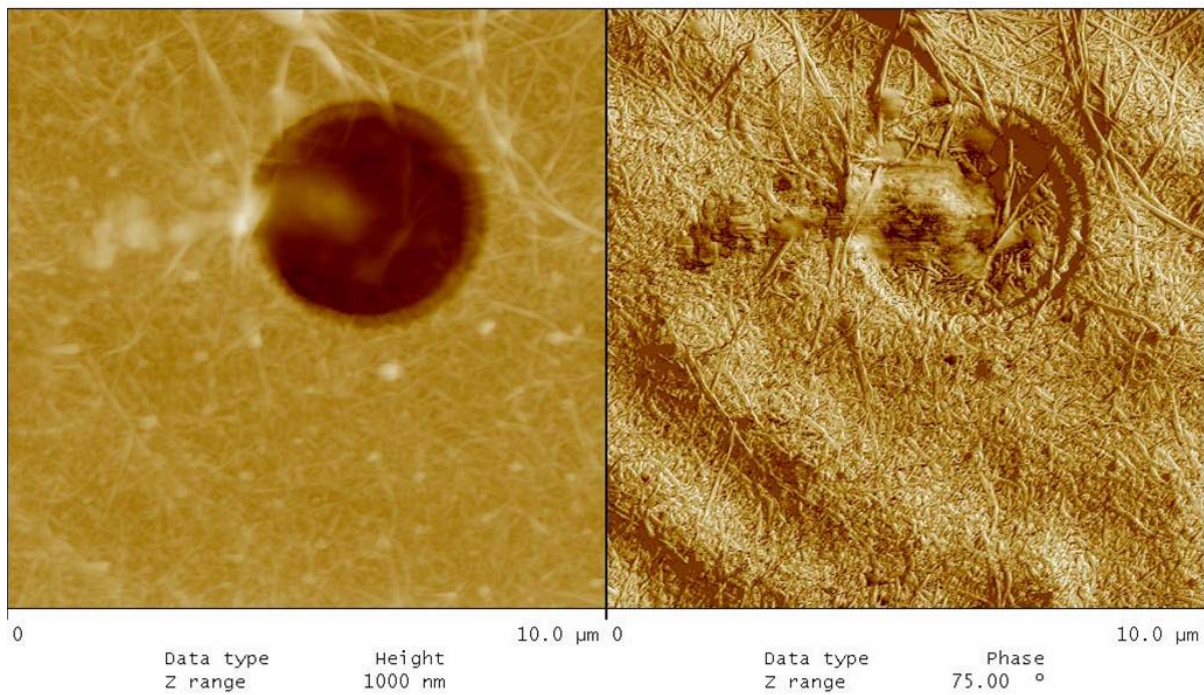


Figure 3.23. Tapping mode AFM height and phase image of a single nanofiber membrane as grown on a ProtoChips<sup>TM</sup> DuraSIN<sup>TM</sup> TEM mesh.

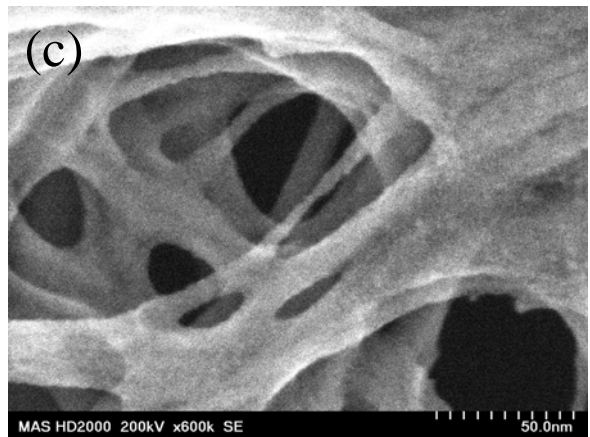
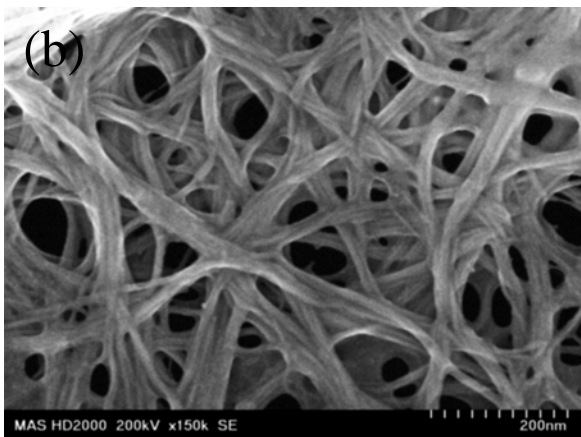
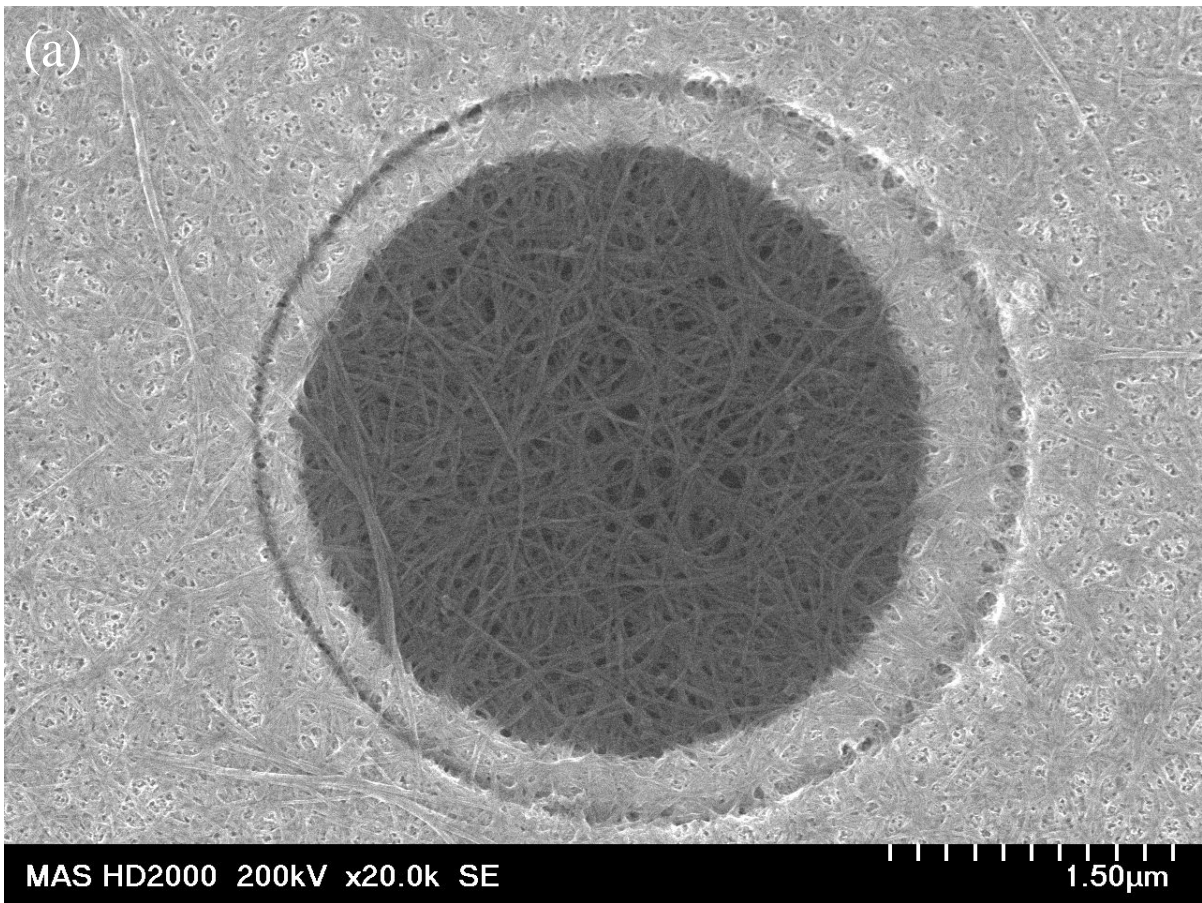


Figure 3.24. STEM SE images of increasing magnification (a-c) showing the structure of a 4  $\mu$ m unsupported SAN membrane on an aluminum coated ProtoChips<sup>TM</sup> DuraSiN<sup>TM</sup> mesh. The aluminum coated substrate was immersed in 8.3 mM C1/EtOH solution for 6 weeks.

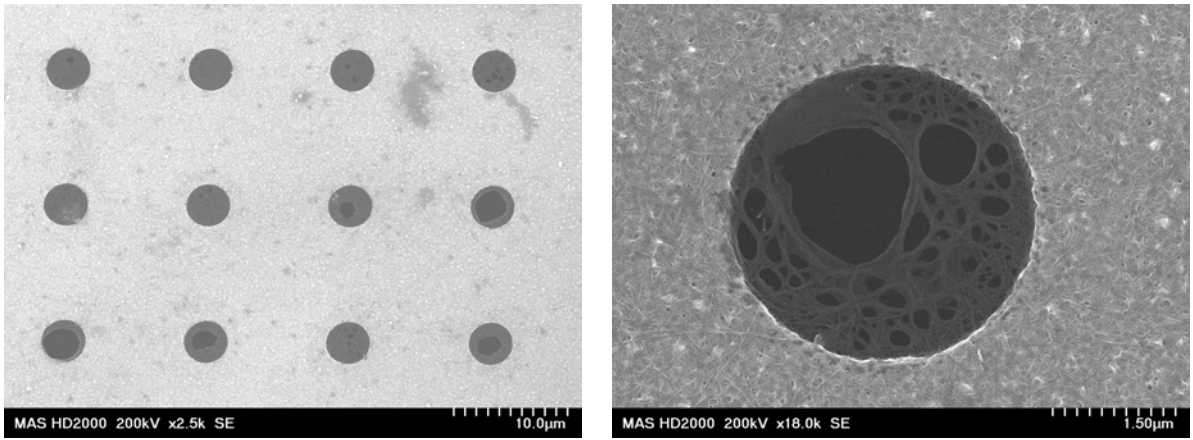


Figure 3.25. STEM SE images of C1 SAN membranes after 1 week of immersion in 8.3 mM C1/EtOH solution.

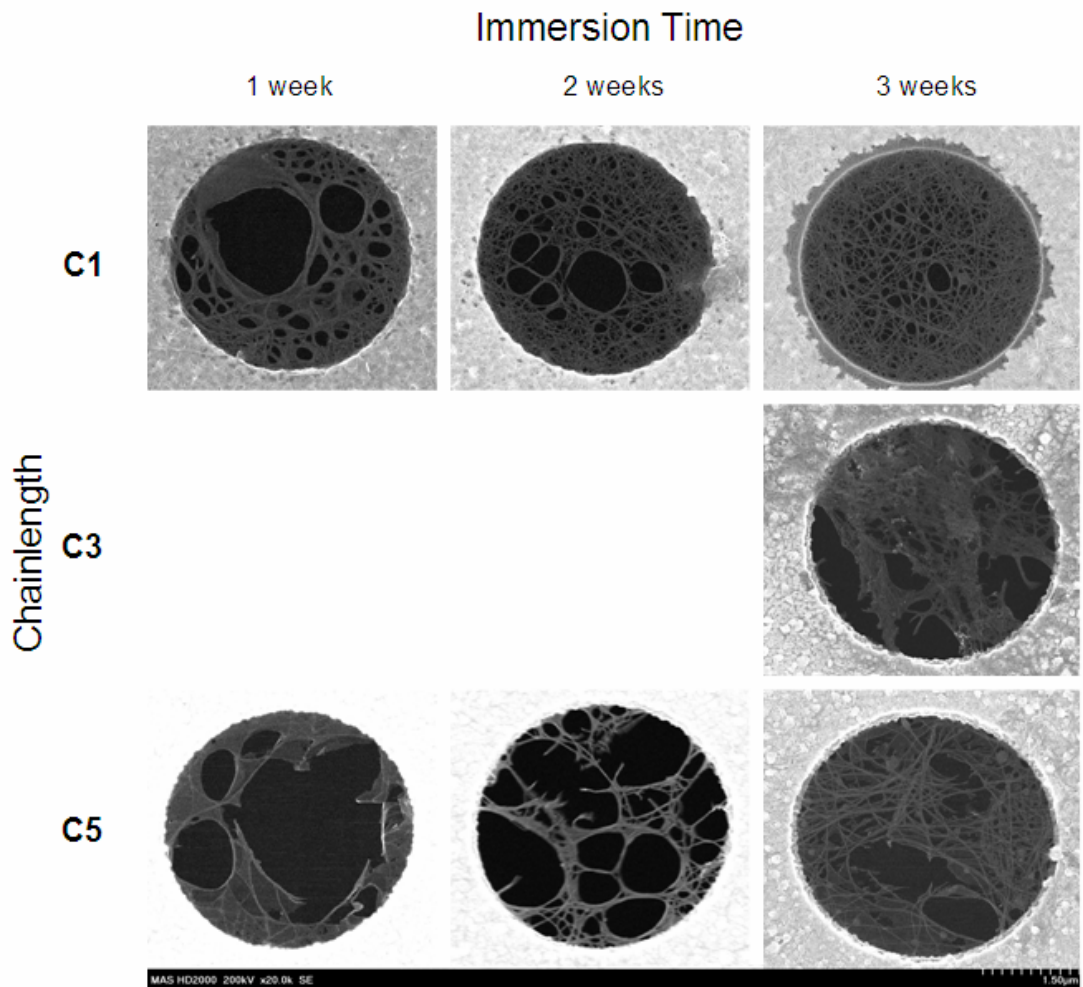


Figure 3.26. STEM Secondary Electron (STEM-SE) images of the time resolved growth of unsupported C1 and C5 SAN membranes over 3 weeks immersion time. C3 nanofiber membranes were not observed for the 1 and 2 week samples. Only the 3 week sample exhibited intact membranes. The C1 membranes were the most robust. The corrosion of aluminum around the edge of the hole is clearly seen in the 3 week c1 image.

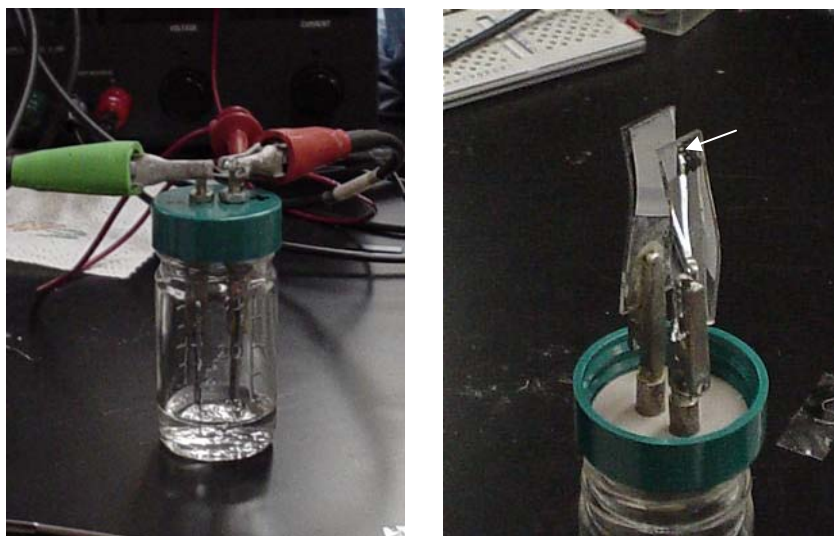


Figure 3.27. The left image is the experimental setup for biasing experiments. The right image shows the electrodes after an experiment showing the removal of aluminum on the immersed area of the anode (arrow).

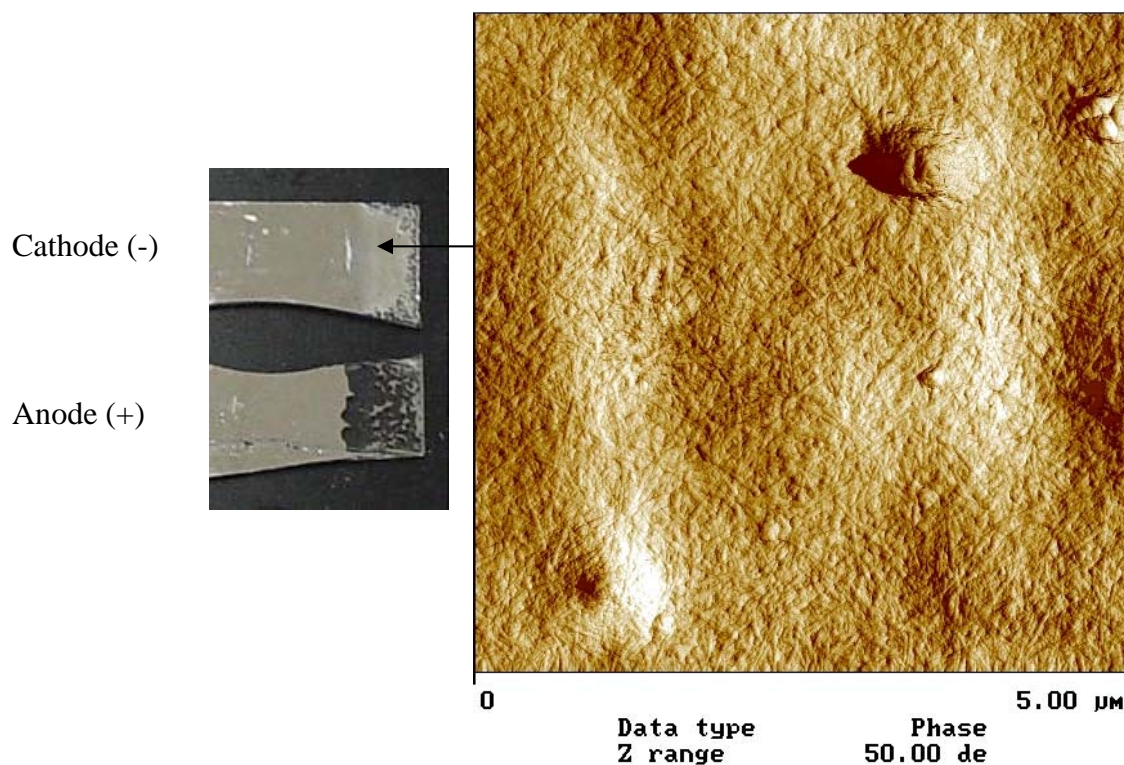


Figure 3.28. The left image is an optical micrograph of aluminum coated glass anode and cathode after 24 hrs of immersion in 8.3 mM C-1 solution solution under 3.5 V DC bias. Right image is a 5 µm AFM tapping mode phase image of resulting SAN on remaining aluminum of the cathode.

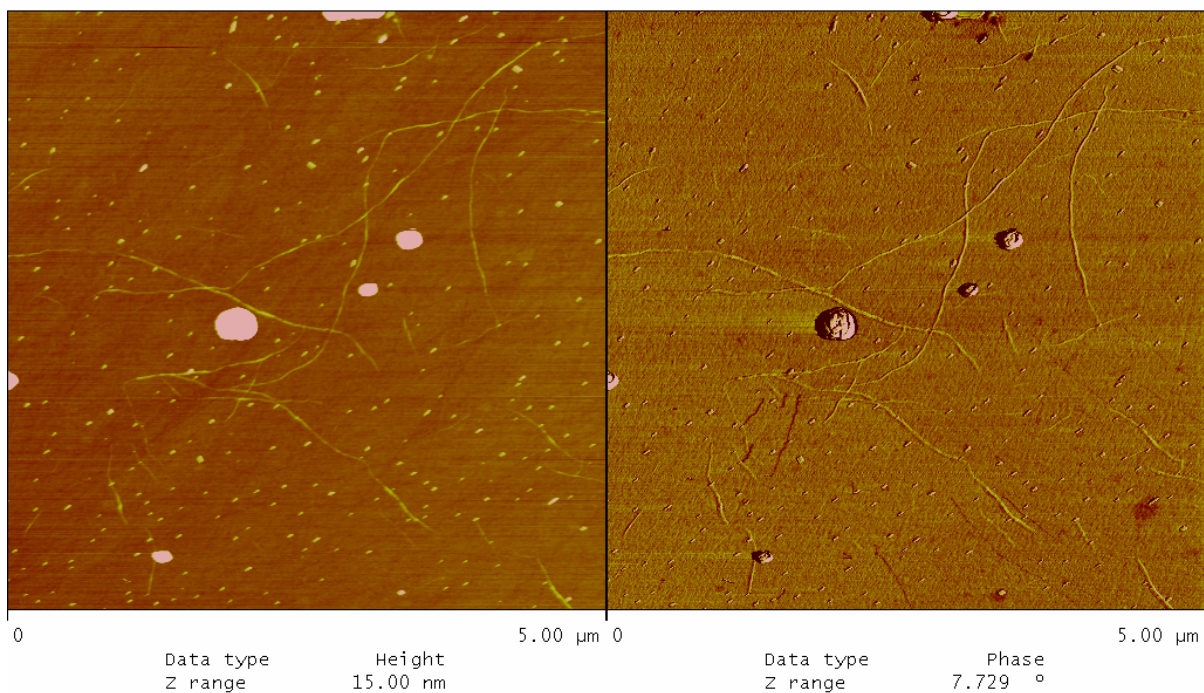


Figure 3.29. Tapping mode AFM height and phase image showing the result of nanofiber growth on a highly doped Si cathode after 5 hrs of immersion in 8.3 mM C-1/EtOH solution at 3.5 V DC bias.

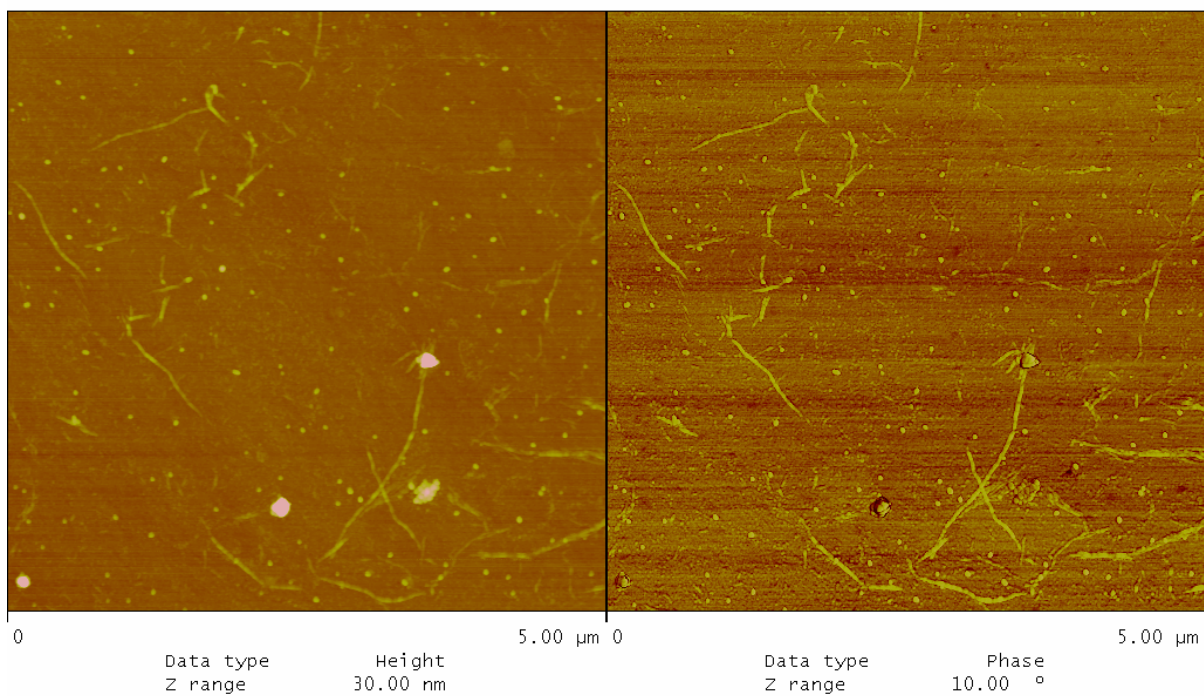


Figure 3.30. Tapping mode AFM height and phase images of the Si cathode after 24 hrs of immersion at 3.5 V bias.

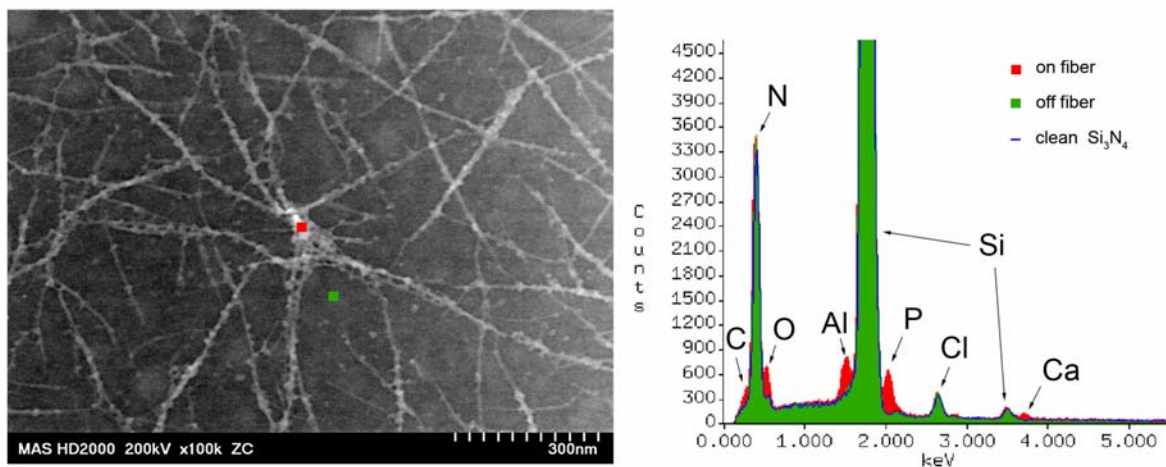


Figure 3.31. STEM with EDS analysis of C1 SANs grown directly on a Protochips<sup>TM</sup> DuraSIN<sup>TM</sup> Si<sub>3</sub>N<sub>4</sub> membrane using a biased growth method.

### 3.7. References

- [3.1] Fontes, G.N., et al., *Structural investigations of octadecylphosphonic acid multilayers*. Langmuir, 2003. **19**(8): p. 3345-3349.
- [3.2] Fontes, G.N., R.L. Moreira, and B.R.A. Neves, *Thermally induced stacking of octadecylphosphonic acid self-assembled bilayers*. Nanotechnology, 2004. **15**(5): p. 682-686.
- [3.3] Fontes, G.N. and B.R.A. Neves, *Effects of substrate polarity and chain length on conformational and thermal properties of phosphonic acid self-assembled Bilayers*. Langmuir, 2005. **21**(24): p. 11113-11118.
- [3.4] Neves, B.R.A., et al., *Observation of topography inversion in atomic force microscopy of self-assembled monolayers*. Nanotechnology, 1999. **10**(4): p. 399-404.
- [3.5] Neves, B.R.A., et al., *Scratching and healing investigations on self-assembled monolayers using Atomic Force Microscopy*, in *Microbeam Analysis 2000, Proceedings*. 2000. p. 367-368.
- [3.6] Neves, B.R.A., et al., *Thermal stability study of self-assembled monolayers on mica*. Langmuir, 2000. **16**(6): p. 2409-2412.
- [3.7] Neves, B.R.A., et al., *Spread coating of OPA on mica: From multilayers to self-assembled monolayers*. Langmuir, 2001. **17**(26): p. 8193-8198.
- [3.8] Neves, B.R.A., et al., *Self-healing on OPA self-assembled monolayers*. Nanotechnology, 2001. **12**(3): p. 285-289.
- [3.9] Richards, J.F., *Atomic force microscopy studies of microstructure and properties of self-assembled monolayers*. 1997 MS Thesis, North Carolina State University.

## 4 Structure and Composition

### 4.1. Introduction

The novel formation of alkylphosphonic acid (APA) self-assembled nanofibers (SANs) by immersion of aluminum and/or gallium in ethanolic APA solutions was previously unreported in the literature and potentially a unique method for the creation of 1-Dimensional inorganic-organic hybrid nanostructures through self-assembly. 1-Dimensional nanostructures are of current technological importance having applications in microelectronics[4.1], composites[4.2, 3], and bioengineering[4.4-6] among others. Since APA SANs are a novel material, there was no previous knowledge regarding their structure, composition, or physical properties.

The growth of (C1) SANs on aluminum thin films has been shown to be a repeatable phenomenon and the details are described in detail in Section 3.2.1. Direct compositional analysis of the SANs on treated aluminum surfaces was impossible due to the aluminum that remained underneath the SANs. It was then discovered that SAN growth was not limited to the surface of the immersed metal, Section 3.2.1.5. This led to the development of growth techniques for the successful isolation of supported SANs on previously characterized  $\text{Si}_3\text{N}_4$  coated Si substrates as well as unsupported, free-standing SAN membranes, both suitable for localized nanoanalysis of both structure and composition.

This chapter describes the determination of the structure and composition of individual isolated APA SANs utilizing a variety of accepted surface analysis and microscopy based techniques, with a focus on a combination of high resolution microscopies and spectroscopies. Since all analytical techniques have limitations and artifacts, complimentary

techniques were employed to provide increased confidence in the obtained results and for comparison with the results of similar materials previously reported in the literature.

## **4.2. Supported APA SANs**

### **4.2.1. Aluminum Coated Glass Substrates**

Initially, analysis of SAN structure and composition was limited to C1 SANs grown directly on aluminum surfaces. The progression of C1 SAN formation on aluminum surfaces over a 177 day period, as observed with AFM, is detailed in Chapter 3.2.1. Generally, aluminum surfaces removed after immersion for 14 days, exhibit a complex non-woven, mat-like morphology. Further immersion times are observed to create more dense SAN coverage with the largest SANs always observed on the outer most surface.

#### **4.2.1.1. AFM and FESEM of C1 SANs**

Examination of the 28 day immersion sample was performed utilizing conventional tapping mode AFM techniques. In Figure 4.1, we find that the C1 SANs are typically less than 100 nm wide and ~ 50 nm tall with many of the larger fibers longer than the 2 um field of view. They often branch as well as exhibit inhomogeneous sub-structure along their lengths as seen in Figure 4.1 (b). Cylindrical, ~1 micron diameter, precipitates of unknown origin are also observed to grow along with the C1 SANs. The coloration of the precipitates as seen in the AFM Phase Image in Figure 4.1 more closely resembles the coloration observed for the darker shading of the underlying aluminum surface film than the bright coloration of the SANs. Since the AFM Phase signal is known to be highly sensitive to material properties such as modulus and/or chemistry, it is highly likely that the precipitates have a composition or structure more similar to the underlying film than that of the SANs. Further evidence of this difference is observed in the thermal stability studies. The precipitates appear to have a lower transition temperature, ~ 440C, covering still intact

SANs. This is in comparison to the observed, ~ 550C transition temperature, observed for C1, C3, and C5 SANs grown on Si<sub>3</sub>N<sub>4</sub>. Further details of thermal stability experiments are found in Chapter 5.2.

Figure 4.1 (b) is an AFM scan of the zoomed area from Figure 4.1 (a), showing that the individual C1 SANs have a complex, non-uniform, sub-structure with indications of possible segmentation or grain boundaries occurring along their lengths.

FE-SEM images were taken of the 28 day C1 SAN sample as well as an 84 day sample to further examine and compare the SAN surface structure as well as to assess coverage over wider areas. The samples were imaged directly without coating. Accelerating voltages between 1.5 keV and 0.5 keV were utilized to maximize surface sensitivity and to reduce charging effects while scanning.

FE-SEM analysis of the 28 day sample finds highly uniform coverage of SANs and precipitates over the entire 1  $\mu\text{m}^2$  aluminum film with increased coverage around the edges. The ratio of the length and width of 10 of the largest SANs from Figure 4.2 (a) is ~ 50:1. Comparing images taken of the same area using 1 kV and 3 keV accelerating voltages, Figure 4.2 (a-b), the increased interaction volume of the 3 keV beam reveals the presence of sub-surface cavities. This seems to be consistent with the types of pitting corrosion widely reported for aluminum[4.7, 8]. Figure 4.3 shows a comparison of a higher magnification FE-SEM and an AFM phase image (inset) taken of the same 28-day sample at the same scale. The two images confirm the existence of the sub-fiber nodular structures along the lengths of some SANs. Examination of a larger C1 SAN, Figure 4.4 Inset 1, shows a good example of C1 SAN branching and what appears to be geometric surface structures. There also appears to be indications of sub-structural features as previously observed with AFM occurring along

the length of the fiber, Figure 4.4 Inset 2, further hinting at highly organized or possibly crystalline internal structure.

FE-SEM examination of the 84 day C1 SAN sample show the surface morphology consistent with that of a highly layered fibrous mat with  $\sim 1\mu\text{m}$  diameter scattered seemingly randomly throughout. The largest SANs are always observed to be on the outermost surface of the fabric as seen in Figure 4.5. Closer inspection of one of these larger SANs,  $\sim 100\text{ nm}$  wide, shows that the SANs do indeed exhibit branching as initially observed with AFM. It is also of interest that the branching angles of the SANs seem qualitatively regular, but an extensive analysis is beyond the scope of this work.

FE-SEM and AFM of the 28 and 84 day samples reveal the C1 SANs as complex linear structures, often branching, and having a ribbon-like appearance with a length to width ratio of 50:1. The SANs exhibit two major structural motifs, smooth and nodular. The nodular features, observed with both AFM and FE-SEM, seem to randomly occur along the length of the fibers.

#### **4.2.1.2. XRD of C1 SANs**

Examination of C1 SANs grown on aluminum coated glass substrates after immersion in 8.3 and 83 mM solutions of C1 and EtOH indicate that the aluminum is being attacked by the APA, possibly dissolving the aluminum into solution as ions or possibly as some complex with the APA molecules, which through some limited solubility are able to transport the aluminum through the solution, and self-assembling into the fibrous structures observed with AFM and SEM. X-Ray Diffraction (XRD) was performed in an attempt to confirm that indeed the poly-crystalline aluminum that was initially deposited onto glass was being

converted from its Face Centered Cubic metallic form to some other form with a different structure. XRD measurements were taken on three aluminum coated glass substrates. Each substrate was a 1 cm<sup>2</sup> piece of a glass slide coated with ~ 200 nm of evaporation deposited aluminum. Each substrate was subjected to a different environment for 1 year. The first substrate was immersed in pure ethanol. The second substrate was exposed to air under the ambient conditions of the laboratory. The third substrate was immersed in an 8.3 mM solution of C1 and EtOH.

The substrate after a 1 year immersion in the C1 solution appeared to no longer be metallic with a hazy off-white film present on the surface of the glass. AFM of this sample confirmed the presence of a thick SAN mat as well as the typically observed precipitates. For comparison, both of the other substrates, subjected to EtOH and air both appeared metallic and AFM revealed their surface to be nearly identical to the initially deposited aluminum surface (data not shown).

The XRD analysis was performed using a 1.54 nm Cu  $\alpha$  radiation source. Intensity data for each sample was collected over a  $2\theta$  range from 5 to 75 degrees using a step size: 0.05 degrees, taking ~ 24 hrs to complete the scan. The results from the three scans, shown in Figure 4.7, were then plotted and background corrected using commercial DRXWin software (<http://icmuv.uv.es/drxwin>).

The results from the samples exposed to EtOH and air show the presence of the characteristic aluminum d-spacing of 0.236 nm. This is generally the most intense peak for aluminum and is the only peak observed since the film is so thin. The results from the sample exposed to air shows a distinct broad peak at 0.565 nm along with some smaller peaks at 0.321 nm, 0.189 nm, and 0.134 nm. Examination of the C1 sample shows some

similar peaks to the sample exposed to air with the major exception that there are no characteristic aluminum peaks present. This lends more evidence that the aluminum is likely being corroded by the interaction with the C1. There are also several other peaks at 1.38 nm, 0.29 nm, and 0.157 nm that are unique to the C1 sample and are not observed on the EtOH or the air exposed samples. Several attempts were made to match the peaks observed for the C1 sample with peaks of known crystalline materials, but all were unsuccessful. It was also impossible to know whether the observed peaks are due to the SANs, the precipitates, the underlying film, or possibly crystallized C1 molecules. The similar peaks on both the C1 sample and the air sample would seem to suggest there are similar materials present in both cases, possibly some form of aluminum hydroxide.

#### **4.2.1.3. SEM and EDS of C1 Micro Fibers**

In an effort to better understand the process of C1 SAN growth, hopefully increasing the growth rate, evaporated aluminum films on glass were immersed in a 10X concentration (83.3 mM) C1/EtoH solution. Details of the sample growth can be found in Section 3.2.1.2. Instead of nanometer sized fibers, the average fiber widths increased to hundreds of nanometers to microns. After only 19 days of immersion, a translucent white film formed on the glass slides with one large acicular crystal and what appeared to be a fabric that was observed to roll up, all just barely visible with the naked eye. Further inspection using optical microscopy and SEM revealed the majority of the white film as a highly fibrous mat with floral shaped microstructure, Figure 4.6. More images detailing the observed microstructures can be found in Chapter 3.2.1.2. EDS performed on a region of floral fibers indicates that aluminum, phosphorus, carbon, and oxygen are present in the fiber structure.

Aluminum, phosphorus, and silicon EDS maps, correlating spatially resolved compositional information with the fibrous structure, are seen in Figure 4.6. EDS mapping analysis shows that the aluminum signal is highly localized along with phosphorus in fibrous structures relative to the substrate. This provides conclusive evidence that the evaporated aluminum initially coating the entire glass surface has been transported through the C1/EtOH solution. For comparison, aluminum films immersed in pure EtOH without C1 present retain their shiny appearance even after a year in solution. No fibrous structures have been observed with AFM or SEM on aluminum substrates immersed in solutions with without APAs.

#### **4.2.2. Si<sub>3</sub>N<sub>4</sub> Substrates**

Strong evidence from AFM, SEM, EDS, and XRD of C1 SAN mats grown on aluminum films suggests that growth of SANs are very likely some type of aluminum and phosphorus containing corrosion product. It was impossible to directly correlate the findings with the actual SAN structures due to their contamination with the initial underlying aluminum film, precipitates, etc. Increased C1 concentration allowed for definitive correlation of aluminum and phosphorus to the fibrous structures with EDS, but the overall fiber sizes were also greatly increased. To further examine the structure and composition of individual SANs, growth techniques were developed to isolate the SANs on clean semiconductor grade Si<sub>3</sub>N<sub>4</sub> coated Si substrates. This growth method utilized the fact that SAN formation was observed to occur on surfaces other than the initially deposited aluminum, Section 3.2.1.5, as well as the propensity for SANs to grow on Si<sub>3</sub>N<sub>4</sub>, as described in Section 3.2.2., relative to other surfaces such as SiO<sub>2</sub>. Partial, ~200 nm thick, aluminum films were created by simple shadow masking of the Si<sub>3</sub>N<sub>4</sub> coated silicon wafers in a Denton evaporator at a base pressure

of  $1 \times 10^{-6}$  torr. The patterned wafers were then broken into  $\sim 1 \text{ cm}^2$  pieces with approximately  $2 \text{ mm} \times 1 \text{ cm}$  of aluminum coating along one edge. Immersion of the substrates for 1, 2, and 3 weeks in 8.3 mM C1, C3, or C5 in EtOH solutions produced samples with isolated nanofibers as well as single and multi-layered nanofibrous mats on the  $\text{Si}_3\text{N}_4$  surfaces. SAN growth was generally dependant on the duration of the immersion and the chainlength of the alkyl-phosphonic acid used, seen in Figure 3.26. The 3 week immersion samples of C1, C3, and C5 were chosen for examination with XPS, AFM and FE-SEM for their uniform surface coverage. Additionally lift-out cross-sections of C1 SANs were made using a Focused Ion Beam (FIB) and examined utilizing Scanning Transmission Electron Microscopy (STEM). For consistency, portions of the same 3 week samples were also subjected to thermal treatments and mechanical testing as discussed in detail in Chapters 5 and 6.

#### **4.2.2.1 XPS**

X-Ray Photoelectron Spectroscopy (XPS) was performed utilizing a Riber XPS with Mg source. XPS is a highly surface sensitive compositional analysis technique which is described in more detail in Section 2.5. The major advantages of XPS are that it provides not only information about composition but also bonding information as well as being a very surface sensitive technique allowing for analysis of thin layers of materials like APA SANs.

Four samples consisting of patterned aluminum on  $\text{Si}_3\text{N}_4$  were analyzed. Three of the samples were immersed in solutions of C1, C3, and C5 each for 3 weeks as described in Section 3.2.2. The fourth sample was utilized as a control and was not subjected to immersion in solution, but stored in a typical fluoroware wafer container under ambient

conditions. AFM scans of the desired XPS analysis areas were performed on each sample before XPS analysis to verify the presence of SANs in the XPS analysis areas. Before performing the XPS analysis, the remaining aluminum coated portion of each substrate was carefully cleaved off and the sample dusted off with a pressurized jet of UHP N<sub>2</sub>. This was to make sure that any aluminum detected during XPS analysis was not from the initially deposited aluminum and only from aluminum that had been transported through the solution to the previously clean Si<sub>3</sub>N<sub>4</sub> analysis areas now covered with SANs.

XPS analysis of the 3 immersed samples detected the presence of carbon, phosphorus, aluminum, silicon, nitrogen, oxygen, and calcium as compared to only carbon, silicon, nitrogen, and oxygen on the surface of the clean Si<sub>3</sub>N<sub>4</sub> control. No detectable amounts of aluminum or phosphorus were present on the control. However, the presence of carbon and oxygen on the control rendered the carbon and oxygen signals as essentially useless for any kind of semi-quantitative compositional analysis. Only the phosphorus and aluminum signals were deemed suitable for semi-quantitative analysis and a comparison of the results are seen in Figure 4.8. The calcium detected was believed to be a contaminant; with apparent concentrations of less than 1%. Its presence in the unsupported SANs has also been verified with EDS as described later in the chapter in Section 4.3.2.4. The source of the calcium has not yet been determined, but one possibility is that it is from the glass bottles utilized for the SAN growth. Calcium was not previously observed in EDS of any other previously grown SANs.

Analysis of the XPS data was performed utilizing CASA (<http://www.casaxps.com/>). The XPS binding energy scale (BE) was calibrated to the advantageous carbon peak (285 eV). A summary of the aluminum and phosphorus data for the C1, C3, and C5 samples can

be found in Table 4.1. The phosphorus  $2p^{3/2}$  BE values range from 133.5 to 134.0 eV while the aluminum  $2p^{3/2}$  BE values range from 75.0 to 75.2 eV. Both the aluminum and phosphorus BE's for the C1, C3, and C5 nanofiber samples were significantly shifted to higher values relative to the reported 72.8 eV for metallic aluminum and 130.0 eV reported for elemental phosphorus[4.9]. These shifts towards higher BE's are indicative of a aluminum-oxygen bonding as the aluminum  $2p^{3/2}$  values for C1, C3, and C5 agree well with the reported aluminum values of 74 to 77 eV for aluminum oxide ( $Al_2O_3$ ), aluminum hydroxide ( $Al(OH)_3$ ), and aluminum phosphate ( $AlPO_4$ )[4.10-13]. The measured phosphorus  $2p^{3/2}$  values of the C1, C3, and C5 samples were slightly lower than the reported value of 135.1 eV for  $P_2O_5$ [4.14], but generally agree well with the reported phosphorus  $2p^{3/2}$  values of 133.9 eV to 135 eV for  $AlPO_4$ [4.10].

In addition to looking at aluminum and phosphorus bonding information, estimates of the relative amounts of aluminum and phosphorus present were made. A semi-quantitative compositional analysis of the C1, C3, and C5 data was performed by utilizing a weighted comparison of the aluminum and phosphorous peak areas. This gave relative phosphorus to aluminum ratios for each of the samples. Commercial CASA analysis software was utilized for this procedure. Shirley background fitting and the Schofield cross-sections for aluminum  $2p^{3/2}$  and phosphorus  $2p^{3/2}$  were utilized for the relative sensitivity factors (RSFs) values (as outlined in the CASA software manual). The RSF corrected peak areas gave phosphorus to aluminum ratios of 2.6, 4.2, and 3.2 for C1, C3, and C5 SANs on  $Si_3N_4$  respectively, Figure 4.8.

XPS analysis of the APA SANs on  $Si_3N_4$  further confirmed the presence of aluminum and phosphorous on  $Si_3N_4$  coated silicon substrates. AFM of the same XPS analysis areas

revealed the presence of APA SAN structures. Due to the high levels of carbon and oxygen contamination of the  $\text{Si}_3\text{N}_4$  control, it was impossible to discern further information relating to the carbon and oxygen within the APA SAN structures.

#### **4.2.2.2. AFM and FE-SEM**

FE-SEM and AFM analysis was performed on the same C1 SAN sample and the results are compared in Figure 4.9. The C1 SAN sample examined was immersed in 8.3 mM C1/EtOH solution for 3 weeks. FE-SEM revealed the aluminum to be highly corroded along the Al/ $\text{Si}_3\text{N}_4$  interface. 100 nm wide SANs were scattered about on the aluminum as well as on the  $\text{Si}_3\text{N}_4$  surfaces. They had the appearance of bundles or layers of smaller fibers. The bundles, ~ 20 – 25 nm wide, were also observed in the AFM phase image inset of Figure 4.9 as well as in the 3D representation of the height information in Figure 4.10. The C1 SANs grown on  $\text{Si}_3\text{N}_4$  exhibited less branching and did not exhibit the familiar nodular features as compared with the C1 SANs grown on aluminum coated glass shown in Section 4.2.1.1. It is still unclear why there are differences between the morphology of the SANs grown on different substrates, but it is thought that the use of patterned aluminum substrates, with lower aluminum surface areas, led to lower aluminum concentrations in solution

Further evidence of bundled SAN sub-structures were observed with tapping mode AFM of C3, and C5 SANs grown on  $\text{Si}_3\text{N}_4$  after 3 weeks immersion. Tapping mode AFM images were acquired under high damping conditions utilizing force modulation cantilevers having a spring constant,  $k$ , of ~ 4 N/m (as determined by the manufacturer). High damping was utilized to rub away the outer layers of the SANs allowing for imaging of internal structures. Approximately 200 scans were made, capturing ~ 125 images showing what appears to be

remarkable molecular scale resolution of the SAN substructure. Figure 4.14 (a) is one of these images, a 200 nm scan area showing the intersection of several C3 SANs. The middle SAN exhibits distinct 6 – 8 nm fibril structures that are visible in both the height and phase images. The fibrils appear to have a layered structure and the height of the different layers was then measured utilizing an averaging cross-sectional analysis of the SAN height image as shown in Figure 4.14 (b). Figure 4.15 is a higher magnification image of a region on the lower fiber in Figure 4.14 (a). The 75 nm scan was taken with the same set point and scan rate as the previous image showing that the C3 SAN has a corrugated structure on the order of 2-3 nm which scales with decreasing scan size and is consistent from scan to scan. Similar sub-fibril corrugations were also observed, in Figure 4.16, for C5 SANs utilizing the same cantilever previously used to acquire the images in Figure 4.14. Although C3 and C5 molecules have different lengths of  $\sim 0.65$  nm and  $\sim 0.90$  nm respectively, a quantitative comparison of the C3 and C5 corrugations has proven difficult, due to the resolution of the AFM images as well as the poor long range order. The C5 corrugation was slightly larger and more pronounced than that observed for the C3 SANs. No similar nm sized corrugations have been observed in the AFM images of C1 SANs. In both the C3 and C5 SANs the corrugations appear to have a similar geometric relationship with the overall linear shape of the SANs, having a smaller repeat distance parallel and a larger repeat distance perpendicular to the length of SAN. This is consistent with observations obtained in the STEM ZC imaging of unsupported APA SANs presented later in this chapter.

It is also important to note that subtle changes in the corrugation patterns were observed from scan to scan with more significant changes in individual SAN morphologies after a 5-10 scans under high damping.

#### **4.2.2.3. FIB Cross-Sections of C1 SANs**

In an attempt to better understand the internal structuring of the C1 SANs as observed with AFM, cross-sections were made using a Focused Ion Beam (FIB). Details of the FIB can be found in Section 2.6. C1 SANs as grown on  $\text{Si}_3\text{N}_4$  after a three week immersion were utilized for cross-sectioning. Before putting the sample in the FIB, an  $\sim 200$  nm thick protective film of polycrystalline copper was evaporated directly onto the C1 SAN sample using a Denton evaporator having an  $\sim 5 \times 10^{-6}$  torr base pressure. Copper was chosen because it provides ample protection against the gallium beam, as well as the fact it doesn't have any EDS peak overlaps with phosphorus, aluminum, oxygen, or carbon.

Several "lift-out" thin sections for TEM observation were created using a Hitachi FIB and then examined using A Hitachi HD-2000 STEM. The Sections were prepared using a cross-section protocol provided by Hitachi High Technology. A final 10 keV polish step was performed on both the front and back side faces to remove beam damage prior to imaging in the STEM.

##### **4.2.2.3.1. STEM and EDS of FIB Cross-Sections**

Figure 4.11 shows STEM images of a typical lift out C1 SAN cross-section sample. Figure 4.11 (a) is an overview SE image of the entire cross-section, with the 100 nm thick region isolated near the top edge of the sample. The tungsten (W), copper (Cu), C1 SANs, and  $\text{Si}_3\text{N}_4$  layers are labeled in the TE image of Figure 4.11 (b). Several voids in the copper film are also noticeable. The voids are thought to be due to shadowing effects caused by off-axis positioning of the C1 SAN sample relative to the evaporation source. There is also evidence of round areas of lower density or voids within the two largest SANs. These are

most likely due to embedded voids between fibril bundles. Interestingly, the ZC image of Figure 4.11 (b) indicates that the C1 SANs have an overall lower average Z than both the copper and the  $\text{Si}_3\text{N}_4$  as they are lighter in contrast. Figure 4.12 shows higher magnification SE, TE, and ZC images of the two larger SANs from Figure 4.11. The SE image shows a contrast difference between the copper and the C1 SAN, but not between the C1 SANs and the  $\text{Si}_3\text{N}_4$ . This was the case for all the cross-sections analyzed in the STEM. However, the TE and ZC images clearly show contrast differences between each of the three different materials. The right most SAN in Figure 4.12 appeared to be more parallel to the electron beam, so it was chosen for further inspection.

Looking further at the TE image of the single C1 SAN as seen in Figure 4.13 (a), we see that there is little noticeable difference between the SAN's internal structure and that of the amorphous  $\text{Si}_3\text{N}_4$  beneath it. However, there is a slight contrast difference with the SAN being lighter than the  $\text{Si}_3\text{N}_4$ . The ZC image, Figure 4.13 (b), reveals more internal layered structuring along the  $\text{Si}_3\text{N}_4$  interface and the arrow denotes an interesting internal planar feature. Out of the 30+ SAN cross-sections investigated, there were several planar internal features observed, but none seemed consistent with the others. Other SAN cross-sectional samples were examined with a double tilt holder in an attempt to find any fiber orientations that exhibited distinct crystal structure. C1 SAN cross-sections were imaged through a wide range of tilts in both X and Y, but no evidence of crystallinity was found. Additionally, there was no evidence of repeatable internal structures, akin to the fibrils observed with AFM or STEM. There were, however, many instances of what appeared to be faceting of the SANs along their interfaces with the copper. The internal structure of C1 SANs appears as non-crystalline or amorphous in the TE images, having a structure more similar in

appearance to the underlying amorphous  $\text{Si}_3\text{N}_4$  than the polycrystalline copper. One other important feature is that all the C1 SAN cross-sections observed with the STEM appear to lay flat on the supporting  $\text{Si}_3\text{N}_4$ .

In addition to imaging, EDS analysis was performed on a variety of C1 SAN cross-sections utilizing the Hitachi HD-2000 STEM with a Noran Vantage EDS system. A beryllium double-tilt sample holder made by Gatan was utilized to avoid any possible aluminum contributions from the normal Hitachi sample holder. Figure 4.13 shows the results from two spot analyses carried out on both the SAN (Spot 1) and on the underlying  $\text{Si}_3\text{N}_4$  (Spot 2). All spot analyses were performed by acquiring spectra for 60 sec live time in high resolution mode. It is easy to see that the phosphorus and aluminum are isolated to the SAN structure and not present in the underlying  $\text{Si}_3\text{N}_4$ . A semi-quantitative analysis performed using the Noran Vantage software of the resulting spectra from Figure 4.13 shows a phosphorus:aluminum ratio of 1.4, a carbon:phosphorus ratio of 1.2, and a oxygen:phosphorus ratio of 6.2. The silicon peak in Spot 1 is considered an artifact as the HD-2000 STEM utilized was known to deposit a silicon based contaminant which gives a false positive for silicon and was left out of all semi-quantitative analyses. A total of nine spot mode EDS analyses were performed on different C1 SAN cross-sections and the summary of the results can be found in Table 4.2.

## **4.3. Unsupported APA SANs**

### **4.3.1. C1 SANs – 6 Week Immersion**

Unsupported C1 SAN membranes were created for high resolution STEM/TEM imaging EDS analysis and future EELS analysis. Initially, as a proof of concept, SAN samples were prepared by immersion of aluminum coated ProtoChips<sup>TM</sup> DuraSIN<sup>TM</sup> substrates in 8.3 mM C1/EtOH solution for 42 days. This created a single 3 mm diameter, (S)TEM ready, substrate with hundreds of 4  $\mu$ m diameter unsupported SAN membranes with no substrate in the e-beam path. A detailed description of unsupported SAN growth can be found in Section 3.3. The membranes were analyzed using a Hitachi HD-2000 dedicated STEM, which is described in more detail in Section 2.4. The HD-2000 STEM was operated at 200 keV accelerating voltage and has three main imaging modes allowing for a both surface (SE) as well as internal analysis (ZC and TE) of thin specimens. It is also equipped with a Noran Vantage EDS system for elemental analysis of thin specimens. The combination of surface and internal imaging modes, a small sub-nm spot size, and thin specimen EDS analysis makes the HD-2000 STEM well suited for the investigation of APA SAN structures and composition with high spatial resolution.

#### **4.3.1.1. STEM and EDS**

Figure 4.17 (a) is a 200 keV Secondary Electron (SE) micrograph taken of a typical C1 SAN membrane. The unsupported SAN regions have the same general appearance as SANs observed on supported regions of the same sample, but without the precipitates or underlying aluminum morphology obscuring observation of the internal SAN substructure. The observed SAN morphology is consistent from membrane to membrane across the sample and

coverage over the entire 1mm window is highly uniform. Figure 4.17 (b) is a higher magnification image of the edge of a different membrane showing the complex overlapping and layering of the non-woven bundled fibrillar SAN structure. The individual SANs are composed of bundles of fibrils along with a webbing of unknown origin and composition observed between some fibers in lower layers of the membranes. The unsupported nanofiber morphology, size and number, appear to be consistent with the previously investigated samples of nanofibers grown directly on evaporated aluminum for similar immersion times.

Since the HD-2000 STEM has the ability to look at both surface (SE) and internal (ZC & TE) structures of thin specimens, sequential images of the same area were acquired with each of the detectors. A series of images taken at one area, Figure 4.18, show visible evidence of a surface layer as the observed width of fiber 2 in the SE image, Figure 4.18 (a), is noticeably larger than the width of the same fiber observed in both the ZC image, Figure 4.18 (b), and TE image, Figure 4.18 (c). This difference in observed SAN width is quite possibly related to the observed webbing noted in Figure 4.17 (b). One possible explanation for the webbing is that it is a contamination layer left after incomplete rinsing of the excess C1 solution prior to imaging. Further evidence in support of a contamination layer was the rapid formation of thick scan boxes on the SANs while scanning the SANs at magnifications above 600 kX. It is also important to note that significant sample damage is observed to occur due to radiation with the e-beam as well which made higher magnification analysis difficult. Direct evidence of destructive sample damage can be seen in Figure 4.18 (a-b), where the small 5 nm fiber, fiber 1, has broken due to scanning with the beam. The majority of SAN breakage was typically confined to the smallest of fibers, but significant structural changes were also observed in larger fibers after prolonged exposures at higher magnifications. Interestingly,

low magnification scanning of areas for several minutes prior to high magnification imaging seemed to improve nanofiber stability most likely through stabilization with carbon contamination. There are indications that some of the observed instabilities are due to charging effects as entire portions of C1 SAN membranes have been folded over utilizing electrostatic interactions with the beam as seen in Section 6.2.

Figure 4.19 shows sequential SE (a) and ZC (b) images of the same C1 SANs. The SANs are either thicker along their centers or have a core of higher Z material as noted by the bright contrast observed in the ZC image. In the SE image the SANs appear to have a flat morphology, which would tend to support the contrast observed in the ZC image as being truly Z-Contrast with higher Z materials at the core. To further understand the differences between the core and outer regions of the SANs an EDS analysis with mapping was performed. EDS analysis identified that the elements phosphorus, oxygen, aluminum, and carbon were present in the fibers. EDS mapping of the phosphorus, oxygen, aluminum, and carbon signals was then performed on the same area, along with a TE image of the SAN membrane, Figure 4.20, allowing for spatially resolved compositional information to be obtained. It is easy to see from the elemental maps in Figure 4.20, that the width of the SANs in the carbon map are wider than in the corresponding phosphorus, oxygen, or aluminum maps. It is important to note that the maps for each element are acquired simultaneously.

The observed internal substructure within individual C1 SANs is best described as highly complex with a significant amount of disorder. The individual SANs are composed of bundles or layers of fibrils. Figure 4.21 shows a group of C1 SANs where ~ 5 - 6 nm fibrils are clearly visible. Figure 4.21 Inset 2 is a digital zoom of an individual fiber which appears

to have a helical quality with individual fibrils wrapping around each other along the central fiber axis. The individual fibrils exhibit nm scale speckling along their lengths. The speckling may be due to short range ordering of the carbon, aluminum, and phosphorus in some type of networked structure with the dark corresponding to carbon rich regions and the bright areas corresponding to phosphorus, oxygen, and aluminum rich regions. Another possibility is that the dark regions are actually pores. Figure 4.22 shows another example of the mesostructured fibrils observed within individual nanofibers. There appears to be qualitative similarities between the corrugations observed with AFM of the C3 and C5 SANs and the ZC STEM images of the C1 SANs.

#### **4.3.2. C1, C3, and C5 SAN Membranes**

Unsupported C1, C3 and C5 SAN membranes were created by immersion of the same aluminum coated ProtoChips™ DuraSIN™ substrates in 8.3 mM solutions of C1, C3, and C5 and 95% EtOH for 1, 2, and 3 week immersion times. Further details of the sample preparation are found in Section 3.3.3. From the unsupported C1 SAN results presented in the previous section, it was hypothesized that the observed complexity of the SAN membranes could be significantly reduced by decreasing the immersion time. With less immersion time there should be less SAN growth and thus reduced amounts of layering. The resulting SAN membranes were examined with a Hitachi HD-2000 STEM. The addition of the C3 and C5 chain lengths was utilized to examine whether SANs could be grown with other chain lengths less than 8, and to provide consistency with the supported SAN growth. It was hoped that the addition of the extra carbon, a quantifiable difference in the structure would be observed providing important information about the formation of APA SANs.

#### 4.3.2.1. STEM of C1, C3, and C5 SAN Membranes

The SAN membranes created with shorter immersion times, especially 1 week immersions of C1, did indeed exhibit significantly less layering and bundling. The C1 SAN membranes were the most robust, and are the main focus of this section, surviving the removal from solution and rinsing. Instead of the complex multi-layered non-woven morphology observed for longer immersion times of 6 weeks, as in Figure 4.17 (b), the resulting 1 week SAN membranes have a much more clearly defined substructure, Figure 4.23. The SANs are composed of highly oriented individual,  $\sim 2$  nm wide, fibrils that are bundled together within or on a thin film of unknown composition. Attempts to characterize the composition of the thin film with EDS were unsuccessful as beam irradiation caused almost immediate destruction and collapse of the film.

The width of the fibrils varies widely as it appears the individual  $\sim 2$ nm fibrils often come in pairs or triples, often twisting along the length of the fiber. Figure 4.24 shows a higher magnification STEM ZC image of a single C1 SAN as a clustering of twisting fibril ribbons that are likely composed of 2 -3 smaller fibrils. In this case the widest fibrils at the lower right are measured to both be 6.8 nm wide with the doublet  $\sim 18$  nm wide including the space between them.

STEM imaging of C3 and C5 SAN membranes after 1 week immersion was also performed. In the case of the C3 samples, no complete membranes were observed. It is believed that the majority of the membranes were destroyed when removed from solution. There were only a few individual instances of unsupported C3 SAN formation found intact on the entire sample. This low yield of SANs was also observed for the C5 1 week sample, but a few isolated SANs were found suitable for imaging in the STEM. Figure 4.25 are

STEM ZC images of C3 (a) and C5 (b) unsupported SANs. Such definitive fibril structures as seen in the C1 1 week SANs are not as clearly observed for the C3 and C5 1 week SANs, although there are indications of linear striping and layering along the lengths of the fibers.

#### **4.3.2.2. Measurement of C1 SAN Fibrils**

STEM Z-Contrast imaging of the C1 1 week SANs reveal them to have a distinctive fibril substructure with widths on the order of  $\sim 2$  nm. In an attempt to better quantify the fibril widths of multiple SANs, a Fast Fourier Transform (FFT) analysis technique was utilized. FFT analysis is a known powerful method for measurement of periodic structure in images. If the SANs exhibited constant fibril widths, they should show up as definitive spots along a direction perpendicular to the SANs length in the FFT image. The distance from the observed spot to the center of the FFT was then measured, corresponding to the inverse of the repeat distance. Specific regions within Figure 4.26, that exhibited highly parallel fibrils, insets A-D, were chosen for FFT analysis. Figure 4.27 details the procedure utilized to determine the fibril spacings for all four of the 128 x 128 pixel regions from Figure 4.26.

FFT filtering of the selected areas was carried out utilizing Reindeer Graphics Inc. (<http://www.reindeergraphics.com>), Image Processing Tool Kit 3.0, image processing filters for Adobe Photoshop. The FFT's of each of the regions show definite directionality with indications of discernable repeat distances (discernable spots) corresponding to specific fibril widths in the image. These spots are subtle, and appear to be strongest along a direction perpendicular to the length of the SANs. By application of slight, 1 pixel, Gaussian blurring and histogram stretching to the FFT image, individual spots were isolated. Complete analysis and indexing of the FFT of all the spots observed was out of the scope of this work,

so only the spots along the direction perpendicular to the SANs were utilized to quantify fibril widths. Since the FFT image is in reciprocal units, measurements made directly from the FFT image were converted back to real space values. A comparison of the widths obtained from each of the areas reveals a few correlations. 1.5 nm, 2.2 nm, and 4.9 nm appear at least twice between the four different selected areas. The smallest width was between 1.6 nm and 2.2 nm, but was difficult to definitively determine due to several experimental limitations. The limitations included low image resolution, electron beam astigmatism and fibril orientation relative to the beam axis, and possible beam damage of the SANs

#### **4.5.2.4. EDS of Individual C1, C3, and C5 SANs**

Semi-quantitative EDS analysis of C1, C3, and C5 unsupported SAN samples was performed utilizing a Hitachi HD-2000 STEM with a Noran Vantage EDS system. In each case the 3 week immersion sample of the C1, C3, and C5 was used for consistency with the XPS data, Section 4.2.2.1, as well as the analysis of thermal and mechanical stabilities presented in Chapters 5 and 6 respectively. Details of the sample preparation can be found in Section 3.3.3. All EDS data presented in this section was acquired with a 200KV accelerating voltage for 100 sec live time at a tilt angle of 12 deg towards the EDS detector to improve the signal to noise and to avoid any detected signal originating from secondary fluorescence of the aluminum coated  $\text{Si}_3\text{N}_4$ . A Gatan beryllium sample holder was used to avoid any possible aluminum contributions from the normal Hitachi sample holder. SANs for analysis were specifically chosen as close to the center of the membranes as possible to avoid any signal from the surrounding aluminum coated  $\text{Si}_3\text{N}_4$  support film. The nitrogen

signal was monitored during acquisition and in post processing as an indicator of X-ray contributions from the surrounding support film instead of solely from the SANs. To make sure that all the counted X-Rays were coming from the SANs, spectra with significant amounts of nitrogen were thrown out and new areas chosen.

Figure 4.28 shows three EDS spectra taken on single unsupported C1, C3, and C5 SANs respectively, showing the presence of carbon, oxygen, aluminum, silicon, phosphorus, and calcium in each case. Figure 4.29 (a) shows a STEM Z-Contrast image of a single C1 SAN and the acquired EDS spectrum, quantitative analysis, and calculated phosphorous:aluminum, carbon:phosphorous, and oxygen:phosphorous ratios Figure 4.29 (b), corresponding to the outlined area of the SAN shown in (a). More attention was paid to performing EDS of C1 SANs than for the C3, and C5 SANs, with 10 spectra acquired from C1 SANs, two spectra acquired from C3 SANs and one spectrum acquired from a C5 SAN. The results of the EDS are summarized in Table 4.3.

#### **4.3.2.5. STEM EELS of C1 SANs**

Electron Energy Loss Spectroscopy (EELS) was performed on unsupported C1 SANs grown for 3 week immersion time. STEM EELS utilizes a spectrometer to filter and count the incident focused beam electrons after they have passed through a specimen. The beam electrons are then energy filtered creating a spectrum of intensity (number of electrons) vs. energy loss (relative to the initial accelerating voltage). The detected energy losses correspond with specific electron sample interactions, such as phonons and core-shell ionizations[4.15]. EELS spectra have been utilized to determine not only the composition, but also the chemistry of materials with very high spatial resolutions of less than a nm[4.15].

Unlike EDS, which has issues related to secondary fluorescence, EELS information is highly localized to the exact area of the sample irradiated by electrons. Due to the recent advancements in parallel acquisition spectrometers, EELS data collection has become far less tedious than with older scanned slit spectrometers. Since EELS is still undergoing rapid development its implementation has mostly been limited to research institutions for investigation of well known material systems. One of the main issues with EELS is the fact that the technique creates data in the presence of high background counts, meaning that the signal to noise ratios are typically low and correct background modeling is a necessity if the desired function is to perform quantitative elemental analysis[4.16]. This means that for samples of unknown composition it is even more difficult to perform quantitative elemental analysis because the background shape is not well understood.

However, qualitative analysis of an unknown sample is fairly straight forward, allowing for determination of the both the elements present as well additional information pertaining to the bonding or local chemical environment of the elements within the structure. The determination of composition is done by identifying the ionization edges and comparing them with the energies of known edges of materials. Understanding the local chemistry of that element can possibly be deduced by examination of the ionization edge near edge structure[4.15]. Typically, the valence shell ionization edge carries this information as it is the valence electrons that are involved in bonding between elements. For instance in the case of the aluminum L<sub>2,3</sub> edge, there are drastic differences in the edge shape for aluminum metal versus aluminum in Al<sub>2</sub>O<sub>3</sub>[4.17]. The bonding of the aluminum to the oxygen in the Al<sub>2</sub>O<sub>3</sub> has a higher energy associated with it thus shifting the onset of the edge to higher energy values as well as changing the shape of the near-edge structures as it relates to the

different types of bonding occurring. It has been shown that even the coordination (tetrahedral vs. octahedral) of aluminum in  $\text{Al}_2\text{O}_3$  can be determined by use STEM EELS when very high resolutions and low dispersions are utilized[4.18]. Data collected with EELS, like XPS, are both rich in information about the bonding and chemistry within a sample, but STEM EELS has advantages over XPS for correlation of chemical bonding information with localized structure imaging. However, together one can directly compare the results from XPS with STEM EELS to confirm the composition as well as bonding within APA SANS.

EELS data was acquired utilizing a JEOL 2010F Field emission scanning transmission electron microscope (STEM) fitted with an ultra high resolution pole piece and Gatan Imaging Filter. All spectra were obtained while operating the microscope in STEM mode at 200 keV. The energy resolution achieved for these experiments was 1.8 eV as measured from the FWHM of the zero-loss energy peak acquired in vacuum. This resolution is not high enough for aluminum coordination determination, but edge onset and overall shape determination was possible. Spectra were acquired utilizing an energy dispersion of 0.3 eV per channel were acquired by scanning a 5 nm x 5 nm areas of single and overlapping SANs. The convergence and collection semi-angle, 10 mrad and 16 mrad respectively, were used in this study and allowed collection of sufficient amount of electrons increasing the Signal to Noise Ratio (SNR). Processing and plotting of EELS spectra was done utilizing Gatan Digital Micrograph software.

Approximately 20 EELs spectra were acquired from different C1 SANs from the same sample. Figure 4.30 shows a STEM Z-Contrast image acquired of a representative area of overlapping C1 SANs. An “X” marks the location of a 5 nm x 5 nm area where a single

EELS analysis was performed. The raw data from that EELS analysis (blue) are presented in Figure 4.31. A power law background (red) was applied to a 10 eV window of the raw data 5 eV before the observed aluminum edge onset. The resulting aluminum background corrected spectrum, plotted in green, shows the presence of aluminum, phosphorus, and carbon L edges. Figure 4.32 shows the power-law background corrected aluminum and phosphorus  $L_{2,3}$  edges from Figure 4.31. Here one sees that in both cases, the aluminum and phosphorus have very interesting near edge structures which undoubtedly relate to their chemical environments. To fully understand the significance of these peak shapes, further EELS analysis would be required. EELS spectra were also acquired over a different energy range needed to observe the oxygen L edge.

A comparison of the aluminum  $L_{2,3}$  edge from the C1 SAN with that of aluminum metal and  $Al_2O_3$ [4.17] is seen in Figure 4.33. In this case we find that the C1 SAN L edge onset of  $\sim 75$  eV is nearly the same as the alumina. The shape of the C1 SAN L edge while slightly different than the alumina is more similar to the Alumina than that of the metallic Al.

The aluminum present in the C1 SANs appears to be in an oxygen environment as opposed to an elemental aluminum one. This was also the case for the Phosphorus as the  $L_{2,3}$  edge onset is  $\sim 135$  eV as seen in Figure 4.32. These values of 75 eV for aluminum and 135 eV for are in good agreement with the binding energies observed with XPS of C1 SANs on  $Si_3N_4$ , from Section 4.2.2.1. EELS spectra, not shown, also showed the presence of both oxygen and Ca in the C1 SANs as previously observed with EDS of the same sample and reported in Section 4.3.2.4. The correlation between EELS and XPS evaluation of C1 SAN chemistry provides very strong evidence that both the aluminum and phosphorus are in an oxygen environment.

While the initial EELS analysis presented here confirms the presence of aluminum, oxygen, phosphorus, carbon, and calcium in the C1 SAN structure, further STEM EELS analysis would be required to more fully understand the chemistry, such as the coordination of the aluminum, within the individual SANs. Further optimization of analysis parameters as well as utilization of a STEM EELS system with an increased energy resolution of 0.3-0.5 eV would be needed for the determination of the coordination of aluminum[4.18]. Further understanding of the aluminum coordination along with that of the phosphorus and oxygen could provide a novel route to nanometer level structure and chemistry correlation.

#### 4.4. Discussion

C1 SANs grown on aluminum coated glass slides were examined using AFM and SEM. C1 SANs after 28 days of growth exhibited an approximate 50:1 length to width ratio, branching, and often randomly placed nodular surface features. Examination of aluminum surfaces immersed for longer times, 84 days, showed that the largest SANs occur on the outer most surface, with smaller, thinner SANs forming a complete mat. AFM phase imaging provided evidence that the SANs have a different composition and mechanical properties than the surrounding precipitates and underlying aluminum film. This finding is in agreement with the observed lower melting temperature for the precipitates as described in Chapter 5.

High resolution AFM and SEM images of the SANs' reveal surface features that are indicative of complex internal structuring and in some cases of possible internal crystal structure. SEM images taken of the same areas using different accelerating voltages revealed the presence of sub-surface pitting, an indication that corrosion of the aluminum film was occurring due to exposure C1. XRD of an aluminum coated glass substrate subjected to a 1 year immersion in a solution of C1 and EtOH exhibited defined peaks corresponding to an unknown crystalline phase not observed for similar aluminum coated glass slides exposed to pure EtOH and air for the same amount of time. Additionally, the main XRD peak for the metallic aluminum was present on the two samples exposed to air and pure EtOH, but absent on the sample treated with C1 providing strong evidence that the aluminum is indeed corroded or converted and that the structure of the SANs is in a large part due to the influence of the aluminum.

In an effort to effectively determine the composition of the C1 SANs alone, specialized growth techniques as described in Chapter 3 were developed. The discovery that SAN growth was not isolated to the aluminum surface allowed to SAN deposition onto substrates with controlled composition. C1 SANs were grown on clean  $\text{Si}_3\text{N}_4$  thin film TEM substrates in an effort to directly correlate the composition and structure of the SANs utilizing AFM and SEM with EDS. EDS analysis of the  $\text{Si}_3\text{N}_4$  substrate before and after immersion in a C1 solution on top of an aluminum coated glass slide revealed the formation of a continuous C1 SAN mat along with the presence of aluminum to the previously aluminum free  $\text{Si}_3\text{N}_4$  surface.

XPS and AFM analysis of C1, C3, and C5 SANs grown on  $\text{Si}_3\text{N}_4$  coated Si substrates again confirmed the solution transport of aluminum as well as correlated the presence of aluminum along with SAN surface coverage on previously aluminum free surfaces. Semi-quantitative elemental analysis gave phosphorus:aluminum ratios of 2.6, 4.2 and 3.2 for C1, C3, and C5 SANs respectively. Additionally, the measured binding energies for both the aluminum and phosphorus peaks were indicative of oxygen environments. All indications were that none of the detected aluminum was in metallic form.

Tapping mode AFM under high damping conditions of C3 and C5 SANs provided evidence of a layered fibril substructure. Additionally, a 1 – 2 nm corrugated structures were observed for both C3 and C5 SANs. STEM examination of FIB cross-sections through C1 SANs revealed their internal atomic structure as similar to the underlying amorphous  $\text{Si}_3\text{N}_4$ . Few indications of ordered internal structures were observed even utilizing Z-contrast. Possible faceting was observed on the outer surface of several SANs in contact with the overlying poly crystalline copper. Copper was utilized to prevent any EDS peak overlaps

with aluminum and phosphorus which are prevalent when utilizing platinum or gold. Semi-quantitative elemental EDS analysis of nine cross-sections provided an average phosphorus:aluminum ratio of 2.11

Novel free-standing unsupported C1, C3, and C5 SAN membranes were created by the immersion of aluminum coated ProtoChips<sup>TM</sup> DuraSIN<sup>TM</sup> meshes into solutions of C1, C3, and C5 and EtOH and examined with STEM, EDS, and EELs. Longer immersion times produced thicker and more robust membranes having highly complex multi-layered fibril substructures. Z-contrast imaging of C1 SAN membranes after shorter immersion times of 1 week revealed that individual SANs were composed of much smaller fibrils. The fibrils were often observed to form ribbon like structures composed of 2 – 5 fibrils often twisting along their long axis. FFT analysis of images determined the smallest fibril widths to be from 1.5 – 2 nm wide. Semi-quantitative elemental EDS analysis of individual SANs found average phosphorus:aluminum ratios of 2.41, 1.94, and 1.5 for ten C1 SANs, two C3 SANs, and one C5 SAN respectively.

Looking to the literature for comparison, there are a growing number of reports detailing the growth and characterization of metal-phosphonate inorganic-organic hybrid materials. These new materials, having large surface areas and controllable mesoporosity, are attracting more attention for use as catalysts and molecular sieves. Phosphonates created with metals such as zirconium have been successfully reported to exhibit layered structures[4.19-22] with applications for fuel cell technology. Aluminum phosphonates are becoming more widely studied as well and are observed to form layered structures[4.23, 24] or as in the case of aluminummethylphosphonate (AlMePO)[4.25, 26] are reported to have long one-dimensional channels lined with methyl groups. The phosphorus:aluminum ratios reported for aluminum

phosphonates are typically between 1 and 3[4.24-31]. Although the composition and chemistry of the APA SANs and the various aluminum alkylphosphonates are similar there is a major difference in how they are produced. The majority of metal phosphonates are produced by reacting an aluminum salts or aluminum alkoxide with an alyklphosphonic acid under hydrothermal processing conditions that are carried out at fairly high temperatures in aqueous solutions. This results in much larger amounts of single crystalline material suitable for x-ray diffraction and crystal structure determination as compared to the small amounts of APA SANs created through immersion of aluminum metal in ethanolic solutions.

In the case of the SANs, only the C1's phosphorus to aluminum ratio as determined by EDS and XPS was within the as reported P:aluminum range of 1-3. Considering that the XPS analysis was performed over a 3 mm diameter area of the sample, it is highly likely that the phosphorus signal might be elevated due to residues of C1, C3, or C5 remaining on the surface. There is further evidence of a contamination film is observed in STEM imaging of unsupported nanofiber membranes.

There is also a report in the literature of a micelle templated growth mechanism for the creation of aluminum hydroxide (AlOOH) nanotubes and nanorods[4.32, 33]. The AlOOH structures are believed to form within surfactant bilayers or cylindrical micelles, nucleating along the headgroup-headgroup interfaces. This type of surfactant templated growth has also been utilized for the creation of silicate based material with controlled porosity and is considered a viable route to the formation of novel mesoporous materials[4.34].

One of the main drawbacks to successfully utilizing highly localized nanoanalysis for characterization of materials is that during the course of analysis the material is often changed simply due to the analysis itself. This was very much the case when utilizing

electron microscopy such as STEM to examine unsupported SANs. There was clear evidence of sample damage and contamination due to beam interactions. This made it difficult to examine any one area for very long without causing changes to the structure as well as the composition. This made quantitative elemental EDS analysis very challenging, especially for the carbon and oxygen since both are common surface contaminants. Without understanding the exact composition of the SANs it was impossible to distinguish whether the formation of the SANs was occurring as a type of -O-Al-O-P- polymer or whether AlOOH nanorods were being templated by the APAs. Without definitive crystal structure information it was impossible to distinguish between the two structures.

STEM EELS analysis was performed to try and further distinguish the true structure of the APA SANs. EELS core loss analysis definitively determined the presence of O, C, P, and aluminum to within the structure of overlapping unsupported C1 SANs which was in good agreement with the EDS findings. Additionally, examination of the aluminum L<sub>2,3</sub> edge provided an onset energy of 75 -76 eV which was more indicative of an oxygen environment. Unfortunately, the spectrometer resolution of 1.8 eV was too low to definitively determine the coordination of the aluminum as tetragonal or octahedral, which may have helped to further distinguish the chemical structure of the SANs.

APA SANs have a layered fibril morphology which becomes more complex for longer growth times exhibit a 50:1 length to width ratio as measured by SEM. They are composed of oxygen, carbon, phosphorus and aluminum as determined by EDS, XPS, and EELS analysis. XPS and EELS further correlated the presence of aluminum and phosphorus within a group of overlapping C1 SANs. The EELS and XPS data proved strong complimentary evidence that both the aluminum and the phosphorus present in the SANs is non-metallic and

most likely bonded with oxygen. It is believed that the novel SANs are either Aluminophosphonate polymers or APA templated aluminum hydroxide nanorods. It was impossible to definitively determine whether or not the detected oxygen was bonded to both aluminum and phosphorus with either EDS or STEM EELS, but it should be possible to be determined with further experimentation utilizing STEM EELS.

## 4.5. Figures

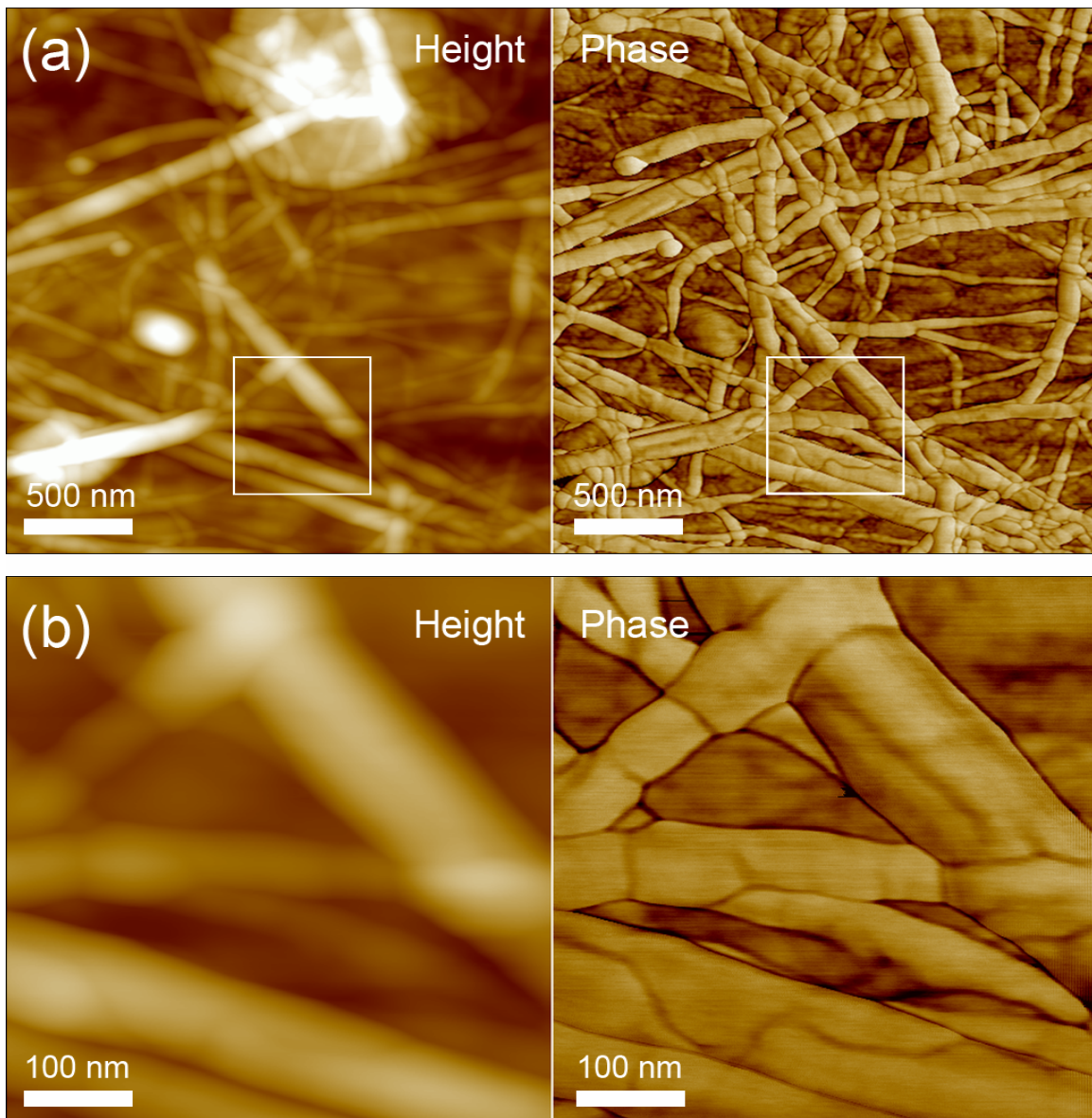


Figure 4.1. C1 nanofibers grown on aluminum. AFM tapping mode images with 150 nm z range. 2000 nm (a) and 500 nm (b) height and phase image pairs. Olympus tapping cantilever.

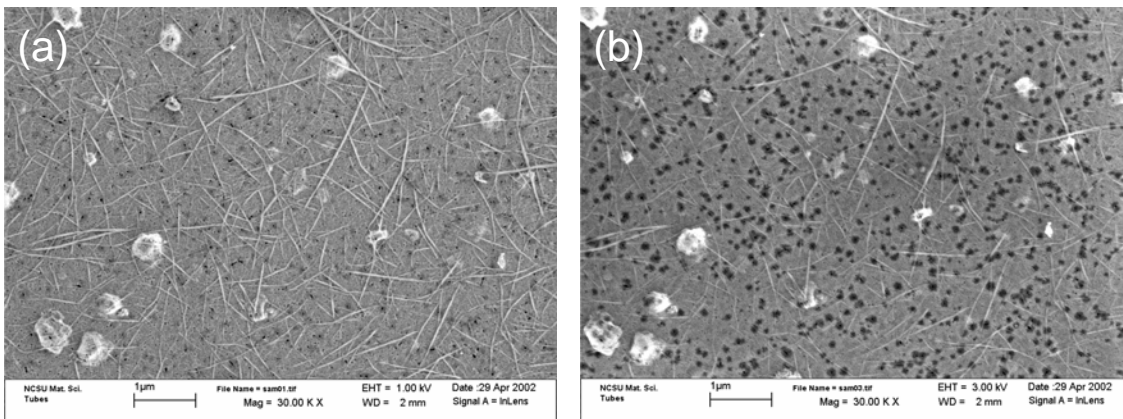


Figure 4.2. Two FE-SEM Images taken of the same area of the same 28 day immersion sample at two different accelerating voltages: 1.0 kV, image (a), and 3 kV, image (b). The increased dark contrast using 3 kV reveals the presence of sub-surface corrosion pits.

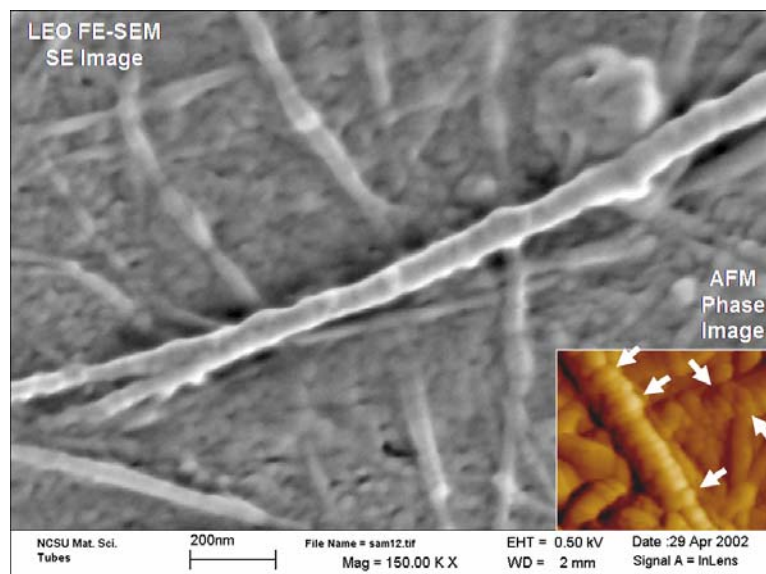


Figure 4.3. A comparison between LV-FESEM and AFM tapping mode phase (inset) images of the same C1 nanofibers sample showing similar nodular features present along the length of the fibers. The images are the same scale.

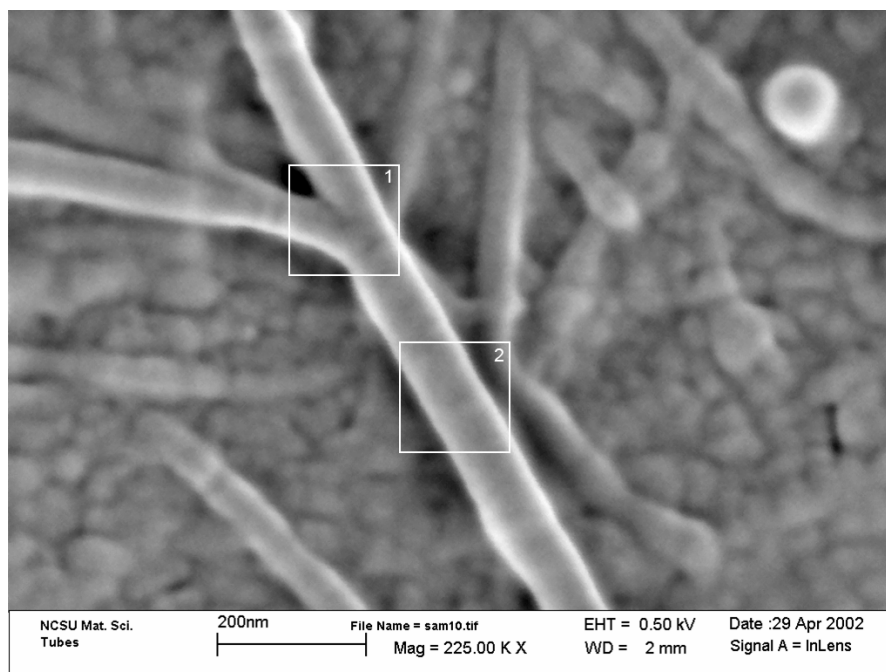


Figure 4.4. Low voltage FE-SEM image of a single large C1 nanofiber from the same 84 day sample as imaged in Figure 2. The use of a very low accelerating voltage, in this case 500V improves the surface detail at high magnification while minimizing damage to the nanofibers. This image confirms that the fibers do indeed branch and Inset 1 denotes triangular surface defect structures associated with the branching. Inset 2 denotes another possible defect structure along the length of the fiber. Unfiltered image with histogram stretch to increase contrast of fibers.

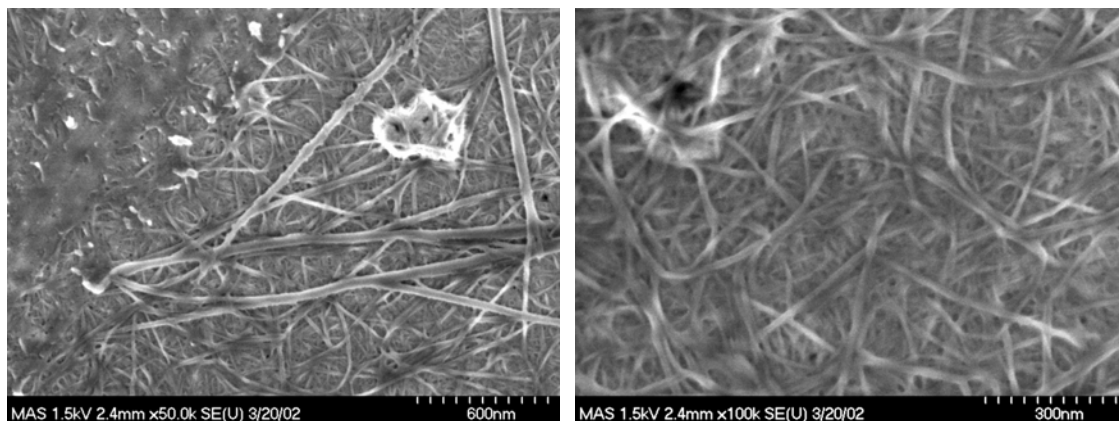


Figure 4.5. FE-SEM images of the surface of an evaporated aluminum surface after immersion in 8.3 mM C1/EtOH solution for 84 days. Image (a), is essentially the same field of view as the 2  $\mu$ m AFM image in Figure 1 (a) and shows the multi-layered character of the nanofabric. The nanofiber morphology is very similar to the AFM images although there appears to be a bit better edge details with the SEM. Image (b) show the details of one of the precipitates as it appears to be a highly defected clump of nanofibers. Images were histogram stretched and a slight, 1 px, Gaussian blur applied to increase the contrast and reduce noise.

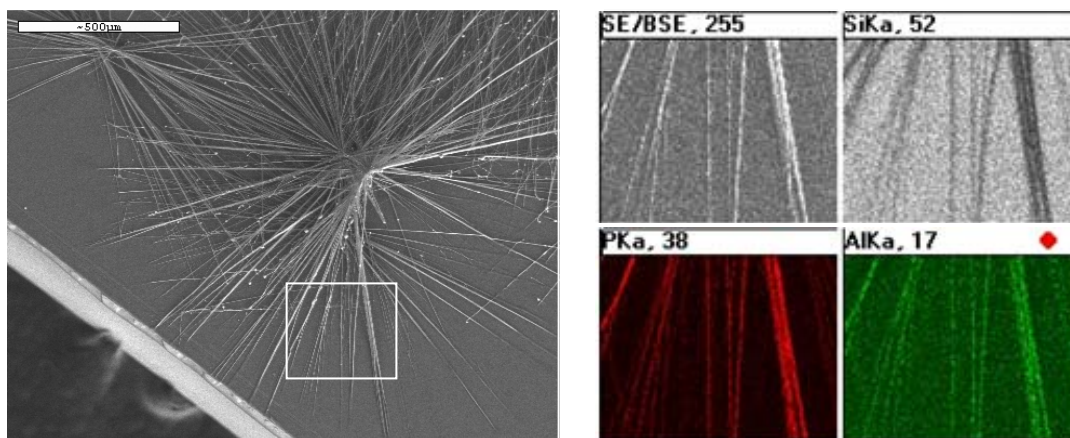


Figure 4.6. SEM image and EDS mapping of C1 microfibers formed after immersion of an aluminum coated glass slide in a 83 mM C1/EtOH solution for 19 days. EDS mapping shows that the aluminum and phosphorus are highly localized to the fiber structures.

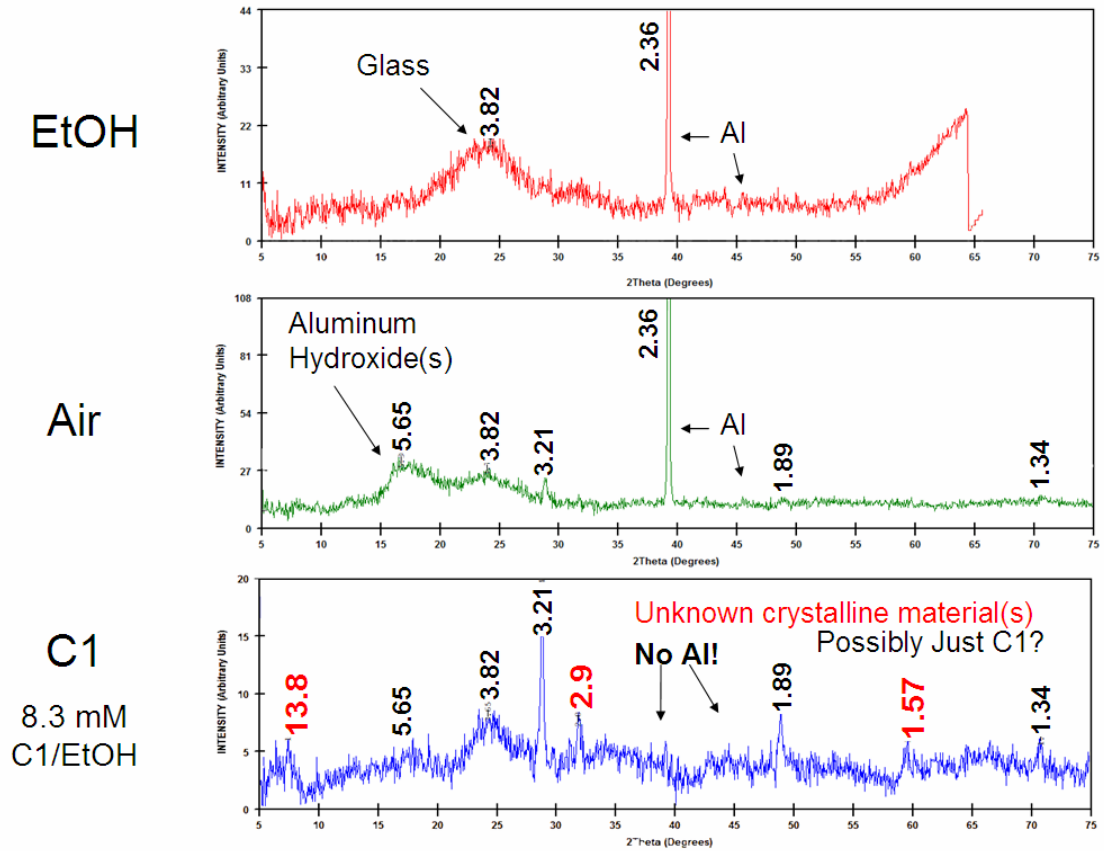


Figure 4.7. XRD results from aluminum films after 365 day exposures to: immersion in EtOH, air, and immersion in an 8.3 mM solution of C1 in EtOH.

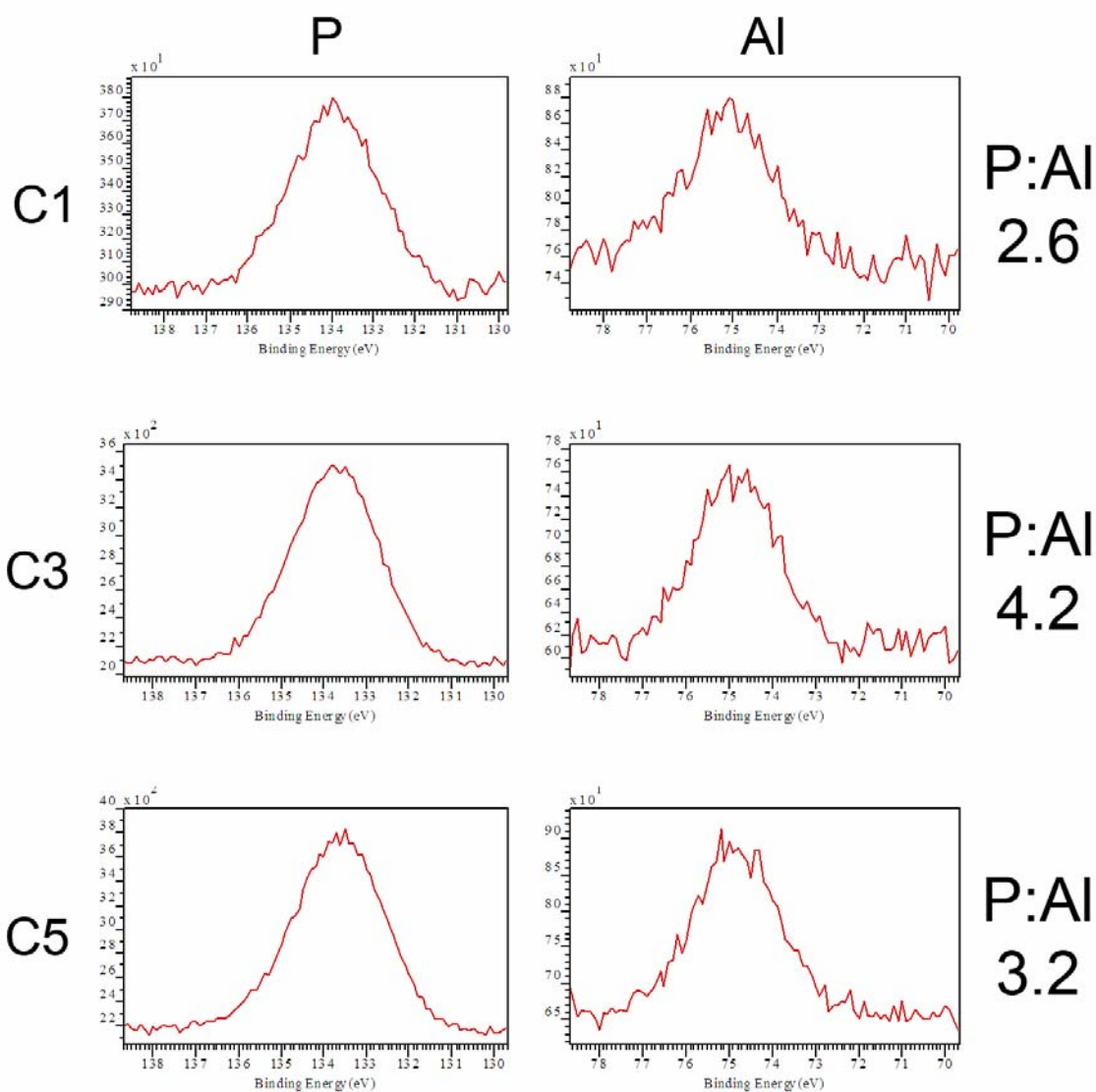


Figure 4.8. XPS phosphorus 2p and aluminum 2p data from C1, C3, and C5 nanofibers grown on Si<sub>3</sub>N<sub>4</sub>. Showing the phosphorus to aluminum ratio as explained in 4.2.2.1.

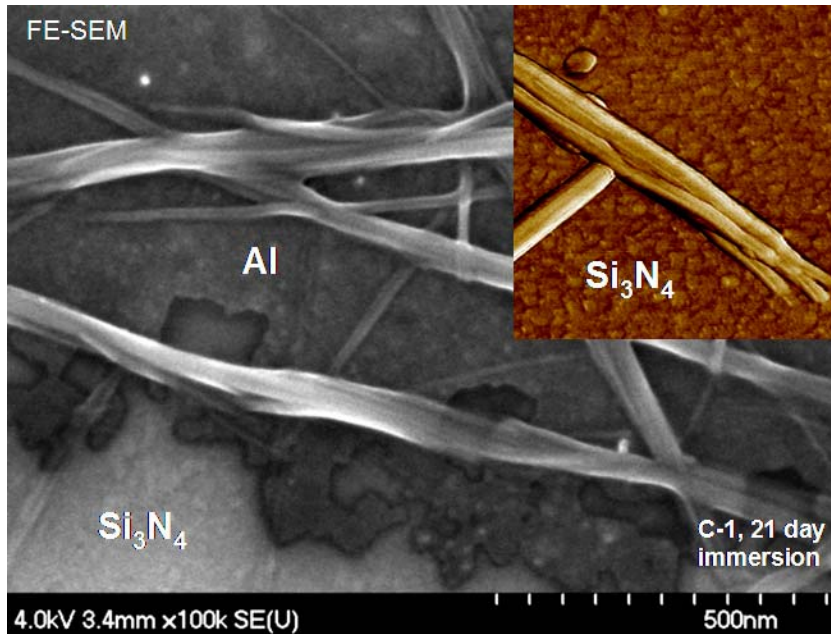


Figure 4.9. A comparison of C1 SAN fibril morphology observed with FE-SEM and AFM. The FE-SEM image shows the formation of SANs as well as the corrosion of the aluminum film at the interface with the underlying  $\text{Si}_3\text{N}_4$  film after immersion for 3 weeks. The inset is a tapping mode phase image of C1 SANs (inset) at the same scale as the FE-SEM image. Both images are of the same sample, taken from different regions of the sample.

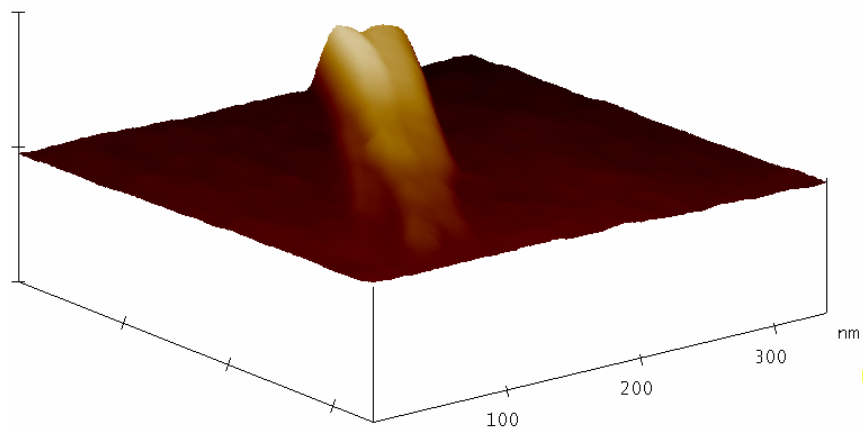


Figure 4.10. 3D image of the same C1 SAN shown previously in Figure 8. Here we can see the fibril morphology of the fibrils are not parallel to the substrate surface but instead are layered at  $\sim 30$  deg angle. 50 nm Z scale.

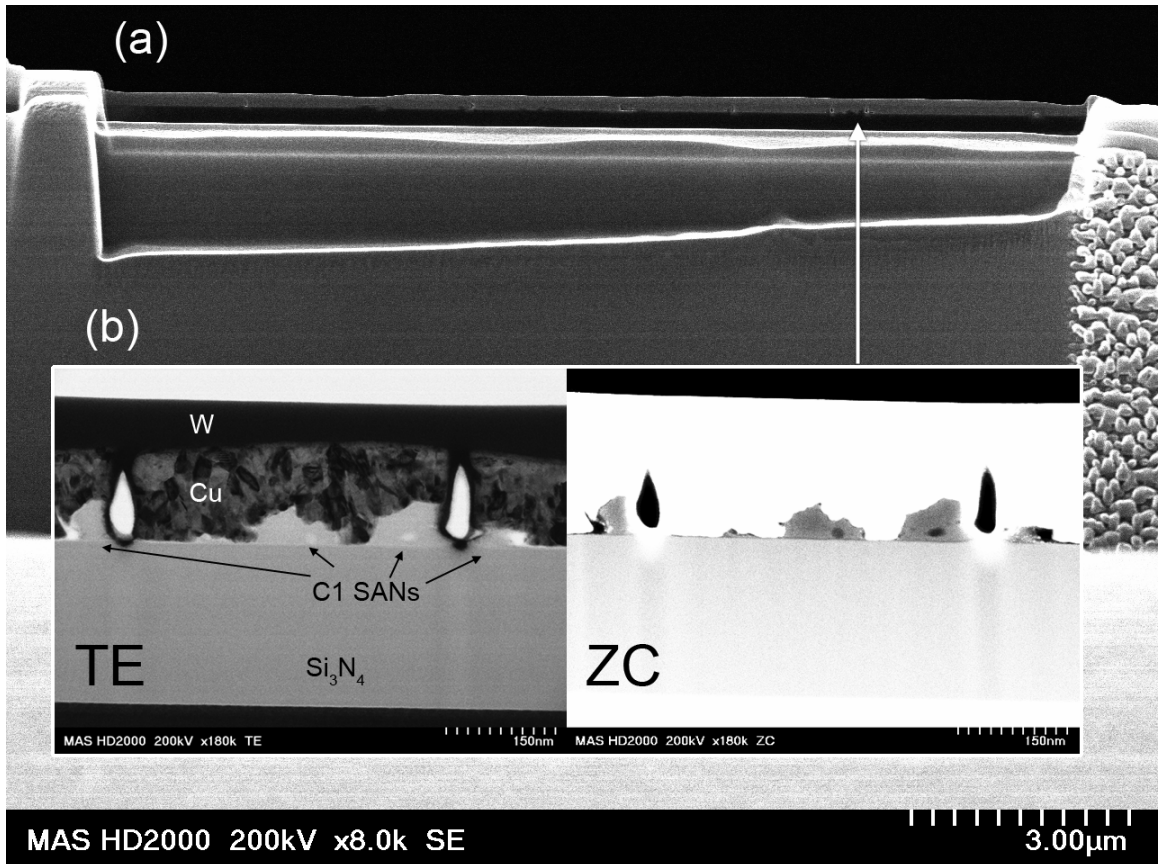


Figure 4.11. FIB Cross-section through individual C1 SANs on Si<sub>3</sub>N<sub>4</sub>. Image (a) shows an overview SE image of the entire cross-section. Inset (b) shows higher magnification TE and ZC images of the same group of C1 SANs.

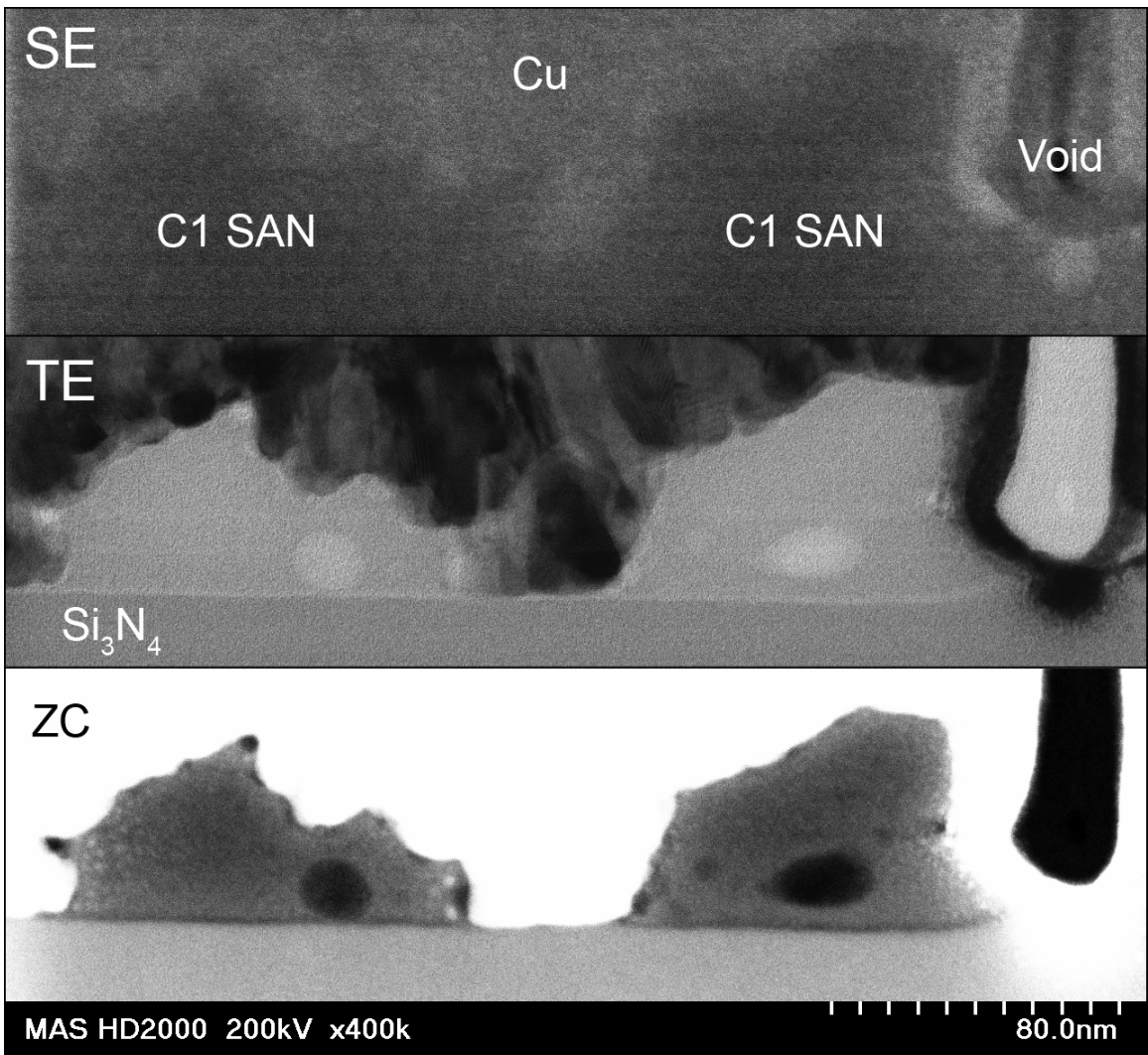
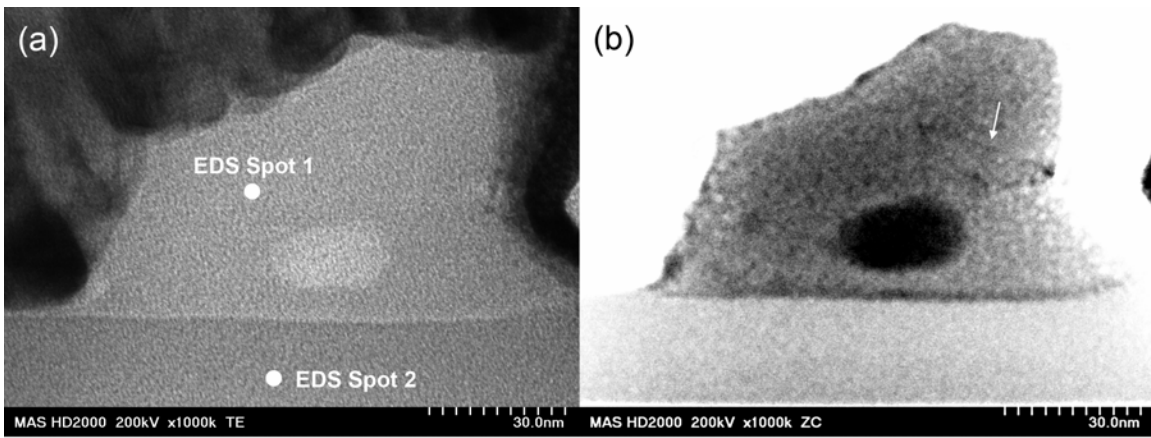
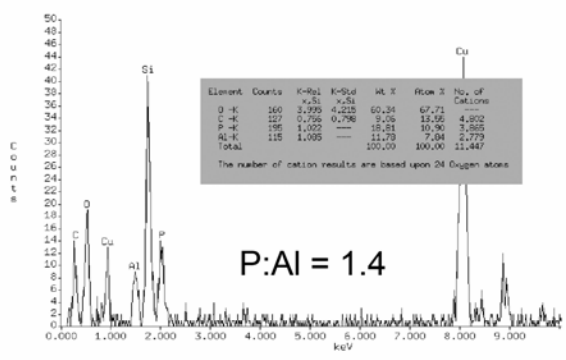


Figure 4.12. Higher magnification SE, TE, and ZC STEM images of two copper coated C1 SANs on Si<sub>3</sub>N<sub>4</sub>.



(Spot 1 - C1 SAN)



(Spot 2 - Si<sub>3</sub>N<sub>4</sub>)

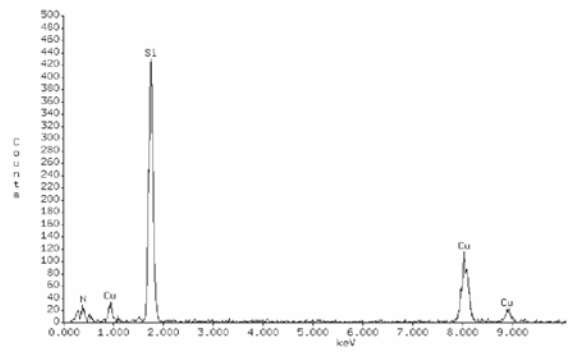


Figure 4.13. A 1000 KX TE (a) and ZC (b) images of a single Cu coated C1 SAN on Si<sub>3</sub>N<sub>4</sub>. The arrow in (b) denotes interesting geometric feature observed within the SAN. EDS analysis was performed on the C1 SAN at the spot denoted in (a) and the results shown (c). The results of a semi-quantitative EDS analysis are shown in (d).

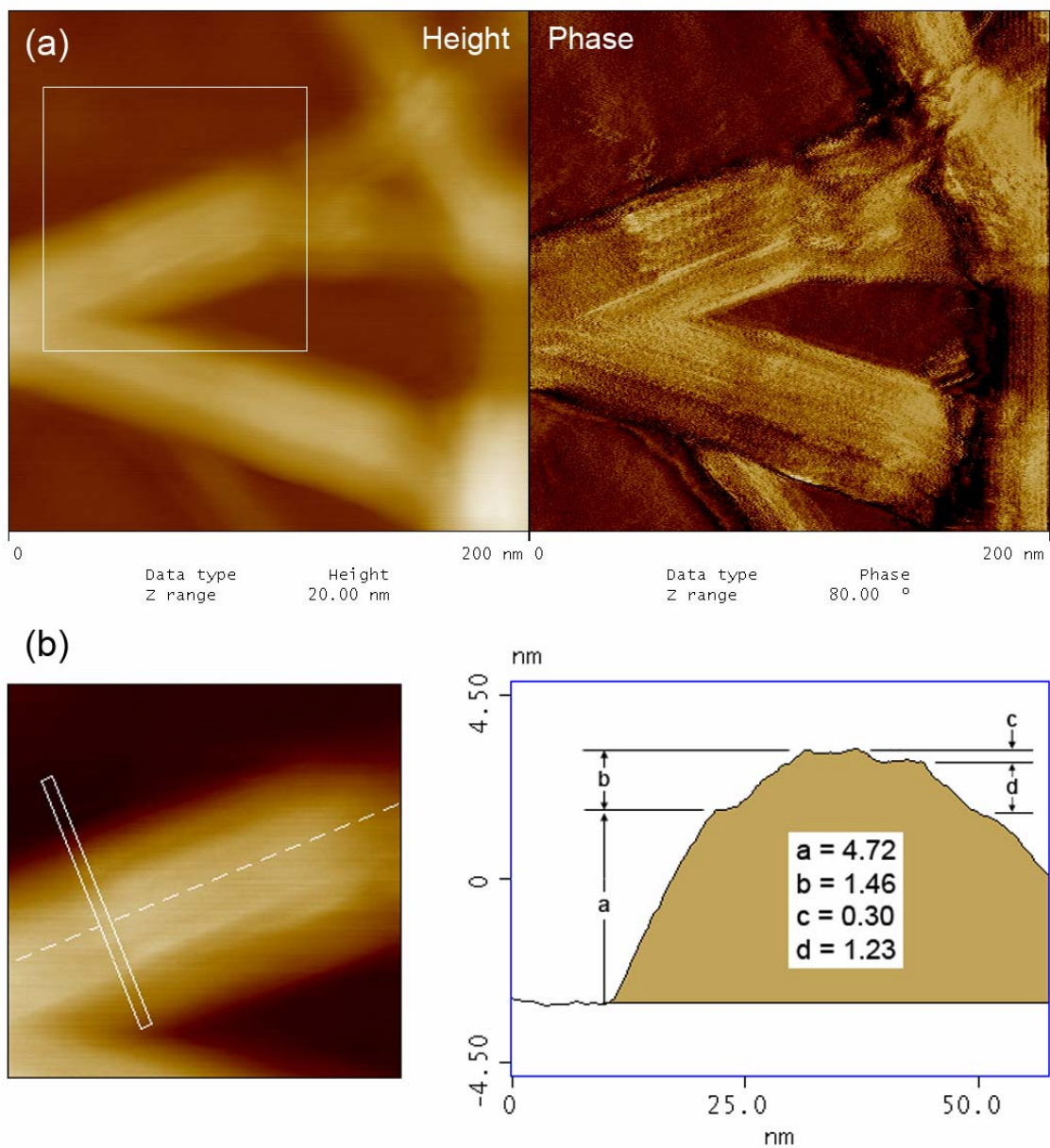


Figure 4.14. AFM tapping mode height and phase images of a C3 3 week SAN, image (a). The images were acquired utilizing very high damping of a force modulation cantilever ( $k \sim 4 \text{ N/m}$ ) at 2.5 Hz scan rate. Observation of fibrils and cross-sectional analysis of the observed layered fibrils, image (b).

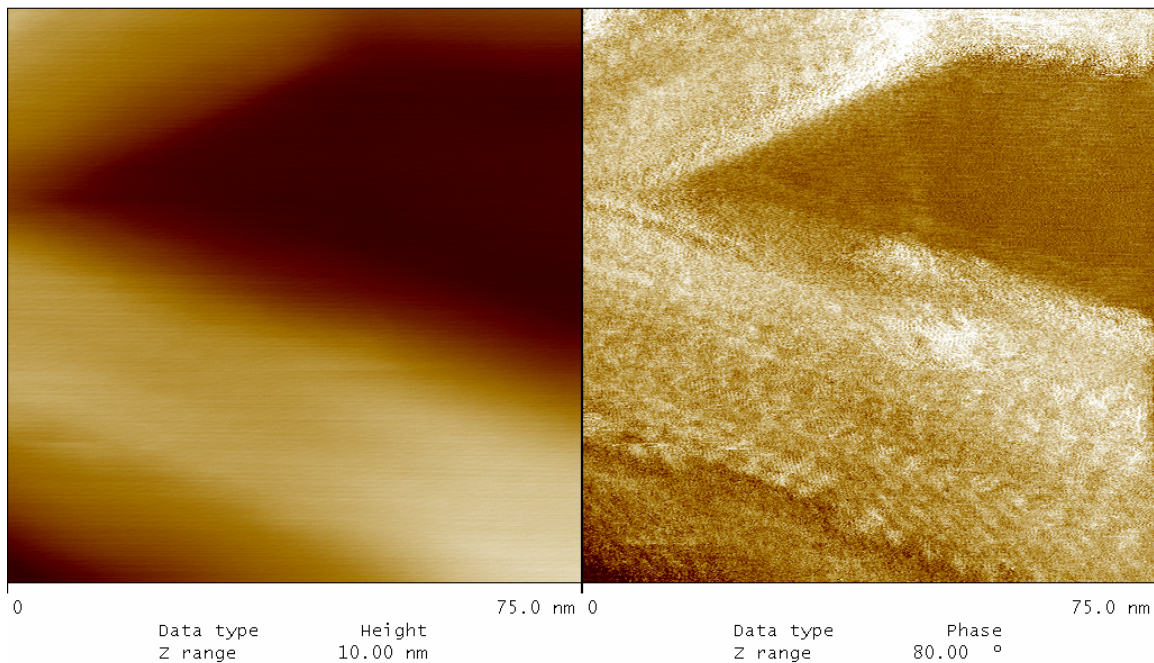


Figure 4.15. Higher magnification AFM tapping mode height and phase images of C3 SAN from Figure 8 image (a). This image was taken using the same scan parameters as the image in Figure 8 and was the next image in sequence showing that the sub-fiber corrugations scale with scan size and there is good correlation between the features seen in Figure 9 with those observed in the previous scan in Figure 8 image (a) indicating repeatability between scans.

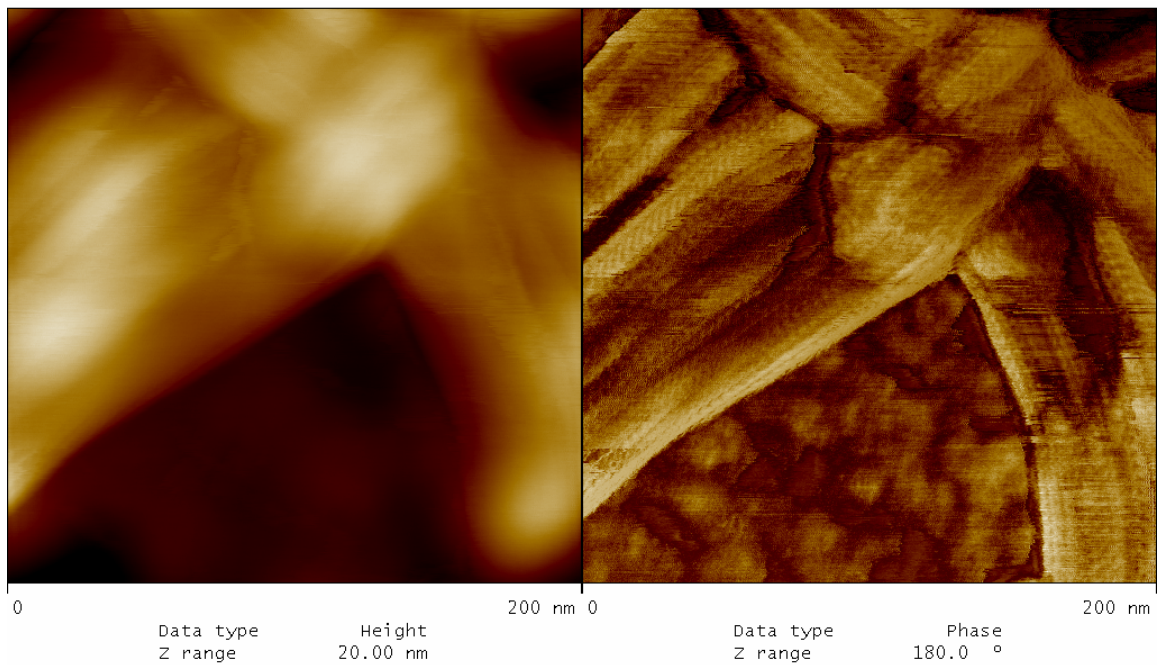


Figure 4.16. High damping tapping mode AFM height and phase image of a C5 SAN on  $\text{Si}_3\text{N}_4$  showing evidence of an oriented corrugated molecular substructure.

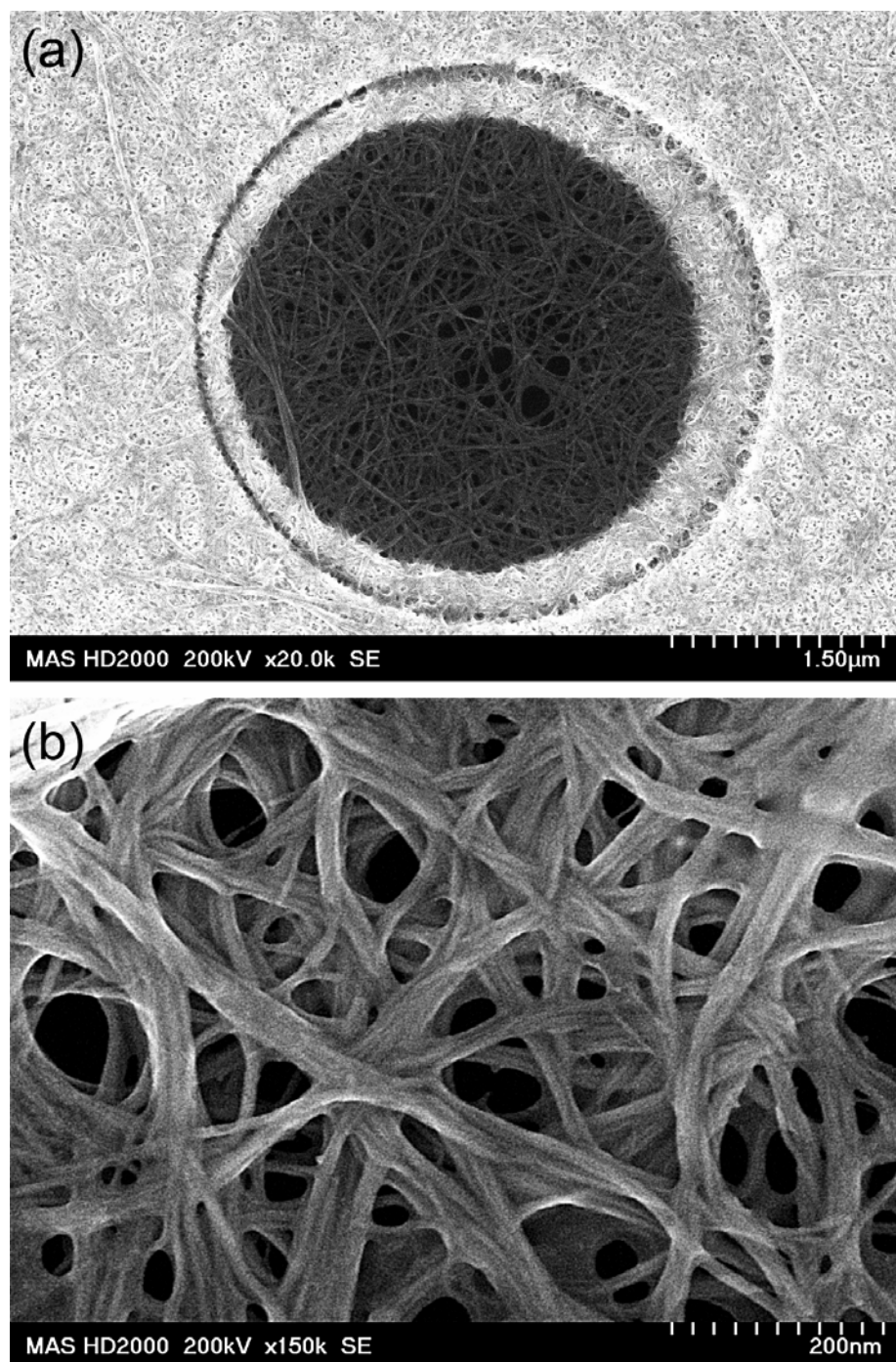


Figure 4.17. STEM SE images of unsupported 4 µm C1 nanofiber membranes after immersion of an aluminum coated ProtoChips™ DuraSiN™ membrane in 8.3 mM C1/EtOH solution for 42 days. Image (a) shows the overall morphology of an individual membrane. Image (b) shows a higher magnification of an edge region of a different membrane showing the complex layering, sub-fiber detail, and residual webbing between certain fibers. Images histogram stretched and slightly Gaussian blurred to improve contrast and reduce noise.

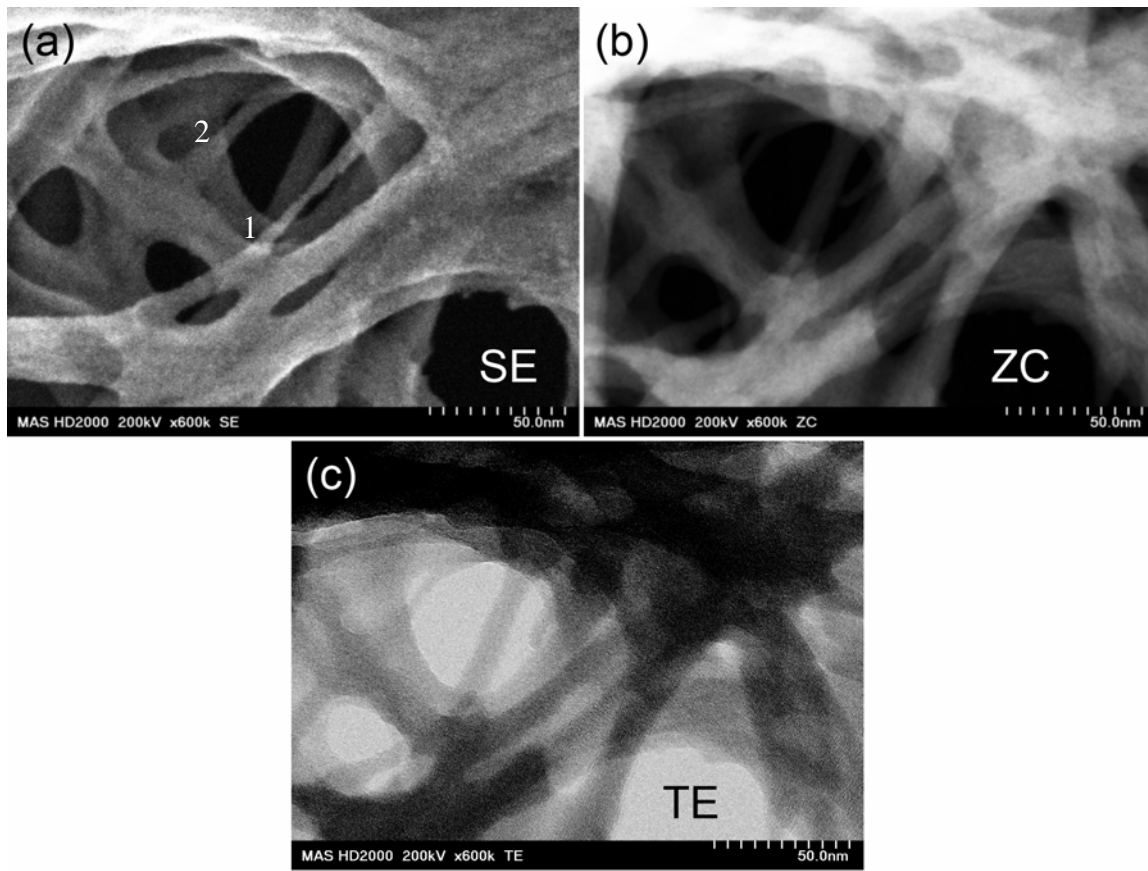


Figure 4.18. A Secondary Electron (SE) (a), Z - Contrast (ZC) (b), and Bright Field (TE) (c), images of the same region of nanofibers in a C1 membrane. The SE image provides surface details while the ZC and TE images provide information about the internal structures. These are also sequential slow scans and the effect of the beam on the smallest fiber (1) in the center of (a) can be seen in (b) and (c) as it breaks due to beam interactions. It is also of interest to note the increased nanofiber widths (2) in the SE image vs. ZC and TE hinting at possible surface structural differences. Raw images with slight 1 px Gaussian blurs.

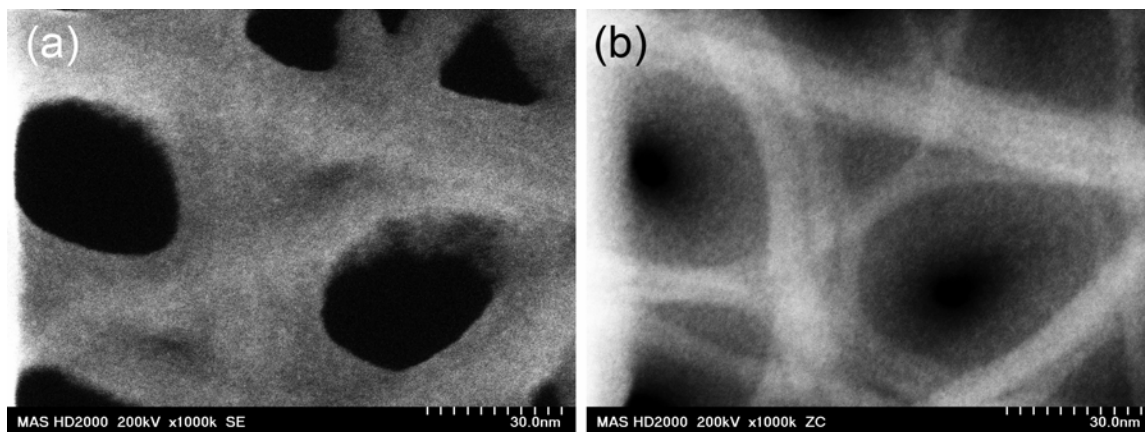


Figure 4.19. Sequential SE (a) and ZC (b) images taken of the same group of C1 nanofibers, 42 day growth. Some type of contamination coating or surface film is clearly evident in comparing the SE (a) the ZC images (b). Raw images with slight histogram stretching.

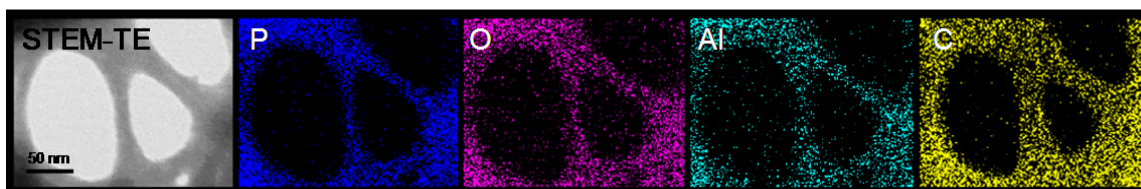


Figure 4.20. STEM TE image of a C1 nanofiber cluster and the corresponding EDS mapping of P, O, Al, and C. The Mapping provides further evidence of a carbon surface layer is seen as increased fiber widths in the carbon map compared to the P, O, and aluminum maps.

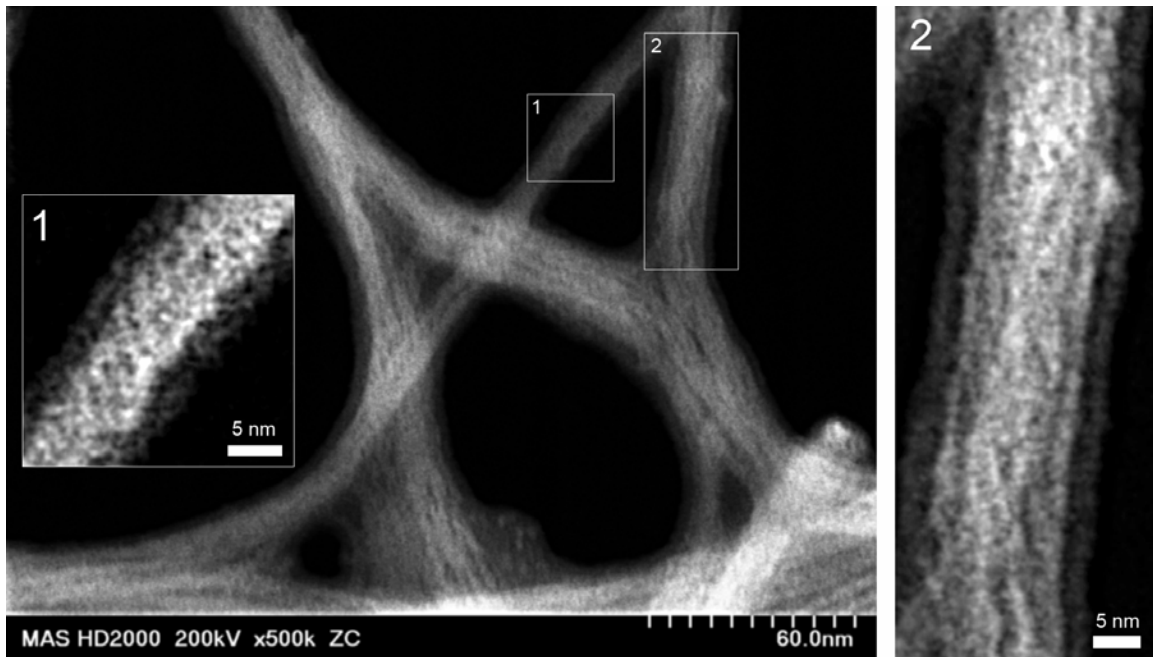


Figure 4.21. STEM ZC image with insets showing indicating the presence of both bundled fibrils and layered structures within nanofiber cores. Inset 1 and 2 are digital zooms of two fibers showing markedly different structures. The images have been histogram stretched, slightly Gaussian blurred and unsharp-masked to increase the contrast of the central nanofiber core structures.

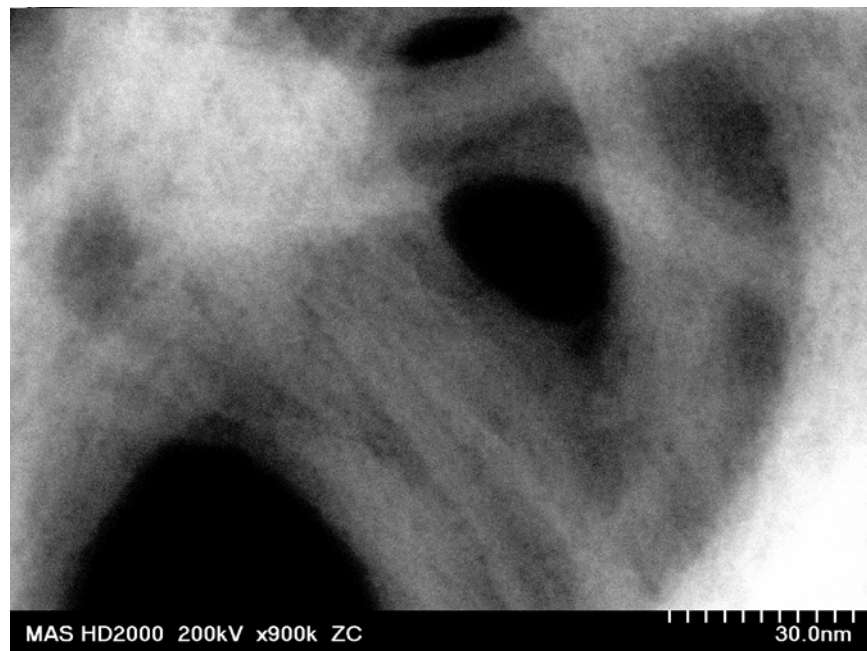


Figure 4.22. STEM ZC image of overlapping nanofibers showing evidence of fibrils and layering within individual nanofibers. Unfiltered image with only slight histogram stretch and gamma correction to increase contrast.

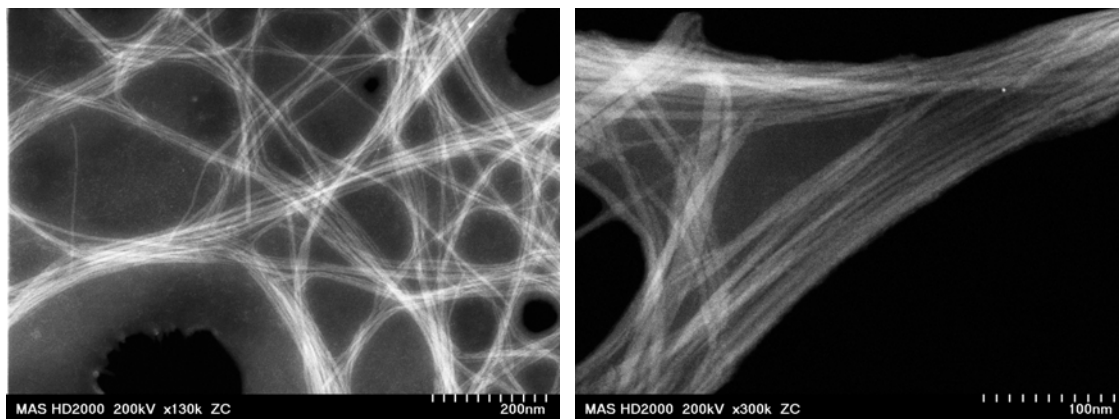


Figure 4.23. STEM ZC images of C1 1 week SAN membrane showing how individual SANs are composed of bunches of fibrils that vary in width from  $\sim 5 - 20$  nm wide.



Figure 4.24. STEM ZC image of an individual C1 SAN showing the internal fibril substructure. The fibrils appear to have a ribbon like morphology and are observed to twist along their lengths.

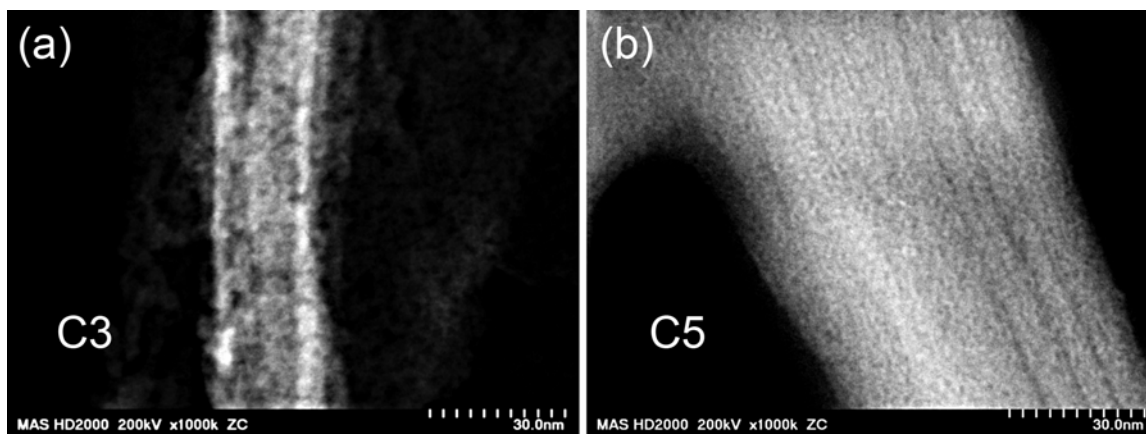


Figure 4.25. STEM ZC images of C3 (a) and C5 (b) SANs after 1 week immersion. In both images there is evidence of fibril structures within the C3 and C5 SAN, but are less definitive than with C1.

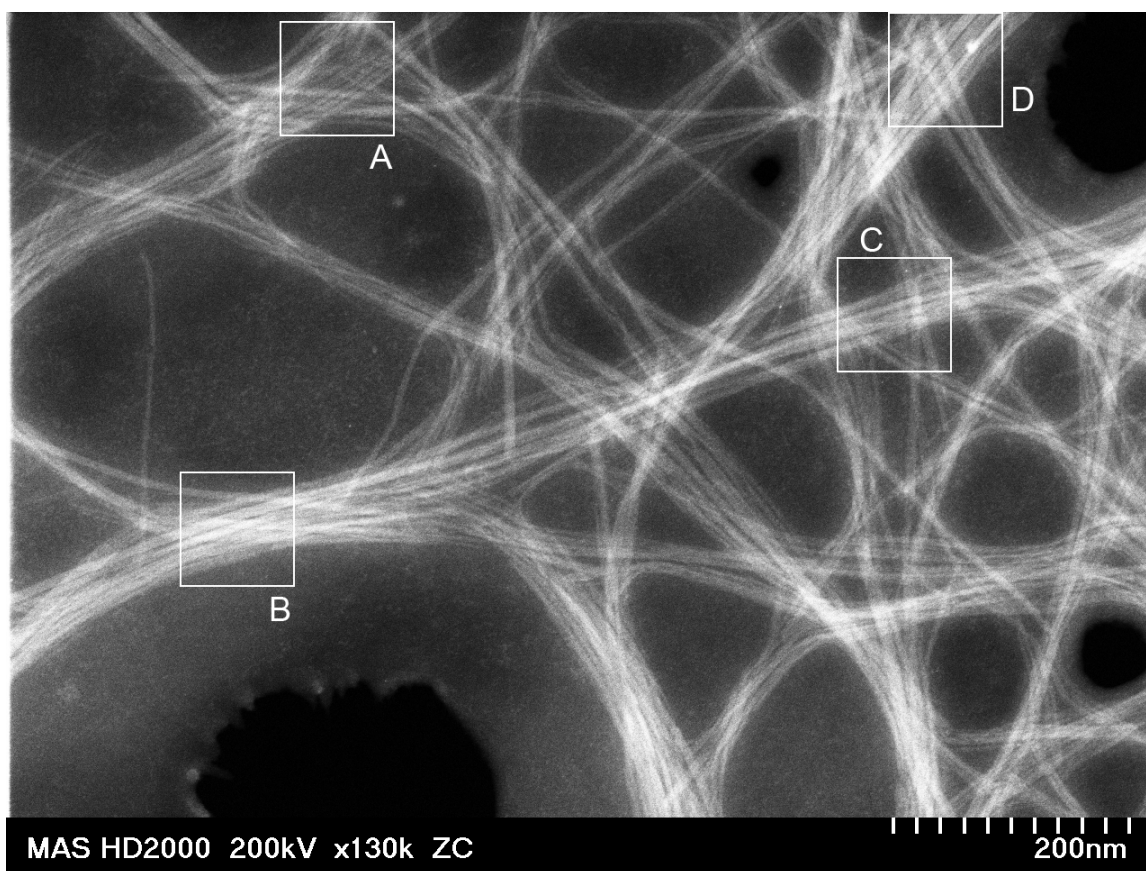


Figure 4.26. STEM ZC image of C1 nanofiber membrane after 1 week immersion time. Bundles of ~5nm wide fibril structures that comprise the individual C1 SANs. The lettered boxes, A-D, denote areas chosen for further FFT analysis of individual fibril widths as shown in Figure 4.23.

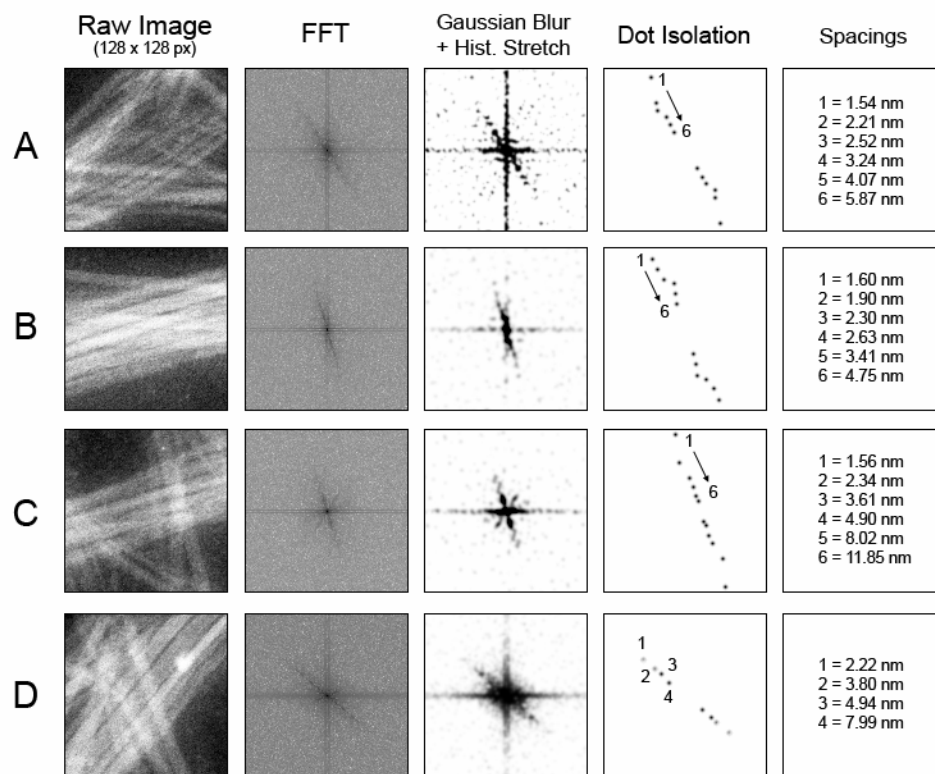


Figure 4.27. FFT analysis of fibril repeat distances within 128 x 128 px regions from Figure 4.26. Each individual region is first FFT filtered, then the FFT is blurred and histogram stretched. This is to increase the contrast of the FFT. Spots are then isolated and the spacings measured and reported looking for correlation in fibril spacings between each area. It is important to note that the accuracy of this analysis is severely limited due to the limited number of pixels comprising a single fibril, as well as effects on the image due to astigmatism of the scanning electron beam and orientation of the fibrils relative to the beam.

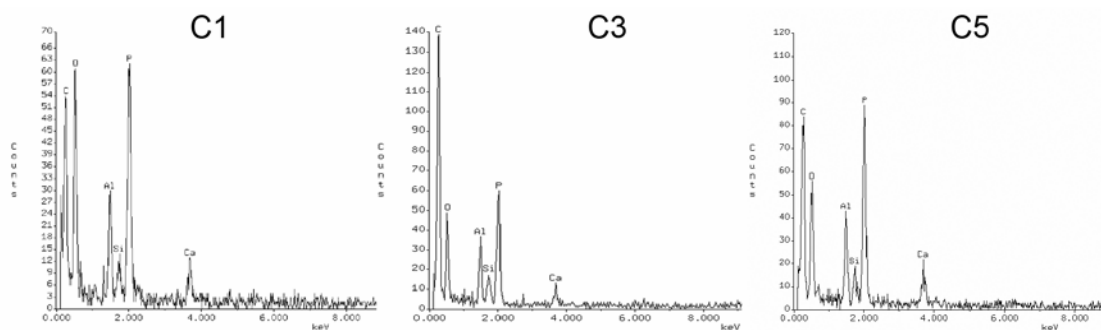


Figure 4.28. Representative EDS spectra taken on individual unsupported C1, C3, and C5 SANs showing the presence of aluminum, oxygen, phosphorus, carbon, silicon, and calcium. The silicon and calcium present are believed to be contaminants.

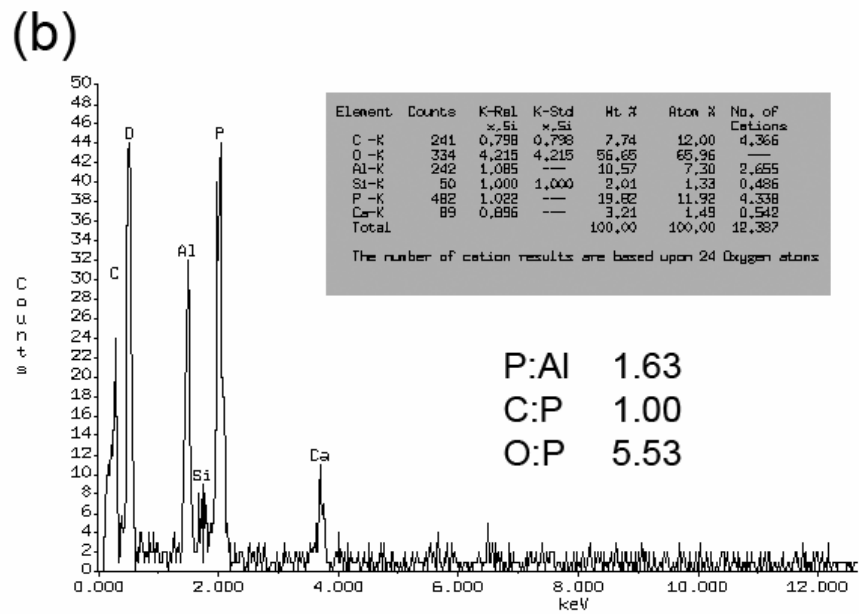
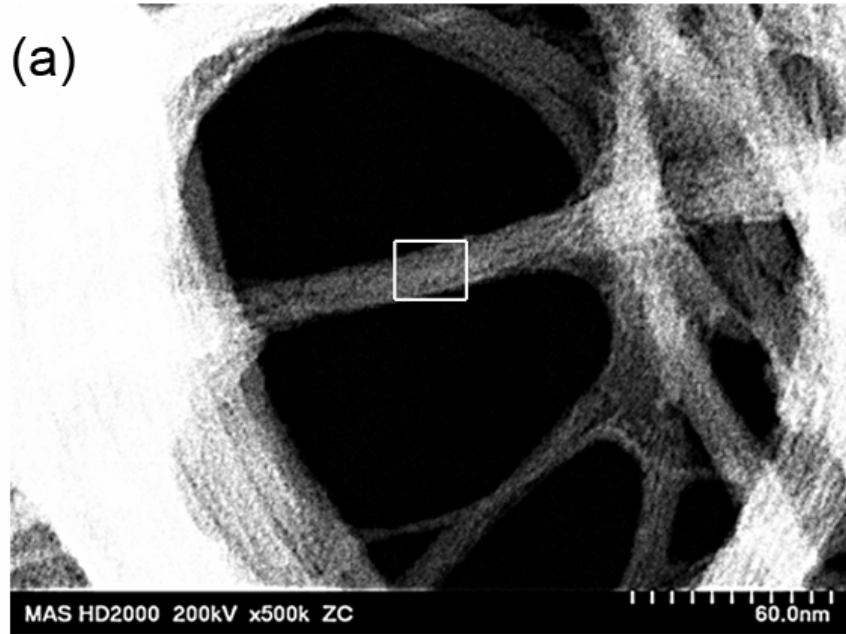


Figure 4.29. STEM ZC image (a) and corresponding qualitative EDS and semi-quantitative elemental analysis (b) of a single unsupported C1 SAN.

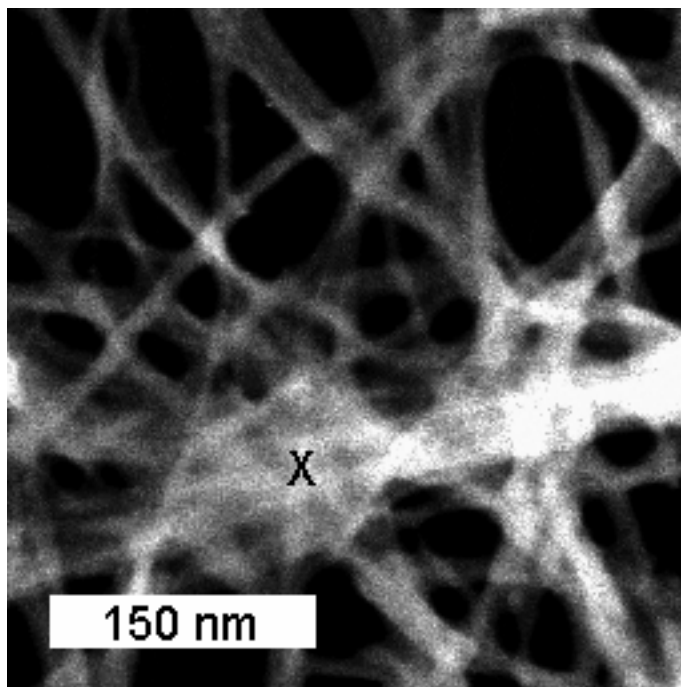


Figure 4.30. STEM Z-Contrast image of overlapping C1 SANs. X denotes the location of a 5 nm x 5 nm area utilized for EELS analysis.

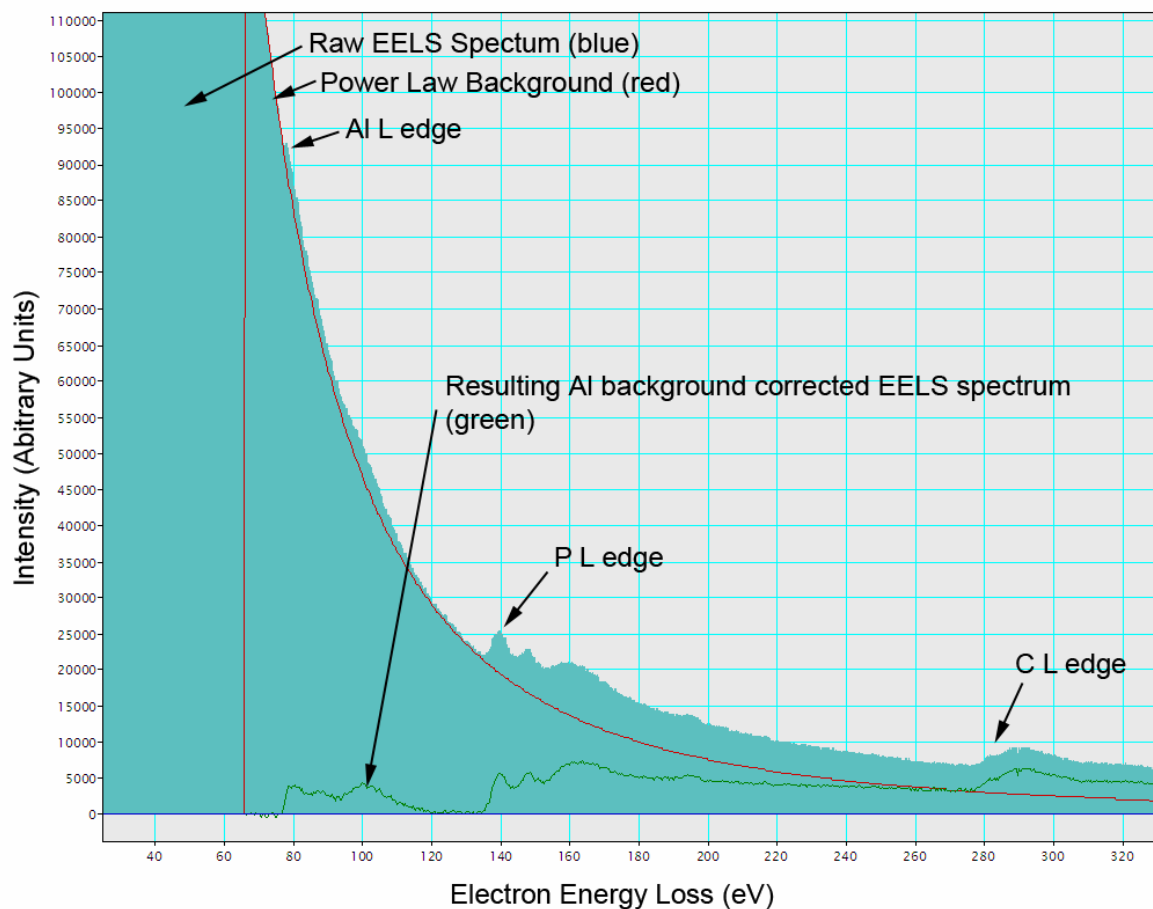
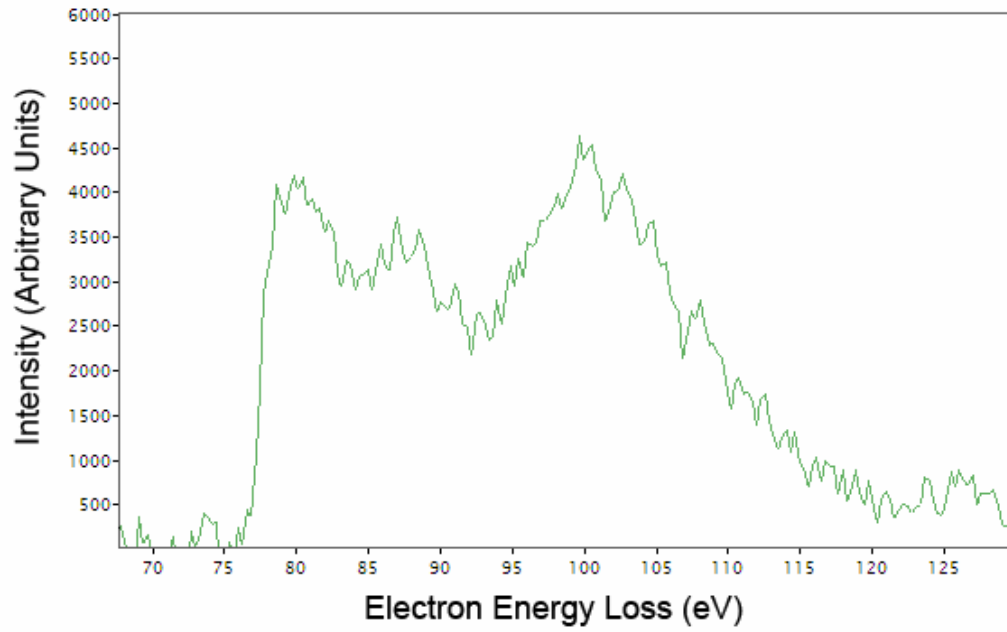


Figure 4.31. Raw EELS spectrum (blue) acquired from the location denoted in Figure 4.30. with the aluminum, phosphorus, and carbon  $L_{2,3}$  edges clearly visible. A power law background (red) was applied to the raw EELS data using a 10 eV window ahead of the aluminum edge. The resulting aluminum background corrected spectrum is shown in green. This definitively proves that aluminum, phosphorus, and carbon are present in the SAN structure.

Al



P

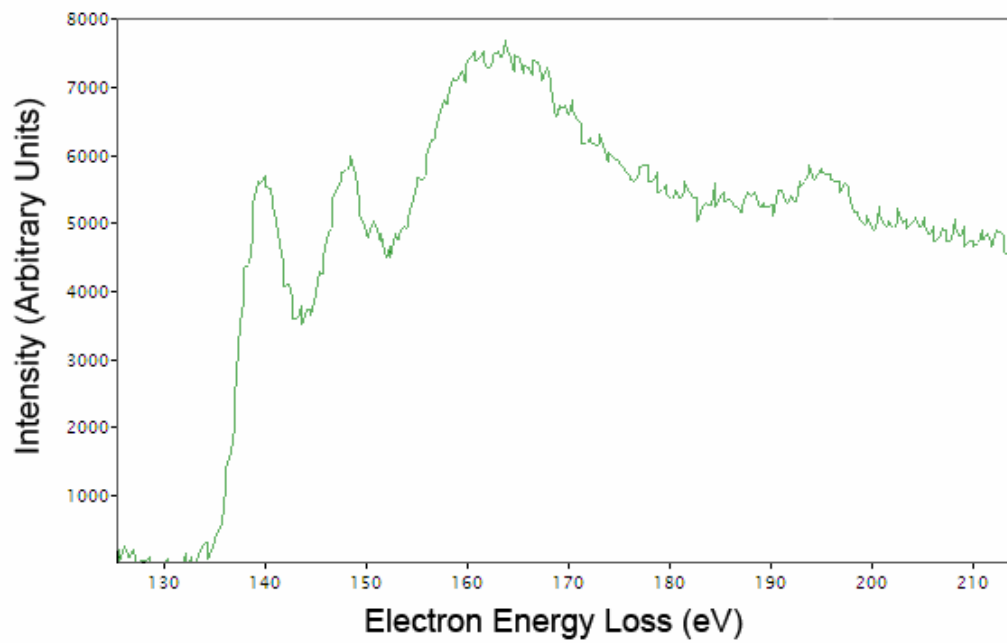


Figure 4.32. Aluminum and phosphorus background corrected L edges. A power-law model was utilized for background correction.

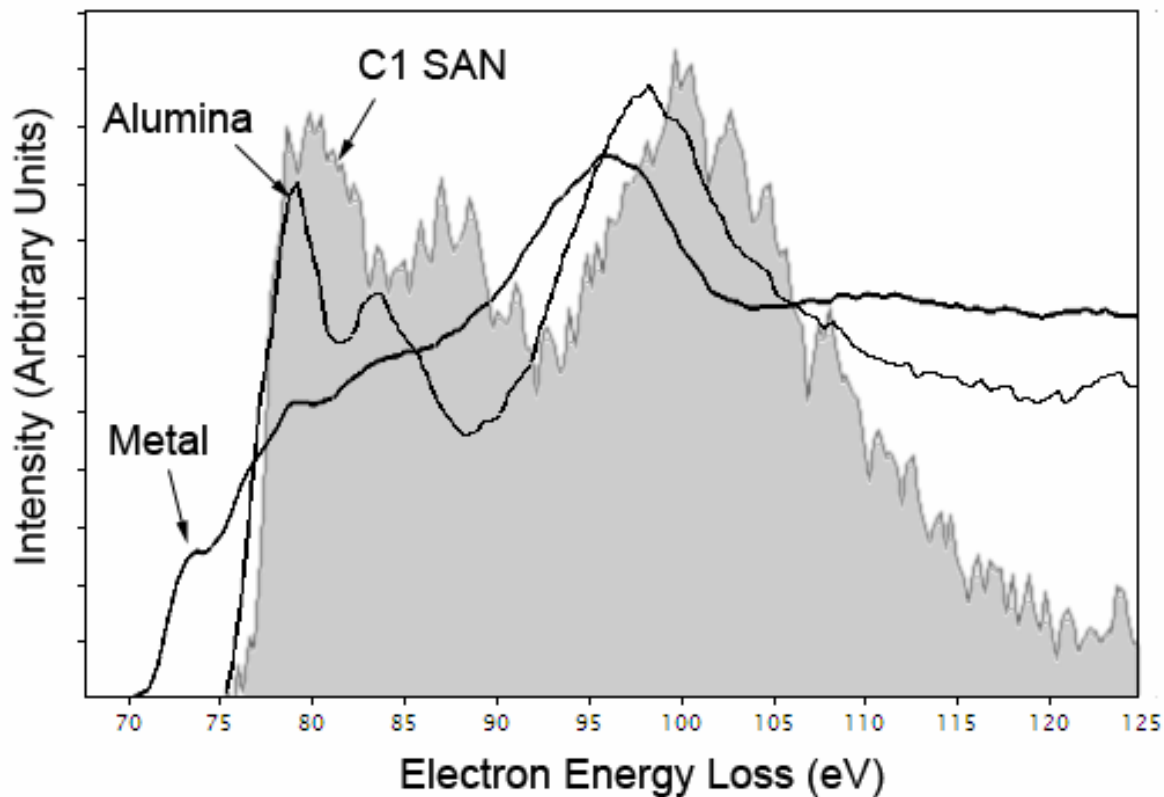


Figure 4.33. Comparison of aluminum L edge from C1 SAN with aluminum L edges from EELS Atlas for aluminum metal and alumina ( $\text{Al}_2\text{O}_3$ ). Edge onset for the C1 SAN is more similar to that for alumina than for metallic aluminum, suggesting an Oxygen environment for the aluminum in the C1 SANs. All edges were power-law background corrected using a 10 eV energy window. The background correction for the C1 SANs may possibly be improved utilizing other models.

## 4.6. Tables

Table 4.1. Measured XPS BE peak positions (eV) for the aluminum 2p 3/2 and phosphorus 2p 3/2 for C1, C3, and C5 samples. All spectra were calibrated to the carbon 1s peak at 285 eV.

APA	Al 2p 3/2	P 2p 3/2
C1	75.1	134
C3	75	133.8
C5	75.2	133.5

Table 4.2. Summary of the average elemental ratios of nine C1 SAN cross-sections as determined by semi-quantitative EDS analysis.

Elements	Ratio	Std. Dev.
P:Al	2.11	0.49
C:P	4.44	2.76
O:P	5.46	2.04

Table 4.3. Average atomic ratios and standard deviations for ten C1, two C3, and one C5 unsupported SANs as determined by semi-quantitative EDS analysis.

C1	Elements	Ratio	Std. Dev.
	P:Al	2.41	0.64
	C:P	2.69	2.59
	O:P	4.45	1.10
C3	Elements	Ratio	Std. Dev.
	P:Al	1.94	0.53
	C:P	4.19	2.23
	O:P	4.76	1.38
C5	Elements	Ratio	Std. Dev.
	P:Al	1.50	N/A
	C:P	13.80	N/A
	O:P	5.41	N/A

## 4.7. References

- [4.1] Law, M., et al., *Nanowire dye-sensitized solar cells*. Nature Materials, 2005. **4**(6): p. 455-459.
- [4.2] Lozano, K. and E.V. Barrera, *Nanofiber-reinforced thermoplastic composites. I. Thermoanalytical and mechanical analyses*. Journal of Applied Polymer Science, 2001. **79**(1): p. 125-133.
- [4.3] Kim, J.S. and D.H. Reneker, *Mechanical properties of composites using ultrafine electrospun fibers*. Polymer Composites, 1999. **20**(1): p. 124-131.
- [4.4] Shin, S.Y., et al., *Biological evaluation of chitosan nanofiber membrane for guided bone regeneration*. Journal of Periodontology, 2005. **76**(10): p. 1778-1784.
- [4.5] Zhang, S.G., F. Gelain, and X.J. Zhao, *Designer self-assembling peptide nanofiber scaffolds for 3D tissue cell cultures*. Seminars in Cancer Biology, 2005. **15**(5): p. 413-420.
- [4.6] Fletcher, B.L., et al., *Microarrays of biomimetic cells formed by the controlled synthesis of carbon nanofiber membranes*. Nano Letters, 2004. **4**(10): p. 1809-1814.
- [4.7] Aballe, A., et al., *Localized alkaline corrosion of alloy AA5083 in neutral 3.5% NaCl solution*. Corrosion Science, 2001. **43**(9): p. 1657-1674.
- [4.8] Aziz, P.M. and H.P. Godard, *Pitting Corrosion Characteristics of Aluminum - Influence of Magnesium and Manganese*. Industrial and Engineering Chemistry, 1952. **44**(8): p. 1791-1795.
- [4.9] Wagner C.D., R.W.M., Davis L.E., Moulder J.F., Muilenberg G.E., *Handbook of X-Ray Photoelectron Spectroscopy*. 1979: Perkin-Elmer Corporation, Physical Electronics Division, Eden Prairie, Minn. 55344
- [4.10] Hasha, D., et al., *Studies of Silicoaluminophosphates with the Sodalite Structure*. Journal of the American Chemical Society, 1988. **110**(7): p. 2127-2135.
- [4.11] Lindsay, J.R., et al., *X-Ray Photoelectron Spectra of Aluminum Oxides - Structural Effects on Chemical-Shift*. Applied Spectroscopy, 1973. **27**(1): p. 1-5.
- [4.12] Taylor, J.A., *An Xps Study of the Oxidation of Alas Thin-Films Grown by Mbe*. Journal of Vacuum Science & Technology, 1982. **20**(3): p. 751-755.
- [4.13] Wagner, C.D., et al., *Auger and Photoelectron Line Energy Relationships in Aluminum-Oxygen and Silicon-Oxygen Compounds*. Journal of Vacuum Science & Technology, 1982. **21**(4): p. 933-944.

- [4.14] Nishitani, R., et al., *Xps Analysis of Thermally Grown Oxide Film on Gap*. Japanese Journal of Applied Physics, 1978. **17**(2): p. 321-327.
- [4.15] Williams, D.B. and C.B. Carter, *Transmission electron microscopy : a textbook for materials science*. 1996, New York: Plenum Press. xxvii, 729 p.
- [4.16] Egerton, R.F., *Electron energy-loss spectroscopy in the electron microscope*. 2nd ed. Language of science. 1996, New York: Plenum Press. xi, 485 p.
- [4.17] Ahn, C.C., *Transmission electron energy loss spectrometry in materials science and the EELS atlas*. 2nd ed. 2004, Weinheim [Germany]: Wiley-VCH. xiii, 457 p.
- [4.18] Kimoto, K., et al., *Coordination and interface analysis of atomic-layer-deposition Al<sub>2</sub>O<sub>3</sub> on Si(001) using energy-loss near-edge structures*. Applied Physics Letters, 2003. **83**(21): p. 4306-4308.
- [4.19] Kong, D.Y., *Hydrothermal synthesis of organic-inorganic layered hybrid metal phosphonate [Zr(C<sub>5</sub>H<sub>3</sub>NPO<sub>3</sub>CL)F<sub>2</sub>](H<sub>2</sub>O)*. Abstracts of Papers of the American Chemical Society, 2004. **228**: p. U836-U836.
- [4.20] Libera, J.A., et al., *Comparative X-ray standing wave analysis of metal-phosphonate multilayer films of dodecane and porphyrin molecular square*. Journal of Physical Chemistry B, 2005. **109**(4): p. 1441-1450.
- [4.21] Chaudhari, A. and C.V. Kumar, *Intercalation of proteins into alpha-Zirconium phosphonates: tuning the binding affinities with phosphonate functions*. Microporous and Mesoporous Materials, 2005. **77**(2-3): p. 175-187.
- [4.22] Doron-Mor, I., et al., *Layer-by-layer assembly of ordinary and composite coordination multilayers*. Langmuir, 2004. **20**(24): p. 10727-10733.
- [4.23] Gomez-Alcantara, M.M., et al., *Synthesis and characterization of metal carboxyalkylphosphonates hybrid materials*. Solid State Sciences, 2004. **6**(5): p. 479-487.
- [4.24] Hix, G.B., et al., *Synthesis and characterisation of Al(O<sub>3</sub>PCH<sub>2</sub>CO<sub>2</sub>)center dot 3H(2)O, a layered aluminium carboxymethylphosphonate*. Journal of the Chemical Society-Dalton Transactions, 1998(20): p. 3359-3361.
- [4.25] Maeda, K., et al., *Almepo-Alpha - a Novel Open-Framework Aluminum Methylphosphonate with Organo-Lined Unidimensional Channels*. Angewandte Chemie-International Edition in English, 1995. **34**(11): p. 1199-1201.
- [4.26] Maeda, K., et al., *Structure of Aluminum Methylphosphonate, Almepo-Beta, with Unidimensional Channels Formed from Ladder-Like Organic-Inorganic Polymer-Chains*. Journal of the Chemical Society-Chemical Communications, 1995(10): p. 1033-1034.

- [4.27] Cabeza, A., et al., *Aluminum phenylphosphonates: A fertile family of compounds*. Inorganic Chemistry, 1998. **37**(17): p. 4168-4178.
- [4.28] El Haskouri, J., et al., *The first pure mesoporous aluminium phosphonates and diphosphonates - New hybrid porous materials*. European Journal of Inorganic Chemistry, 2004(9): p. 1804-1807.
- [4.29] El Haskouri, J., et al., *S+I- ionic formation mechanism to new mesoporous aluminum phosphonates and diphosphonates*. Chemistry of Materials, 2004. **16**(22): p. 4359-4372.
- [4.30] Edgar, M., et al., *Structure solution of a novel aluminium methylphosphonate using a new simulated annealing program and powder X-ray diffraction data*. Chemical Communications, 2002(8): p. 808-809.
- [4.31] Cabeza, A., et al., *Two new organo-inorganic hybrid compounds: Nitrilophosphonates of aluminum and copper*. Journal of Solid State Chemistry, 2001. **160**(1): p. 278-286.
- [4.32] Kuiry, S.C., et al., *Solution-based chemical synthesis of boehmite nanofibers and alumina nanorods*. Journal of Physical Chemistry B, 2005. **109**(9): p. 3868-3872.
- [4.33] Hou, H.W., et al., *Preparation and characterization of gamma-AlOOH nanotubes and nanorods*. Nanotechnology, 2005. **16**(6): p. 741-745.
- [4.34] Di Renzo, F., et al., *Textural control of micelle-templated mesoporous silicates: the effects of co-surfactants and alkalinity*. Microporous and Mesoporous Materials, 1999. **28**(3): p. 437-446.

## 5 Thermal Properties

### 5.1. Introduction

Thermal properties such as melting point and thermal conductivity are often important factors in the determination of a material's potential applications as well as providing insights into the molecular or atomic arrangement. It is well known that there are correlations between the thermal transitions such as the melting or boiling point and the type of bonding between the atoms or molecules in bulk materials. Although the investigation into the thermal properties of nano-sized materials has been ongoing since the 1960's[5.1, 2], the actual processes involved in melting at the nanoscale are still not well understood. Generally, as the size of a discrete structure is reduced into the nanoscale, more and more of the constituent atoms within the material comprise its surface, giving an increasing, non-zero surface to volume ratio. Molecular dynamics simulation report predicted melting point depressions of metal nanowires, attributed to nanoscale surface energy size effects[5.3-6].

If we imagine that as the size of a structure decreases, a larger percentage of the atoms constitute surface rather than bulk material. These surface atoms are not fully coordinated and thus are not as tightly bound as are the internal atoms and as a result are more susceptible to dynamical processes such as melting or chemical attack. While melting point depression due to nanometer length scales is widely accepted both experimentally and theoretically, Alexander et al. report that tin clusters of 10's of atoms exhibit an increase in melting temperature[5.7]. It is surmised that this discrepancy is due to the formation of a unique crystal reconstruction only possible below a critical number of atoms.

Previous thermal annealing studies of C18 monolayers on mica reveals physisorption type bonding between the C18 and the mica[5.8]. As temperatures were increased above

100C the film disorganized forming disordered C18 nanodroplets. Above temperatures of ~120C, the SAM partial coverage morphology disappeared completely as all the molecules migrated in to large droplet type precipitates. The bond energy was calculated to be ~9 kcal/mol, evidence that weak interactions hold the C18 SAM together.

In the case of C18 self-assembled bilayers, Fontes et. al. report the destruction of C-18 bilayer structures at annealing temperatures of ~120C [5.9], indicating a thermal breakdown of the stabilizing hydrogen bonding between the PA headgroups. This caused a disordering of the layers into the familiar disordered nanodroplet structures that are seen when heating ODPA partial SAMs above ~120C [5.8]. The temperatures required for monolayer and bilayer breakdown are only slightly higher than the melting point for the pure ODPA crystals (99C).

Methylphosphonic acid (C1), similar to C18, is a crystalline solid at room temperature. It also has a similar melting temperature to C18, of ~106°C. The bonding between molecules is a combination of fairly weak Van der Waals bonding between methyl groups and the slightly stronger hydrogen bonding between phosphonic acid groups. Pure C1 crystals are white, sheet-like, and flaky, appearing to have a layered structure.

The observation by John Richards in his 1997 NCSU Master's Thesis of "worm-like" nanostructures on evaporated aluminum films after immersion in C1 solution was considered a surprising and undesirable result. Previous investigations of alkylphosphonic acids adsorptions on the native aluminum oxide as well as single crystal Al<sub>2</sub>O<sub>3</sub> report the P-O – Al bond as strong and highly stable[5.10-14].

It was of interest to investigate the thermal stability of the resulting APA SANs to further elucidate and provide insight on the SAN sub-structure and internal bonding. Three different

experiments were utilized to examine the thermal stability of APA SANs. First an *ex-situ* annealing experiment was performed utilizing C1 SANs grown directly on aluminum surfaces. A second annealing experiment was performed in-situ by heating and imaging C1 SANs grown on Si<sub>3</sub>N<sub>4</sub> in an environmental AFM equipped with a hot-stage. Finally, a second e-situ annealing experiment was performed on C1, C3, and C5 SANs as grown on Si<sub>3</sub>N<sub>4</sub> substrates.

## 5.2. Ex-Situ Annealing of C1 SANs on Aluminum

### 5.2.1 Experimental Details

Originally, SANs were prepared by immersion of aluminum coated glass slides into a 30 mL solution of 0.1 wt% (8.3 mM) Methylphosphonic acid (C1) dissolved into 200 proof Ethanol (EtOH) over a period of days to weeks. The longer the immersion time, up to ~ 28 days there was a steady increase in nanofiber coverage of the aluminum surface. See section 3.2.1 for details concerning growth of C1 SANs on aluminum coated glass slides.

The 35 day and 84 day immersion samples were chosen for annealing experiments as they were generally representative of mature SANs, allowing for ease of imaging 5um X 5um areas while having what appeared to be some underlying aluminum still present. Before annealing, both samples were first imaged using AFM to make sure that initial morphology of the nanofibers was still present after being stored in ambient conditions for a number of months after being removed from solution.

A digitally controlled, Thermolyne 21100 tube furnace was used for all of the ex-situ annealing experiments presented in this work. The furnace is capable of heating samples quickly up to 1000C in air or under inert gas flow. A 5 cm x 1 cm x 1cm alumina boat was used to hold the sample within the furnace. A digital Fluke high temperature thermocouple was affixed to the ceramic boat and positioned as to be within a few mm's from the sample in the boat. Due to temperature fluctuations depending on position within the furnace, it was important to utilize the thermocouple to accurately measure the temperature at the sample during each anneal. The thermocouple temperature reading at the sample was verified using 250C Omegalaq, thermally sensitive temperature paint. The ceramic boat and thermocouple were preheated for at least 30 minutes at the desired annealing temperature

before inserting a sample. A ceramic plug with a small 0.5 cm hole was utilized to cap the end of the furnace during annealing.

All samples were placed in the ceramic boat aluminum side up, heated in for 30 minutes then removed and quenched back to room temperature on a heat sink for ~5 minutes. The samples were then immediately imaged using a Digital Instruments D-3000 AFM. After each anneal 5  $\mu\text{m}$  and 1  $\mu\text{m}$  tapping mode images were obtained from several areas on the sample. Occasionally, additional images were taken to investigate individual fiber substructures that looked interesting.

### **5.2.2. Results**

The 35 day sample, was heated in air in ~10C increments from 27C up to 240C and then in ~75C increments from 350C to 500C. For each anneal, the temperature in the furnace was first stabilized prior to insertion. Between each anneal, AFM images were taken and then the sample subjected to another anneal. A measurable change in the surface morphology occurred between 350C and 500C, so a second sample was heated in ~30C increments from 350C to 500C in a similar manner to further narrow the transition temperature range. Figure 5.1 is a series of AFM height images showing the effect of annealing on the typical SAN morphology after anneals between 27C - 490C. The most apparent changes occur between 430C and 460C. The SANs appeared to melt or widen along their lengths as many of the larger precipitates appear unaffected. This progression continues after annealing at 490C as distinct SANs are no longer observable as their structures have all melted together. Figure 5.2 shows the corresponding 1  $\mu\text{m}$  AFM height images to those seen in Figure 5.1. The 1  $\mu\text{m}$  images make it much easier to assess the effect of annealing on the individual fibers, helping

delineate what could be deemed SAN morphology changes in comparison to the changes of the adjoining material. It is clearly evident that the SAN morphology is still present even after the 460C, Figure 5.2 (h), and quite possibly after the 490C anneal, Figure 5.2 (i). Small round precipitates formed, beginning initially after the 430C anneal. They seemed to grow in number and size as the annealing temperature was increased. This behavior is very similar to the heating of C18 SAMs on mica.

In an attempt to be certain that the results from anneals in air were not due to the oxidation and were indeed melting phenomena, another C1 SAN sample was subjected to a similar ex-situ thermal treatment under dry nitrogen flow. The observed morphology changes were the same for the 460C anneal whether performed under N<sub>2</sub> or air. In both cases the SAN structures appeared to melt.

The observed transition temperature between 430C - 460C was considerably higher than the melting reported temperatures of 100C for C18 SAMs and 120C for C18 bilayers on mica[5,8, 9, 15]. This seems to indicate that the bonding within the SANs is more likely covalent or ionic in nature. This is distinctly different than the hydrogen bonding typical of C18 SAMs and bilayers as well as pure C1. Although the SANs appeared to melt between 430C and 460C it was impossible to discern whether it was the SANs or the precipitate structures or possibly an underlying film of unknown composition causing the observed changes in the SAN morphology. To more fully investigate the properties of the SAN, new growth techniques were then created to isolate the SANs away from the precipitates as well as the remaining aluminum.

### 5.3 In-situ Annealing of C1 SANs on Si<sub>3</sub>N<sub>4</sub>

C1 SANs grown on aluminum showed remarkable thermal stability with morphology changes occurring between 430C and 460C. To further investigate the morphology changes, an in-situ heating experiment was performed. For clarity, in-situ annealing, refers to heating the sample and imaging that sample utilizing the same instrument, ideally monitoring the response of a single SAN or set of SANs during thermal annealing. In this case a JEOL JSPM-5200 environmental AFM/STM with hot stage capability was utilized to both controllably heat the sample and image the result of each successive annealing step.

#### 5.3.1. Experimental Details

Advances in sample preparation as detailed in Section 3.2.4, enabled the investigation of the thermal stability of isolated C1 SANs grown on Si<sub>3</sub>N<sub>4</sub> coated silicon wafers. The sample utilized for this experiment was prepared essentially the same way as the previous ex-situ experiment with the exception that a partially aluminum coated  $\sim 1 \text{ cm}^2$  Si<sub>3</sub>N<sub>4</sub>/Si substrate was used instead of aluminum coated glass. The majority of the Si<sub>3</sub>N<sub>4</sub> surface was shadow masked using a silicon wafer shard during the aluminum evaporation. Aluminum coverage was confined to  $\sim .25 \text{ cm}^2$  on each of the substrates. The sample was the second of three patterned and layered substrates that shared the same 5 mL of 8.3 mM C1 solution. It was removed after 34 days of immersion, rinsed with 95% EtOH, and blown dry with UHP N<sub>2</sub>. The first sample was removed after 14 days.

In an attempt to monitor an individual SAN while annealing, a JEOL JSPM-5200 equipped with a hot state and digital temperature controller was utilized to perform both the heating and the imaging of the nanofiber sample. While a detailed description AFM can be

found in Section 2.2, the specifics of the hot stage and the experimental procedure are described here.

The JEOL hot stage, consisted of a small resistive heating element embedded in a ceramic material that was approximately 1.0 cm long, 0.5 cm wide, and 1.0 mm in thickness. The sample was mechanically clamped onto the heating element. A thermistor was integrated into the sample holder stack for precise temperature sensing. The entire stack, sample, thermistor, and heating element were then attached to the top of the piezo driven stage with an additional heat shield for protecting the piezo from being de-poled. The thermistor was attached to a Hewlett Packard digital temperature controller allowing for precise control over the heating of the sample.

### **5.3.2. Results**

Two experiments were performed utilizing 2 different pieces from the same 34 day immersion sample. The first piece was first imaged at room temperature and then heated and imaged at 100C, 200C, and 300C. The sample was imaged using tapping or intermittent contact mode. Imaging was performed only after the temperature had equilibrated for 10 minutes. The sample was heated under  $10^{-7}$  torr vacuum conditions. Heating the sample to such high temperatures required the use of high vacuum to protect the piezo scanner from being de-poled. The tip was retracted between temperature increases to avoid any possibility of tip crashes due to sample expansion, but in theory the sample could have been imaged continuously as the heating took place with careful attention paid to the z piezo range. Imaging at temperature made it more easy track the evolution of a single fiber as the heating progressed.

This methodology of imaging at temperature was quite successful until the temperature reached 300C, where it appeared that the imaging of the sample was causing degradation of the SANs and generally removing them from the Si<sub>3</sub>N<sub>4</sub> surface. If the scan area was then increased there was no appearance of material pile up around the previous scan box. Either the SANs were softening due to heating and being deposited on the tip or they were vaporizing and being removed through the vacuum. As the resolution of the tip was not seen to drastically change during SAN removal the later notion of scan induced vaporization is deemed more likely although no significant changes in vacuum level were observed.

To avoid fiber degradation due to scanning effects, images were acquired at a temperature previously found to be safe for the sample at 150C where no fiber changes were observed during the previous annealing. So another piece of the sample was chosen and scanned at room temperature before annealing. The sample was then heated to 300C for 30 minutes and quenched in vacuum to 150C at a rate of 50C/min and allowed to equilibrate for 10 minutes before imaging with AFM. Once again no drastic morphology changes occurred, in agreement with the previous experiment. It was much more difficult however, to track a single fiber utilizing this technique as the heating and cooling cycle would cause significant sample drift. The sample was heated through four more cycles, 350C, 400C, 450C, and 500C, the maximum instrument temperature, and imaged after each successive annealing.

Figure 5.3 is a summary showing the results of the in-situ heating showing no obvious changes other than possible thinning of the fibers after the 500C anneal. It is impossible to be certain that the SAN structure is changing due to the possibility of imaging artifacts caused by subtle changes in the tip shape. The stability of C1 SAN's structure above 460C supports the theory presented in Section 5.2.2, that previous observed melting phenomena are

likely due to the melting of precipitates or the underlying film rather than the SANs. Additional support for this idea is found in Figure 5.3 (500C), where in the lower right corner of the image a single precipitate looks melted in somewhat the same fashion as previously observed in the previous ex-situ study. It is also possible that there is a contribution due to differences in the surface energy between  $\text{Si}_3\text{N}_4$  and aluminum giving the appearance of increased melting temperature of the SANs. Due to the JEOL AFM instrument limitation of 500C, further in-situ heating of the SANs to higher temperatures was not possible.

## **5.4. Ex-situ annealing of C1, C3, and C5 SANs on Si<sub>3</sub>N<sub>4</sub>**

In the previous thermal experiments it was found that C1 SANs grown on aluminum were thermally stable to temperatures between 430C and 460C when annealed in ambient air or under N<sub>2</sub> flow. Subsequently, C1 SANs grown on Si<sub>3</sub>N<sub>4</sub> and annealed under vacuum conditions were thermally stable up to the 500C instrument maximum. The increased stability of C1 SANs on Si<sub>3</sub>N<sub>4</sub> under vacuum was thought to be due to several different factors, including surface energy effects due to the difference between Si<sub>3</sub>N<sub>4</sub> and aluminum as a substrate, or that the melting of C1 SAN structures presented in Section 5.2.2 was due to precipitate melting which then covered the SANs, obscuring any changes in the SANs due to annealing above 460C.

In an attempt to clarify the results from the previous two C1 thermal experiments and to examine the effect of alkyl-chain length on the thermal stability of nanofibers a third experiment was carried out. Since the previous experiment it was found that SANs could be also produced utilizing phosphonic acids with longer alkyl chains, specifically 3 (C3), and 5 (C5). In an attempt to better understand the effect of chainlength on nanofiber properties, nanofibers grown on Si<sub>3</sub>N<sub>4</sub> substrates using all three chain-lengths, C1, C3, and C5. This produced APA SAN samples with homogenous surface coverage and without precipitates allowing for observation of only SAN related morphology changes. The samples were subjected to a series of ex-situ anneals from 470C to 650C.

### **5.4.1. Experimental Details**

C1, C3, and C5 nanofibers were grown on Si<sub>3</sub>N<sub>4</sub> coated silicon substrates as described in Section 3.2.5. Samples that had been immersed for three weeks were used. Each of the samples was first imaged as grown at room temperature with AFM before successive heat

treatments. All samples were heated in the same tube furnace in air as described earlier in this chapter. The C1 sample was heated to 470C, 490C, 500C, 510C, 550C and 575C all for 30 min each, then at 600C and 650C each for 6 hrs. The C3 sample was heated at 550C and 575C for 30 min each and then 600C and 650C for 6 hrs each. The C5 sample was heated at 470C, 490C, 500C and 550C for 30 minutes, and then reheated at 550C for 12 hrs to examine long term high temperature stability, 575C for 30 min, then 600 and 650 for 6 hrs each. All samples were imaged immediately after each successive annealing step.

#### **5.4.2. Results**

In an attempt to understand what was happening to the C1 SANs as observed in the previous two experiments it was decided to heat the sample initially to 470C paying close attention to exact location of imaging to hopefully image the same area of the sample before and after annealing. This method was successful on the first attempt, shown in Figure 5.4, where images of the same SANs before (a) and after annealing at 470C for 30 min (b) were captured. There is a marketable decrease of  $\sim 1/3$  in the average height along a portion of one of the fibers chosen due to its prominence in the image, Figure 5.4 (c-d), showing definitive changes in C1 SAN morphology when heated to 470C in air. It is unclear where the lost material has gone as it has either flowed across the sample as a very thin undetectable film or it has oxidized or sublimed away. Although there are noticeable changes in the volume of individual SANs the larger SANs retain their fibrous morphology. Interestingly, small 25-50 nm round structures are observed also similarly to the ones seen in the first annealing experiment on Al. They appear to be at the ends of the individual nanofibers or at the intersections, providing evidence of detwetting.

In addition to C1 SANs, C3 and C5 SANs were also tested. A comparison of all three before and after annealing at 550C for 30 minutes can be seen in Figure 5.5. Generally, it appears that the C5 SANs show the greater thermal stability followed by the C1 and lastly, C3 SANs which show higher amounts of droplet formation than either the C1 or C5.

In each case the SAN morphology persists even after the 550C anneal. Due to the observed greater thermal stability than the C1 or C3 SANs, the C5 sample was annealed at 550C for 12 hrs to investigate their long term high temperature stability. Figure 5.6, shows AFM images, before (a), and after (b), annealing at 550C for 12 hrs. The C5 SANs have remarkable high temperature stability as only a few droplets are seen after annealing for 12 hrs.

Figure 5.7 shows the progression of C1 SANs annealed at 575C for 30 minutes followed by 6 hr anneals at 600C and 650C. The C3 and C5 SAN samples were subjected to the same thermal annealing, see Figure 5.8 and Figure 5.10. In the case of the C1 SANs, the 5  $\mu\text{m}$  images show that the SAN morphology stays intact for the largest SANs even up to 650C. However, if we look at the progression of the SAN morphology in the 1 mm images, we can clearly see evidence of melting and dewetting after the 575C anneal. Dewetting of the C1 SANs is most clearly observable in Figure 5.7 (e), forming a “beads on a ribbon” morphology.

In the case of C3 SANs the formation of small beads is more wide spread after annealing at 575C. The formation of the beads appears to occur mostly at intersections with the eventual disappearance of any SAN structure after the 600C anneal. Eventually, after the 650C anneal the C3 SANs are completely gone with only small precipitates remaining.

The C5 SANs exhibited the highest thermal stability of the three chain-lengths investigated. Only subtle morphology changes occurred after the 600C anneal as seen in Figure 5.9. The “beads on a ribbon” morphology was observed after the 650C anneal.

## 5.5. Discussion

Methylphosphonic acid (C1) SANs grown on evaporated aluminum and  $\text{Si}_3\text{N}_4$  substrates were subjected to a variety of thermal anneals to examine their thermal response. *Ex-situ* anneals in air and  $\text{N}_2$  environments of C1 SANs grown on aluminum exhibited a melting transition between 460C and 490C. Due to the complexity of the aluminum surface, it was impossible to correlate the observed melting directly to the C1 SANs.

In an attempt to isolate the melting event directly to the SANs, *in-situ* annealing and imaging of C1 SANs grown on  $\text{Si}_3\text{N}_4$  was performed. A decrease in SAN stability was observed when imaging the SANs at elevated temperatures of 300C and above under high vacuum conditions, indicating the possibility of tip induced sublimation of the SANs. Further *in-situ* annealing with imaging at room temperature revealed C1 SANs to be stable up to the maximum instrument temperature of 500C. There were also some indications of possible mass loss as the C1 SANs after annealing at 500C appeared thinner. The results of the *in-situ* experimentation verified the previous thermal stability findings for the C1 SANs on aluminum as well as helping show that the observed melting between 460C and 490C was most likely due to structures other than the C1 SANs.

Finally, a second set of *ex-situ* annealing experiments were conducted to further examine the behavior of C1 SANs on  $\text{Si}_3\text{N}_4$  at temperatures greater than 500C as well as SANs grown using longer chain-length APAs. C1, C3 and C5 SANs on  $\text{Si}_3\text{N}_4$  were all subjected to various anneals up to 650C. Evidence of mass loss was only observed for C1 SANs as a single C1 SAN was imaged with AFM before and after annealing at 470C. The decrease in SAN volume was consistent with the *in-situ* experimental findings. C1, C3, and C5 SANs were all observed to dewet, forming a “beads on a ribbon” type morphology. The C5 SANs

were the most resilient, with their SAN morphology stable to 650C. The C3 SANs dewet the most easily and eventually all evidence of SAN structure was removed leaving only small round precipitate structures.

APA SANs exhibit significantly higher transition temperatures as compared to octadecylphosphonic acid (C18) SAMs and bilayer structures grown on mica[5,8, 9, 15]. In the later it has been determined that the layered bilayered structures disassemble at temperatures greater than 120C attributing to the breakdown of the hydrogen bonding between the phosphonic groups of the individual molecules causing widespread mobility and the formation of disordered precipitates. The marketed increase in thermal stability of the SANs relative to the SAMs and bilayers is thought to be most likely due to the presence of significant amounts covalent or ionic bonding within the structure.

## 5.6. Figures

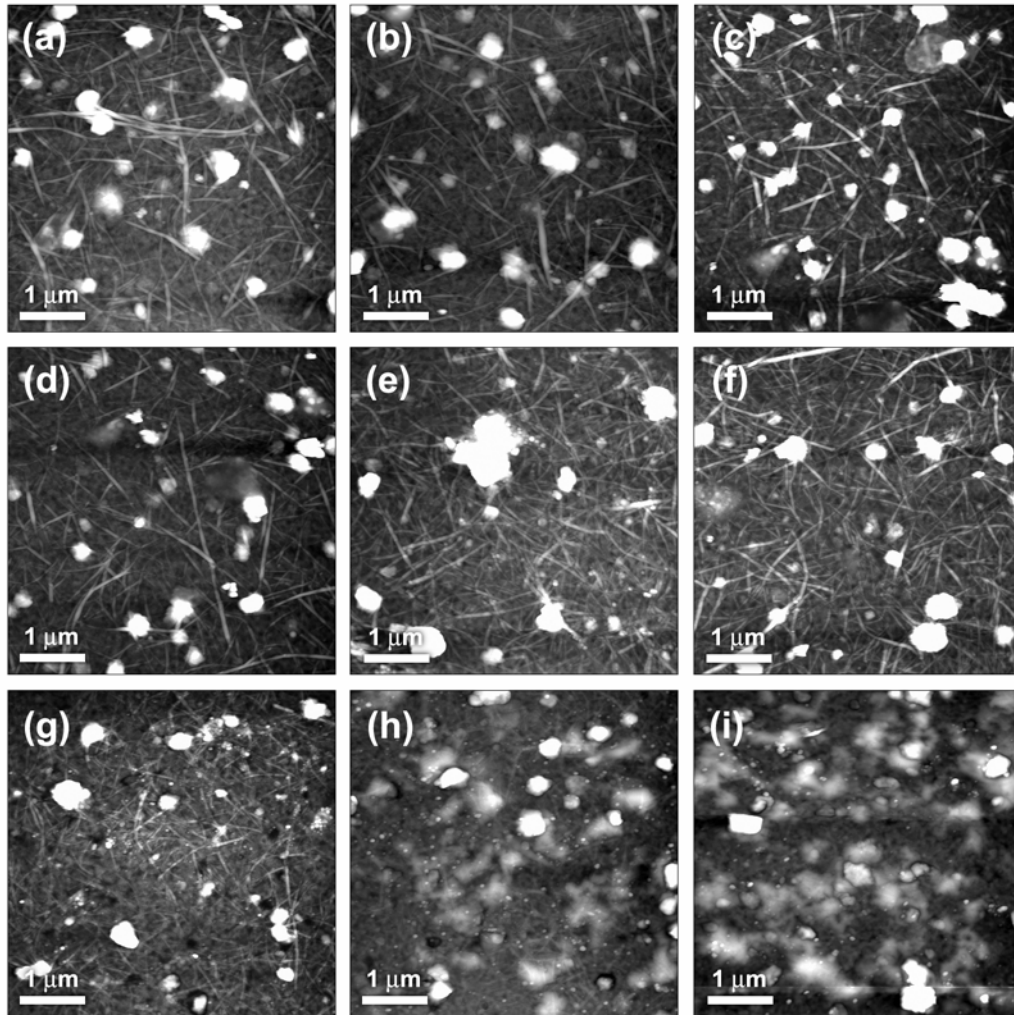


Figure 5.1. A series of 5 μm x 5 μm AFM height images of a typical C1 SAN mat with precipitates acquired at room temperature ~27C (a) and after 30 min anneals at 105C (b), 160C (c), 220C (d), 300C (e), 325C (f), 430C (g), 460C (h), and 490C (i).

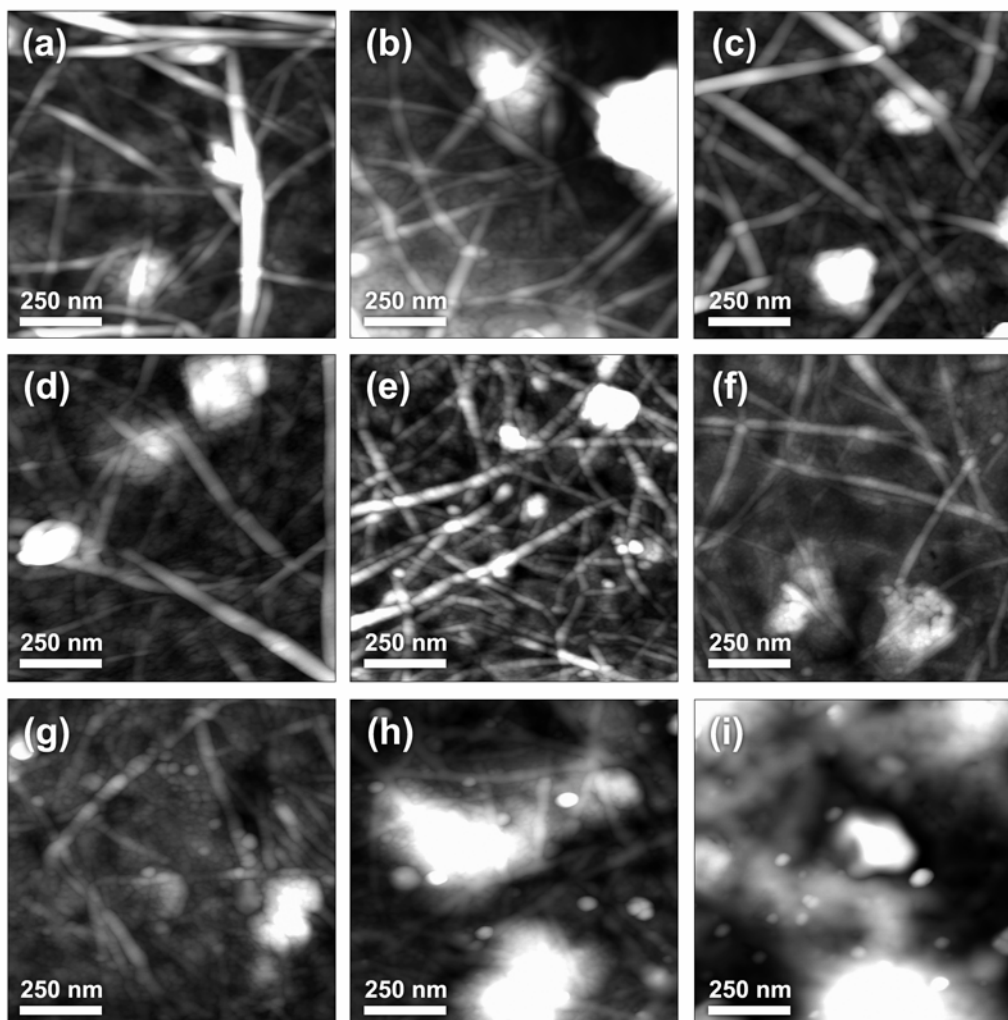


Figure 5.2. Corresponding  $1\ \mu\text{m} \times 1\ \mu\text{m}$  AFM height images of the same sample as in Figure 5.1 acquired at the same temperatures: room temperature (a) and after 30 min anneals at 105C (b), 160C (c), 220C (d), 300C (e), 325C (f), 430C (g), 460C (h), and 490C (i). A melting event occurs between 430C and 460C with SAN structures still present after 490C (i).

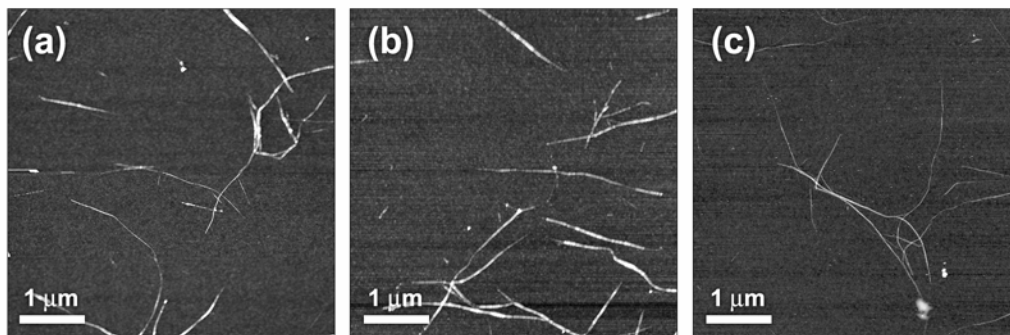


Figure 5.3. 5  $\mu\text{m}$  x 5  $\mu\text{m}$  AFM height images of C1 SANs on  $\text{Si}_3\text{N}_4$  at room temperature (a), and after annealing under a vacuum of  $\sim 1 \times 10^{-6}$  torr for 30 minutes at 450C (b), 500C (c).

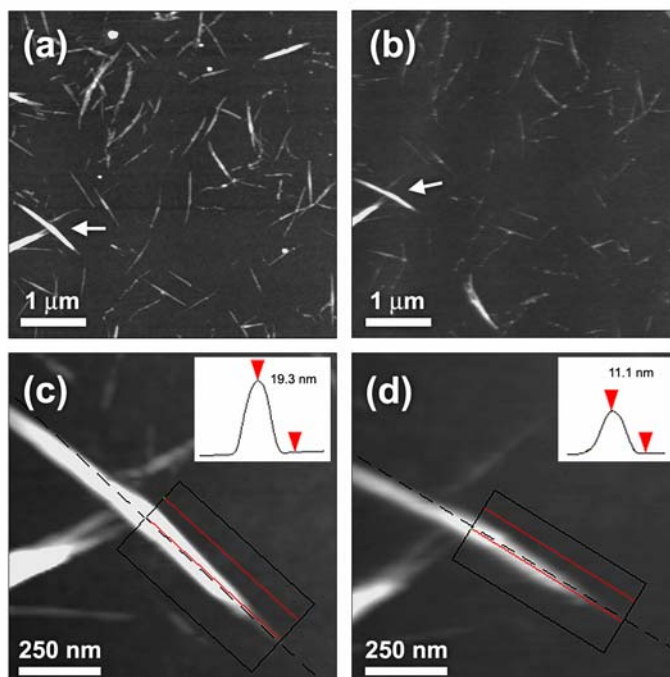


Figure 5.4. AFM height images of the same area of C1 SANs on  $\text{Si}_3\text{N}_4$  before (a), and after annealing in air for 30 minutes at 470C (b). The arrow in (a) and (b) point at the same nanofiber for reference within the images. Electronic zooms of the same nanofiber before (c), and after (d) reveal a significant decrease in fiber height due to annealing. The insets in (c) and (d) show the averaged cross-section of approximately the same region of the same nanofiber.

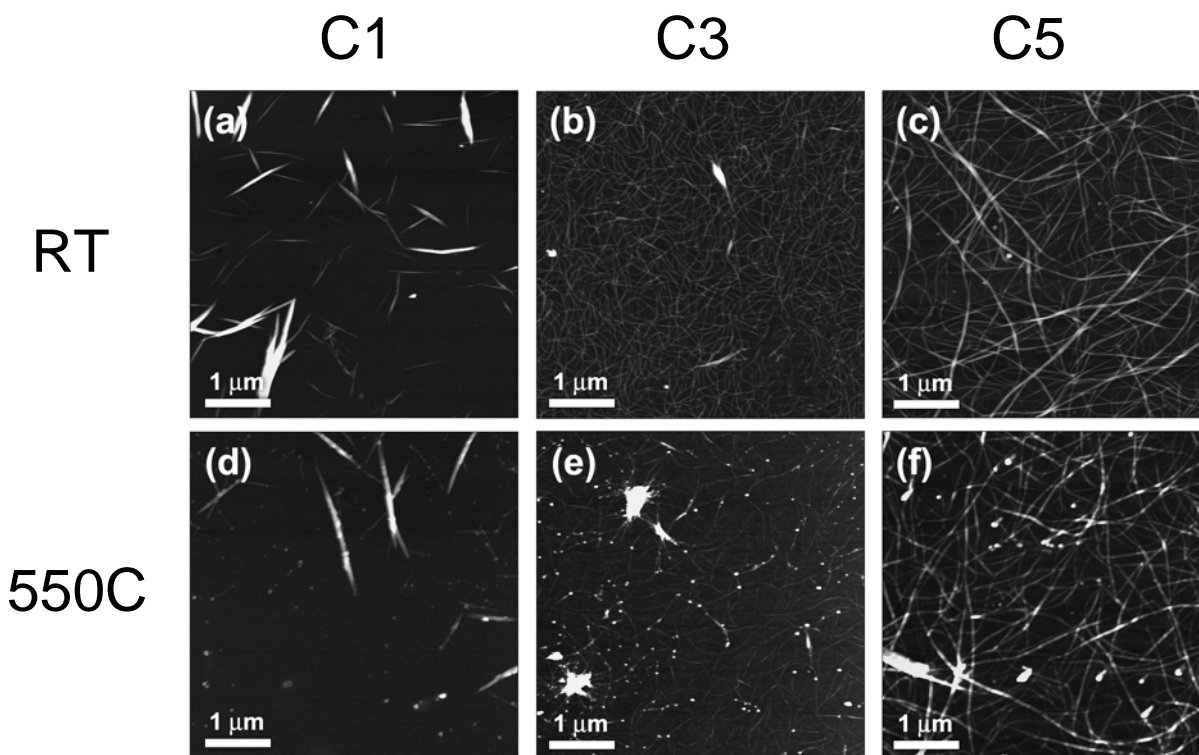


Figure 5.5. Pairs of 5  $\mu\text{m}$  x 5  $\mu\text{m}$  AFM height image of APA SANs on  $\text{Si}_3\text{N}_4$  taken at room temperature: C1 (a), C3 (b), and C5 (c) and after annealing for 30 min in air at 550C: C1 (d), C3 (e), and C5 (f).

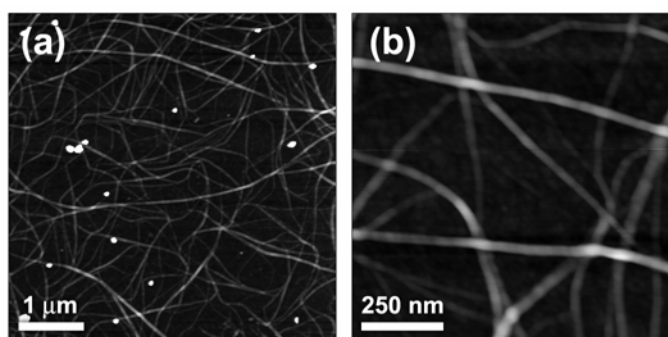


Figure 5.6. AFM height images of C5 SANs on  $\text{Si}_3\text{N}_4$  taken after annealing in air for 12 hrs at 550°C, 5 $\mu\text{m}$  (a) & 1 $\mu\text{m}$  (b).

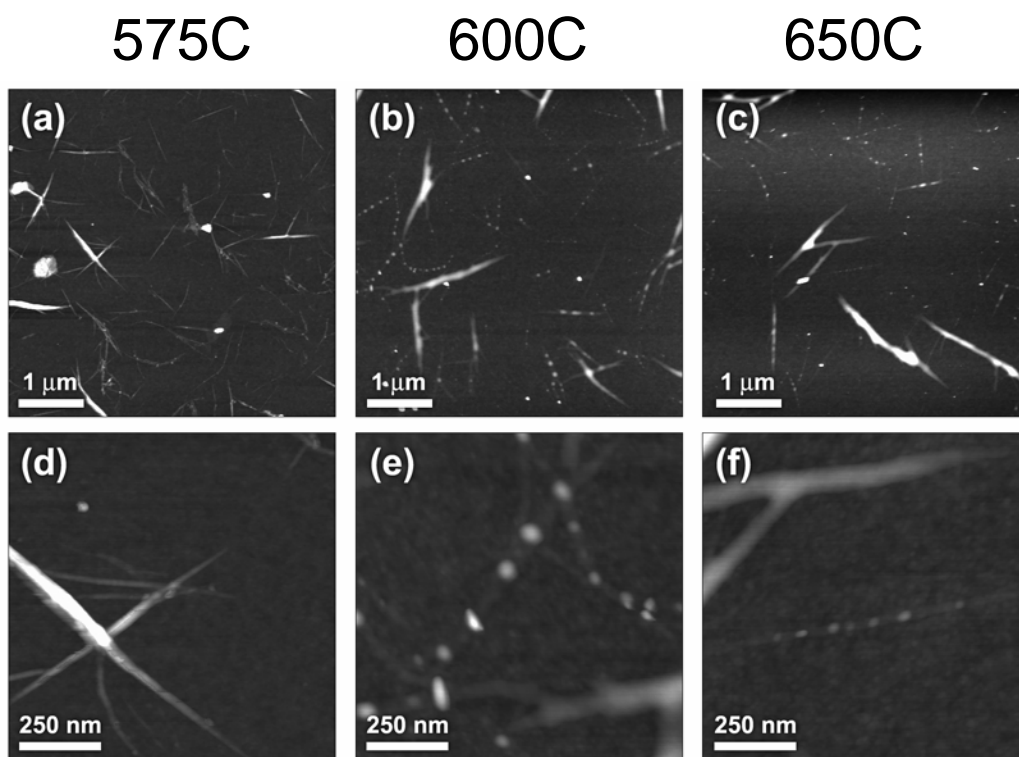


Figure 5.7. AFM 5  $\mu\text{m}$  and 1  $\mu\text{m}$  height image pairs of C1 SANs on  $\text{Si}_3\text{N}_4$  taken after annealing in air for 30 min at 575°C (a) & (d), for 6 hrs at 600°C (b) & (e), and for 6 hrs at 650°C (c) & (f).

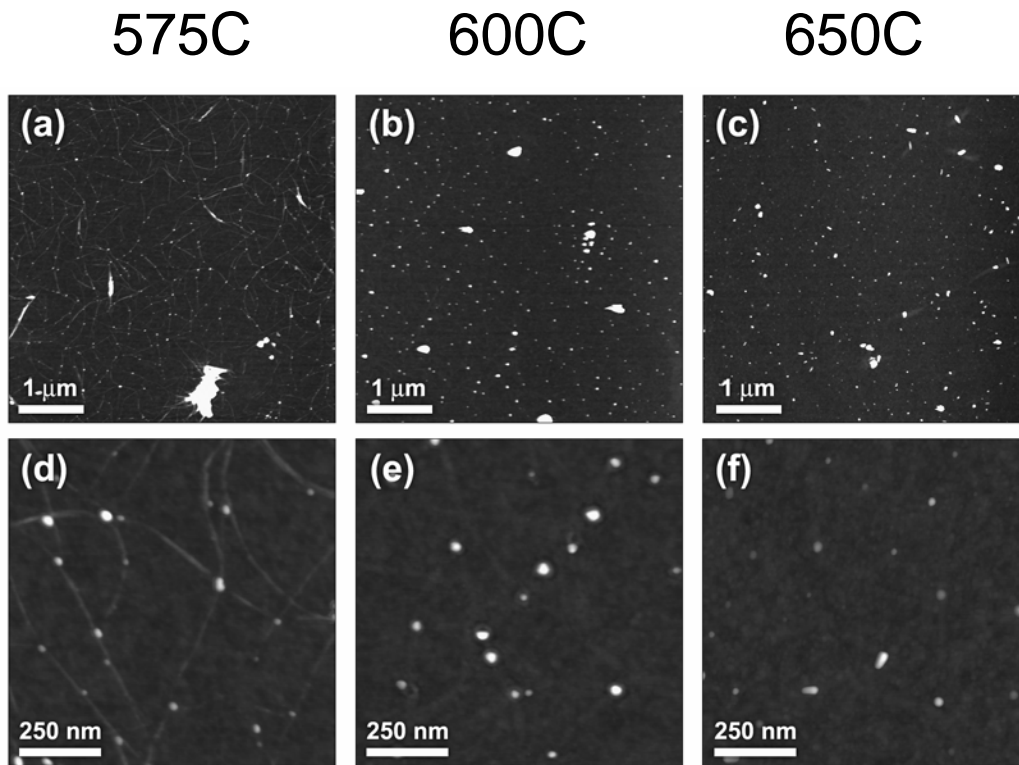


Figure 5.8. AFM 5  $\mu\text{m}$  and 1  $\mu\text{m}$  height image pairs of C3 SANs on  $\text{Si}_3\text{N}_4$  taken after annealing in air for 30 min at 575°C (a) & (d), for 6 hrs at 600°C (b) & (e), and for 6 hrs at 650°C (c) & (f).

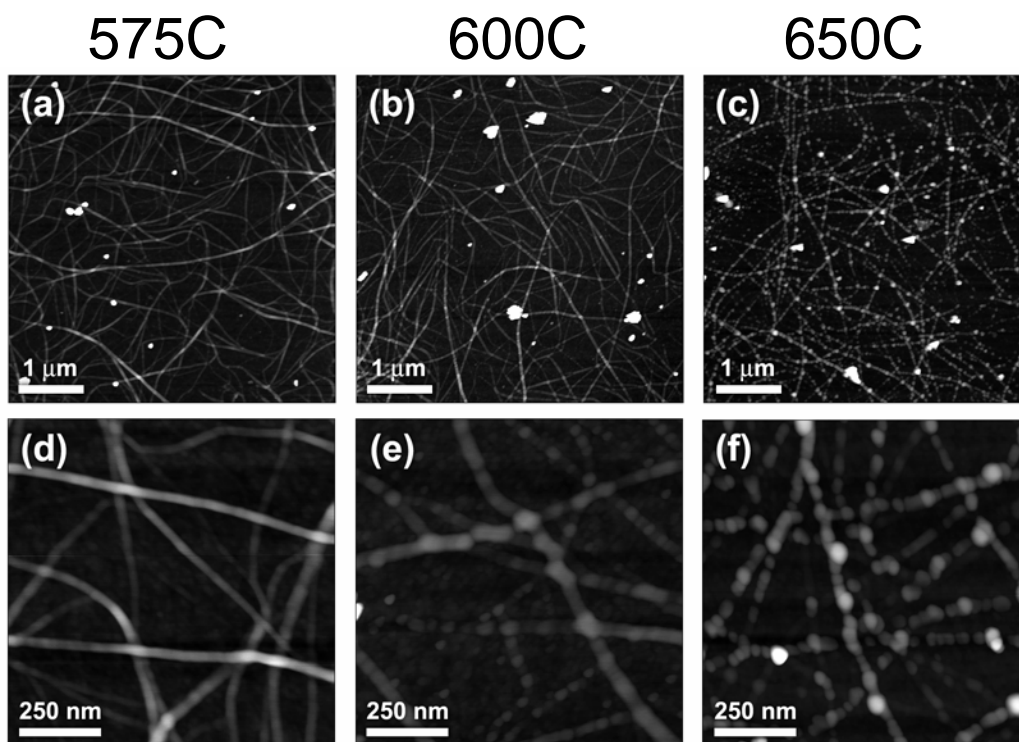


Figure 5.9. AFM 5  $\mu\text{m}$  and 1  $\mu\text{m}$  height image pairs of C5 SANs on  $\text{Si}_3\text{N}_4$  taken after annealing in air for 30 in at 575°C (a) & (d), for 6 hrs at 600°C (b) & (e), and for 6 hrs at 650°C (c) & (f).

## 5.7. References

- [5.1] Hanszen, K.J., *Theoretische Untersuchungen Uber Den Schmelzpunkt Kleiner Kugelchen - Ein Beitrag Zur Thermodynamik Der Grenzflachen*. Zeitschrift Fur Physik, 1960. 157(5): p. 523-553.
- [5.2] Wronski, C.R.M., *Size Dependence of Melting Point of Small Particles of Tin*. British Journal of Applied Physics, 1967. 18(12): p. 1731-&.
- [5.3] Hui, L., et al., *How does the nickel nanowire melt?* Applied Physics Letters, 2005. 86(1).
- [5.4] Hui, L., et al., *Melting behavior of one-dimensional zirconium nanowire*. Journal of Chemical Physics, 2004. 120(7): p. 3431-3438.
- [5.5] Qi, W.H., *Size effect on melting temperature of nanosolids*. Physica B-Condensed Matter, 2005. 368(1-4): p. 46-50.
- [5.6] Wang, J.L., et al., *Melting behavior in ultrathin metallic nanowires*. Physical Review B, 2002. 66(8).
- [5.7] Shvartsburg, A.A. and M.F. Jarrold, *Solid clusters above the bulk melting point*. Physical Review Letters, 2000. 85(12): p. 2530-2532.
- [5.8] Neves, B.R.A., et al., *Thermal stability study of self-assembled monolayers on mica*. Langmuir, 2000. 16(6): p. 2409-2412.
- [5.9] Fontes, G.N., R.L. Moreira, and B.R.A. Neves, *Thermally induced stacking of octadecylphosphonic acid self-assembled bilayers*. Nanotechnology, 2004. 15(5): p. 682-686.
- [5.10] Mutin, P.H., G. Guerrero, and A. Vioux, *Hybrid materials from organophosphorus coupling molecules*. Journal of Materials Chemistry, 2005. 15(35-36): p. 3761-3768.
- [5.11] Vioux, A., et al., *Hybrid organic-inorganic materials based on organophosphorus derivatives*, in *New Aspects in Phosphorus Chemistry Iv*. 2004. p. 145-174.
- [5.12] Guerrero, G., P.H. Mutin, and A. Vioux, *Anchoring of phosphonate and phosphinate coupling molecules on titania particles*. Chemistry of Materials, 2001. 13(11): p. 4367-4373.
- [5.13] Gawalt, E.S., et al., *Enhanced bonding of alkanephosphonic acids to oxidized titanium using surface-bound alkoxyzirconium complex interfaces*. Langmuir, 1999. 15(26): p. 8929-8933.
- [5.14] McElwee, J., R. Helmy, and A.Y. Fadeev, *Thermal stability of organic monolayers chemically grafted to minerals*. Journal of Colloid and Interface Science, 2005. 285(2): p. 551-556.

[5.15] Fontes, G.N. and B.R.A. Neves, *Effects of substrate polarity and chain length on conformational and thermal properties of phosphonic acid self-assembled Bilayers*. *Langmuir*, 2005. 21(24): p. 11113-11118.

# 6 Mechanical Stability

## 6.1. Introduction

The mechanical properties of new engineering materials play an important role in the determination of their potential applications and possible integration into existing manufacturing processes. With the growing importance of nanostructural engineering components being utilized throughout the majority of technologies today, it is of increasing interest to effectively characterize the mechanical properties of discrete structures with dimensions on the order of nanometers to 10s of nanometers. How will a nanostructure respond to an applied stress? Will it fracture like a ceramic or exhibit elasticity followed by plasticity like a metal? Or will it be some sort of combination of the two like in composite type materials? Ideally we would like to know the response of a nanostructure to externally applied stresses and to correlate it with its structure and composition as well as other physical characteristics such as thermal stability and electrical properties, developing useful structure property relationships.

Traditionally, the elastic modulus, or stiffness, is one property often utilized for making quantitative comparisons between different materials. Determination of the elastic modulus as well as a variety of other important mechanical properties of bulk materials has become routine. The development of equivalent nanoscale techniques for the determination of mechanical properties have greatly improved over the past decade as quantitative high resolution microscopy tools such as SEMs, TEM's and AFMs have also improved and become more commonplace. Reports in the literature of quantitative measurements of the mechanical properties of nanofibers, nanowires, and nanotubes generally fall into 3 basic methods: bending[6.1-3], pulling[6.4], and vibration[6.5-7], with each of these methods

having a variety of issues related to sample preparation as well as instrumentation limitations. To overcome some of the shortcomings of individual techniques, some methods utilize a combination of techniques. TEM with an integrated mechanical manipulation has been utilized for the extraction of elastic properties of nanotubes[6.8, 9] as well as direct observation of the fracture of polymeric nanofibers due to tensile loading[6.10]. In these cases however, the authors were able to manipulate and/or position individual nano(fibers-wires-tubes) into the required conformations needed for the specific testing methods. Since it was not yet possible to controllably manipulate individual alkylphosphonic acid (APA) self-assembled nanofibers (SANs), mechanical analyses were confined to SANs as grown. Specialized growth methods, as described in Section 3.2.5.1, were developed creating isolated APA SANs for qualitative and quantitative mechanical analysis on mechanically ridged  $\text{Si}_3\text{N}_4$  surfaces.

The work in this chapter focuses on the qualitative analysis of fractured SAN membrane surfaces with atomic force microscopy (AFM) and scanning transmission electron microscopy (STEM) as well as application of Hertzian mechanics to AFM nanoindentation data for the quantitative determination of the elastic modulus of individual SANs.

## 6.2. Qualitative STEM Analysis of Fractured C1 SAN Membranes

As described in Section 3.3.2 unsupported C1 SAN membranes were grown on aluminum coated ProtoChips™ DuraSIN™ TEM meshes in 8.3 mM solutions of C1 and EtOH. Structural and compositional analyses were performed utilizing STEM, EDS, and EELS, and details of that analysis presented in Section 4.3. In one case the resulting membranes were broken due to mishandling with tweezers. Figure 6.1 shows the broken DuraSIN™ TEM mesh with many C1 SAN membranes. The majority of the  $\sim 1 \text{ mm}^2$  support film remained intact. Instead of failing completely, cracks propagated through a large portion of the aluminum coated  $\text{Si}_3\text{N}_4$  thin film, around some individual windows as seen in Figure 6.1 (a), and into others Figure 6.1 (b). Overall, tens of membranes were affected by the cracking of the film and many were examined utilizing STEM. STEM SE and Z-Contrast imaging of the broken SAN membranes provided images of both the surface and internal structure of fractured SANs as well as SANs still under applied stresses.

In many instances, membranes were broken with no apparent crack propagation through the membrane or the surrounding film, as seen in Figure 6.2. Large pieces of the membrane remain intact with other smaller pieces, or chips, still attached. The presence of jagged fracture surfaces and planar chips seem indicative of a brittle fracture event. Examination of another fractured membrane, Figure 6.3 (a) shows how cracks propagating through the membrane are stopped by a single large SAN. Higher magnification Z-Contrast imaging reveals possible plastic flow or sliding between cracked layers or fibrils, Figure 6.3 (b-c). Direct evidence layer cracking and sliding is observed in Figure 6.3 (b). Within the individual fiber there are a series of dark regions with geometric edges denoted by the small white arrows. It is imagined that this kind of behavior could be expected of a stressed

structure composed of individual brittle layers, sheets, or fibrils interconnected through weaker van der Waals interactions of the alkyl chains.

While significant strain occurred, there was no evidence of necking that might be indicative of typical plastic flow as seen in metals[6.11]. Figure 6.3 (c) shows another region at a crack tip where we find further evidence of the crack propagating through fracture of different layers within the individual SANs. In this case, the crack propagated through the membrane from right to left until it encountered the large SAN, or mass of SANs, impeding its path and causing it to change direction. The same large SAN was responsible for slowing the propagation of both cracks.

The breakage of C1 SANs appears complex. While the breakage of entire membranes gives the appearance of simple brittle fracture, closer inspection of crack tip propagation provides evidence of a mixed failure mode. This kind of mixed behavior seems indicative of a composite type material having a strong brittle component embedded in a softer matrix. A fibril and layer sliding mechanism is thought to be the cause of observed plastic deformations. These deformations are contained within short 50 – 100 nm lengths due to pinning caused by the interaction of overlapping SANs.

### **6.2.1. E-Beam Manipulation of a Broken C1 SAN Membrane with STEM**

Imaging of C1 SAN membranes with the 200KV STEM e-beam at high magnifications (1,000,000 X) caused noticeable changes, such as stretching and movement of the SANs within individual membranes. It was surmised that these changes were possibly due to uneven heating or possibly charging effects between SANs. First, a suitable broken C1 SAN membrane was found having only one side attached to the surrounding support film. It was

first scanned at lower magnification to both document its initial state as well as charge the membrane, Figure 6.4 (a). After several scans, the magnification was slightly increased and the membrane was observed to curl upwards slightly Figure 6.4 (b). The magnification was increased further to 80KX so that the majority of the scan box was rastered into the vacuum and the membrane curled upwards even more, almost so that the end of the membrane was in a vertical position, Figure 6.4 (c). The magnification was then reduced back to 20KX and the membrane relaxed a little from its previous position while scanning at 80KX, but did not recover completely back to its initial position, Figure 6.4 (d). Another smaller chip of the membrane on the left side of the crack was also observed to roll upward, creating the appearance that the crack has widened. This process of zooming to 80KX and then zooming back out to 20KX was repeated several times as the entire chip of fabric on the right eventually folds over onto it self, Figure 6.4 (f).

Interestingly, the SAN membrane appears flexible enough to be folded over onto itself without breaking or fracturing along the bend giving the appearance of a fold with a radius of curvature. Unfortunately, no side-view images of the folded membrane were taken, making it impossible to fully determine the geometry of the fold itself. If we utilize the layered fibril model as previously described in Section 6.2, it would be expected that the radius of curvature of the fold would be large enough to accommodate layer sliding without complete breakage of the individual SANs. The direct manipulation of the SAN membrane with the e-beam seems to be indicative of columbic repulsion. This is possible evidence that the SANs are poor conductors, but this is still considered conjecture since no conductive control sample was utilized for comparison.

### 6.3. Nanoindentation

The majority of quantitative nanoindentation work now takes place with specialized equipment that utilizes capacitive load cells with highly stiff indenters, either in stand alone systems or as add-ons to AFM systems like the systems produced by Hysitron or the interfacial force microscope (IFM). In an attempt to make truly quantitative measurements of materials on the nanoscale, the flexible AFM cantilever has been replaced by a load cell with a diamond tipped indenter of known geometry. Successful quantitative analysis utilizing load-cell type nanoindenters of elastic modulus as well as the hardness of a variety of bulk materials, thin films and microstructures has been previously reported[6.12-17].

Nanoindentation of C1 SANs grown on  $\text{Si}_3\text{N}_4$  was attempted utilizing a stand alone Hysitron Triboscope at Oak Ridge National Laboratory with a highly trained Hysitron representative. Indentations were made using a cube corner indenter (the sharpest offered commercially), but from analysis of the resulting data it was impossible to distinguish the mechanical properties of the fibers from that of the underlying  $\text{Si}_3\text{N}_4$  support surface. Essentially, the Hysitron was able to reliably measure the modulus of the supporting  $\text{Si}_3\text{N}_4$ , as the indenter just pushed right through the fiber. The fibers were also greatly damaged due to the scanning of the sample in contact mode before and after each of the indents. This could not be avoided even when scanning with the lowest possible normal forces (still  $\mu\text{N}$ ). These results from the Hysitron nanoindentation experiment showed that higher force sensitivity during indentation and imaging were needed for the analysis of the C1 SANs.

AFM nanoindentation has been shown to be an effective way for making semi-quantitative mechanical response comparisons of polymers at nanometer length scales[6.18]. Many AFM nanoindentation studies have been carried out on a variety of bulk materials and

thin films of various materials from metals to semi-conductors to insulators to polymers[6.18-27]. By semi-quantitative, I mean, quantitative comparisons between different materials utilizing the same cantilever and tip can be made as long as careful attention is paid to the experimental setup.

Traditionally, semi-quantitative AFM nanoindentation experiments on a variety of bulk materials and thin films have been carried out utilizing a stainless steel cantilever with a Berkovich diamond indenter[6.28, 29]. These cantilevers are calibrated, giving the exact spring constant of the cantilever as well as having a known indenter geometry required for extraction of elastic modulus and hardness. After acquisition of a diamond tipped steel indenter, indentations were made on C1 SANs from the sample previously investigated utilizing the Hysitron Triboscope. The results of this experimentation suffered from essentially the same problems as with the Hysitron. In both cases, the techniques exhibited too little force sensitivity (the stainless steel cantilever  $k \sim 150\text{-}200\text{ N/m}$ ) required for making 1 – 5 nm sized indentations into a 20 nm wide structure, along with poor imaging resolution and sample destruction while scanning. However, unlike the Hysitron which only has one load sensor with a fixed sensitivity, the AFM's force sensitivity can be changed by changing the stiffness of the cantilever.

SAN sample preparation techniques available at the time of experimentation confined mechanical testing to the indentation of SANs on supporting  $\text{Si}_3\text{N}_4$ . Even though AFM nanoindentation is at best a semi-quantitative technique, known to have potentially 50-100% errors, it was chosen to investigate the mechanical properties of APA SANs due to its increased force sensitivity for making very small indentations and non-destructive tapping mode imaging capabilities.

### 6.3.1. General AFM Nanoindentation Procedure

The basic use and operation of the Digital Instruments D-3000 AFM is described in more detail in Section 2.2. Individual nanoindentation experiments performed with an AFM utilized tapping mode to first find a point of interest on the sample acquiring an image before indentation. Then the scan control was switched to point spectroscopy mode within the software for acquisition of a force curve, as seen in Figure 6.6. A force curve is simply a plot of the measured deflection of the cantilever (nm) vs. the piezo extension (nm), acquired during extension and retraction of the tip at a single point on the sample. The force curve has an extending portion where the tip is first pushed towards the surface (blue trace) by extending the Z piezo until a desired or threshold amount of deflection is measured by the photo-detector and then the tip is pulled back off the sample creating the retraction portion (pink trace). To avoid z-piezo creep issues influencing the measurements all indentations were made at rates of 4 Hz. This parameter was previously determined through experimentation for a similar DI D3000 instrument here[6.30]. A force curve contains information about the response of the material as well as the response of the cantilever. To decouple the sample response from the cantilever response, careful calibration of the piezo scanner and the cantilever must be performed.

The response of every cantilever is slightly different. In fact the response of the same cantilever is slightly different every time it is mounted and re-mounted in the AFM. Although the force constant of the cantilever does not change, the nature of the optical detection system is very sensitive to changes in path length, so we must calibrate the deflection sensitivity every time the cantilever is mounted and re-mounted. The deflection

sensitivity is calibrated by taking a force curve on a highly stiff sample, Figure 6.6, where no sample deformation, either elastic or plastic, occurs for the given forces utilized and the measured response is due only to the bending of the cantilever. Since we know how much the cantilever bends due to the length change of the z-piezo we can then convert the acquired deflection in Volts to nanometers. This conversion value is known as the cantilever sensitivity. It is simply the slope of the linear portion of the force curve taken on the calibration sample. This sensitivity value must be periodically checked between indentations to make sure it remains constant otherwise it will be impossible to make accurate comparisons between different indentations. The required stiffness of the sample utilized for determining the cantilever sensitivity depends on the stiffness of the given cantilever, but sapphire and fused silica are typically utilized. In the case of this work, the  $\text{Si}_3\text{N}_4$  support films the nanofibers were grown on were sufficiently stiff enough,  $E \sim 180 \text{ GPa}$ , for performing the required sensitivity calibrations for the silicon cantilevers having force constants up to  $\sim 70 \text{ N/m}$ .

### **6.3.2. Qualitative Analysis of Sample Stiffness**

To see if differences in elastic modulus could be observed utilizing AFM nanoindentation, force curves were acquired by making indents into a variety of samples having a range of known elastic moduli. Indentations were made utilizing the same cantilever on a sputtered 100 nm Au thin film on Si, a 200 nm thick evaporated aluminum film on Si, a bulk PET film, as well as a C5 SAN on  $\text{Si}_3\text{N}_4$ . The cantilever utilized was a typical tapping mode cantilever with a force constant estimated to be between 40 and 80 N/m (by the manufacturer) and total cantilever deflection was kept below 30 nm to minimize

damage to the tip as well as lateral translation during indentation. Figure 6.7 shows a comparison of the individual force curves obtained from indentations into each of the materials using the same cantilever. The steeper the slope of the linear portion of the force curve, the stiffer the material being indented, with  $\text{Si}_3\text{N}_4$  the stiffest (180 GPa), then Au (~80 GPa), then aluminum (~70 GPa), the PET film (~4 GPa), and lastly the C5 SAN (unknown modulus) being the least stiff.

The results of this experiment provided several insights about the investigation of the C5 SANs' mechanical properties. First, comparison of the trend of the force curve slopes matches well to the known modulus estimates of the materials utilized for comparison. The C5 SANs are observed to be considerably less stiff than the rest of the materials examined, which helps to put an upper limit on C5 SANs elastic modulus as being lower than the PET films at ~4 GPa. C5 SAN deformation began after only 1-2 nm of cantilever deflection. This made it difficult to examine the nuances of the individual indentations. It was deemed important to keep indents small as there is such a small volume of material with nanofibers generally 10 - 100 nm wide and 5 - 40 nm tall. Attempts were made to keep sample deformations in the elastic regime with small amounts of plastic deformation to try and minimize tip shape related errors. In this case the force constant of the cantilever was too large and the onset of plastic deformation occurred at very low deflections, ~0.25 nm, which was approaching the AFM's deflection precision of 0.1 nm [6.30]. To increase the AFM sensitivity, the cantilever force constant needed to be lowered even further. A lower force constant would allow for lower applied loads avoiding the early onset of plastic deformations and hopefully helping resolve the nuances of the SANs mechanical response.

### 6.3.2.1. Determination of Suitable Cantilevers

After the previous experiment it was determined that utilizing a cantilever with a lower force constant should greatly enhance the sensitivity of the measurements made into the SANs. It is important to note here that there is a major known issue with using an AFM cantilever to make controlled indentations. Once the tip makes contact with the sample and the cantilever begins to deflect a lateral displacement of the tip also occurs. There can be quite a large lateral motion of the tip as cantilever deflection increases. So while we want a cantilever that is flexible enough to provide increased levels of force sensitivity, we also don't want it to be so flexible as to introduce large lateral motions of the tip due to larger cantilever deflections needed to apply the required loads. It was important to optimize the force constant of the cantilevers as well as correcting for the lateral motion of the tip during indentation utilizing the X motion piezo correction factors built into the Digital Instruments Software[6.30]. For this work the correction parameter, was set in the software to 12 deg for all the indentations.

The actual determination of the ideal cantilever force constant needed for indentation of APA SANs was essentially a trial and error process. A variety of lower force constant silicon and  $\text{Si}_3\text{N}_4$  cantilevers, with force constants reported by their manufacturers as ranging from 0.1 N/m – 40 N/m, were deemed likely candidates. Indentations were then made into a variety of APA SANs using the variety of cantilevers. The results showed that cantilevers with force constants between 1 N/m and 15 N/m were deemed the most suitable. Cantilevers in this range were able to apply lower forces on the order of 10's of nN, for improved sensitivity while only increasing cantilever deflections slightly, minimizing the lateral motion of the tip during indentation.

### **6.3.2.2 Observation Cracking in C5 SANs**

During the efforts to determine the appropriate force constant cantilevers to use, many indentations were made into different SANs. Although the individual nanoindentation themselves were not quantifiable, a significant amount of information was learned by comparison of the before and after images of the indented SANs. Figure 6.8 shows a series of before (a) and after (b) images of a single  $\sim 25$  nN indent into a C5 SAN using a cantilever with  $k \sim .75$  N/m and tip radius  $\sim 2$  nm. From the digital zoom of the indentation area, Figure 6.8 (c), one can see that cracks propagate across the SAN emanating from the indentation site. The phase image in Figure 6.8 (c) shows that the SAN is comprised of vertical layers or lamellae that have shifted together, as denoted by the white lines. The C5 SANs also seem to exhibit a similar cracking and sliding phenomenon as the fractured C1 SAN membranes examined with STEM.

### **6.3.3. Quantification of AFM Nanoindentation Measurements**

#### **6.3.3.1. Double Spring Model**

The qualitative nanoindentation comparison presented in Section 6.3.2 provided an upper limit for the elastic modulus of C5 SANs as well as a range for the optimum cantilever force constants to use. To try and further quantify the elastic response of the individual SANs, the obtained deflection vs. piezo motion data must be converted into force vs. sample displacement data. The first step towards extraction of the SANs elastic response was to model the Tip-Sample interaction of the AFM with an individual APA SAN. Figure 6.9 shows a schematic of the tip-sample interaction modeled as two springs in series. This is the

model that was utilized throughout this work and has been shown elsewhere to be a feasible way of modeling the tip sample interactions[6.31]. We then consider the cantilever to be one spring and the SAN the other with the silicon tip making contact between them.

To understand the contributions of the cantilever deflection to the deflection of the cantilever when indenting an unknown sample, we first calibrate the cantilever on a very stiff material as described previously in Section 6.3.2. A single nanoindentation then produces a force curve of cantilever deflection in nm vs. Piezo length in nm. This must then be converted to Force vs. sample displacement so an appropriate model can be applied to extract the elastic response.

#### **6.3.3.2. Converting to Force vs. Displacement**

Conversion of the deflection (nm) vs. piezo data (nm) into force (nN) vs. displacement (nm) was required in order to apply a contact mechanics model to estimate the elastic modulus of individual SANs. The conversion of the data was a multi-step process. First, the two spring model was applied to deflection force curve data, subtracting the measured deflection  $D$  from the change in piezo length  $\Delta Z$ . This difference gave the change in sample height,  $h$ , occurring during the acquisition of the force curve. Determination of the force applied to the sample was then calculated from Hooke's law for a cantilever beam:

$$F=k_T x$$

where  $k_T$  equals the force constant of the cantilever and  $x$  equals  $D$  or the measured cantilever deflection at each point. The Sader method was utilized to estimate the force constant  $k_T$  of a given cantilever[6.32]. The Sader method gives an estimate of the cantilever force constant to within +/-10%. Sader provides an online calculator for cantilever  $k$

calculations at <http://www.ampc.ms.unimelb.edu.au/afm/calibration.html> as well as theory and Mathematica workbooks for further experimentation. The dimensions of the cantilevers utilized in this work were measured using a calibrated optical microscope and the resonance peak frequency and Q factor obtained from the DI nanoscope IIIa software tuning subroutine.

The force curve data was exported from The DI software and into an excel spreadsheet. The data was converted from DI LSB values to Volts and then to nm utilizing the measured cantilever sensitivity and Z-piezo calibration. The Deflection vs. Z-piezo force curves were then normalized so that the baseline deflection and Z-piezo position were offset to zero at the point of contact. The normalized deflection data was then converted to Force vs. Sample Displacement for comparison between indents and estimations of the elastic modulus using a simple Hertzian contact mechanics model. This conversion can be seen in Figure 6.10 where both the deflection vs. piezo travel force curve and the resulting Force vs. Sample deformation are plotted side by side.

### **6.3.3.3. Elastic Modulus Determination Using Hertzian Contact Model**

Classical contact mechanics models are typically utilized for the analysis of nanoindentation data[6.33, 34]. The methods for determining the mechanical properties from the measured force curves were initially developed in 1986 by Doerner and Nix, and further refined by Oliver and Pharr[6.35] and Field and Swain[6.36]. These methods, for indents typically 100's of nm deep, utilized the unloading portion of the force vs. displacement curve to derive the Young's modulus and hardness for bulk materials. The extension of these methods for analysis of thin films poses many challenges due to the influence of the substrate on the calculated modulus values[6.37]. This substrate influence was considered a major

issue when dealing with measurements taken on individual SANs having yet smaller volumes of material than thin films.

To help minimize substrate effects when indenting thin films, it has been found that the indentation depth needs to be less than  $1/10^{\text{th}}$  of the thickness of the film being indented[6.38, 39]. Although substrate effects can possibly be minimized by making shallow indents, tip-surface interactions can then dominate, causing the calculated modulus values to appear higher than expected[6.38]. Due to this substrate influence, it is expected that the values obtained by quantitative nanoindentation of SANs on  $\text{Si}_3\text{N}_4$  will at best provide an upper limit for the actual value for the SANs elastic modulus. For this work the SANs were assumed to be isotropic, which is an admitted oversimplification necessary for the application of Hertzian contact models.

In this work a simple Hertzian mechanics model was utilized for estimating the elastic modulus of individual C1, C3, and C5 SANs grown on  $\text{Si}_3\text{N}_4$  thin film substrates. The Hertzian solution for the force  $F$  in terms of the contact radius  $R$  of a sphere with a plane is described by the expression[6.38].

$$F = \frac{4}{3} E^* R^n h^m \quad (1)$$

where  $F$  is the force applied by the tip,  $E^*$  is the reduced elastic modulus of the sample,  $R$  is the tip radius,  $h$  is the sample displacement and  $n$  and  $m$  are fitting parameters based on the indenter geometry. For Hertzian interaction model  $n = 0.5$  and  $m = 3/2$ . The reduced elastic modulus  $E^*$  is then given by the following expression,

$$\frac{1}{E^*} = \frac{(1-\nu_s)}{E_s} + \frac{(1-\nu_t)}{E_t} \quad (2)$$

Where  $\nu_s$ ,  $\nu_t$ ,  $E_s$ , and  $E_t$  are the Poisson's ratios and the Elastic Moduli of the sample and silicon tip respectively. In this case the contribution to the reduced modulus  $E^*$  due to the silicon tip ( $E_t \sim 110$  GPa) is considered to be much less than that of the SANs and is considered to be essentially 0. Since the Poisson's ratio of the SANs is unknown, only comparisons of the reduced modulus could be made. Application of the Hertzian model to the Force vs. Displacement data from a single indentation into a C5 SAN as seen in Figure 6.10 shows that it fits excellently. All fitting of Hertzian models was done by eye within Excel. Further development of software fitting was deemed too intensive for the scope of this work and simple visual fitting methods were utilized. Future work to examine the accuracy of the techniques utilized for this study would also need to include the development of fitting software for better extraction of elastic properties and statistical analysis of the results.

#### **6.3.3.3.1. Determination of Tip End Radius**

One of the major uncertainties associated with utilizing the Hertzian model or any other model for elastic modulus determination is related to accurate assessment of the tip end radius. This effect on the Hertzian model is shown in Figure 6.11, where a 20 nm variation in the tip radius causes an observable difference in the slope of the curve when holding elastic modulus constant at values of 1, 5, 10, and 100 GPa. The Elastic modulus varies inversely with tip radius, but with careful tip characterization an error of 20 nm will create errors of far less than an order of magnitude in the value of the calculated elastic modulus allowing differences of several GPa possible.

The main requirement for the Hertzian mechanics model to be valid is that the end of the tip needs to be spherical, else the fitting parameters,  $n$  and  $m$ , must be adjusted to account for any irregularities. As the tip shape deviates from spherical it becomes increasingly difficult to discern between contributions to the measured modulus value due to the material itself or rather to irregular changes in the contact area as a function of indentation depth. So in an effort to avoid deviations for spherical contact areas, indentations are kept to a minimum, with total deformations of the SAN to  $\sim 10$  nm.

Two methods were developed to estimate the tip radius in an attempt to provide self-consistency between indentations. The first method was to make indentations into a material with a known modulus. Figure 6.12 shows a series of force vs. displacement curves for four indents of increasing loads made in succession at the same location on a PET thin film with a known elastic modulus. The PET film had a measured RMS roughness of  $\sim 1$  nm and an elastic modulus of  $\sim 4$  GPa. The modulus of the film was previously determined using Dynamic Mechanical Analysis (DMA). The data from the four indentations show very good correlation between the unloading curves of each indent. An overlay of the Hertzian model fits the retraction curves excellently. Setting the value of  $E^*$  to 4 GPa, as previously measured by DMA, a value of 35 nm is obtained as a good estimate of the tip end radius.

The second method utilized for estimating the tip end radius was to utilize a commercially available, Micromasch TGT01 tip probe characterizer, as seen in Figure 6.13. The characterizer is comprised of an array of high aspect ratio silicon spikes with nominal end radii of less than 10 nm. Multiple images of the tip are formed since the characterizer spikes are generally as sharp or sharper than a typical tip, Figure 6.14 (a). By zooming in on the height image at the very apex of the tip, Figure 6.14 (b-c), an estimate of the end radius

and tip geometry can be made, Figure 6.15. If the tip shape deviates too much from spherical, especially for  $< 5\text{nm}$  indentation depths utilized in this work, then the fitting parameters utilized in the Hertzian analysis would have to be corrected[6.37].

In the case of indentation of the nanofibers, the indents were kept small, 1-5 nm to minimize effects from the  $\text{Si}_3\text{N}_4$  substrate and to try and minimize the plastic deformation of the SANs. These values helped to define the portion of the tip that needs to be examined and further modeled as a sphere. The section analysis, Figure 6.15, of the tip image from Figure 6.14, shows that in this case the tip is not symmetric and an estimate from the image would appear that the radius is  $\sim 15\text{ nm}$  in one direction and  $\sim 25\text{ nm}$  in the other.

Although the end of the tip is not spherical, the associated errors were not considered to be greater than any of the other errors associated with these kinds of measurements. The estimate of 35 nm given by the Hertzian fit of the PET film is in good agreement with the directly measured values to within the 20 nm error previously deemed acceptable. It is quite likely that the error between the two measurements could be due to the 10% error associated with the cantilever force constant determination utilizing the Sader Method[6.32].

#### **6.3.4. Quantitative Nanoindentation of APA SANs on $\text{Si}_3\text{N}_4$**

Quantitative nanoindentation measurements of SANs were performed after calibration of the AFM's sensitivity, Sader estimation of the cantilever force constant ( $k \sim 8.4\text{ N/m}$ ) and the tip's end radius determined as outlined in the previous sections. C1, C3, and C5 SANs on  $\text{Si}_3\text{N}_4$  thin films were utilized for AFM nanoindentation measurements. The samples utilized were grown according to the procedure described in Section 3.2.5.1. The three week immersion samples were chosen for measurements.  $\text{Si}_3\text{N}_4$  was chosen as a substrate partially

for its high mechanical and chemical stability and ease of sample preparation as the nanofibers grow quite readily on  $\text{Si}_3\text{N}_4$  as compared to other mechanically suitable surfaces. Generally, C1, C3, and C5 nanofibers at least 50 nm wide and 20 nm tall were utilized. It was also deemed important to indent on SANs that appeared to be laying flush against the  $\text{Si}_3\text{N}_4$  surface, so that odd twisting or bending effects could be avoided. In one case an indentation was purposefully made at the point of overlap of two C5 SANs in an attempt to discern whether there were any differences in mechanical stability relative to a single fiber.

#### **6.3.4.1. C5 SANs**

Figure 6.16 (a-a2) shows an individual 40 nm tall C5 SAN before indentation with the indentation site carefully centered in the field of view. Figure 6.16 (b-b2) shows the same fiber after a series of 10 indentations in the same spot. There appears to be a single indentation that appears to be completely contained within the fiber. This is more clearly seen in Figure 6.16 (b2).

The resulting Force vs. Displacement curves for each of the 10 indentations was plotted in succession to show the progress of the surface after each indentation, Figure 6.17. The first indentation, corresponding to 1 nm of deflection ( $\sim 8.4$  nN), appears to be entirely elastic as there is nearly perfect correlation between the extending and retraction data. It is important to note that the total fiber displacement measured over the course of the 10 indents exceeds the height of the SAN measured from the before height images in Figure 6.16 (a). This was at first a bit disconcerting, but will be explained later in this section.

Utilizing 35 nm as the tip radius, Hertzian fits were applied to the retraction curves of the first 6 indentations as seen in Figure 6.18. We see an interesting trend as the modulus is

observed to increase from  $\sim 1.5$  GPa in the case of indent 1 and indent 2 to  $\sim 35$  GPa for indentation 6 which starts almost  $\frac{3}{4}$  of the way through the initially measured fiber height. This trend of increasing elastic modulus with indentation depth is exactly as predicted. With the first 5 indents we see the same initial slope of the extending curve with a yield of slightly less than 10 nN. The 6<sup>th</sup> indent is missing this feature. It also appears that there may be viscoelastic properties influencing the retraction data for indents 3 – 10. The relaxation of the sample appears as a deviation from the Hertzian behavior with additional displacement occurring after the initial retraction of the sample. Since we are interested in determining the elastic properties of the nanofibers as accurately as possible, the first 2 indents are chosen as being better representative, minimizing sample deformations, possible contact area issues, and substrates influence on the measured modulus value.

In an attempting to learn more about the mechanical stability of overlapping C5 CANs an indentation was made at the intersection of two C5 SANs. The initial height of the pair was  $\sim 50$  nm. Figures 6.19 (a-b) are the tapping mode height images showing the indentation site before and after respectively. In this case, the indent is nice and centered in the intersection with no uneven pile up showing that the motion of the tip is essentially vertical and the lateral compensation is working well. Figure 6.19 shows the resulting force vs. displacement data for this  $\sim 84$  nN indentation. Interestingly, the same initial slope ( $E^* \sim 1.5$  GPa) with yield point between 10 – 15 nN is present just as in the single fiber indentation series. If we compare the first two indents of the single fiber with the indent of the overlapping fibers we see very good correlation between the separate indentation events, Figure 6.19. The Hertzian fit of the overlapping fiber retraction data gives us an  $E^*$  value of  $\sim 5$  GPa. The fit also shows significant deviations from ideal Hertzian behavior, quite

possibly due to viscoelastic properties[6.18]. The viscoelastic behavior seen in the overlapping fiber indent data correlates well with the data from indent 5 in the single SAN series. Both have approximately the same overall displacement and presumably similar contact areas during the indentation event. Confidence in the techniques was greatly increased as indentation measurements made on separate SANs exhibit nearly similar responses for indentations of nearly equivalent depths no matter if it is a single or overlapping SAN.

#### **6.3.4.2. C3 SANs**

Next, a series of 10 indentions was performed at the same spot on a single C3 SAN. Figure 6.20 (a-b) show the C3 nanofiber before and after the indentations. Unlike the slightly larger C5 SANs, this C3 SAN is ~10 nm tall at the point of indentation. From the shape of the resulting indentation figure 6.20 (b) it appears that the indentation spot moved during 10 indentations. From the Force vs. Displacement data in Figure 6.21 we see that the first 4 indents exhibit nearly complete elastic behavior with good correlation between the extending and retracting curves. Indent 5 shows the first evidence of plastic deformation occurring after approximately a 1 nm indent of 40 nN of force and indent 6 shows strikingly different loading behavior with much more plastic deformation. If we compare the initial elastic indents 1, 3, and 4 with indent 6, Figure 6.22, we see that  $E^*$  is observed to increase from 3.3 GPa to 9 GPa. Once again it is assumed that the measured  $E^*$  value from deeper indentation measurements contain more substrate contributions as previously noted in the C5 nanofiber analysis. Thus the value of 3.3 GPa is considered more accurate.

#### **6.3.4.3. C1 SANs**

Lastly, 2 indents were made into a single C1 SAN at the same position, Figure 6.23. Just as in the C3, and C5 indentations discussed previously, an increase in the measured modulus with increased applied forces and sample displacements is observed. There is little evidence of plastic deformation excepting slight changes in the height and width of the SAN. Figure 6.24 shows the Force vs. displacement curves along with their corresponding Hertzian fits. There is no discernable yield point as observed in the case of C5 and to a lesser extent the C3 indentations. This correlates well with the lack of cracking observed. The measured modulus of the C1 SAN appears to be higher with a value of  $\sim 10$  GPa. A familiar viscoelastic response similar to both indents into C5 and to a lesser extent C3 nanofibers is observed in the second indentation retraction data. This effect is noticed as a significant deviation from Hertzian behavior.

#### **6.3.4.4. Comparison of C1, C3, and C5 SANs Stiffness**

The data previously shown in this section for C1, C3, and C5 SANs was taken utilizing the same cantilever ( $k = 8.4$  N/m). The cantilever sensitivity and tip radius were checked made between the indentations made on each sample to ensure consistency between indentation experiments and to allow for direct comparisons. The instrument and cantilever remained very stable with negligible changes to the sensitivity and no perceivable changes to the tip radius occurred during the acquisition of the data. Indentations were also made into a PET film of known modulus using the same cantilever and tip. Hertzian fits of the retraction curves utilizing the known elastic modulus of 4.0 GPa provided an estimate of 35 nm for the

tip radius. A comparison of selected results from the SANs with the PET film gives both a qualitative as well as a quantitative estimate for the reduced elastic modulus ( $E^*$ ) of the SANs. Figure 6.25 shows a comparison between selected Force vs. Displacement curves of C1, C3, and C5 SANs with that of PET all plotted with the same scale. The curves presented correspond to selected indentations where the response of the sample was observed to be mostly elastic with a minimum of plastic deformation. Table 6.1 then shows a summary of the experimentally determined reduced elastic modulus ( $E^*$ ) values for C1, C3, C5 SANs utilizing Hertzian fits of the retraction curves. At least 5 indentations were utilized to calculate the average  $E^*$  of 10.52 GPa, 3.78 GPa, and 1.25 GPa for C1, C3, and C5 SANs respectively. In this case the  $E^*$  of the PET was considered to be 4.0 GPa.

In an effort to ascertain the reliability of the technique, the Hertzian model was applied to data from indentations made into C5 SANs utilizing cantilevers having force constants of 0.73 N/m and 66.0 N/m and tip radii of 35 nm and 20 nm respectively. Once again indentations were also made into the PET control for comparison and tip radius determination. Table 6.2 shows a summary of the results obtained with three different cantilevers. All the values agree quite well and all fall within the respective standard deviations showing that the extracted  $E^*$  values are quite consistent and less than the values determined for the C3 and C1 SANs.

The fact that the measured  $E^*$  values for C5 are so consistent, even between cantilevers, provides strong evidence that the differences in the measured  $E^*$  values for C1, C3, and C5 SANs are likely significant.

## 6.4. AFM Nanoscratching of C3 SANs

In an addition to compressive nanoindentation it was also of interest to examine the mechanical behavior of the nanofibers due to lateral deformations. The results of nanoindentation on individual SANs showed evidence of cracking and lateral translations due to the applied loads. This was in good agreement with the high resolution STEM images of crack propagation sites in SAN membranes that also appear to show cracking and layer sliding within an individual C1 SAN. This type of mechanical anisotropy would allow for increased localized strains without complete failure of the nanofiber bundle as the internal sliding would compensate for the cracking within individual layers or fibrils. The sliding appears to occur along the long axis of the fiber and as the cracking is observed to occur in a direction somewhat perpendicular to the sliding direction. STEM investigation of crack propagation through the membranes indicates that the connections or overlaps of fibers are quite strong creating a ridged, interlocking structure which then limits the compliance of individual SANs. The network structure then limits the lateral translation of strain in the overall structure creating the appearance of a brittle fracture of the entire membrane as these connection points would set up pinning sites for which SANs would be kept from sliding. Closer inspection of cracks propagating through the membrane revealed that in reality the internal mechanisms for failure are two fold, having both brittle and ductile qualities as might be seen for a composite type material.

In this section the results from the lateral deformation of a Single C3 SAN on  $\text{Si}_3\text{N}_4$  are presented. The results are in good agreement with a fibrillar or layered model for the SANs.

### 6.4.1. Nanoscratching Experimental Details

AFM nanoscratching was utilized to examine the behavior of individual SANs to applied lateral or shear forces as well as to examine the connections between adjacent SANs to see if they are indeed rigid contacts as indicated by the STEM imaging.

C3 SANs grown on  $\text{Si}_3\text{N}_4$  were utilized as they provided a good distribution of interconnected single SANs with plenty of  $\text{Si}_3\text{N}_4$  between them making for easier analysis of lateral deformations. To make lateral deformations of the individual C3 SANs, a Digital Instruments D3000 AFM with a typical DI tapping mode tip with a nominal 40 N/m spring constant and 4-sided pyramid geometry was utilized. For each scratch, a normal force of  $\sim 200$  nN was chosen such that scratching would not do excessive damage to the tip, but was high enough to remain in contact with the  $\text{Si}_3\text{N}_4$  as the SANs were displaced laterally. Then for each of the individual scratches the tip was displaced in the +x direction a set amount, typically 10 – 100 nm at 1 Hz scan rate. The scratch direction was always set to zero degrees corresponding to one of the tip edge directions and vertically aligned SANs were chosen to deform so the scratch would be perpendicular to the long SAN direction. Images of the SAN of interest were always taken before and after scratching in tapping mode to examine the effects of lateral deformation on the morphology of the SAN and surrounding SANs.

### 6.4.2. Results and Discussion

Figure 6.26 is a series of AFM images captured before (a), after a 50 nm deformation (b), and after an additional 100 nm deformation (c) of an individual C3 SAN on  $\text{Si}_3\text{N}_4$ . For each instance a height, phase and 3D height image are presented. Figure 6.27 then shows a series of overlays of the thresholded height images from each instance added to the next, such that

(a) is before (white), (b) is the result of the 50 nm deformation (red) overlaid on the result from (a) and in the same manner (c) is the overlay of the result of the 100 nm deformation (blue) overlaid on (b). A schematic of the lateral deformations is also included on each of the images with the arrow length indicating the length of the scratch utilized to create the deformation that is observed. The vertical lines are included as reference. Two black dots were added to represent what are being called “pinning sites” or points on the SAN that appear fixed relative to the rest of the deformations observed to occur between them.

The 50 nm scratch produces slightly less deformation indicating possible elastic recovery. The SAN appears to bend along the entire length of the SAN between the two pinning sites as indicated in Figure 6.27. Failure of the SAN, observed in Figure 6.27 (c), occurs as a break across the fiber some distance from the contact site during the 100 nm scratch. The contact site after the 100 nm deformation exhibits an impression of the edge of the tip with the SAN bending around the tip and the width of the SAN remaining approximately the same as before the scratch. The SAN doesn't slide over the other SANs that it is lying on top of indicating that the connection between SANs is quite strong. This is in good agreement with the previous STEM findings of C1 SAN cracking. There are also indications, most easily seen in the phase image of Figure 6.26 (c) showing what appears to be SAN residue left behind after the majority of the SAN is translated to the right. These residues seem to be located near what appears to be a branching site, possibly indicating that the SANs are connected strongly to the  $\text{Si}_3\text{N}_4$  at branching sites.

Another 100 nm scratch was carried out adjacent to the lower pinning site and documented in Figures 6.28. Once again the the SAN is laterally translated by the scratch amount. Once again small amounts of residue are observed to remain on the  $\text{Si}_3\text{N}_4$  after the

SAN is laterally translated. The residue is denoted by white arrows in the phase image. The SAN in this case actually gets pushed up on top of the adjacent SAN and appears to stay intact with only an impression indicative of the tip edge geometry in the left side. Once again it doesn't appear the SAN has compressed to accommodate the tip edge, but rather it bends around the tip. In this case the points at which the SAN were attached to the surface or an adjacent SAN was approximately twice as large as in the case of the first 100 nm scratch. This could be a possible explanation for why the SAN doesn't break, especially at a point closer to the bottom where it crosses other SANs.

## 6.5. Discussion

Qualitative assessments of C1 SANs mechanical behavior were performed utilizing STEM of broken unsupported C1 SAN membranes. The fracture of SAN membranes appeared to be brittle in nature when investigated at the scale of the whole membrane. The majority of fractured SANs were observed to have broken cleanly, mostly at oblique angles relative to the SANs long axis direction. Further investigation of individual SANs remaining intact within active fractures showed evidence of stress relaxation through a layer cracking and sliding mechanism. This type of failure is often seen in composite type materials where there is a stiff material embedded in a softer matrix. Generally, the individual SANs were in a strong network structure with the other SANs they connected with or crossed over. This caused a pinning of the individual SANs and limited the amount of sliding between layers to relatively short distances, on the order of 100 – 200 nm. It is believed that this pinning or limitation of fibril sliding exacerbated the occurrence of brittle fractures within the whole membrane. In contrast to the fracture in shear caused by the propagation of cracks through the membrane, flexibility of a SAN membrane was observed through e-beam manipulations. An entire SAN membrane was folded over onto itself utilizing a proposed columbic repulsion mechanism. Both the shear and folding responses observed in the STEM provided further evidence that the individual SANs do indeed have a layered or fibrillar internal morphology that has different mechanical responses in different directions being comparable to the response of composite type materials. This type of mechanical behavior agrees well with the internal fibril structuring of APA SANs as previously discussed in Chapter 4.

In addition to the STEM analysis of previously broken C1 SANs, AFM nanoindentation and nanoscratching were performed making highly localized and controlled deformations of

APA SANs. Indentations made into C5 SANs showed evidence of cracking and layer sliding occurring in response to the applied loads from the tip. Lateral deformations of C3 SANs showed further evidence of pinning between overlapping SANs and an internal fibril or layered structure with the SAN bending around the point of contact with the tip. The lateral deformations provided evidence that the C3 SANs do plastically deform under applied stresses. After scratching, individual SANs had kinks in the shape of the tip faceting with breakage of the SAN occurring some distance away from the impact site.

Lastly, an attempt to quantify the elastic modulus of the SANs was performed by application of a Hertzian contact model to the retraction curves of indentations made into C1, C3, and C5 SANs. Indentations were also made into a PET film having a known elastic modulus of 4 GPa for comparison. The reduced elastic modulus ( $E^*$ ) was 10.52 GPa, 3.78 GPa, and 1.25 GPa for C1, C3, and C5 SANs respectively. To examine the repeatability of the technique,  $E^*$  was calculated for indentations made into C5 SANs utilizing cantilevers with 0.73 N/m, 8.4 N/m, and 66 N/m force constants. In each case the indentations into the PET film were utilized as a control for the Hertzian fits providing estimates of the tip radius. 1.20 GPa, 1.25 GPa, and 1.83 GPa were the values for  $E^*$  obtained utilizing the three respective cantilevers. In each case the range of  $E^*$  utilizing the standard deviations obtained was less than the range of  $E^*$  found for C3 and C1 providing evidence that the differences between C1, C3, and C5 SANs are real. From the findings it is believed that the  $E^*$  of the SANs increases with decreasing chain-length giving  $E^*_{C1} > E^*_{C3} > E^*_{C5}$ .

## 6.6. Figures

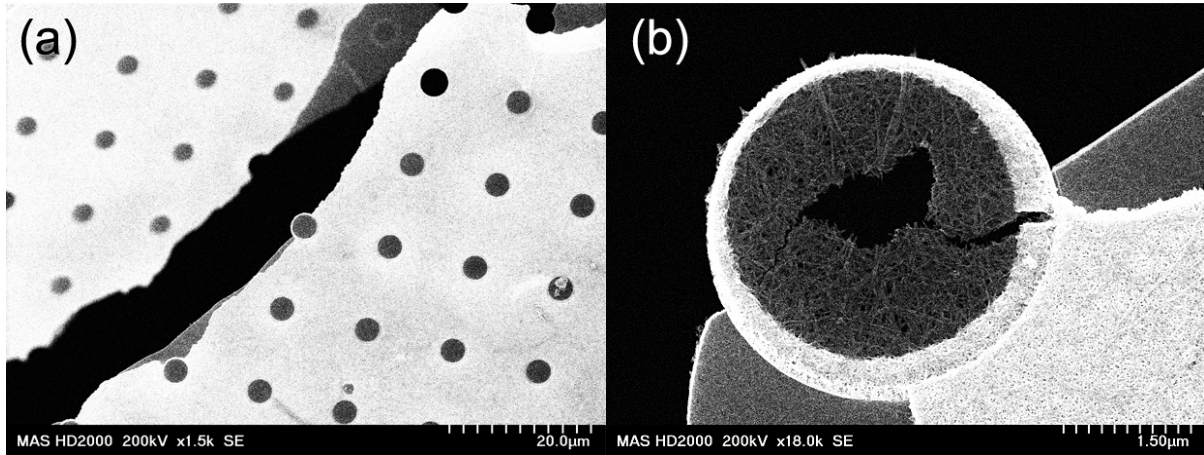


Figure 6.1. STEM SE image of the crack formed in an aluminum coated ProtoChips™ DuraSIN™ mesh (a) and an individual C1 SAN membrane (b) after puncturing with tweezers. In some cases the crack makes it all the way around a window leaving membranes intact (a), but in many cases it propagates right through the SAN membranes in a brittle fashion often with small chips missing (b).

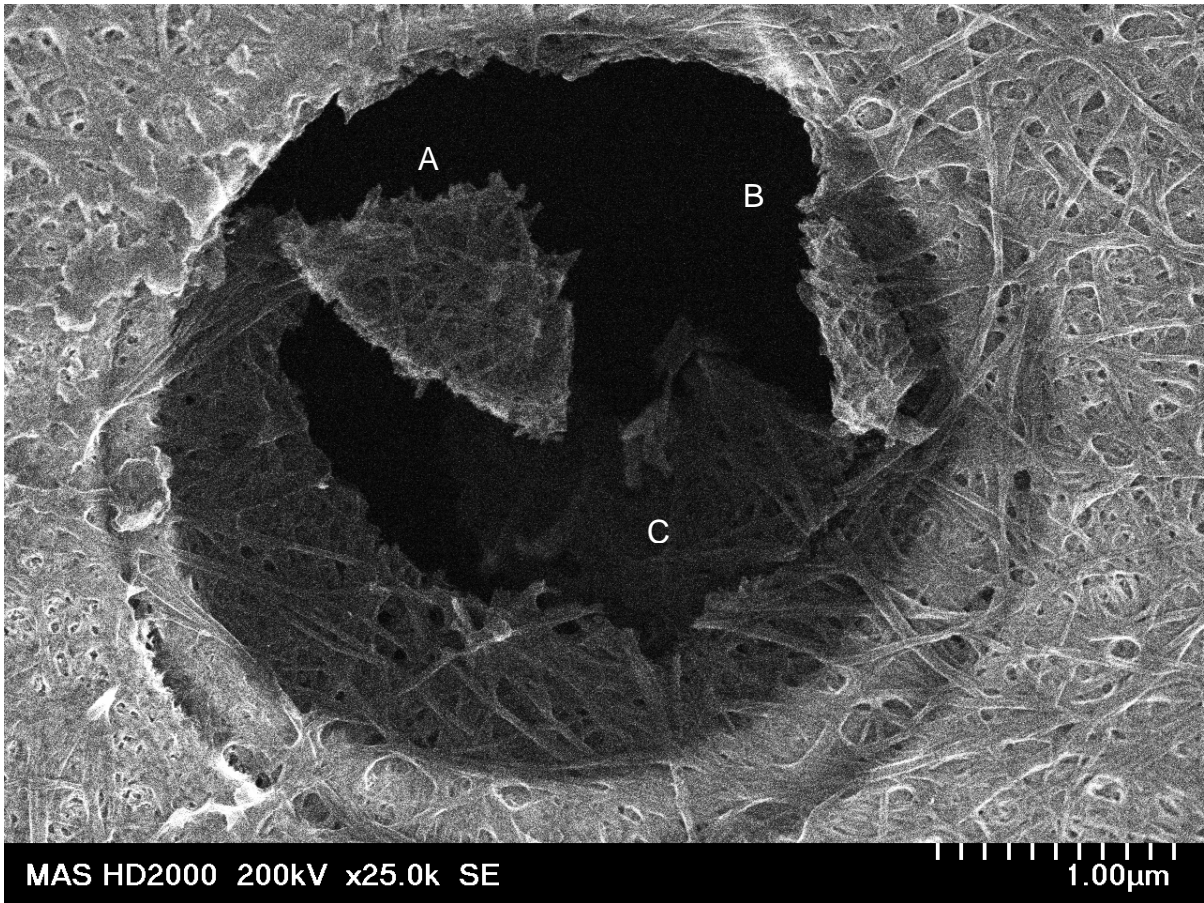


Figure 6.2. STEM SE image of a broken C1 SAN membrane. The resulting jagged fracture edges as well as the remaining intact planar chips provide evidence of brittle fracture.

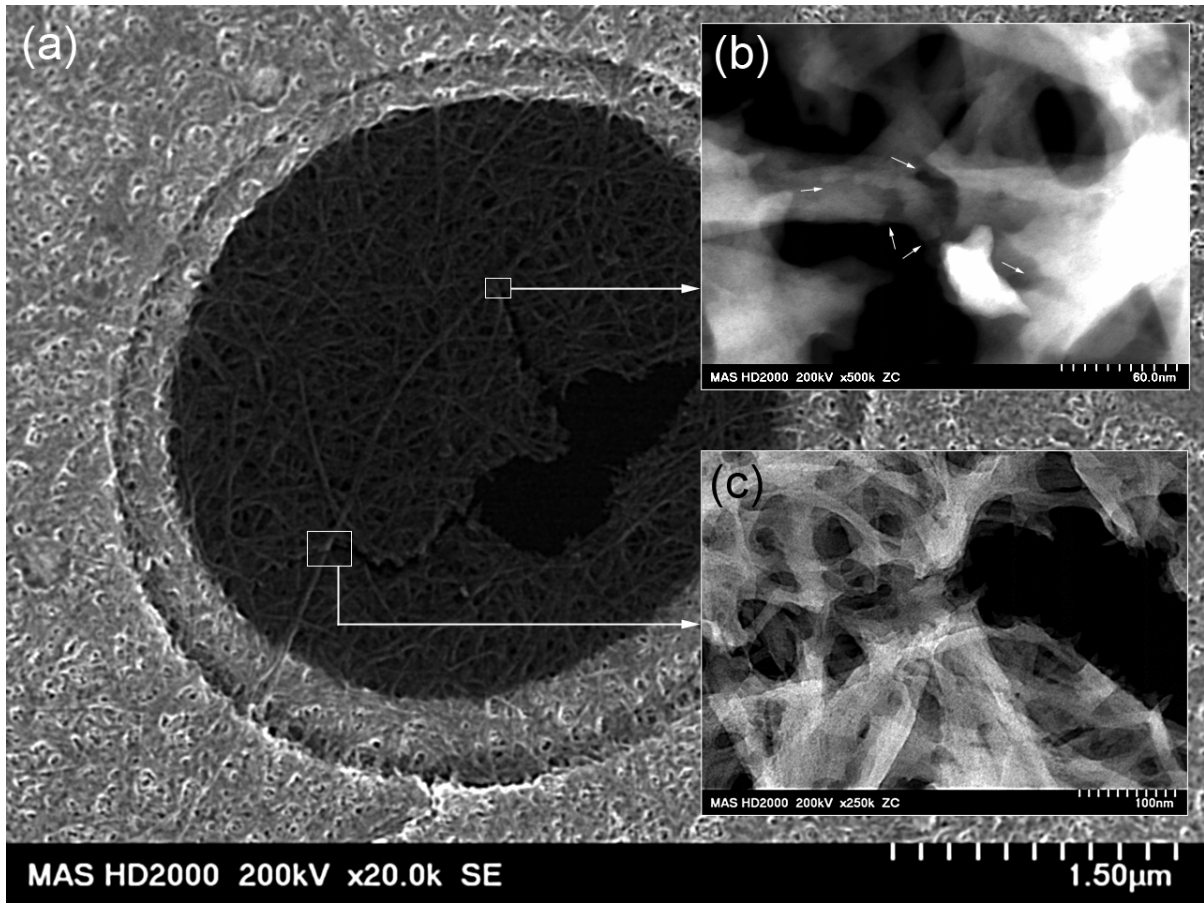


Figure 6.3. HAADF STEM SE image of two cracks propagating through a C1 SAN membrane with one large fiber impeding their progression (a). Investigation of the crack tip areas with Z-Contrast (b & c) clearly show the fracturing of the SAN layered structure. The arrows in (b) denote regions of layer cracking and sliding in a SAN that has not yet failed.

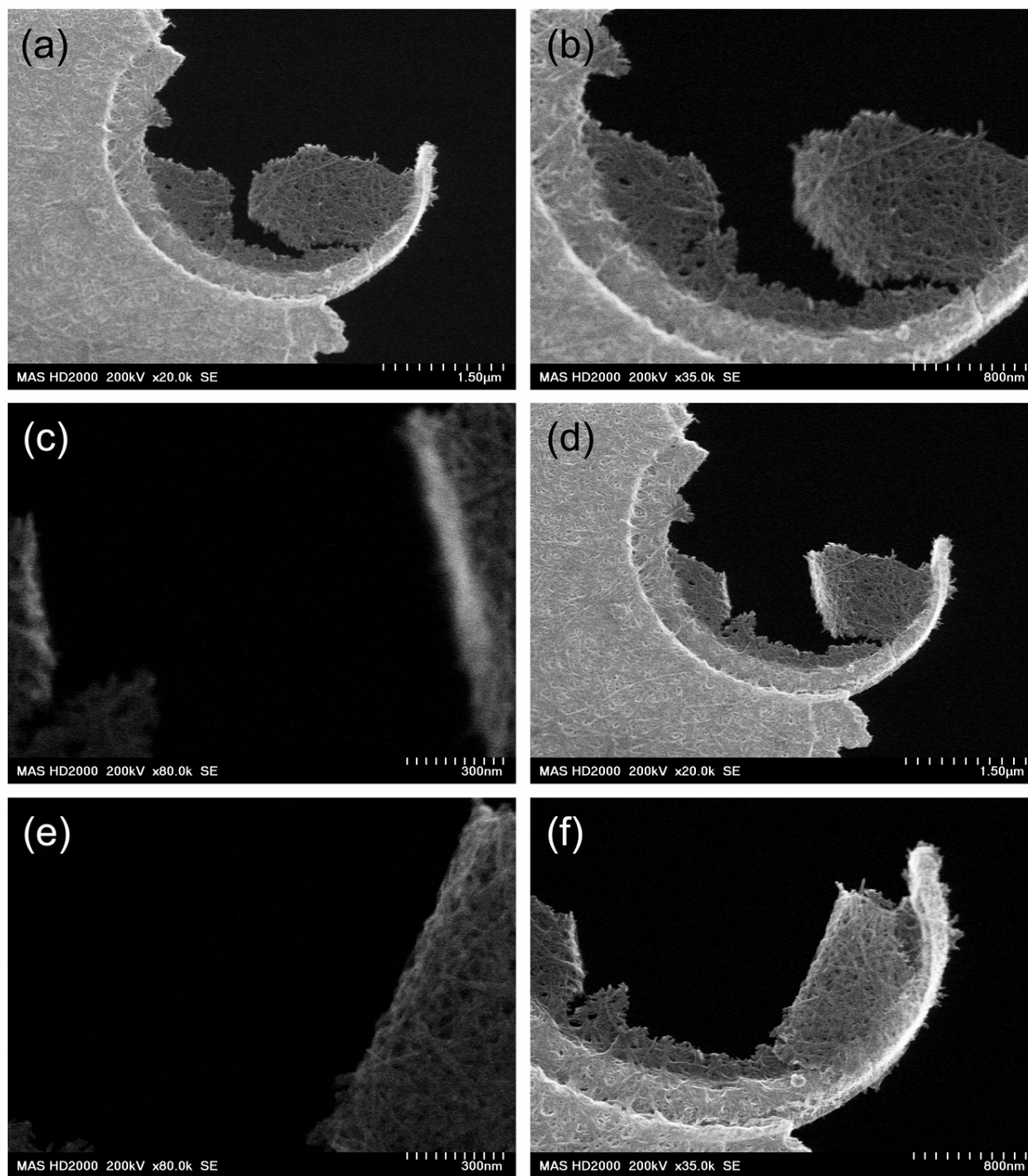


Figure 6.4. Sequence of STEM SE images showing the progression of e-beam manipulation of a broken C1 SAN membrane (a-f). The broken membrane was folded over onto itself by first irradiating the entire membrane with the e-beam at low magnification (a & b). Next, the magnification was increased so that most of the e-beam scan was into vacuum, where the SAN membrane was noticed to flex upwards (c). The magnification was then lowered and the membrane was observed to relax (d). Then the magnification was increased to 5MX and the sample moved into the beam path which resulted in the membrane folding over onto itself (e). Finally the magnification was lowered to show the final state of the folded SAN membrane (f).

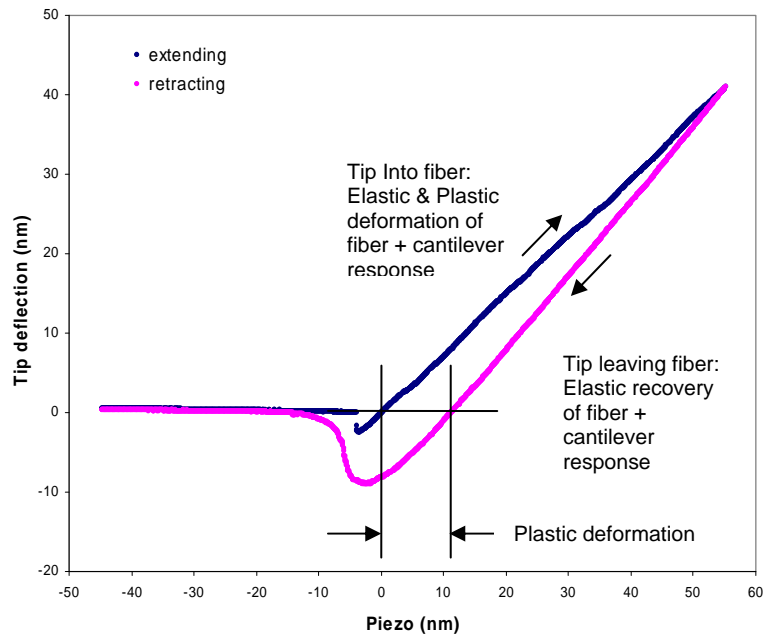


Figure 6.5. An example of a typical AFM “force curve” of Cantilever Deflection vs. change in Piezo length obtained for a single indentation on a C5 SAN on  $\text{Si}_3\text{N}_4$  showing evidence of plastic deformation of the C5 SAN.

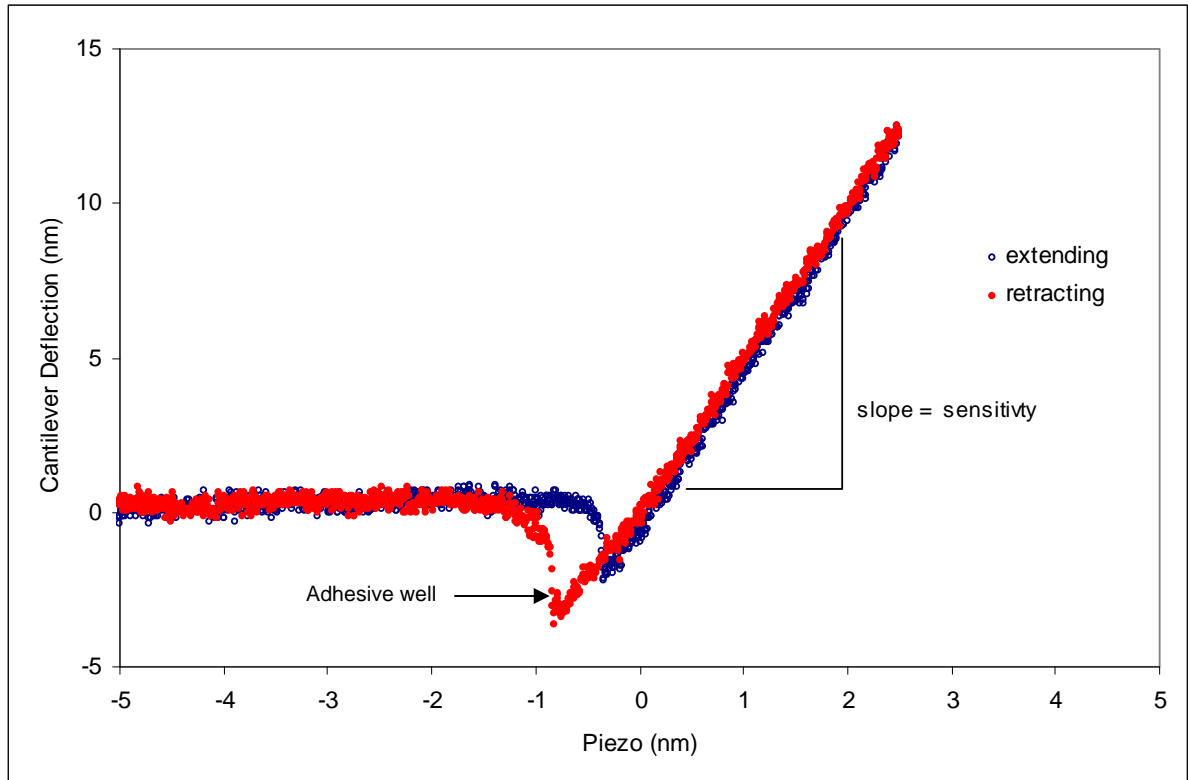


Figure 6.6. A Typical AFM force curve of Cantilever Deflection vs. change in Piezo length, taken on highly stiff  $\text{Si}_3\text{N}_4$  ( $E \sim 180$  GPA) sample using a Olympus tapping mode tip,  $k \sim 66$  N/m, and plotted from exported DI data using Excel. Since the sample is much stiffer than the cantilever, the only contributions to the deflection are from the cantilever where the slope of the linear portion of the extending and retracting data represents the sensitivity of the given cantilever.

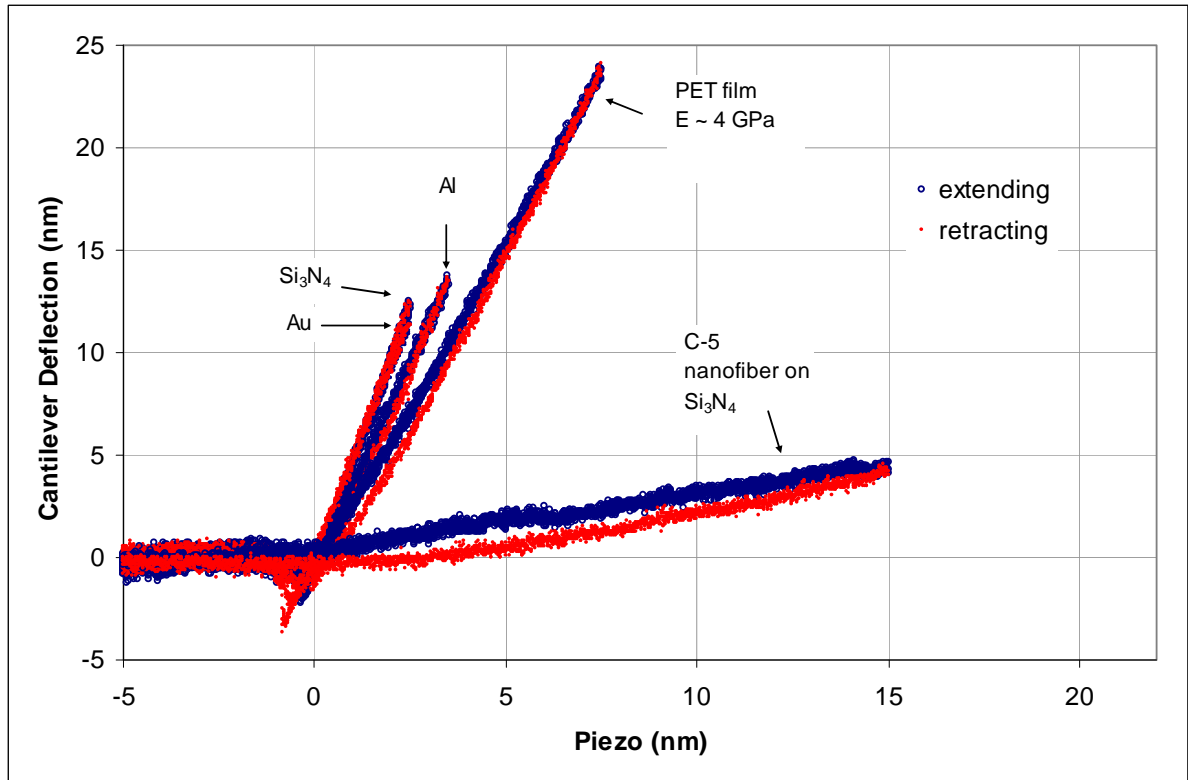


Figure 6.7. The difference in cantilever response as shown by a series of overlaid force curves obtained using the same NSC 15/50  $\mu$ masch cantilever on a 240 nm  $\text{Si}_3\text{N}_4$  thin film on Si, a sputtered Au film, evaporated aluminum film, a PET film, and C-5 nanofiber on  $\text{Si}_3\text{N}_4$  on Si. The force constant of the cantilever was estimated to be  $k \sim 43$  N/m using the Sader method

Furthermore, with a little effort and a few simple assumptions we can model the retraction data to quantify the stiffness, or elastic modulus, of the samples as long as careful attention is paid to several experimental parameters.

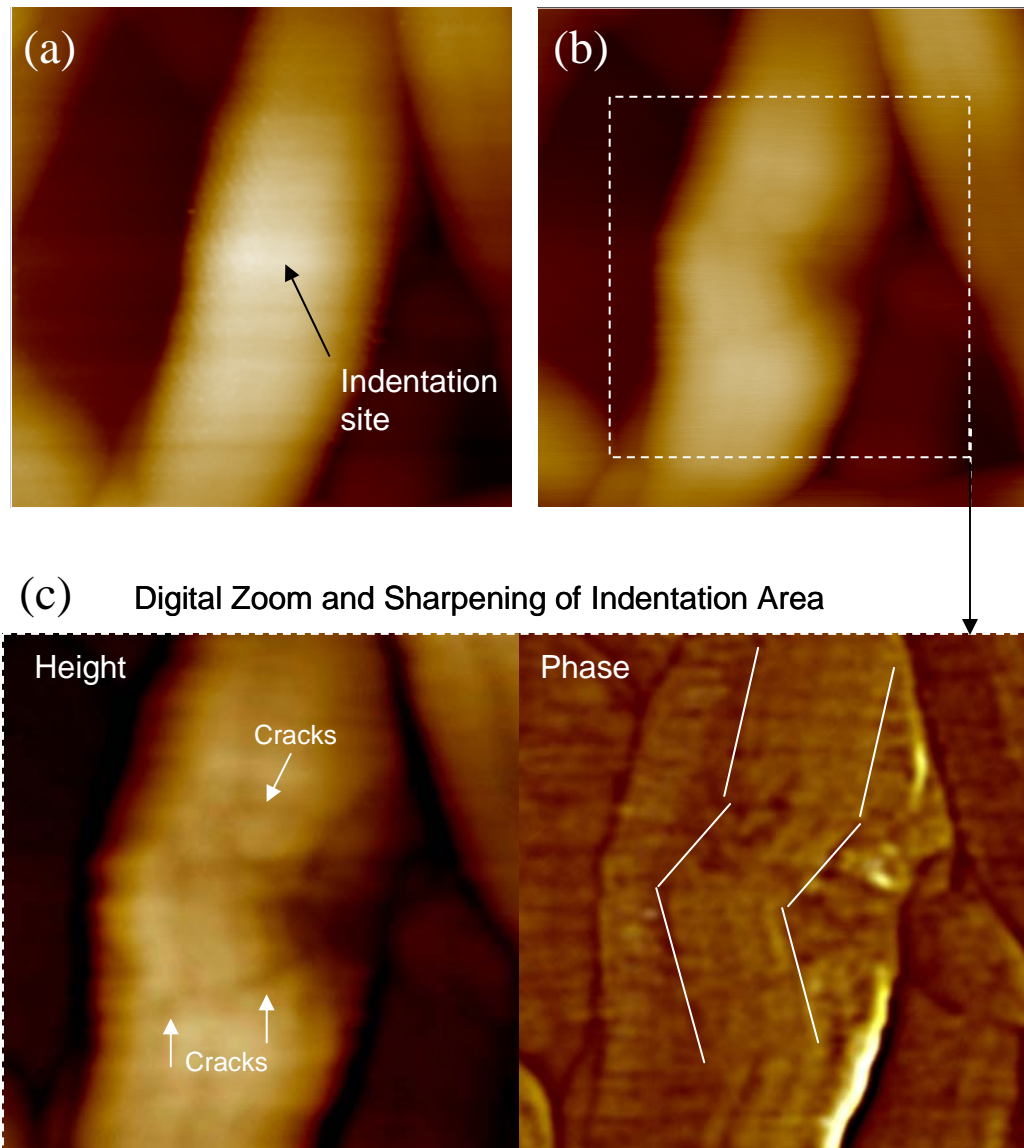


Figure 6.8. 250 nm x 250 nm AFM tapping mode height images of a C5 nanofiber before (a) and after (b) a single 25 nN indentation. Image (c) is the height phase pair from the digitally zoomed area of interest depicted with the dotted lines in image (b). Cracks are clearly visible in the height image while the phase image clearly shows that entire regions have shifted relative to the fiber axis, shown by the white lines.

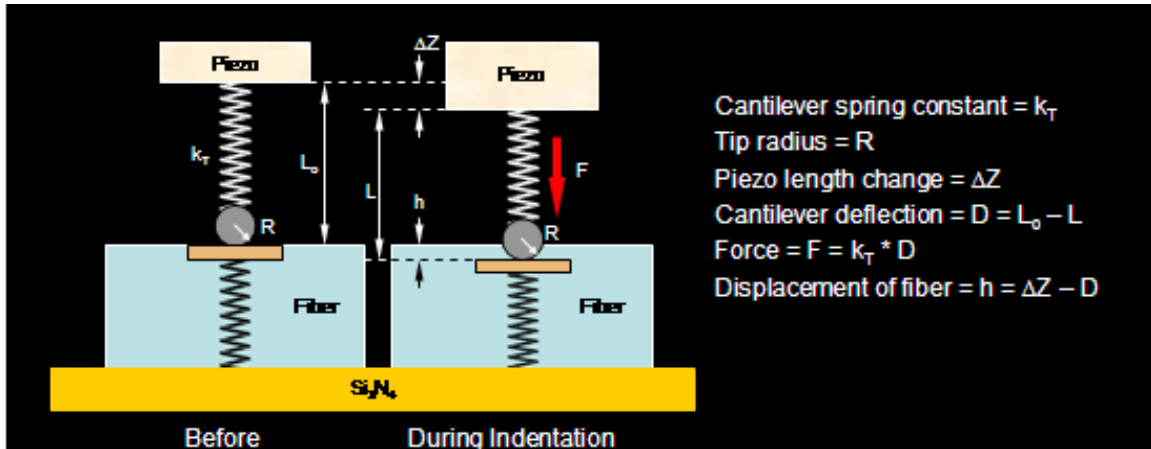


Figure 6.9. AFM Nanoindentation Double Spring, Hertzian Contact Model before and during indentation with a spherical indenter into a nanofiber sample having a rectangular cross-sectional geometry.

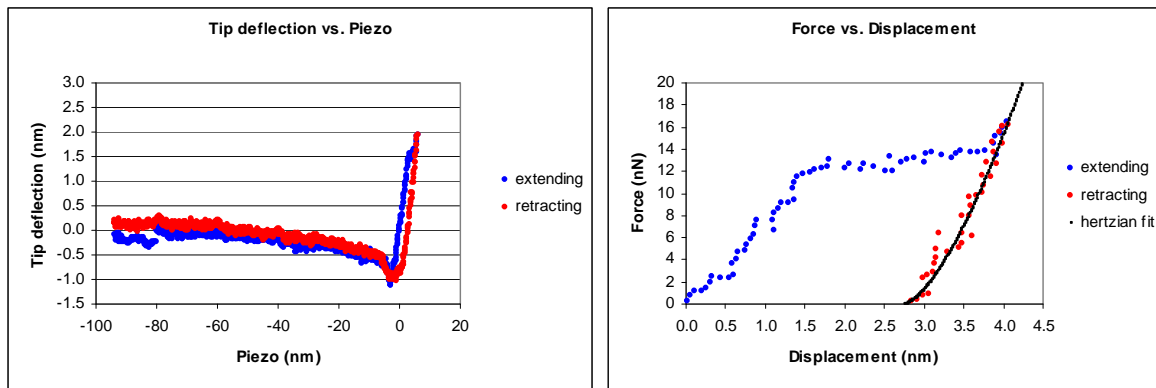


Figure 6.10. The conversion from Deflection vs. Piezo length to Force vs. Displacement utilizing the two spring model for a nanoindentation made in a C5 SAN on  $\text{Si}_3\text{N}_4$ . A hertzian model (black line) has been applied to the retraction portion of the Force vs. Displacement plot. The fit of the model to the retraction data is very good.

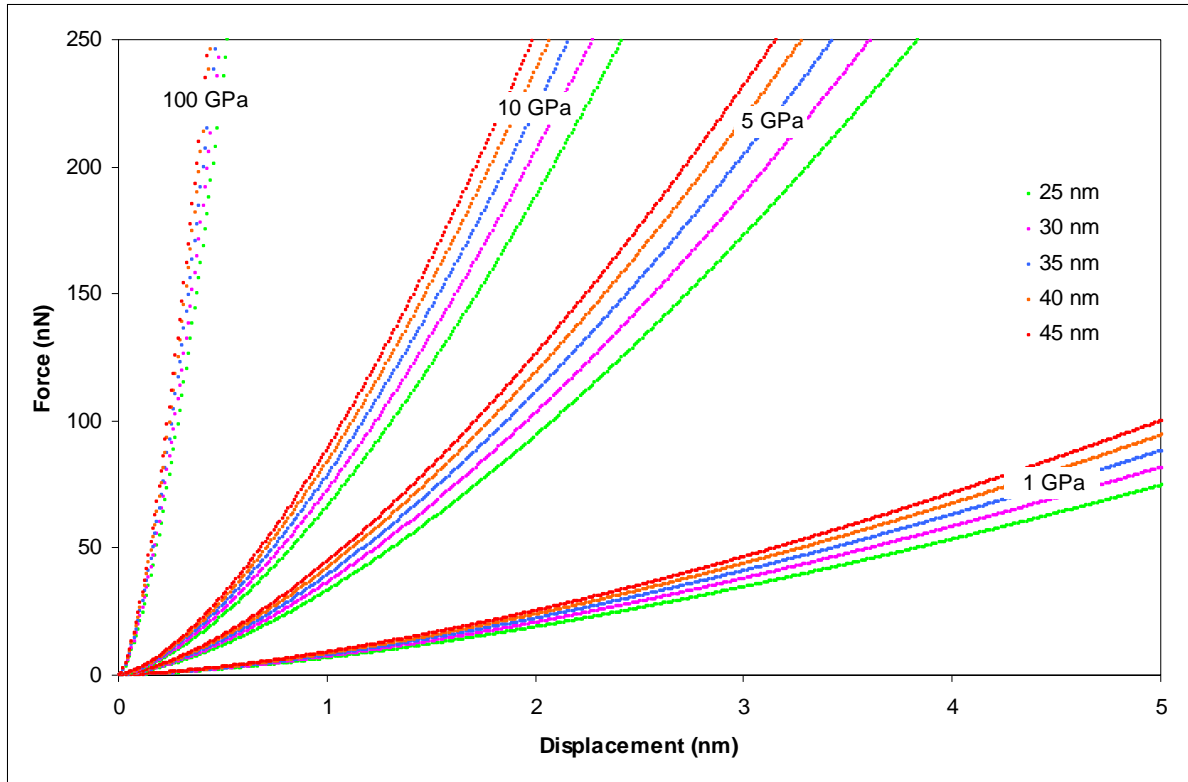


Figure 6.11. Shows the effect of 20 nm tip radius variations on the slope of a Hertzian fits where  $E^* = 1, 5, 10,$  and  $100$  GPa.

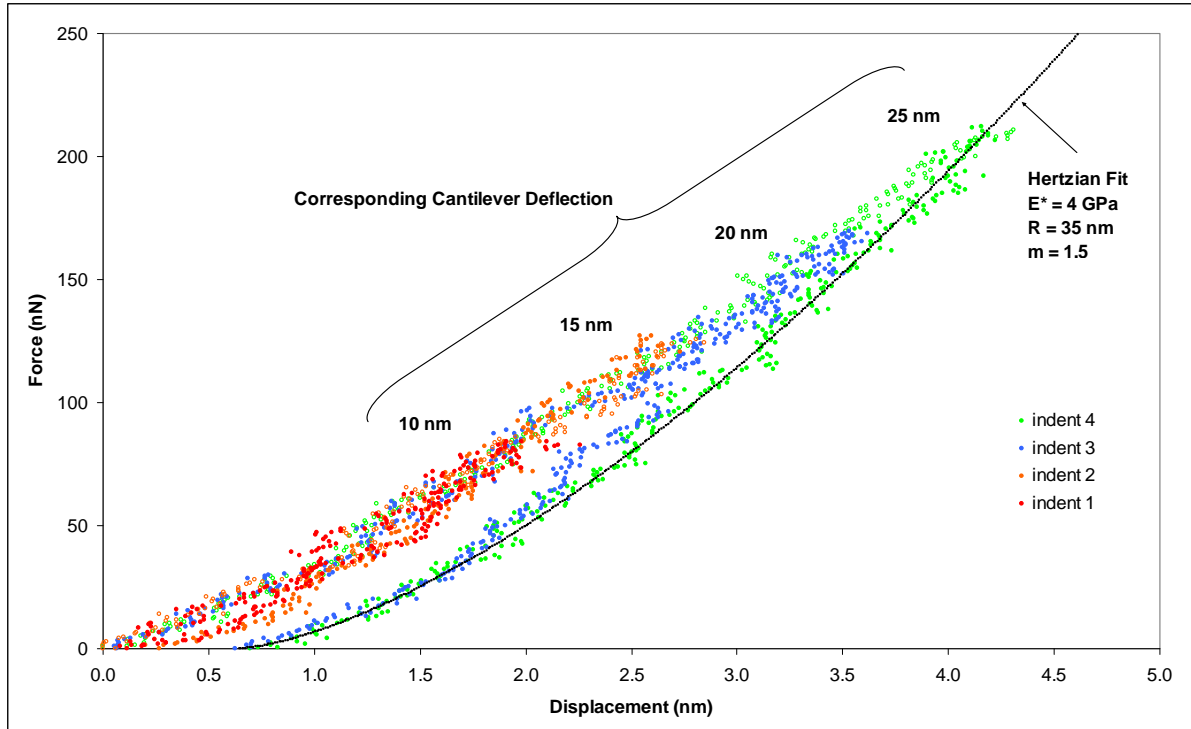


Figure 6.12. Multiple indentations in the same location of a PET film with a known modulus of  $\sim 4$  GPa. A Hertzian fit (black line) estimates the tip radius to be 35 nm.

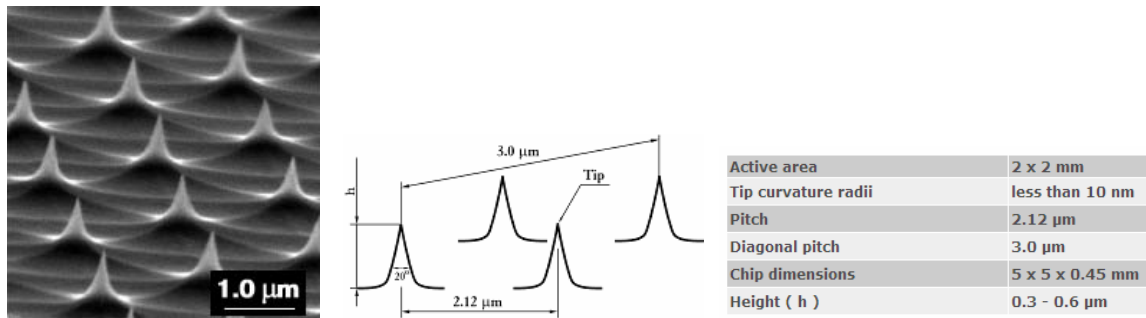


Figure 6.13. SEM image of Micromasch TGT01 tip characterizer along with schematic and specifications, utilized for the determination of the tip end radius and geometry.

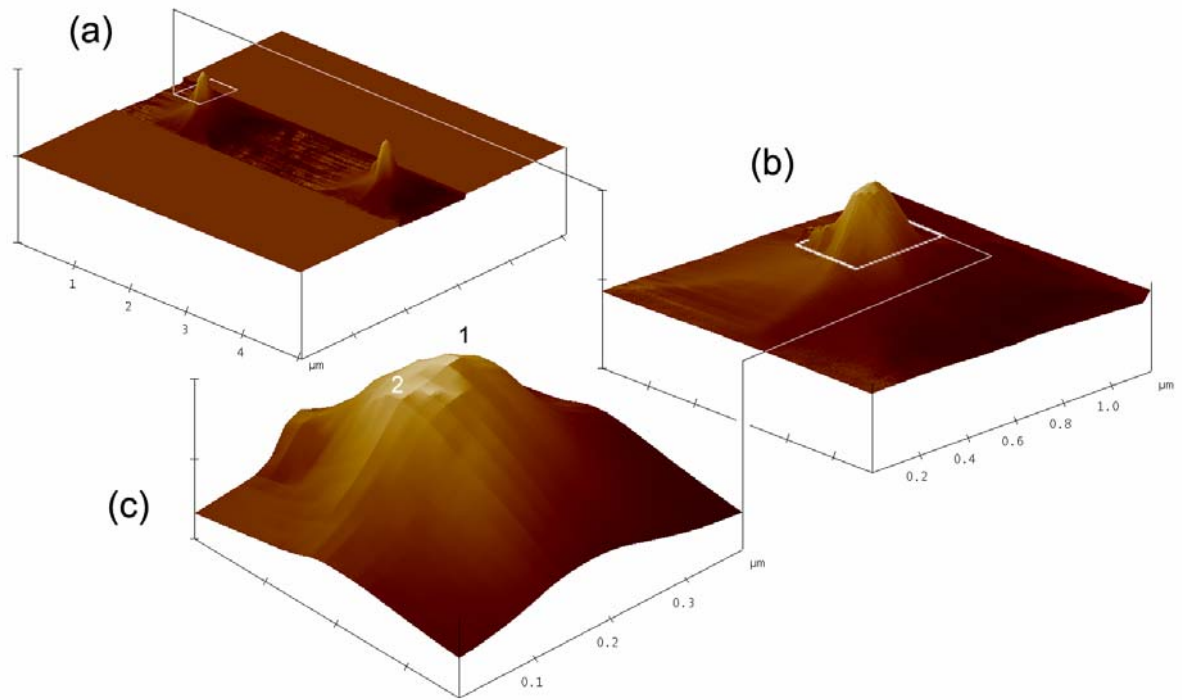


Figure 6.14. 3D AFM height images created by scanning a micromasch tip characterizer, TGT 01. The image of the tip is digitally zoomed in (b) and then to (c) for closer inspection of the tip end radius. The numbers 1 and 2 in image (c) correspond to the points in Figure 6.15.

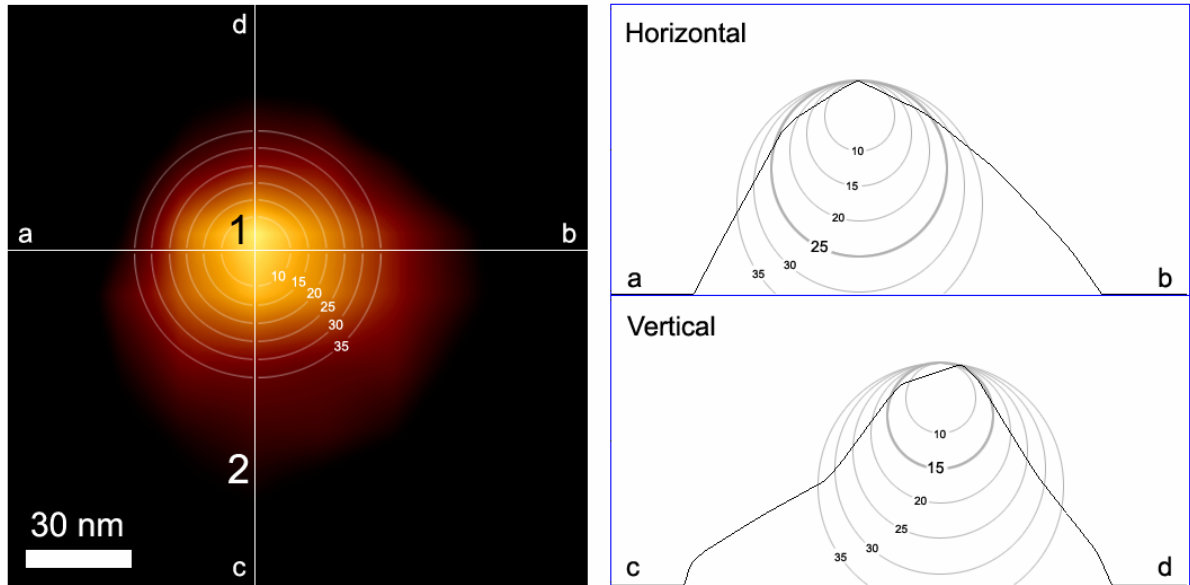


Figure 6.15. Corresponding AFM Height image to Figure 6.14 (c) zoomed in on the very end radius of the tip on the left. On the right are the corresponding horizontal and vertical cross sections through the end radius of the tip. The tip exhibits an end radius of  $\sim 25$  nm in the horizontal and  $\sim 15$  nm in the vertical directions.

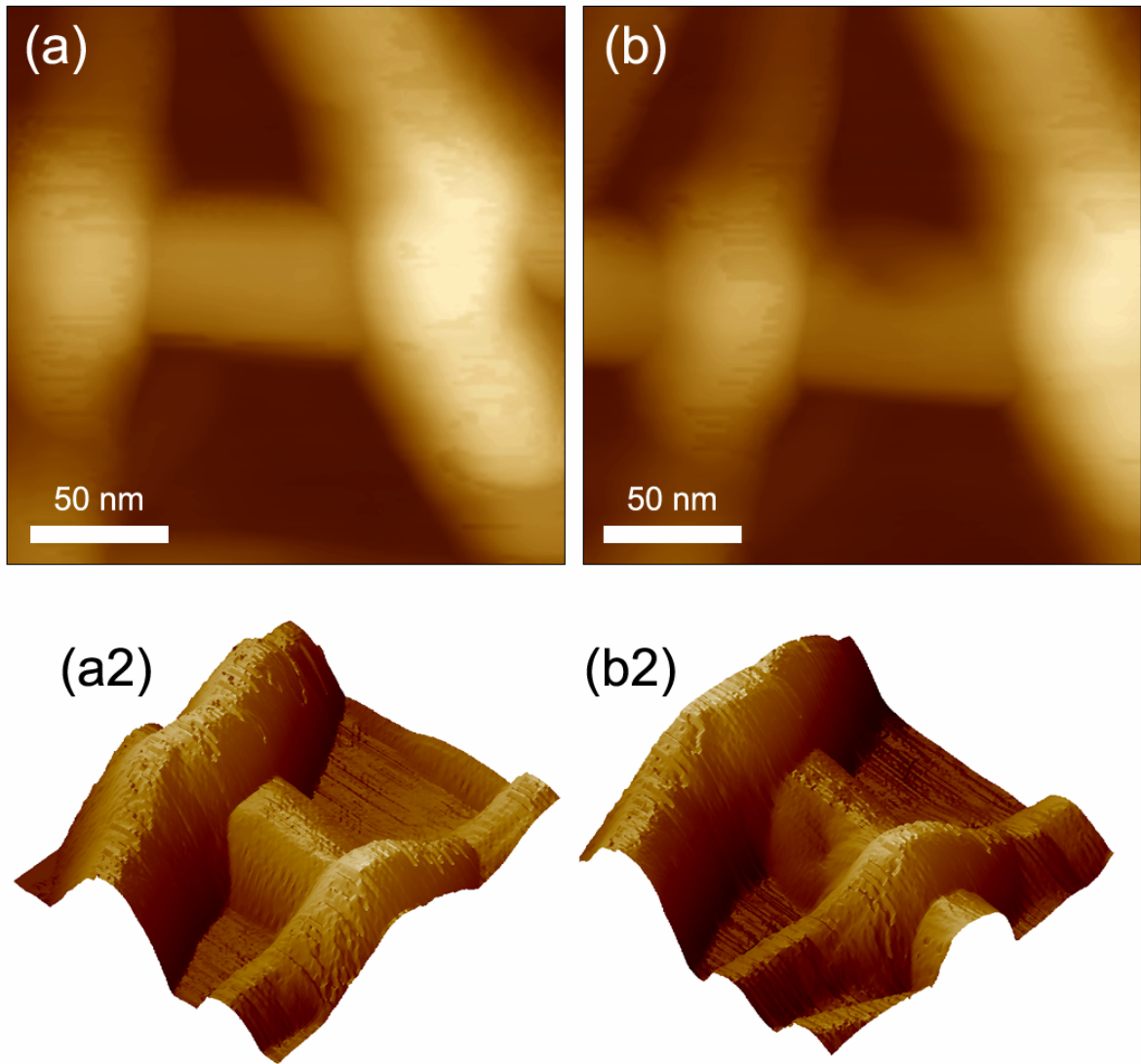


Figure 6.16 AFM height images of before (a & a2) and after (b & b2) a series of 10 indentations in the same spot of single C-5 fiber on  $\text{Si}_3\text{N}_4$ .

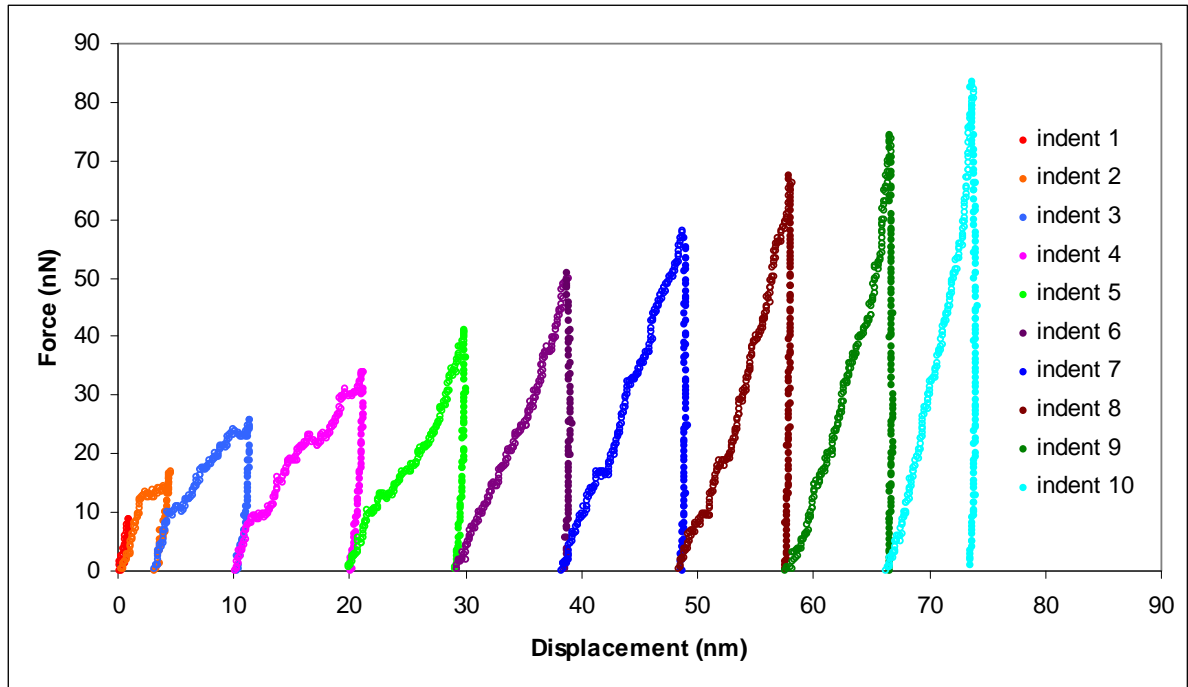


Figure 6.17. Force curves from a series of 10 indentations made at the same spot into a single 40 nm tall C5 nanofiber on  $\text{Si}_3\text{N}_4$ . The successive indentations were plotted in a way to better show the evolution of the fibers displacement over the entire series.

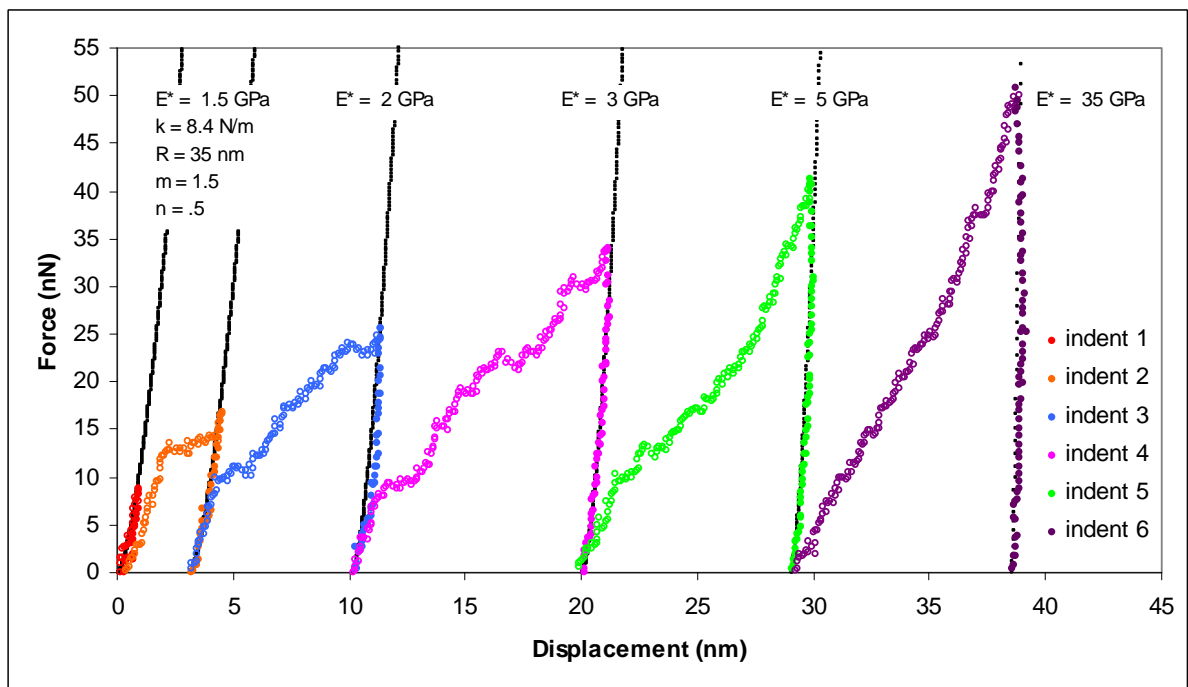


Figure 6.18. The first six Force vs. Displacement curves from Figure 6.17 with corresponding Hertzian fits showing the trend of increasing modulus with increasing sample displacement.

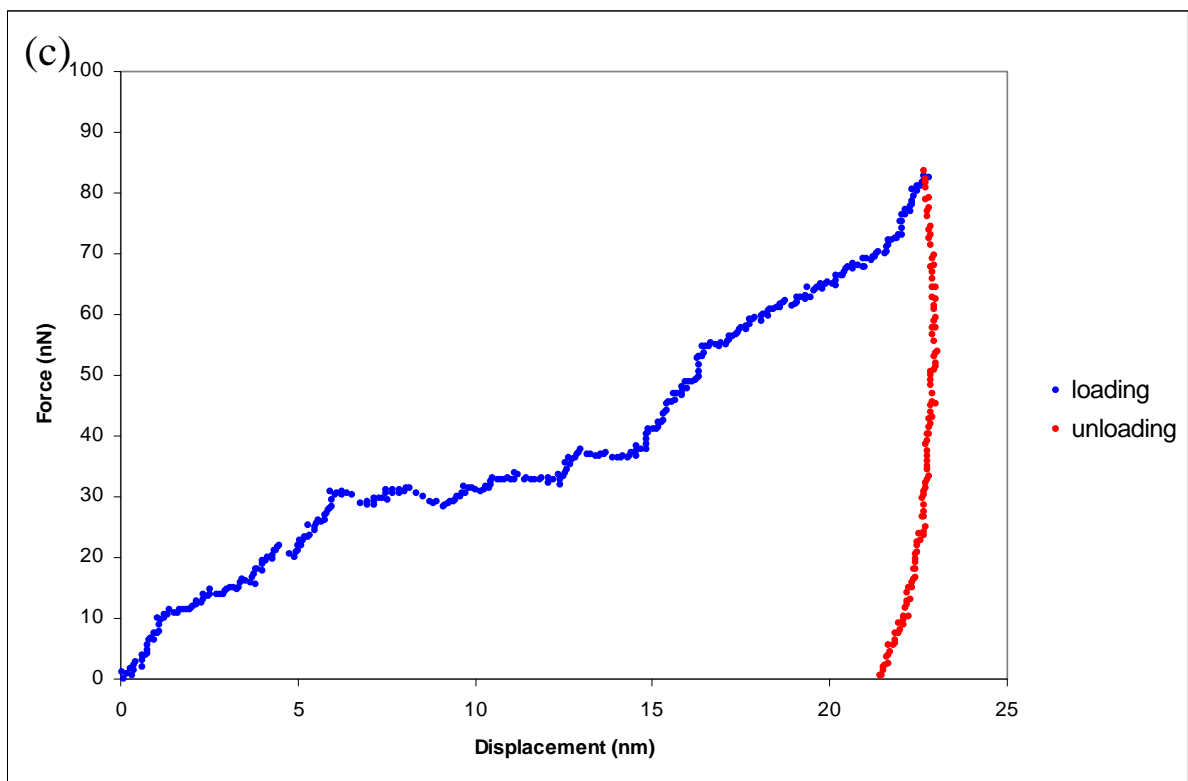
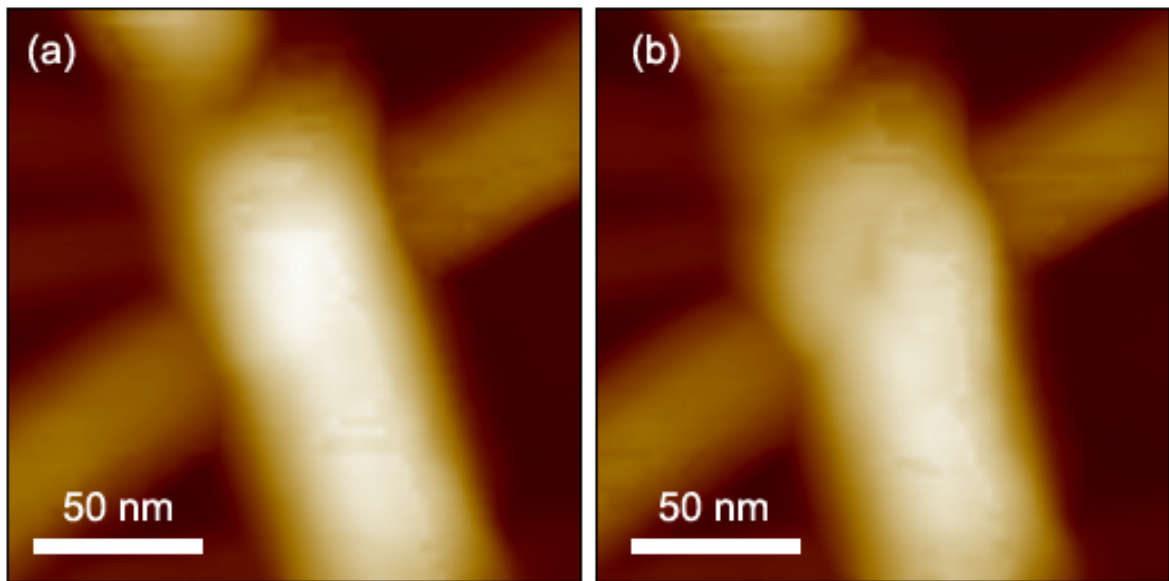


Figure 6.19. AFM height images of overlapping C-5 nanofibers before (a), and after (b), a single ~ 80nN indentation with AFM. Corresponding Force vs. Displacement curve (c) for the single indentation.

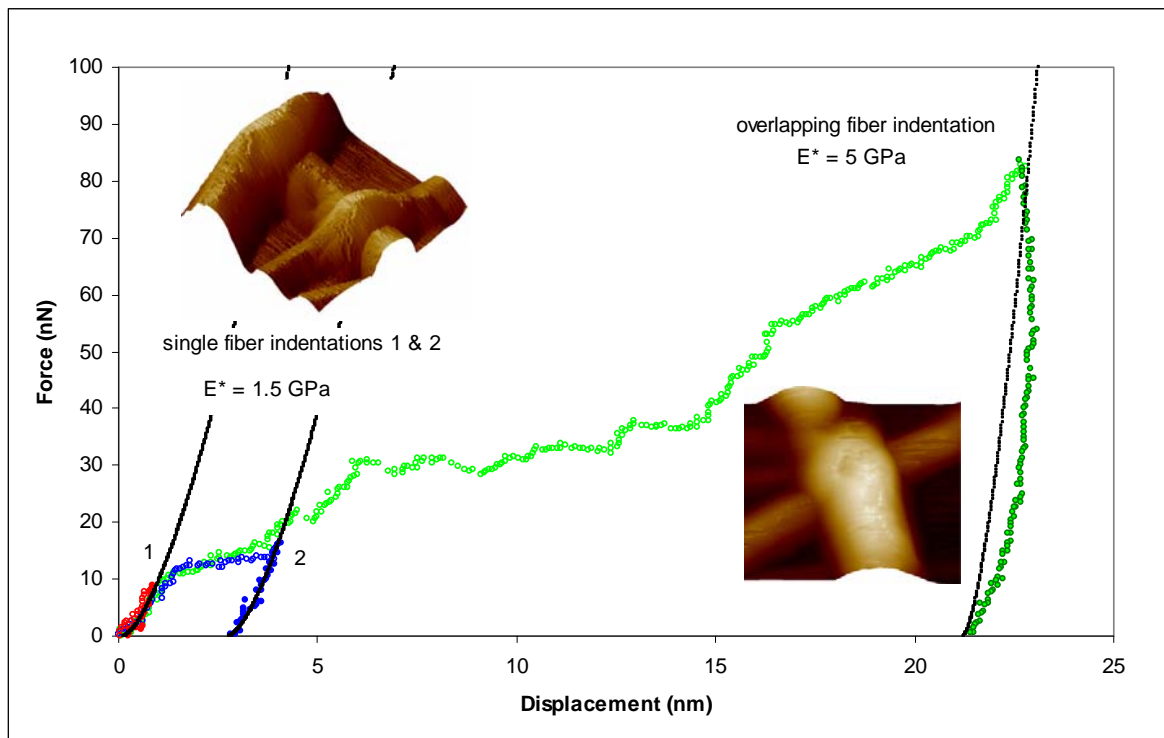


Figure 6.20. Comparison of indentation data from the first two indents in Figure 6.18 and the single indent of Figure 6.19.

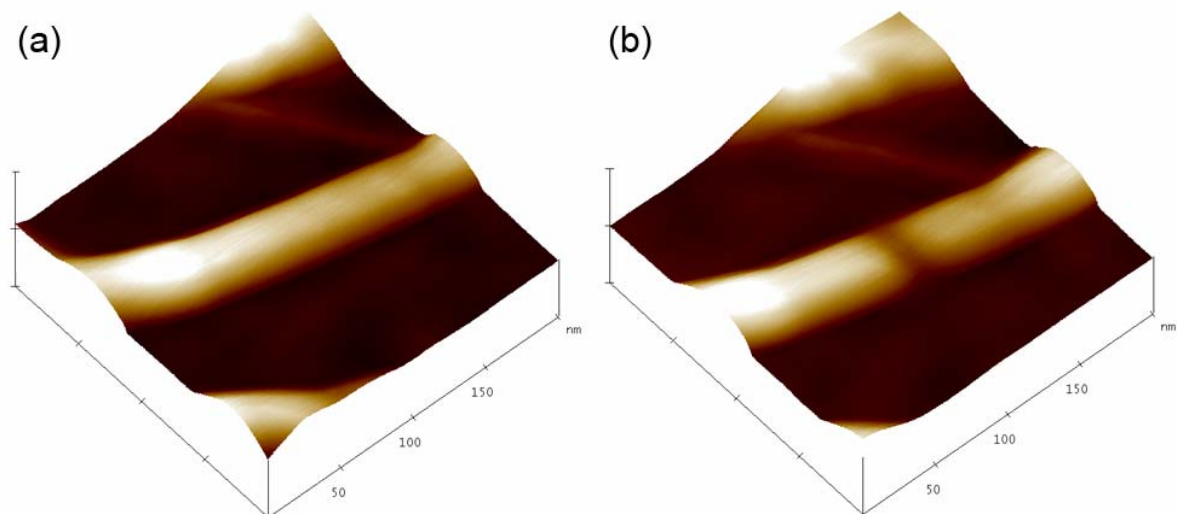


Figure 6.21. AFM 3D Height images of a 50 nm wide by 10 nm tall C3 SAN on  $\text{Si}_3\text{N}_4$  before (a) and after (b) a series of 10 indentations of progressively increasing loads. The shift of the fiber after indenting along with the linear shape of the indent suggest that each successive indentation was not made in the same place.

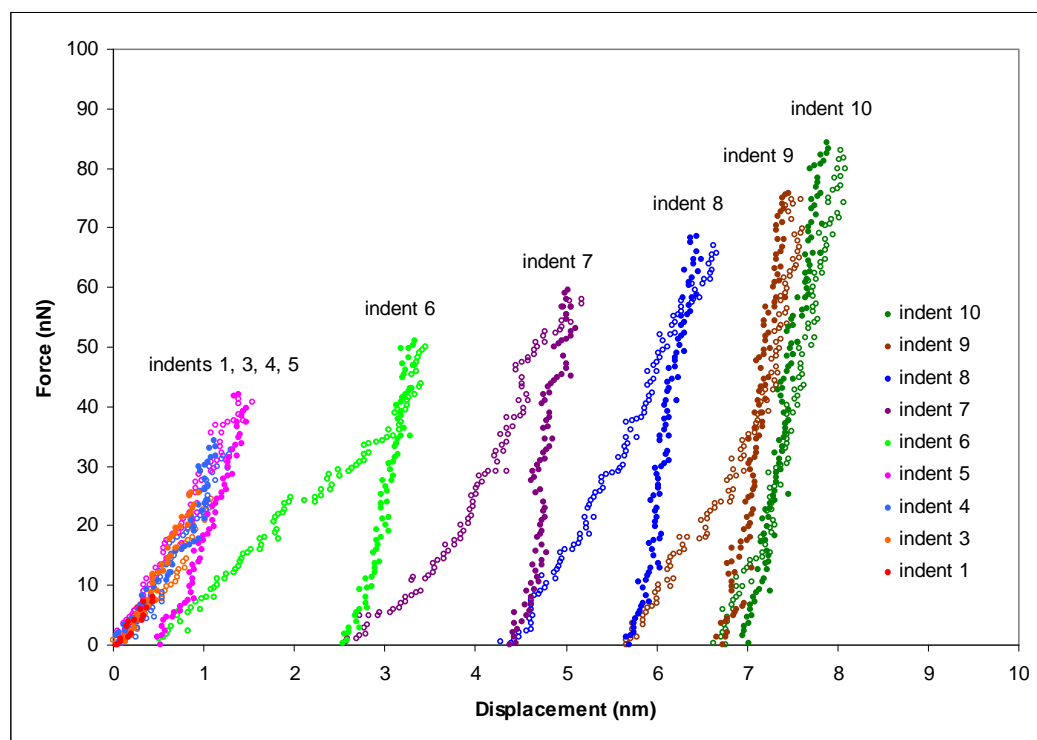


Figure 6.22. Force curves from a series of 10 indents of 1 – 10 nm deflections (8.4 – 84 nN) in a C3 SAN. The 2<sup>nd</sup> indent is left out because it was considered bad.

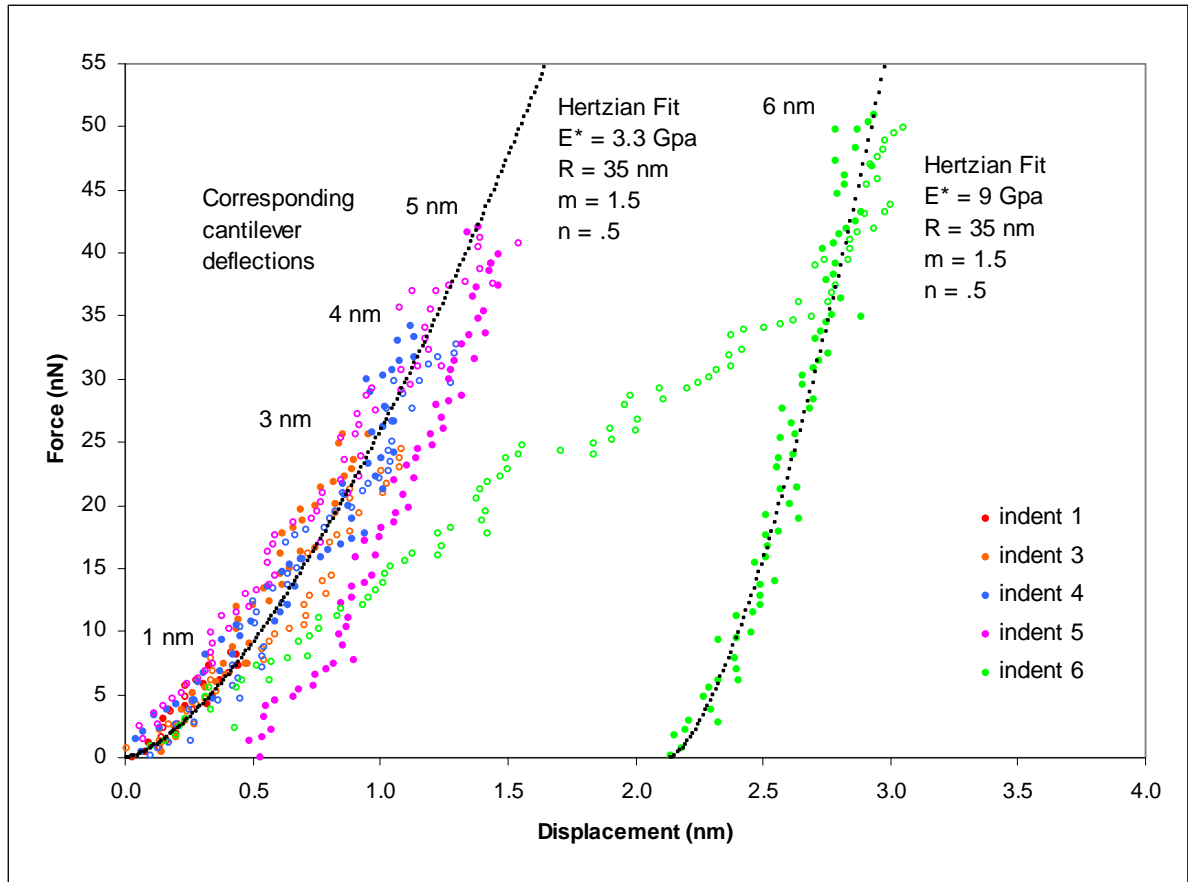


Figure 6.23. The first six force curves from Figure 6.22, with Hertzian fits to the retraction curve of the 4<sup>th</sup> and 6<sup>th</sup> indents (black), showing nearly elastic response from the first 4 indents and then more plastic response after the 5<sup>th</sup>. An increase in modulus is seen with increased sample deformation.

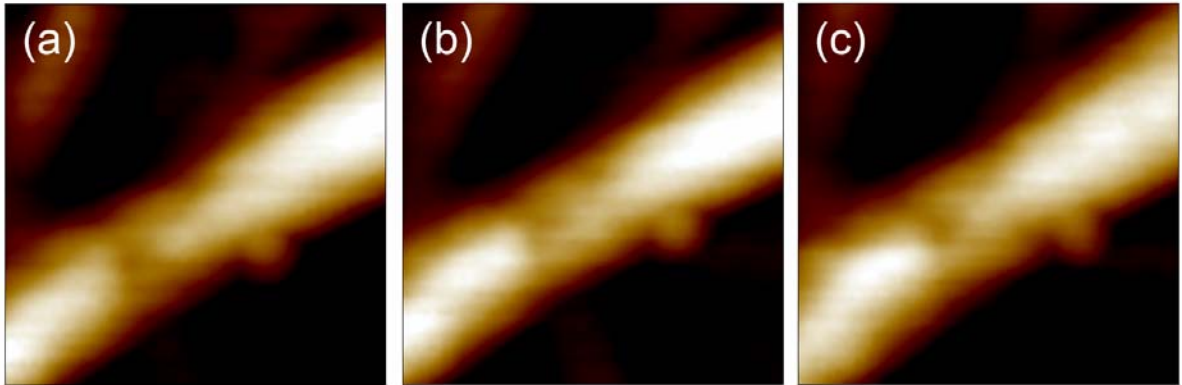


Figure 6.24. 135 nm x 135 nm AFM tapping mode height images of a single 50 nm wide by 11.5 nm tall C1 nanofiber on  $\text{Si}_3\text{N}_4$  before (a), after a  $\sim 84$  nN indent (b), and after a  $\sim 168$  nN indent in roughly the same place. The z-scale on each image is 20 nm. Subtle changes in the fiber morphology are observed as the fiber widens slightly as well as decreasing in height corresponding well with the observed sample displacements in Figure 6.25.

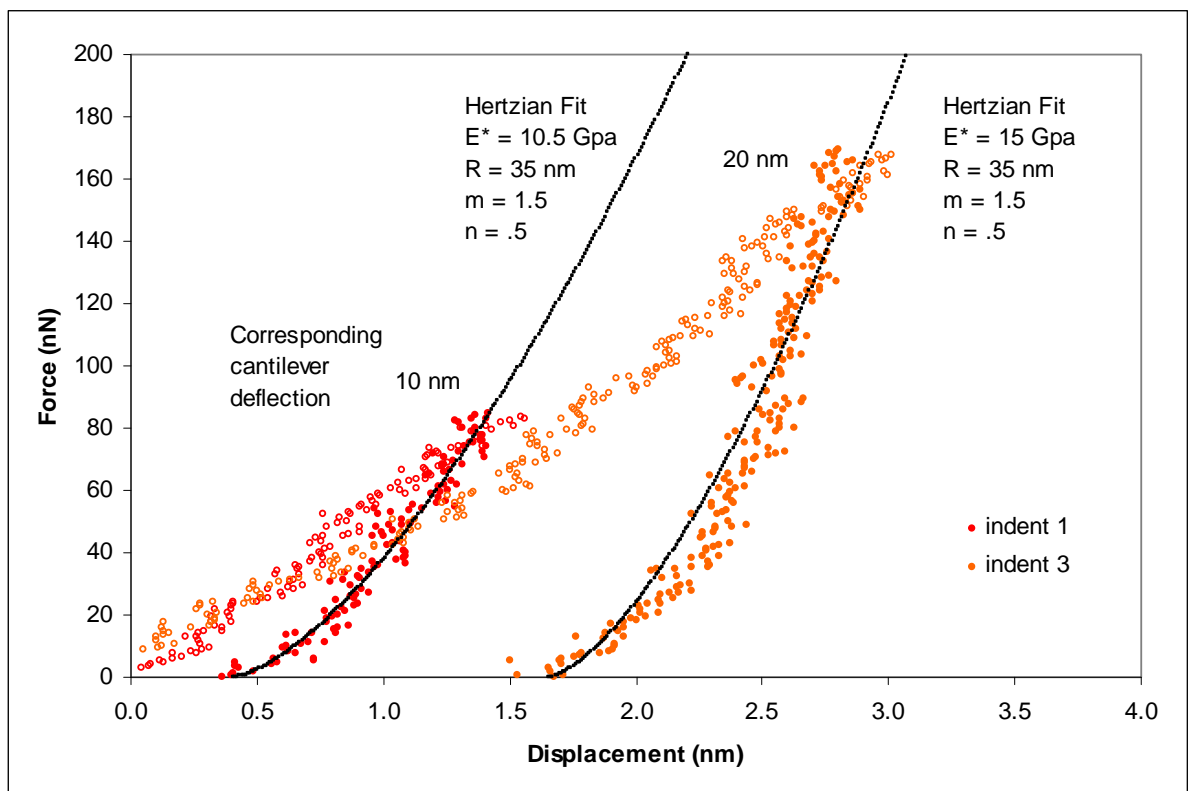


Figure 6.25. Force vs. Displacement curves corresponding to the images in Figure 6.24. A Different type of deformation mechanism is noted as there is no discernable yield point like the C3 and C5 SANs. Hertzian fits estimate the modulus to be  $\sim 10.5 - 15$  GPa for the two indentations.

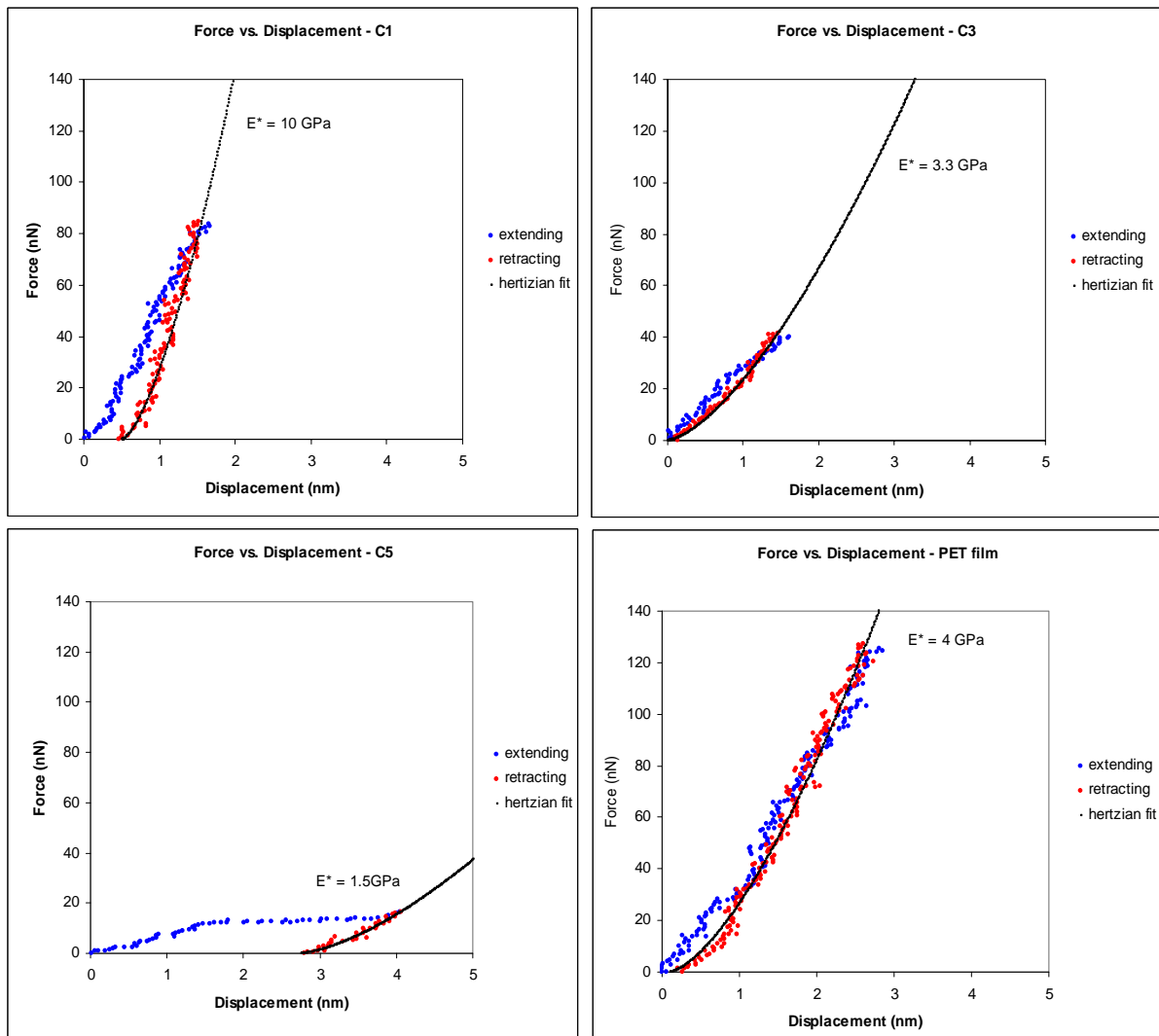


Figure 6.26. A comparison of a representative Force vs. Displacement curves from each of the C1, C3, C5 SANs with one from the 4 GPa PET film series. The measured elastic moduli appears to increase with decreasing chainlength, from 1.5 GPa for the C5 to 10GPa for the C1 SANs.

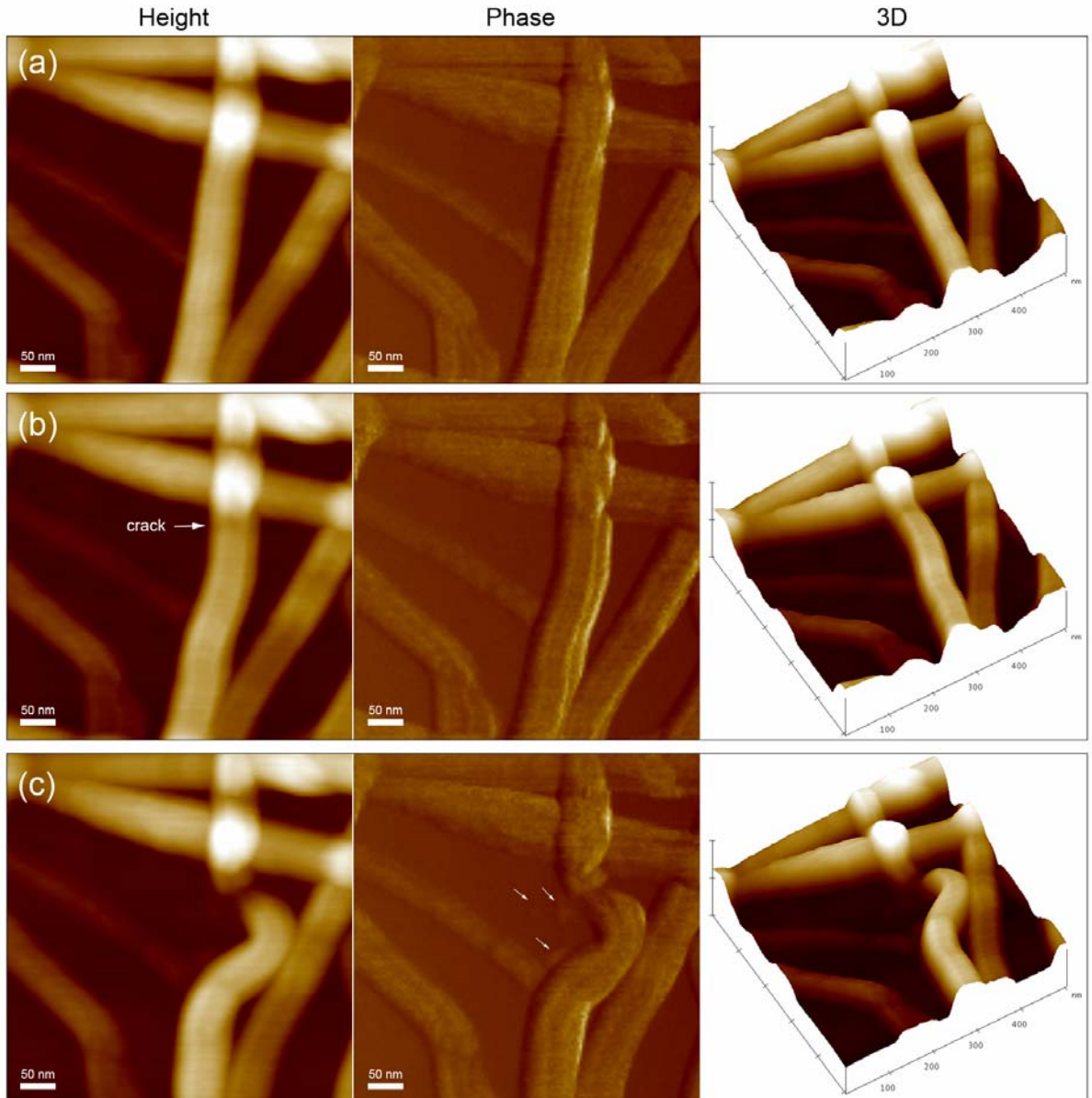


Figure 6.27. AFM height, phase and 3D images showing the sequential changes of a single C3 SAN before (a), after a 50 nm lateral deformation (b), and after an additional 100 nm lateral deformation (c). The arrows in the phase image of (c) denote what appears to be residual SAN left on the surface after it was moved to the right.

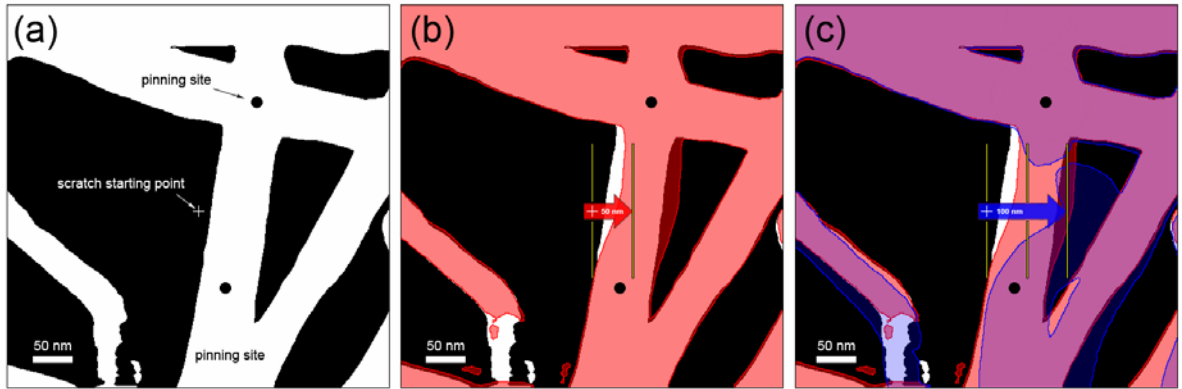


Figure 6.28. Is a series of thresholded AFM height images from Figure helping correlate the changes in SAN morphology with scratches applied. Image (a) is the before image with what is perceived to be two pinning sites where the SAN appears to be stuck to the  $\text{Si}_3\text{N}_4$  as well as the starting point for the scratches. Image (b) is an overlay of the result of the first 50 nm scratch (red) on top of the before image (white) with the scratch represented by the red arrow. Image (c) is an overlay of the results of a second scratch (blue) on top of image (b) with the second scratch represented by the blue arrow.

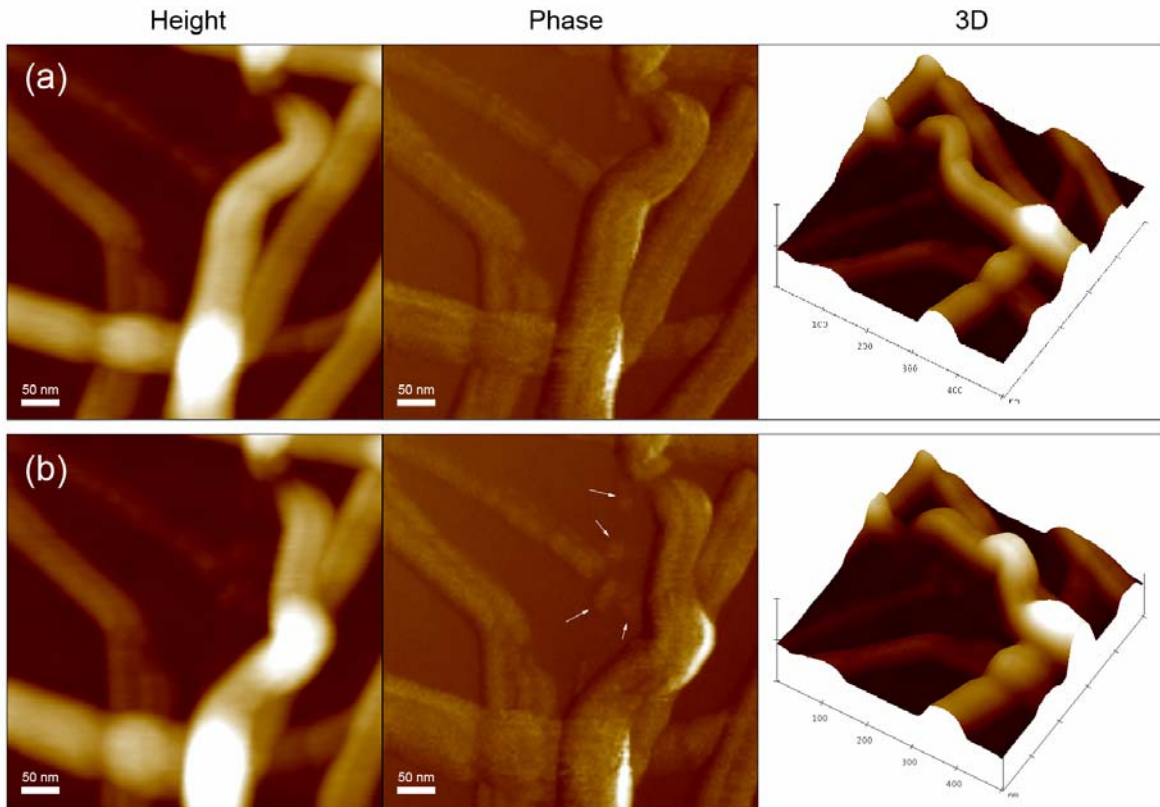


Figure 6.29. After the previous two scratches were made as seen in figure a third scratch was made directly adjacent to the previously observed lower pinning site. The image location was shifted in the y direction and a set of AFM height, phase, and 3D images obtained before the scratch (a) and then a 100 nm scratch was made in the x direction and another set of AFM height, phase, and 3D images obtained (b). The arrows in the phase image of (b) show the residual SAN left behind on the  $\text{Si}_3\text{N}_4$  surface after scratching and lateral translation of the SAN.

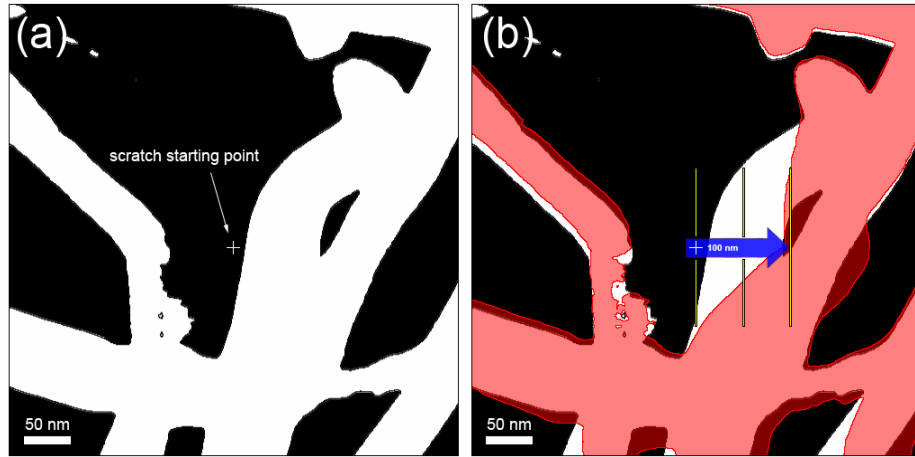


Figure 6.30. Analogous to Figure 6.28, Image (a) is a thresholded AFM height image of the SAN prior to lateral deformation. Image (b) is an overlay of the thresholded AFM height image of the SAN after a 100 nm lateral deformation (red) on top of image (a) (white) with the scratch represented by the blue arrow.

## 6.7 Tables

Table 6.1. Summary of reduced modulus ( $E^*$ ) values for C1, C3, and C5 SANs.  $E^*$  values were calculated by fitting of a Hertzian contact model to the retraction curves. All data was acquired utilizing the same cantilever having a spring constant of 8.4 N/m (Sader Method) and tip radius of 35 nm (characterizer and PET control).

<b>Chain length</b>	<b>Number of indentations</b>	<b>Average Reduced Modulus (GPa)</b>	<b>Std. Deviation (GPa)</b>
C1	5	10.52	2.24
C3	13	3.78	0.72
C5	6	1.25	0.63

Table 6.2. Summary of reduced modulus values for C5 SANs acquired with cantilevers of three different force constants: 0.73, 8.4, and 66 N/m.

<b>Cantilever Force Constant (N/m)</b>	<b>Number of indentations</b>	<b>Average Reduced Modulus (GPa)</b>	<b>Std. Deviation (GPa)</b>
0.73	9	1.20	0.60
8.4	6	1.25	0.63
66	7	1.83	0.67

## 6.8 References

- [6.1] Wu, B., A. Heidelberg, and J.J. Boland, *Mechanical properties of ultrahigh-strength gold nanowires*. Nature Materials, 2005. **4**(7): p. 525-529.
- [6.2] Ahn, C.C., *Transmission electron energy loss spectrometry in materials science and the EELS atlas*. 2nd ed. 2004, Weinheim [Germany]: Wiley-VCH. xiii, 457 p.
- [6.3] Wong, E.W., P.E. Sheehan, and C.M. Lieber, *Nanobeam mechanics: Elasticity, strength, and toughness of nanorods and nanotubes*. Science, 1997. **277**(5334): p. 1971-1975.
- [6.4] Barber, A.H., S.R. Cohen, and H.D. Wagner, *Measurement of carbon nanotube-polymer interfacial strength*. Applied Physics Letters, 2003. **82**(23): p. 4140-4142.
- [6.5] Zhang, Z.B., J.C. Peng, and X.H. Chen, *Research on the elastic modulus of the carbon nanotubes*. Rare Metal Materials and Engineering, 2004. **33**(12): p. 1233-1237.
- [6.6] Yoon, J., C.Q. Ru, and A. Mioduchowski, *Vibration of an embedded multiwall carbon nanotube*. Composites Science and Technology, 2003. **63**(11): p. 1533-1542.
- [6.7] Cuenot, S., et al., *Measurement of elastic modulus of nanotubes by resonant contact atomic force microscopy*. Journal of Applied Physics, 2003. **93**(9): p. 5650-5655.
- [6.8] Kuzumaki, T. and Y. Mitsuda, *Nanoscale mechanics of carbon nanotube evaluated by nanoprobe manipulation in transmission electron microscope*. Japanese Journal of Applied Physics Part 1-Regular Papers Brief Communications & Review Papers, 2006. **45**(1A): p. 364-368.
- [6.9] Kuzumaki, T., et al., *Dynamic observation of the bending behavior of carbon nanotubes by nanoprobe manipulation in TEM*. Carbon, 2004. **42**(11): p. 2343-2345.
- [6.10] Zussman, E., et al., *Mechanical and structural characterization of electrospun PAN-derived carbon nanofibers*. Carbon, 2005. **43**(10): p. 2175-2185.
- [6.11] Dieter, G.E., *Mechanical metallurgy*. 3rd ed. 1986, New York: McGraw-Hill. xxiii, 751 p.
- [6.12] Zhao, M.H., et al., *Probing nano-scale mechanical characteristics of individual semi-conducting nanobelts*. Materials Science and Engineering a-Structural Materials Properties Microstructure and Processing, 2005. **409**(1-2): p. 223-226.
- [6.13] Chang, M.C., et al., *Elasticity of alveolar bone near dental implant-bone interfaces after one month's healing*. Journal of Biomechanics, 2003. **36**(8): p. 1209-1214.

- [6.14] Wei, G., et al., *Thin CN<sub>x</sub> overcoats deposited using various sputtering gases*. Journal of Applied Physics, 2003. **93**(10): p. 8710-8712.
- [6.15] Wei, G., A. Rar, and J.A. Barnard, *Composition, structure, and nanomechanical properties of DC-sputtered CrN<sub>x</sub> (0 ≤ x ≤ 1) thin films*. Thin Solid Films, 2001. **398**: p. 460-464.
- [6.16] Marshall, G.W., et al., *Sodium hypochlorite alterations of dentin and dentin collagen*. Surface Science, 2001. **491**(3): p. 444-455.
- [6.17] Ott, R.D., et al., *Nanotribology and surface chemistry of reactively sputtered Ti-B-N hard coatings*. Thin Solid Films, 2000. **377**: p. 602-606.
- [6.18] VanLandingham, M.R., et al., *Nanoindentation of polymers: An overview*. Macromolecular Symposia, 2001. **167**: p. 15-43.
- [6.19] Cappella, B. and G. Dietler, *Force-distance curves by atomic force microscopy*. Surface Science Reports, 1999. **34**(1-3): p. 1-+.
- [6.20] Clifford, C.A. and M.P. Seah, *Quantification issues in the identification of nanoscale regions of homopolymers using modulus measurement via AFM nanoindentation*. Applied Surface Science, 2005. **252**(5): p. 1915-1933.
- [6.21] Davies, M., et al., *Characterization of drug particle surface energetics and Young's modulus by atomic force microscopy and inverse gas chromatography*. Pharmaceutical Research, 2005. **22**(7): p. 1158-1166.
- [6.22] Goken, M., M. Kempf, and W.D. Nix, *Hardness and modulus of the lamellar microstructure in PST-TiAl studied by nanoindentations and AFM*. Acta Materialia, 2001. **49**(5): p. 903-911.
- [6.23] Hodges, C.S., *Measuring forces with the AFM: polymeric surfaces in liquids*. Advances in Colloid and Interface Science, 2002. **99**(1): p. 13-75.
- [6.24] Hodges, C.S., et al., *Forces between polystyrene particles in water using the AFM: Pull-off force vs particle size*. Langmuir, 2002. **18**(15): p. 5741-5748.
- [6.25] Hues, S.M., C.F. Draper, and R.J. Colton, *Measurement of Nanomechanical Properties of Metals Using the Atomic-Force Microscope*. Journal of Vacuum Science & Technology B, 1994. **12**(3): p. 2211-2214.
- [6.26] Jones, R., et al., *Adhesion forces between glass and silicon surfaces in air studied by AFM: Effects of relative humidity, particle size, roughness, and surface treatment*. Langmuir, 2002. **18**(21): p. 8045-8055.

- [6.27] Mader, E., et al., *Bond strength measurement between glass fibres and epoxy resin at elevated temperatures using the pull-out and push-out techniques*. Journal of Adhesion, 2002. **78**(7): p. 547-569.
- [6.28] Morse, K., et al., *Nanomechanical properties of SiC films grown from C-60 precursors using atomic force microscopy*. Journal of Tribology-Transactions of the Asme, 1997. **119**(1): p. 26-30.
- [6.29] Nagashima, N., S. Matsuoka, and K. Miyahara, *Nanoscope hardness measurement by atomic force microscope*. Jsm International Journal Series a-Mechanics and Material Engineering, 1996. **39**(3): p. 456-462.
- [6.30] VanLandingham, M.R., *The Effect of Instrumental Uncertainties on AFM Indentation Measurements* Microscopy Today, 1997 **97**(10): p. pp. 12-15.
- [6.31] Chizhik, S.A., et al., *Micromechanical properties of elastic polymeric materials as probed by scanning force microscopy*. Langmuir, 1998. **14**(10): p. 2606-2609.
- [6.32] Green, C.P., et al., *Normal and torsional spring constants of atomic force microscope cantilevers*. Review of Scientific Instruments, 2004. **75**(6): p. 1988-1996.
- [6.33] Johnson, K.L., J.A. Greenwood, and J.G. Higginson, *The Contact of Elastic Regular Wavy Surfaces*. International Journal of Mechanical Sciences, 1985. **27**(6): p. 383-&.
- [6.34] Sneddon, I.N., *A Note on Problem of Penny-Shaped Crack*. Proceedings of the Cambridge Philosophical Society-Mathematical and Physical Sciences, 1965. **61**: p. 609-&.
- [6.35] Oliver, W.C. and G.M. Pharr, *An Improved Technique for Determining Hardness and Elastic-Modulus Using Load and Displacement Sensing Indentation Experiments*. Journal of Materials Research, 1992. **7**(6): p. 1564-1583.
- [6.36] Field, J.S. and M.V. Swain, *A Simple Predictive Model for Spherical Indentation*. Journal of Materials Research, 1993. **8**(2): p. 297-306.
- [6.37] Oliver, W.C. and G.M. Pharr, *Measurement of hardness and elastic modulus by instrumented indentation: Advances in understanding and refinements to methodology*. Journal of Materials Research, 2004. **19**(1): p. 3-20.
- [6.38] Cabibil, H., et al., *Nanomechanical properties of polysiloxane-oxide interphases measured by interfacial force microscopy*. Langmuir, 2001. **17**(7): p. 2160-2166.
- [6.39] Fischer-Cripps, A.C., *A review of analysis methods for sub-micron indentation testing*. Vacuum, 2000. **58**(4): p. 569-585.

# 7 Electrical Properties

## 7.1. Introduction

Electrical properties of nanoscale materials has become an important topic in recent years[7.1-9] due to the advancements in synthesis and analysis of discrete nanostructures. Structures with nanometer sized dimensions are often observed to exhibit properties that differ considerably from those of measured for the bulk. Such as use of the quantum confinement effect for creation of tunable optical emission from quantum dots. These new effects are important from a fundamental engineering point of view. Potential applications for 1-Dimensional nanostructures, such as carbon nanotube interconnects between different parts of nanoscale circuit devices have already been envisioned[7.10]. Ultimately, the use of new nanomaterials will be highly dependant on their electronic behavior as well as their other physical properties for integration into previously existing manufacturing techniques.

The utilization of self-assembly techniques to create discrete nanoscale electrical components would provide engineers with unmatched flexibility, precision, redundancy, and scaling as compared to current ‘top-down’ methods. However, two of the major challenges facing the development and successful implementation of self-assembled structures for electronics applications lie in the difficulty of both directly characterizing the properties of discrete nanostructures as well as their precise positioning.

Characterization techniques such as 4-point probing and current-voltage (IV) measurements that provide highly reproducible resistivity measurements for bulk materials have been scaled down and successfully utilized for the probing of nanowires[7.11]. There are also have been a wide variety of scanning probe microscopy

techniques (SPM) techniques developed for probing the electrical properties of a variety of nanostructures such as conductive atomic force microscopy (C-AFM)[7.12], scanning capacitance microscopy (SCM)[7.13, 14], electric force microscopy (EFM)[7.15-18], scanning kelvin probe microscopy (SKPM)[7.19-21], and scanning tunneling spectroscopy (STS)[7.22, 23] to name a few.

However, all of the above techniques require at least one direct contact to be made to the structure with the hope that the contact is ohmic, or at the least consistent from one measurement to the next. The contact itself could tend to dominate the reliability of the obtained measurements. For example it has been reported that the measured resistance of polypyrrole nanotubes with C-AFM is decreased as the contact force is increased[7.24]. This makes it difficult but not impossible to compare results obtained from different tips on different samples.

In the case of alkyl-phosphonic (APA) self-assembled nanofibers (SANs), discrete 1-dimensional nanostructures are formed by immersion of aluminum or gallium into ethanolic solutions of APAs and their growth are previously described in Chapter 3. In this case we are interested in probing the electrical properties of individual SANs.

In an attempt to better understand their electrical properties, C1 SANs have been grown on electrically isolated  $\text{Si}_3\text{N}_4$  surfaces for EFM analysis, directly on Au micro-electrodes creating single SAN devices for direct current-voltage measurements.

## 7.2. Electric Force Microscopy

Electrostatic Force Microscopy (EFM) is a non-contact AFM technique that can be utilized to create two-dimensional voltage contrast images of a sample. There are two main EFM modes: scanning Kelvin probe microscopy (SKM or SKPM) and electrostatic force gradient microscopy (EFM-phase). Although SKPM has been successful at imaging the surface potential in various samples in air, there are large errors and poor spatial resolution due to the non-localized Coulomb interactions causing large contributions from the cantilever and tip cone in addition to the tip apex[7.25]. EFM-phase mode, however, is based on the measurement of the force gradient rather than the force itself[7.26] and has been shown to provide quantitative measurements of the surface potential with better than 20 nm resolution in x and y[7.27, 28]. The EFM-phase technique is a two pass tapping mode technique where the topography of the sample is obtained on the first pass and then on the second pass the topography is retraced with the tip lifted a set height above sample. With a carefully chosen lift height, typically 5-200 nm, the tip then only responds to the influences of the DC fields in the sample and not the topography. A force,  $f(z)$ , is sensed by an oscillating metallic tip at some height,  $z$ , above the sample surface due to its interaction with the sample's electrostatic field caused is given as equation[7.27]:

$$f(z) = \frac{1}{2} V^2 \frac{\partial C}{\partial z} \quad [1]$$

where  $V$ , is the DC potential difference between the tip and sample and  $C$ , is the tip sample capacitance. The changing electrostatic force with  $z$  gives rise to a shift in the resonant frequency of the cantilever which in turn creates a phase shift,  $\Delta\phi$ , between the driving signal and detected signal as given by the following equation[7.29]:

$$\Delta\phi \propto \left( \frac{d^2C}{dz^2} \right) (V_{tip} + \phi - V_s)^2 \quad [2]$$

where  $V_s$  is the voltage of the sample,  $\phi$  is the work function difference between the tip and sample,  $V_{tip}$  is the tip voltage, and  $C$  is the tip-sample capacitance. The measured change in the phase signal is thus proportional to the square of the dc voltage difference between the tip and the sample.

The resulting electrostatic interactions create detectable phase shifts that will always be negative, corresponding to the addition of a damping force, no matter whether the potential difference between the tip and sample is positive or negative. This is then observed to create a dark contrast in the lift-mode phase image corresponding to the conductive parts of the sample.

### 7.2.1. Experimental Setup

For this experiment two samples were utilized. First, C1 SANs were grown on a 240 nm thick semiconductor grade  $\text{Si}_3\text{N}_4$  film on silicon using methods previously described in Section 3.2.5.1. A conductive Au contact was deposited onto the resulting C1 SAN mat. The contact was deposited by evaporation through a broken  $\text{Si}_3\text{N}_4$  TEM thin film window. This process is diagramed in Figure 1 image a. The resulting pad measured approximately  $1 \text{ mm}^2 \times 50 \text{ nm}$  thick with a clearly defined edge. The second sample was a set of two conductive Pt lines, approximately 10  $\mu\text{m}$  in length, deposited by FIB onto a identical  $\text{Si}_3\text{N}_4$  coated substrate. Previous work has shown the ability to create conductive Pt nanowires with FIB[7.30]. Prior to FIB deposition, a Au contact was deposited on the substrate in an identical fashion to the first sample. One Pt line was deposited contacting the Au pad and the second was deposited parallel to the Au pad

edge not contacting the Au. In both cases, the substrates were isolated electrically from the AFM stage by gluing a piece of mica between the substrate and a steel puck. The puck was placed on a magnetic sample holder chuck positioned on the DI 3000 AFM Stage. A thin Au wire was attached to the Au pads on each of the samples by application of a small droplet of Ag paint and then carefully placing the end of the wire into the paint drop and allowing it to dry. The end of the wire was curled a few times to provide greater surface area for adhesion. An insulated wire was attached between the Aux 2 port on the DI 3000 and attached to the small Au wire using alligator clips. The required jumpers were configured to allow for software control of the Aux 2 voltage during scanning. Electrical continuity was tested for each sample with a multimeter by setting the Aux 2 voltages to non-zero values and reading the true voltage between the Ag paint and ground. The measured values were within .1 V of the software entered value in all cases and the continuity was considered good.

Cr coated TESP cantilevers acquired from Digital Instruments were utilized for the measurements with k values from 1-5 N/m. The AFM cantilever holder for the DI 3000 AFM was grounded using the appropriate jumper configurations as outlined in the user manual[7.31]. The cantilever was then held at ground for the duration of the experiments. The resistance between the cantilever and a grounding jack on the laboratory wall was tested using a digital multi-meter and the circuit was found to have a nominal resistance on the order of a few Ohms. Images were acquired utilizing a 1 Hz scan rate. To make sure that the true phase shifts were being measured, plane fitting was turned off for both real time and offline within the software.

### 7.2.2. Results

Figure 7.2. is the AFM height and corresponding EFM phase image from scanning of an individual C1 SAN that is covered on one end with a Au electrode. The EFM image in this case was acquired utilizing an 8 V bias on the Au with the conductive tip held at ground. The tip was then scanned in lift-mode at 20 nm above the sample. There are several other shorter SANs that do not make contact to the Au. In general over a wide variety of sample biases (-10V to 10V) and lift-heights (10 nm -150 nm), whether contacting the Au or not the SANs appear lighter than the Au electrode. In the case of the SAN in contact there is a slight dark outline of unknown origin with the center of the SAN being lighter than the surrounding  $\text{Si}_3\text{N}_4$ . The SAN not in contact appears as completely lighter than the surrounding  $\text{Si}_3\text{N}_4$  with no evidence of dark outlining. The dark outlining may possibly be due to contributions due to physical tip-sample interactions with the taller structures under bias.

In the case of the conductive Pt lines deposited with FIB, as seen in Figure 7.3. (a and b), both Pt lines appear dark relative to the  $\text{Si}_3\text{N}_4$  no matter whether they are touching the biased Au pad or not. The width of the Pt lines in the EFM images appear much wider than their corresponding height image widths indicating detection of increased conductivity of the underlying  $\text{Si}_3\text{N}_4$  surrounding the line most likely due to implanted Ga by the ion beam tails.

The Pt lines are twice as wide as the large SAN from Figure 7.2., but have approximately the same height of between 15 and 20 nm. It appears that the rough Au grains in image (a) that are conductive exhibits the dark-light-dark contrast as observed

for the SAN in Figure 7.2. leading to further confusion as to whether there may be a large sample geometry effect that dominates the detected EFM interactions at the nm scale.

Generally it would appear that if the SANs were truly conductive, they should give a distinctive dark contrast in the EFM image no matter whether they are even contacting the biased Au electrode. The dark contrast observed for the Pt line not in contact is likely due to a capacitive effect documented and utilized by others to examine the conductivity of nanostructures without making direct contact[7.32, 33] and is good candidate for further study.

A range of sample biases from -10 V to 10 V were investigated as well as a range of lift heights from 10 nm to 150 nm for both the SAN samples and the Pt lines. At no point were any of the SANs ever observed to give a dark contrast indicative of a conductive material like the Au electrode or conductive carbon nanotubes as reported in the literature[7.29, 33]. The Pt lines always exhibited a dark contrast relative to the  $\text{Si}_3\text{N}_4$  substrate for all biases and lift heights as would be expected for a conductor. Since C1 SANs do not exhibit negative phase shifts relative to the supporting insulating  $\text{Si}_3\text{N}_4$  substrate, they are believed to be in the least very poor conductors and more likely insulators or semi-conductors.

### 7.3. Single C1 SAN Devices

EFM experimentation of single C1 SANs revealed them to be poor conductors and most likely insulators or semi-conductors. In an attempt to more directly measure the electrical properties of individual C1 SANs, single SAN devices were created by deposition of C1 SANs onto pre-fabricated Au microelectrodes utilizing the biased growth techniques as described in Chapter 3.4. The idea was to isolate a single SAN across a gap of known size and then measure individual SAN IV characteristics utilizing an Agilent 4155C SPA J-micro RF Probe Station with Cascade DCM208 series micromanipulators and Kelvin probes having a picoamp noise floor.

One of the Au microelectrode arrays utilized for this experiment is shown in Figure 7.4. A single array consists of Au lines deposited on a SiO<sub>2</sub> coated Si wafer. The Au lines were then coated with another layer of SiO<sub>2</sub> and then back etched to form small openings in the passivation to allow access to the ends of the Au lines. The Au lines were then addressable through larger pads around the edge of an individual die of ~ 0.5 cm x 0.5 cm in size. Initially the entire structure was coated with photoresist, which was stripped by immersion in Sulphuric Acid for 30 minutes, removed and rinsed with 18 MOhm water for 1 minute, and then dried with UHP N<sub>2</sub>. Before striping, the arrays were imaged with SEM to determine which ones were viable since there was a large number that were not. After selection of viable arrays and striping of the photoresist, AFM was performed to make sure that the electrode structures were free of photoresist and to measure the gaps between adjacent Au electrodes. Figure 7.5. shows both SEM and AFM images of a single array showing that the Au lines are approximately 100 nm tall x

400 nm wide spaced  $\sim$  400 nm apart. For each area A-C the six Au lines are actually pairs separated by an even smaller gap on the order of 50 nm.

Before deposition of C1 SANs, IV measurements were taken between each of the sets of electrodes as well between neighboring electrodes from  $-20\text{V}$  to  $+20\text{V}$  to determine if there were any shorts present.

Deposition of C1 SANs was accomplished by utilizing the biased growth techniques described in more detail in Chapter 3.4. An individual array was immersed into a 8.3 mM solutions of C1 and Ethanol. A 3.5 V bias was applied between two Al coated glass electrodes in the solution resulting in  $\sim 1\ \mu\text{A}$  current. Each Al electrode was immersed so that approximately  $1\ \text{cm}^2$  of Al was under solution. The bias was left on for 24 hrs and then the sample removed. AFM imaging was performed prior to further IV analysis to make sure that SANs were deposited.

### **7.3.1. Results**

Deposition of C1 SANs onto Au electrodes for direct electrical testing was accomplished utilizing the biased immersion growth technique, chapter 3.4., and the SANs presence on the electrodes verified with AFM, as seen in Figures 7.4. and Figure 7.5. After C1 SANs were found on these two electrode structures, then IV curves were obtained between the various electrodes. Initially the electrode combinations where SANs were directly observed with AFM were examined, but in the end many different combinations of all the viable electrode combinations were investigated. A current limit was set to 1 nA to protect the SANs and the voltage ramped to 5 V. After no current was observed over the 5 V range the upper limit voltage was increased to 10 V, then 20V and

then finally 40 V. At no point was any detectible current measured that could be correlated to conduction through the SANs that connected adjacent electrodes separated by ~ 400 nm. In the case of electrodes separated by 50 nm gaps, occasionally biasing to 40 V produced an eventual Ohmic response after repeated ramps to 20 V+. These observed conductive paths could not be correlated to SANs bridging the gap. The observed conductivity is thought to be due to migration of the Au in the electrodes forming an ohmic bridge.

For all SANs examined, none exhibited measurable conductivity between -40 V and + 40 V biases. This was surprising given the large electric fields expected across a 400 nm gap. To better understand the electrode geometry and its possible effect on the electrical measurements, a FIB cross-section for Scanning Transmission Electron Microscopy was prepared. This allowed for examination of the electrode composition as well as the true electrode geometries. Figure 7.8. shows the results of the FIB cross-sectioning where we find that there is a potential problem with the electrodes sitting atop a SiO<sub>2</sub> pillar. This geometry was most likely due to over etching the top SiO<sub>2</sub> layer leaving the Au lines sitting higher than the SiO<sub>2</sub> between the lines. Attempts to create FIB cross-sections of the sample with observed SANs as seen in Figures 7.6 – 7.7 all failed to yield any definitive results showing the location of the individual SANs with respect to the Au electrodes. The C1 SANs observed with AFM between electrodes were all less than 20 nm in height so it is highly likely that they may have appeared to cross between the electrodes when in reality they were spanning that distance but not actually in contact due to the electrode sitting on top of the pillar.

It was found that individual SANs observed to connect adjacent Au electrodes with AFM exhibited no measurable conductivity even under biases of 40V. Further examination of the electrode structures by FIB cross-sectioning and STEM revealed that the electrodes sit atop insulating pillars. This created a non-optimum sample geometry which needs to be further optimized to ensure contact between the SANs and the electrodes providing a more viable route to the direct analysis of the SANs electrical properties. Additionally, AFM might need to be performed after the electrical measurements to ensure that the deposited SANs are not broken due to imaging forces, although many IV curves were obtained between electrodes that had not been imaged prior to testing there was still no definitive instances of conductivity detected even when biases up to 40 V were utilized.

It also might be beneficial to utilize electrode structures that replace the SiO<sub>2</sub> dielectric layer with Si<sub>3</sub>N<sub>4</sub>, as SANs are observed to prefer the less polar surface of Si<sub>3</sub>N<sub>4</sub>. While this likely increase the number of SANs on the electrode it might also make it more difficult to isolate individual SANs. For this reason it would probably be best to alter the electrode geometries and back etch SiO<sub>2</sub> passivation layer less, just exposing the tops of the Au electrodes. This would provide a flat growth surface with access to the electrodes. With the electrode's top surface flush with the surrounding SiO<sub>2</sub>, then AFM imaging of the SANs prior to electrical testing would be less damaging as the entire SAN as they would be supported between the electrodes by SiO<sub>2</sub>.

This experiment also showed that the biased growth techniques created are viable for deposition of SANs onto electrode structures and should be applicable to further investigations on optimized substrates.

## 7.4. Discussion

Analysis of the SANs electrical properties proved to be a very difficult task and mainly focused on the qualitative assessment of their conductivity. The EDS, XPS, and EELS results presented in Chapter 4, show that C1 SANs are mainly composed of Al, P, O, and C. EELS and XPS further provided evidence that the Al and P are in fact in non-metallic, and most likely oxidized environment within the SANs. Given an oxidized and non-metallic chemistry, it is reasonable to expect that the SANs would be non-conductive. Further evidence that C1 SANs are non-conductive was shown in Chapter 6, where the STEM e-beam manipulations succeeded in the folding of an unsupported C1 SAN membrane.

EFM results of individual C1 SANs on  $\text{Si}_3\text{N}_4$  contacted through an evaporated Au film agree once again with the previous findings that the SANs are insulating. The C1 SANs exhibited a lighter contrast similar to the underlying  $\text{Si}_3\text{N}_4$  rather than darker contrast observed for the conductive Au film when biased to 8V. This was the case whether they were in contact with the Au electrode or not. To assess what the contrast should look like for a conductive nanostructure utilizing the EFM techniques employed, a control sample was created by deposition of Pt nanowires utilizing a FIB. Two 20 nm x 120 nm x 5  $\mu\text{m}$  long Pt nanowires were deposited onto a  $\text{Si}_3\text{N}_4$  surface having a previously evaporated Au contact. One of the nanowires was deposited perpendicular to the electrode edge making contact with the Au, the other was deposited a few  $\mu\text{m}$  away from the Au contact. Under bias, the EFM contrast of the Pt nanowires appeared darker than the surrounding  $\text{Si}_3\text{N}_4$  and similar to the darker contrast of the Au electrode. The Pt nanowires appeared darker whether in contact with the Au electrode or not, providing

good evidence that the EFM technique can distinguish between conductive and non-conductive nanostructures concluding that C1 SANs are indeed non-conductive.

Additionally, attempts were made to directly measure the voltage and current characteristics of individual C1 SANs. Individual C1 SANs were grown directly onto previously characterized Au micro electrodes utilizing the biased growth techniques described in Section 3.4. The presence of isolated SANs between electrodes was confirmed by AFM prior to electrical measurements. Measurements performed between electrodes with previously observed SANs showed no conductivity for biases up to 40V. No conductivity was observed for measurements made between all other electrodes whether previously scanned by the AFM or not. FIB cross-sections made of the electrode structures revealed a non-ideal geometry of the Au electrodes with respect to the surrounding SiO<sub>2</sub>. The Au electrodes were observed to sit upon SiO<sub>2</sub> pillars, ~ 15 -20 nm tall, due to over etching of the SiO<sub>2</sub>. In the case of the SANs imaged with AFM prior to electrical measurements, breakage of SANs due to imaging was a likely failure mode. In the case of the electrodes not scanned prior to measurement the non-ideal electrode geometry is thought to have contributed to the lack measurable conductivity under bias.

Recommendations for an improved test structure with the top of the Au electrodes flush to the SiO<sub>2</sub> growth surface were made. The creation of single C1 SAN spanning Au electrodes provided a proof of concept for the possibility of SAN deposition onto any surface utilizing the novel biased growth technique.

## 7.5. Figures

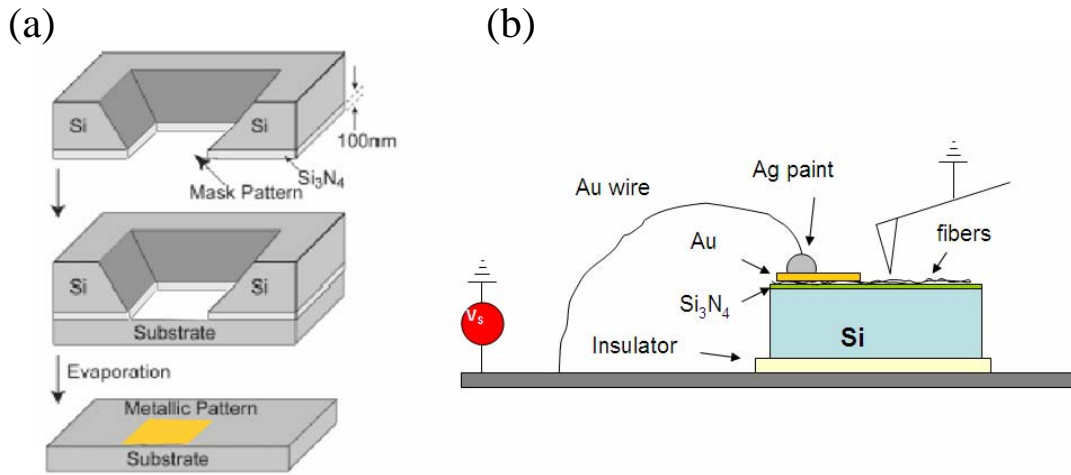


Figure 7.1. The patterned deposition of a  $1 \text{ mm}^2 \times 100 \text{ nm}$  thick Au electrode for making contact to C1 SANs grown on  $\text{Si}_3\text{N}_4$  utilizing a mask made from a broken out  $\text{Si}_3\text{N}_4$  TEM grid, image a. Then electrical contact is made to the isolated Au pad using thin Au wire and Ag paint, image b.

## Height Image

## EFM Image

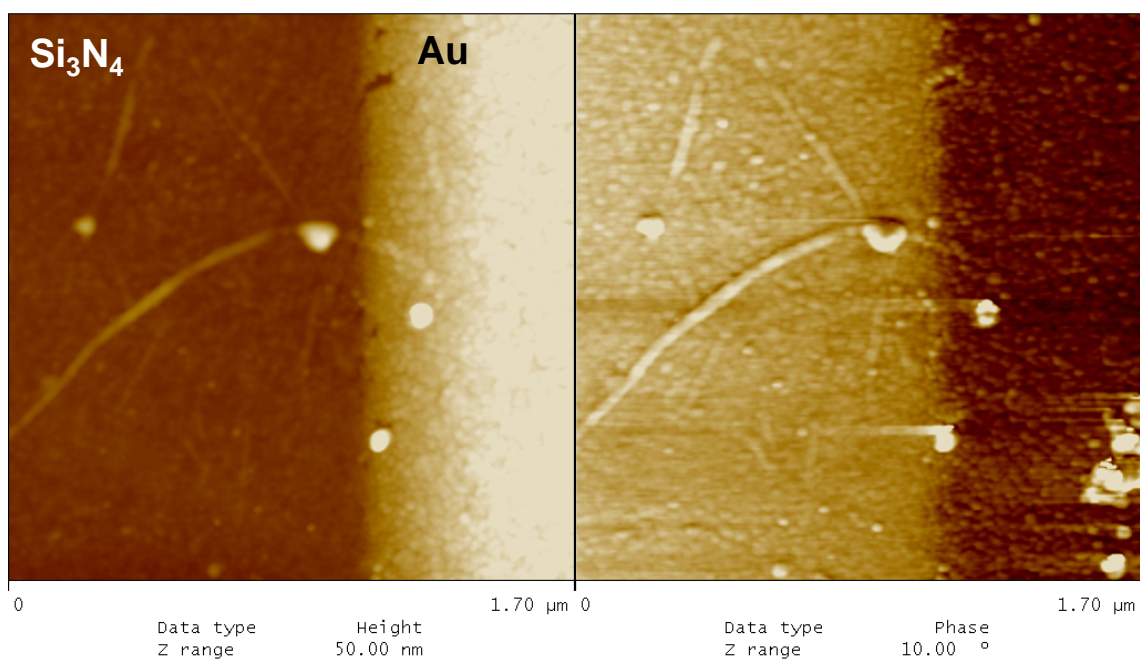
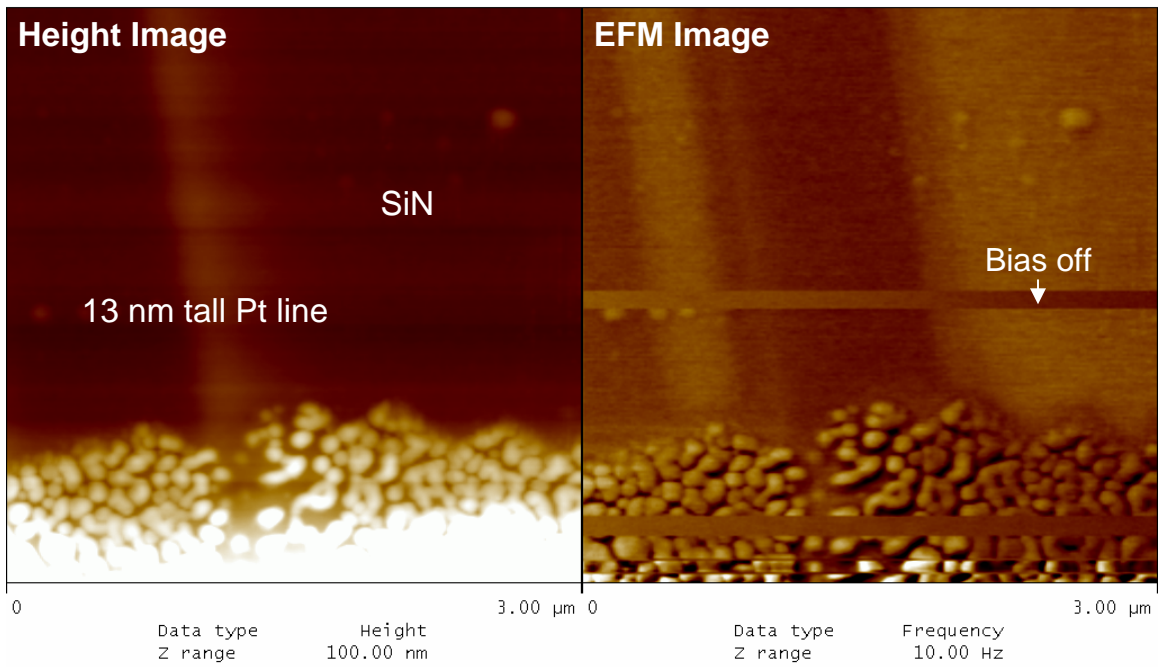


Figure 7.2. AFM height and EFM phase image of C1 SANs on Si<sub>3</sub>N<sub>4</sub> with a 30 nm thick Au electrode. The images were acquired while biasing the Au to 8 V relative to the tip which was scanned at a lift height of 20 nm. The conductive Au electrode appears darker while the SANs appear lighter in the EFM phase image indicating that they are insulating.

### (a) – Pt line in contact with Au



### (b) – Pt line not in contact with Au

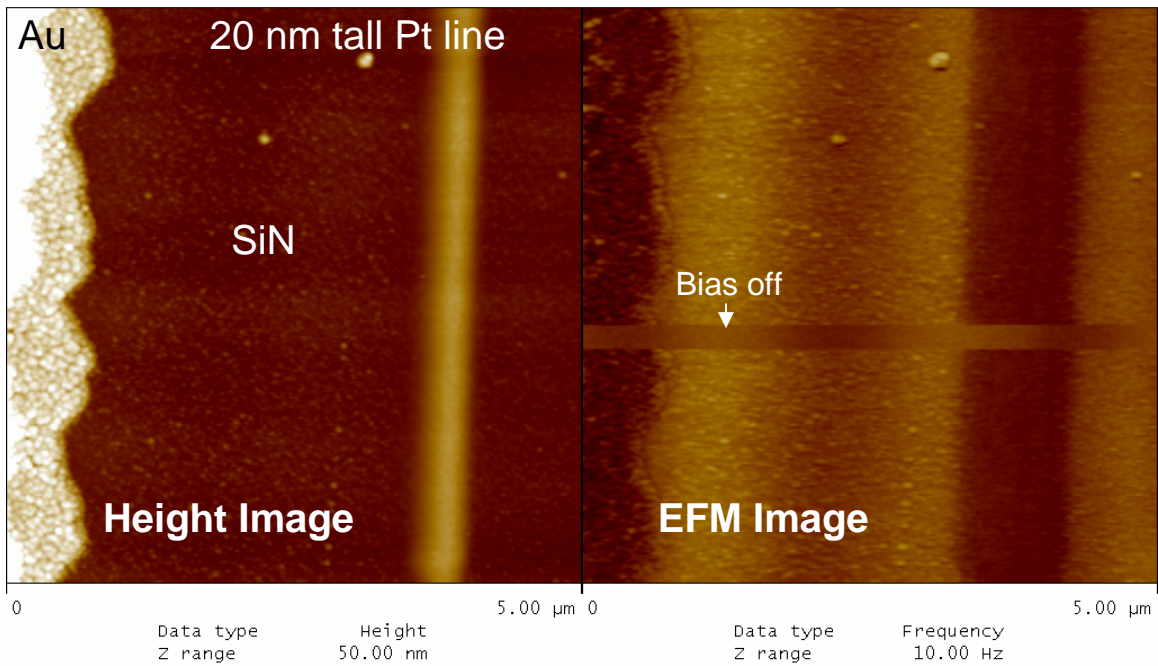


Figure 7.3. AFM height images with corresponding EFM frequency shift images of FIB deposited Pt lines contacting (a) and not in contact (b) with a Au electrode biased at -5 V relative to ground. The lift height was 20 nm and the tip was grounded. Each EFM image a small number of scan lines with the bias set to 0V, two groups in (a) and 1 group in (b) showing the effect due to sample bias.

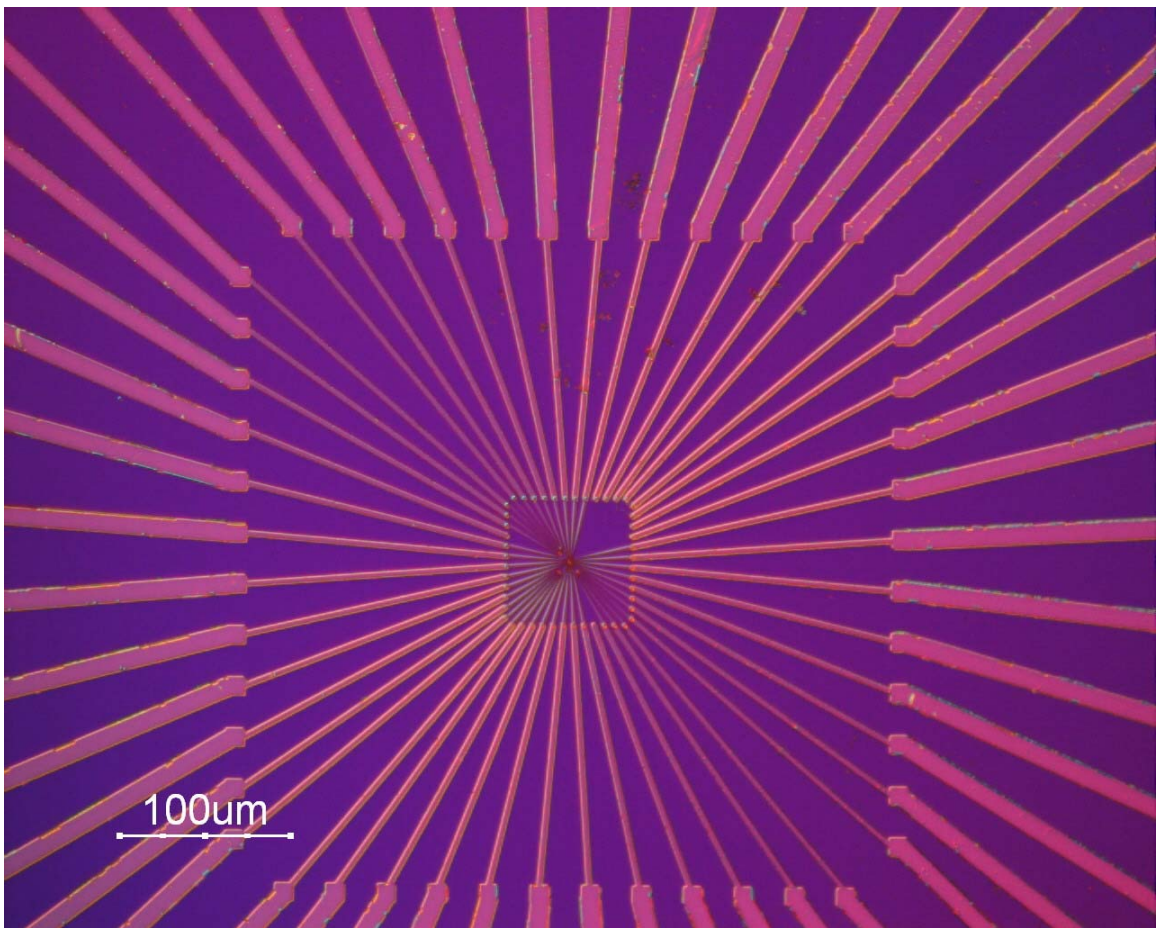


Figure 7.4. Optical Micrograph of Au microelectrode array utilized for creation of single SAN device.

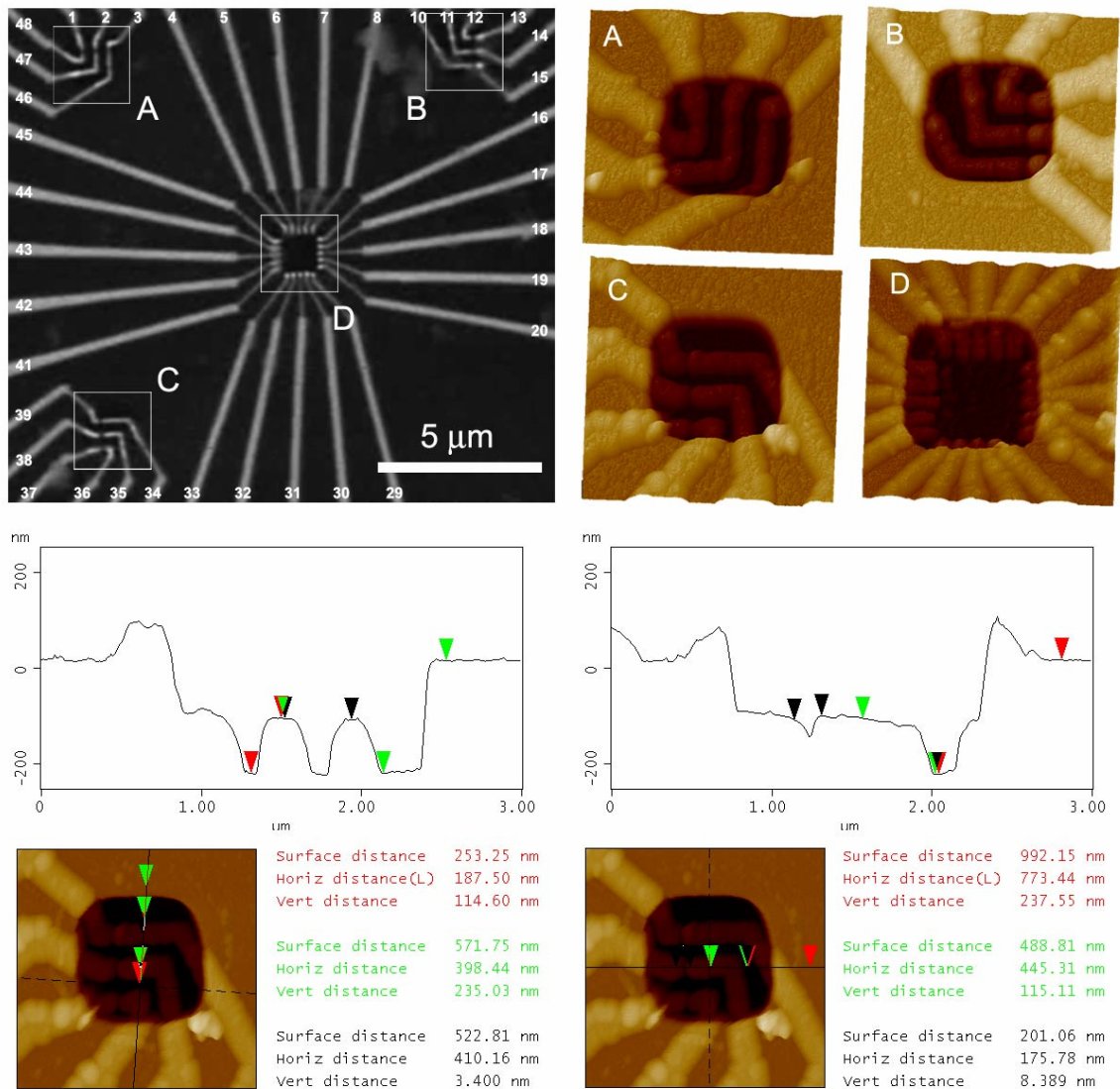


Figure 7.5. SEM image of Au electrode structures, upper left, and corresponding AFM height images, upper right, of the exposed Au micro electrodes (A-D). Areas A-C are essentially the same structure, just rotated. The lower images are cross-sectional analyses of area C showing the dimensions of the Au lines.

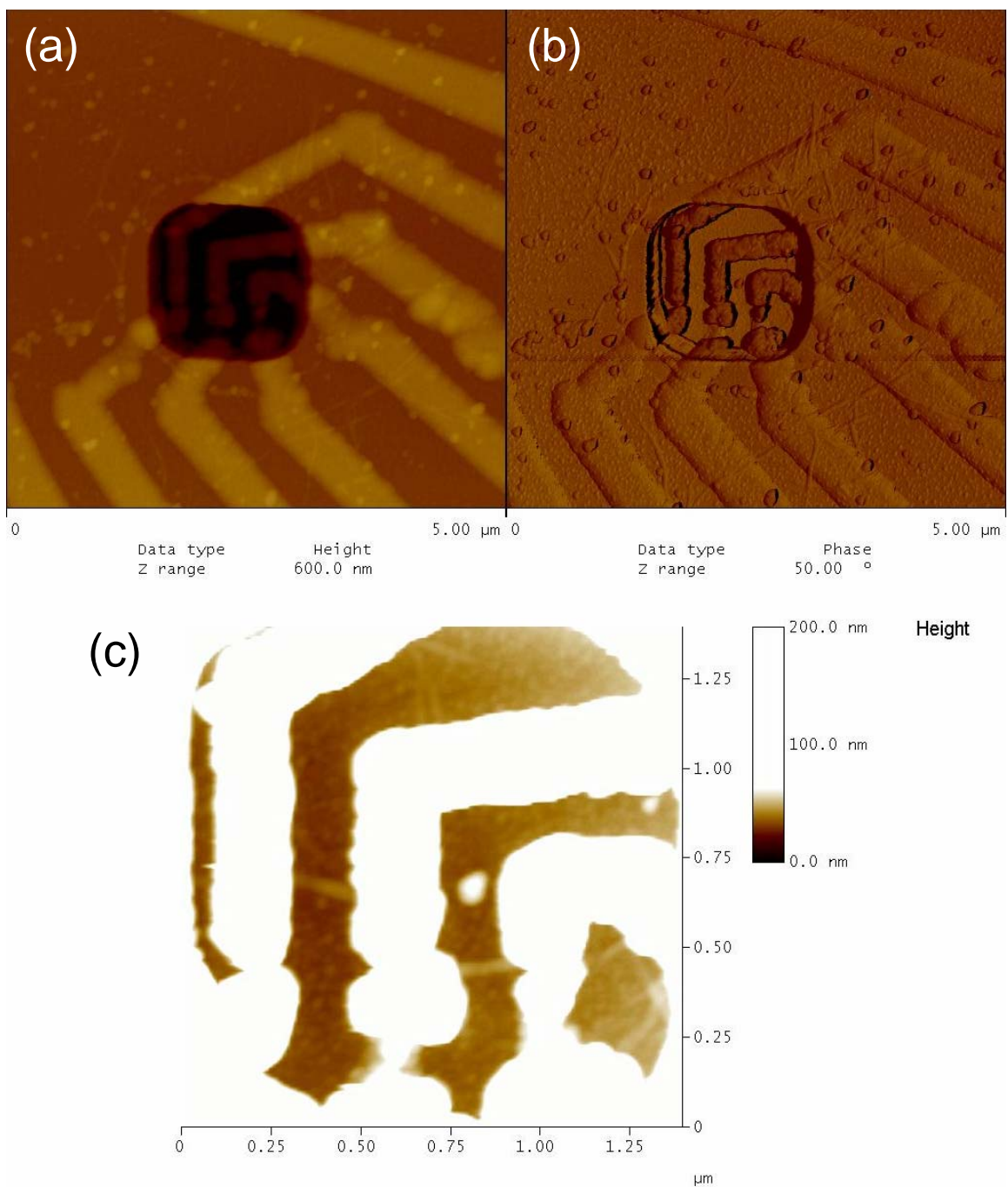


Figure 7.6. AFM height and phase image (a & b) of a single set of electrodes showing the results of 24 hr biased growth of C1 SANs. Height Image (c) shows a zoom in of the electrodes with individual SANs isolated between electrodes.

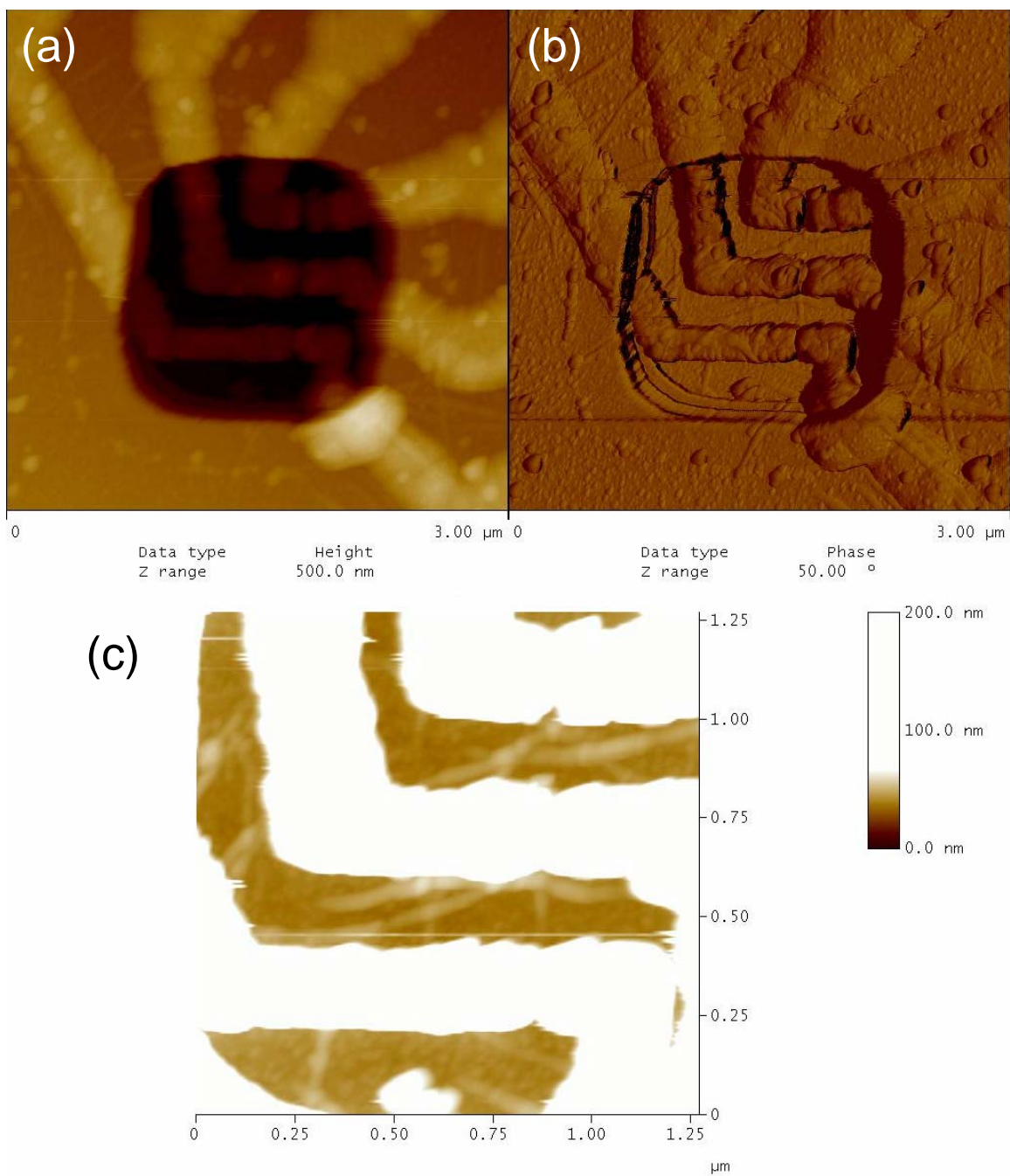


Figure 7.7. AFM height and phase images (a & b) of another electrode set showing more C1 SAN growth between electrodes. Image (c) is a height image zoom of the electrodes emphasizing the SAN growth showing in this case clusters of C1 SANs between the electrodes.

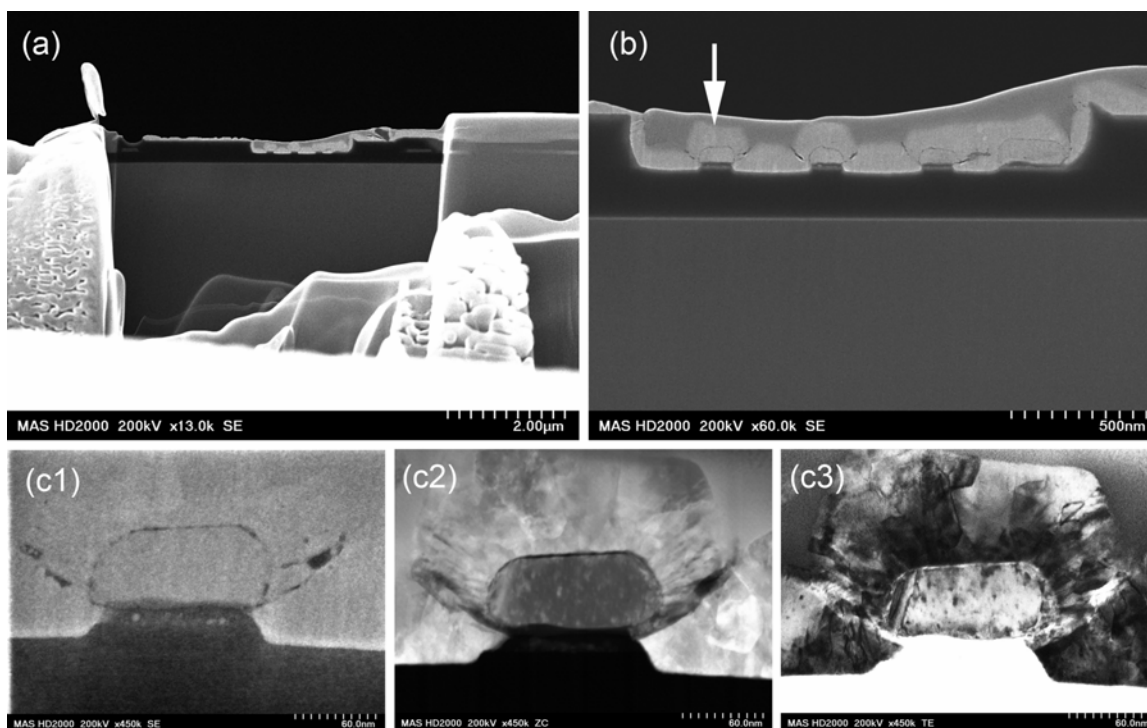


Figure 7.8. A FIB cross-section was created by cutting across the Au electrodes on one array similar to the one shown previously in Figure 7.7. The cross-section was then analyzed with a Hitachi HD-2000 STEM. Image (a) is an SE image showing an overview of the entire cross-section. Image (b) is a SE image showing a zoomed in region of the electrodes. The arrow denotes the individual Au electrode shown in image (c1) SE, (c2) Z-Contrast, and (c3) Bright field. It is clear to see that the Au lines actually sit at top SiO<sub>2</sub> pillars, ~ 20 – 25 nm above the regions between electrodes.

## 7.6. References

- [7.1] Law, M., J. Goldberger, and P.D. Yang, *Semiconductor nanowires and nanotubes*. Annual Review of Materials Research, 2004. **34**: p. 83-122.
- [7.2] Law, M., et al., *Nanoribbon waveguides for subwavelength photonics integration*. Science, 2004. **305**(5688): p. 1269-1273.
- [7.3] Li, D.Y., et al., *Thermal conductivity of Si/SiGe superlattice nanowires*. Applied Physics Letters, 2003. **83**(15): p. 3186-3188.
- [7.4] Choi, H.J., et al., *Self-organized GaN quantum wire UV lasers*. Journal of Physical Chemistry B, 2003. **107**(34): p. 8721-8725.
- [7.5] Goldberger, J., et al., *Single-crystal gallium nitride nanotubes*. Nature, 2003. **422**(6932): p. 599-602.
- [7.6] He, R.R., et al., *Functional bimorph composite nanotapes*. Nano Letters, 2002. **2**(10): p. 1109-1112.
- [7.7] Kind, H., et al., *Nanowire ultraviolet photodetectors and optical switches*. Advanced Materials, 2002. **14**(2): p. 158-+.
- [7.8] Huang, M.H., et al., *Room-temperature ultraviolet nanowire nanolasers*. Science, 2001. **292**(5523): p. 1897-1899.
- [7.9] Hicks, L.D. and M.S. Dresselhaus, *Effect of Quantum-Well Structures on the Thermoelectric Figure of Merit*. Physical Review B, 1993. **47**(19): p. 12727-12731.
- [7.10] Kreupl, F., et al., *Carbon nanotubes in interconnect applications*. Microelectronic Engineering, 2002. **64**(1-4): p. 399-408.
- [7.11] Lin, X., et al., *Four-probe scanning tunnelling microscope with atomic resolution for electrical and electro-optical property measurements of nanosystems*. Chinese Physics, 2005. **14**(8): p. 1536-1543.
- [7.12] Olbrich, A., et al., *A new AFM-based tool for testing dielectric quality and reliability on a nanometer scale*. Microelectronics Reliability, 1999. **39**(6-7): p. 941-946.
- [7.13] Decossas, S., J.J. Marchand, and G. Bremond, *Electrical characterisation of local electronic properties of self-assembled semiconductor nanostructures using AFM*. Physica E-Low-Dimensional Systems & Nanostructures, 2004. **23**(3-4): p. 396-400.
- [7.14] Wiesendanger, R., *Recent Advances in Nanostructural Investigations and Modifications of Solid-Surfaces by Scanning Probe Methods*. Japanese Journal of

Applied Physics Part 1-Regular Papers Short Notes & Review Papers, 1995. **34**(6B): p. 3388-3395.

[7.15] Jespersen, T.S. and J. Nygard, *Charge trapping in carbon nanotube loops demonstrated by electrostatic force microscopy*. Nano Letters, 2005. **5**(9): p. 1838-1841.

[7.16] Zdrojek, M., et al., *Charging and emission effects of multiwalled carbon nanotubes probed by electric force microscopy*. Applied Physics Letters, 2005. **86**(21).

[7.17] Ba, L., et al., *Probing local electric field distribution of nanotube arrays using electrostatic force microscopy*. Journal of Applied Physics, 2003. **93**(12): p. 9977-9982.

[7.18] Zhang, Z.B., et al., *Processing and characterization of single-crystalline ultrafine bismuth nanowires*. Chemistry of Materials, 1999. **11**(7): p. 1659-1665.

[7.19] Nonnenmacher, M., M. Oboyle, and H.K. Wickramasinghe, *Surface Investigations with a Kelvin Probe Force Microscope*. Ultramicroscopy, 1992. **42**: p. 268-273.

[7.20] Nonnenmacher, M., M.P. Oboyle, and H.K. Wickramasinghe, *Kelvin Probe Force Microscopy*. Applied Physics Letters, 1991. **58**(25): p. 2921-2923.

[7.21] Jacobs, H.O., et al., *Surface potential mapping: A qualitative material contrast in SPM*. Ultramicroscopy, 1997. **69**(1): p. 39-49.

[7.22] Kim, H., et al., *Nano-scale structures of a one-dimensional junction*. Thin Solid Films, 2004. **464-65**: p. 335-337.

[7.23] Terrones, M., et al., *N-doping and coalescence of carbon nanotubes: synthesis and electronic properties*. Applied Physics a-Materials Science & Processing, 2002. **74**(3): p. 355-361.

[7.24] Park, J.G., et al., *Electrical resistivity of polypyrrole nanotube measured by conductive scanning probe microscope: The role of contact force*. Applied Physics Letters, 2002. **81**(24): p. 4625-4627.

[7.25] Jacobs, H.O., et al., *Resolution and contrast in Kelvin probe force microscopy*. Journal of Applied Physics, 1998. **84**(3): p. 1168-1173.

[7.26] Gil, A., et al., *Electrostatic force gradient signal: resolution enhancement in electrostatic force microscopy and improved Kelvin probe microscopy*. Nanotechnology, 2003. **14**(2): p. 332-340.

[7.27] Lei, C.H., et al., *Quantitative electrostatic force microscopy-phase measurements*. Nanotechnology, 2004. **15**(5): p. 627-634.

- [7.28] Lei, C.H., et al., *Conductivity of macromolecular networks measured by electrostatic force microscopy*. Applied Physics Letters, 2003. **83**(3): p. 482-484.
- [7.29] Bachtold, A., et al., *Scanned probe microscopy of electronic transport in carbon nanotubes*. Physical Review Letters, 2000. **84**(26): p. 6082-6085.
- [7.30] Marzi, G.D., et al., *Probing intrinsic transport properties of single metal nanowires: Direct-write contact formation using a focused ion beam*. Journal of Applied Physics, 2004. **96**(6): p. 3458-3462.
- [7.31] *Digital Instruments Dimension 3000 Manual*.
- [7.32] Staii, C., A.T. Johnson, and N.J. Pinto, *Quantitative analysis of scanning conductance microscopy*. Nano Letters, 2004. **4**(5): p. 859-862.
- [7.33] Bockrath, M., et al., *Scanned conductance microscopy of carbon nanotubes and lambda-DNA*. Nano Letters, 2002. **2**(3): p. 187-190.

# 8 Conclusions

## 8.1. The Contribution

The focus of this research was the growth and nanoscale characterization of novel alkylphosphonic acid (APA) self-assembled nanofibers (SANs). SANs were initially observed with atomic force microscopy (AFM) on the surfaces of aluminum coated glass substrates after immersion in methylphosphonic acid (C1) ethanolic solutions. Controlled experimentation led to reproducible growth techniques for the creation of novel, supported and free-standing APA SANs, suitable for various complimentary nanoanalysis techniques. Additionally, a novel biased APA SAN deposition technique was realized for the creation of isolated APA SANs on a variety of substrates.

Atomic force microscopy (AFM) and Scanning Transmission Electron Microscopy (STEM) revealed individual SANs were composed of layered fibril bundles. Increased layering was observed for longer immersion times. FFT analysis of C1 SANs' STEM Z-Contrast images revealed the smallest individual fibril width to be 1.5 nm - 2.2 nm. Typically, multiple fibrils clustered together forming larger ribbon type structures. While fibril ordering was observed on 1- 3 nm length scales, unsupported APA SANs imaged in plan view, as well as C1 SANs in cross-section, revealed no evidence of crystallinity under STEM imaging conditions.

A combination of Energy Dispersive Spectrometry (EDS), X-Ray Photoelectron Spectroscopy (XPS), and Electron energy Loss Spectroscopy (EELS) determined the APA SANs as primarily composed of oxygen, carbon, phosphorus, and aluminum with the occasional trace amounts of Ca. XPS compositional analysis of supported C1, C3, and C5

SANs provided phosphorus:aluminum ratios of 2.6, 4.2, and 3.2 respectively. Semi-quantitative STEM EDS analysis of unsupported C1, C3, and C5 SANs provided phosphorus:aluminum ratios of 2.41, 1.94, and 1.5 respectively. Additionally, semi-quantitative STEM EDS analysis of C1 SAN cross-sections provided a phosphorus:aluminum ratio of 2.11. XPS and EELS analyses showed that the aluminum present in the SANs was in a non-metallic and likely oxygen environment. EELS correlated the presence of the aluminum, phosphorus, oxygen, and carbon to a 5 nm area within several overlapping unsupported C1 SANs.

Ex-situ thermal anneals of supported APA SANs with analysis by AFM revealed a nearly 5X increase in thermal stability as compared to the ~ 100C-120C melting points of pure APAs., octadecylphosphonic acid (C18) SAMs[8.5], or C18 bilayers[8.6, 7]. The C5 SAN's structure persisted after a 600C anneal in air. Only after annealing at 650C was melting observed, forming "pearls on a string" type morphology. Slightly lower melting transition temperatures of 550C and 500C were observed for C1 and C3 respectively as both exhibited the same "pearls on a string" morphology as the C5 SANs. The C5 SAN's morphology was observed to remain intact even after a 12 hour anneal at 550C. AFM measurements of the same C1 SAN before and after annealing at 475C provided evidence of mass loss without melting the structure. The observed changes are thought to be due to water evolution or possible calcination of the SAN structure.

STEM Z-Contrast images of broken C1 SAN membranes appeared to undergo brittle fracture exhibiting jagged morphologies and chipping. Z-Contrast imaging of propagating crack fronts provided evidence of a complex fracture mode, with local plastic deformations due to the sliding between cracked fibrils and layers. Plastic deformations were confined to

short 50 – 100 nm distances by the intersections of overlapping SANs. Further evidence of cracking and layer sliding was observed in phase images of C3 and C5 SANs after AFM nanoindentation and scratching. Quantitative AFM nanoindentation was performed on supported C1, C3, and C5 SANs as well as a PET film of known modulus. A Hertzian model was utilized to estimate the reduced elastic moduli ( $E^*$ ). The  $E^*$  of the C1, C3, and C5 SANs were determined to be 10.52 +/- 2.24 GPa, 3.78 +/- 0.72 GPa, and 1.25 +/- 0.63 GPa respectively. Further Hertzian analysis of C5 SANs nanoindentation data acquired with two different cantilevers having force constants of 0.73 N/m and 66 N/m gave  $E^*$  values of 1.20 +/- 0.60 GPa and 1.83 +/- 0.67 GPa respectively. The values for  $E^*$  of the C5 SANs from all three cantilevers were in good agreement showing the consistency of the technique.

Electron beam manipulations of an unsupported C1 SAN membrane with STEM provided qualitative evidence that the SANs were non-conductive. Further experimentation with EFM on supported C1 SANs on  $\text{Si}_3\text{N}_4$  provided additional qualitative evidence of their insulating character. Attempts made at direct electrical measurements of individual C1 SANs deposited across Au microelectrodes were unsuccessful.

## 8.2. Future Work

As described in Chapter 3, the creation of novel unsupported APA SAN membranes allowed for STEM Z-Contrast imaging with EELS that provided definitive correlation of Al, P, O, and C within the C1 SANs structure. Core loss analysis of the aluminum  $L_{2,3}$  edge, showed it to be more indicative of the aluminum in  $Al_2O_3$ . As a reliable FIB lift-out cross-sectioning technique was recently developed, Section 4.2.2.3, STEM EELS of APA SAN FIB cross-sections is proposed. The samples of choice would be made from APA SANs as grown directly on evaporated Al. It is envisioned that these samples would provide access to at least two and possibly 3 to 4 different aluminum chemistries within the same sample. Each of these should be identifiable through observed changes in the aluminum  $L_{2,3}$  edge onset and near edge fine structure[8.8]. EELS data could be collected in line scan mode, or spectral imaging mode if available, across the different allowing comparisons of the acquired EELS spectra with focus on the shape and position of the aluminum  $L_{2,3}$  edge.

In addition to EELS compositional and chemical analysis of core loss data, low loss data analysis should be performed in order to examine the electronic and optical properties of the SANs. Analysis of EELS data and extraction of the dielectric properties of Alumina has been previously reported[8.9]. Low-loss EELS analysis of previously obtained C1 SANs data is currently underway, but initial results have been inconclusive. Much of the problems that need to be overcome are due to large zero-loss contributions from poor spectrometer resolution and non-optimized acquisition parameters. Refinement of the current EELS chemical and electrical characterization methods could be utilized to further illuminate the fundamentals of APA SAN formation.

Additionally, in-situ electrochemical tapping mode AFM (EC-TMAFM) would be particularly well suited for detailed growth investigations. Based on the previous biased growth results, utilization of an EC-TMAFM fluid cell would allow for the controlled creation and deposition of SANs. Various combinations of electrode materials, solvents, or APA chemistries could be examined. Other possibilities might include the alignment of APA SAN growth utilizing magnetic fields and an appropriate magnetic metal precursor such as Fe or Ni.

Specialized substrates could be created with optimized micro-electrode structures, as described in Section 7.5. Ultimately, this optimized electrode structure could be integrated onto a custom ProtoChips<sup>TM</sup> DuraSIN<sup>TM</sup> electron transparent membranes. The membranes could be specially designed for in-situ electrical analysis within a specialized STEM holder. APA SANs or a variety of other materials could be deposited onto the substrates using a variety of methods with in-situ testing in the STEM to follow. This would provide an integrated way to study both growth as well structure and properties of the same APA SANs.

### 8.3. References

- [8.1] El Haskouri, J., et al., *S+I- ionic formation mechanism to new mesoporous aluminum phosphonates and diphosphonates*. Chemistry of Materials, 2004. **16**(22): p. 4359-4372.
- [8.2] Edgar, M., et al., *Structure elucidation of a novel aluminum methylphosphonate, Al-3(CH<sub>3</sub>PO<sub>3</sub>)<sub>2</sub> center dot O center dot(OH)(3), through a combination of X-ray powder diffraction, solid-state NMR spectroscopy, and computational energy minimization*. Chemistry of Materials, 2002. **14**(8): p. 3432-3439.
- [8.3] Maeda, K., et al., *Structure of Aluminum Methylphosphonate, Almepo-Beta, with Unidimensional Channels Formed from Ladder-Like Organic-Inorganic Polymer-Chains*. Journal of the Chemical Society-Chemical Communications, 1995(10): p. 1033-1034.
- [8.4] Maeda, K., et al., *Almepo-Alpha - a Novel Open-Framework Aluminum Methylphosphonate with Organo-Lined Unidimensional Channels*. Angewandte Chemie-International Edition in English, 1995. **34**(11): p. 1199-1201.
- [8.5] Neves, B.R.A., et al., *Thermal stability study of self-assembled monolayers on mica*. Langmuir, 2000. **16**(6): p. 2409-2412.
- [8.6] Fontes, G.N., R.L. Moreira, and B.R.A. Neves, *Thermally induced stacking of octadecylphosphonic acid self-assembled bilayers*. Nanotechnology, 2004. **15**(5): p. 682-686.
- [8.7] Fontes, G.N. and B.R.A. Neves, *Effects of substrate polarity and chain length on conformational and thermal properties of phosphonic acid self-assembled Bilayers*. Langmuir, 2005. **21**(24): p. 11113-11118.
- [8.8] Williams, D.B. and C.B. Carter, *Transmission electron microscopy : a textbook for materials science*. 1996, New York: Plenum Press. xxvii, 729 p.
- [8.9] French, R.H., H. Mullejans, and D.J. Jones, *Optical properties of aluminum oxide: Determined from vacuum ultraviolet and electron energy-loss spectroscopies*. Journal of the American Ceramic Society, 1998. **81**(10): p. 2549-2557.